Phoenix Stereo Surface Imager (SSI)
University of Arizona Document No. 415640-1200 Rev. A
August 24, 2007

FM SSI Calibration Report

Created By: RT 8-31-2007

Reviewed By: RR 8-31-2007

Approved By:_____ Peter Smith

Approved By:_____ Mark Lemmon

Approved By:_____ Christopher Shinohara

Change Record

Change Description	Date	Sections modified

Table of Contents

Radiometry

A - Bias and Dark model – ML

A.1 Test Setup and Data Acquisition

A.2 Data Processing

A.3 Model

B - Flat field -

B.1 Background

The flat field imaging tests was completed using the SSI inside the Thermal Vacuum Chamber (TVC) peering through the windows in the TVC and into a Labsphere INC. integration sphere. Data is used to generate the flat field images used in SSI calibration. The FM SSI was under the control of IFSW for acquisition of the entire imaging set. The image data series was completed in sequential order per eye and one temperature at a time from 23 C^o to -65 C^o to cover the nominal operational range of the SSI on Mars. Various temperatures inside the camera head and the TVC were logged continuously throughout the test, for which there are log files that span from the beginning to end of the test sequence. The final goal of this test was to generate a series of flat fields that mapping the morphology of the SSI CCD's in every filter and over the temperature range of 23 C^o to -65 C^o.

Table B-1 Target temperature range:

Left Eye	Right Eye
23 C	23 C
5 C	5C
-15 C	-15 C
-40 C	-30 C
-65 C	-40 C
	-65 C

Table B-1 outlines the various temperatures that the individual filters have flat field data for.

Table B-2 Filters:

Filter #	Center Wavelength	Application	Filter #	Center Wavelength	Application
L1	672 nm	Stereo Pair	R1	672 nm	Stereo Pair
L2	445 nm	Stereo Pair	R2	445 nm	Stereo Pair
L3	451 nm	Atmospheric	R3	671 nm	Atmospheric
L4	990 nm	Water	R4	935 nm	Water
L5	886 nm	Water	R5	935 nm	Water
L6	830 nm	Surface	R6	445 nm	Diopter
L7	802 nm	Surface	R7	753 nm	Surface
L8	861 nm	Surface	R8	753 nm	Surface

L9	901 nm	Surface	R9	753 nm	Polarizer
L10	932 nm	Surface	R10	604 nm	Surface
L11	1001 nm	Surface	R11	533 nm	Surface
L12	967 nm	Surface	R12	485 nm	Surface

Table B-2 Outlines the 24 filters inside the SSI filter wheel, there center wavelengths, general scientific purpose and allow for correlation to flat field data. The images below show how the SSI was setup in the TVC chamber and with the integration sphere in order to generate the flat field images in the different filter and in both eyes.

B.2 Test Setup and Data Acquisition

Testing and processing steps:

1. Place integration sphere in the field of the SSI
2. Remove external light sources and turn on integration sphere lighting
3. Capture 5 images of the integration spheres flat field with integration times that give good contrast and dynamic range.
4. Capture 1 shutter per every 5 regular images, to capture the shutter light errors (This requires an image with 0 integration time)
5. Switch filter and repeat process
6. Adjust the integration sphere for second eye.
7. Repeat data taking per filter.

Primary Equipment:

The integration sphere used was a custom made by Labsphere inc. and was purchased by the DISR team for there calibration efforts, seen in figure B-3. The specification of the integration sphere is it was one of two, part of the OGSE 1A and OGSE2 12" diameter with an 8 inch open port on the front, the product order number was CSTM-IS-120-SF, ATAG A019924 and A019925.

Images of the TVC chamber open and ready to receive the SSI and an image of the SSI looking out through the copper thermal shield inside the TVC.

Figure B-1 TVC chamber and SSI setup.

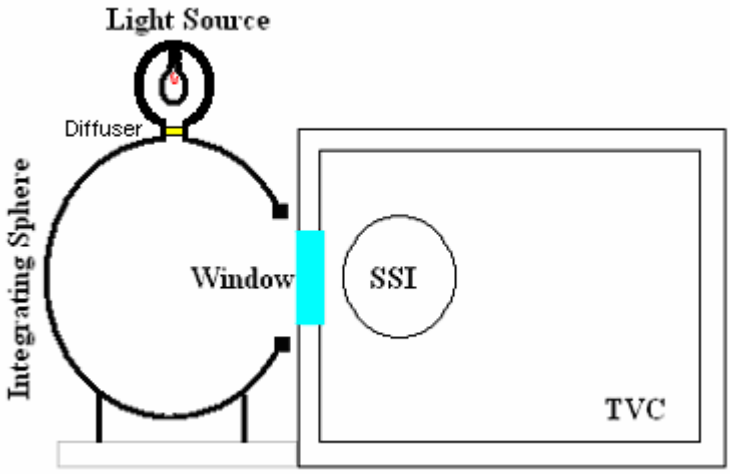

Figure B-2. Drawing of the basic test setup.

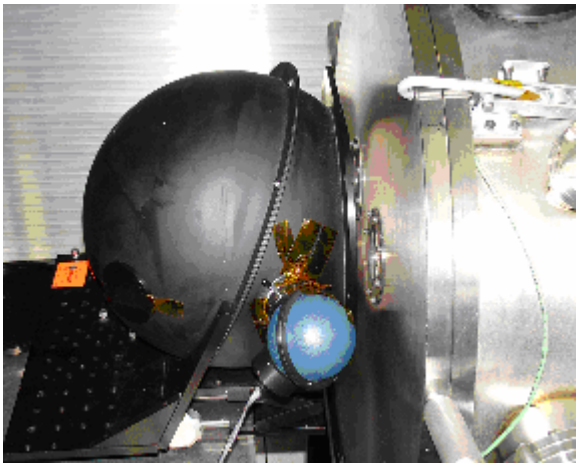

Figure B-3. Image of the test setup.

Software:
There were primarily two software programs used to do the analysis in this report; IDL programs listed below and Microsoft Excel. The IDL programs were used to do image manipulation and measure DN values. Excel was used to collect the data form IDL and to calculate, manipulate and plot the different effect and results of the analysis.

Image Files:

Listed below is the path location to the imaging data used the analysis process.
/support_files_for_flat_fields

Raw data:
/support_files_for_flat_fields/Flats

Processed flat field's images:
/support_files_for_flat_fields/Flat Field Images

Master Flats:
/support_files_for_flat_fields/Master Flats

Spreadsheet:

List below is the path location of the spreadsheets used to calculate the unknown coefficients and store measured data.
/support_files_for_responsivity

1. Flat Field Replacement.xls (filter replacement sheet)
2. SSI_Flat_Fields_main_NEWDARK.xls (data storage sheet)

Log Files:

There are two files that log all of the temperatures, times and header information coming for the SSI.
/support_files_for_flat_fields

1. SEQ_FLAT_FIELD_FM_TESTING_06-17-06.log
2. SEQ_FLAT_FIELD_LOGS_06_14_06.log

Flat Field IDL Programs:

List below is the path location of the IDL tools used to analyze the responsivity data.
/support_files_for_flat_fields/IDL_Code

1. "fmssi_makeflat_wdarkmodel_wSlmodel.pro" (generate stacked images)
2. "im_read.pro" (displays images)
3. "master_flats.pro" (generate master flats)
4. "radial_cosine_plot.pro" (analyze radiometry fall off)
5. "reattach_dark_strips_with_ds.pro" (corrects image acquisition problem)

B.3 Data Processing

Continued analysis steps:

8. Stack the 5 regular image together and subtract image error, creating a flat field for each filter over the normal operational temperature range.
9. Normalize the flat field using the mean of the center 250x 250 to create the master flat series.
10. Test data to obtain list of bad flats
11. Test flats of similar wavelength and temperature to replace bad flats
12. Create final filter list

Flat-field Generation Code:
All IDL code used is located on shell.lpl.arizona.edu in:
/home/mars/Phoenix/SSI/Calibration_reports/Flat_Fields/IDL_Code

To generate the flat-fields the following steps were taken:
1) The images were first corrected for the pixel offset problem and the dark/null strips reattached using reattach_dark_strips_with_ds.pro. Prior to running this routine the central 1024x1024 image region existed in a separate file to the left and right dark/null strips. Also, the dark/null strips had been

removed symmetrically by the flight software when in actuality they are asymmetrical in nature, plus the entire image had been shifted by 1 column on Left Eye images by a flight software error that existed at the time (See: Left Eye Column Slip Issue). The product used for the flat field generation was a 1024x1024 raw image that was re-sliced from the reassembled and corrected (if left eye) image with the correct asymmetrical dark/null strips.

2) The flat-fields were generated by running fmssi_makeflat_wdarkmodel_wSlmodel.pro. When run the code prompts first for flat-field frames and then for shutter frames. The headers are read in and the CCD temperature, exposure time and time of exposure retained. Flight software SEQ logs are then parsed and cross correlated with the times of image exposure to pick out the CCD electronics temperature for the correct eye reported closest in time to the time of image exposure.

3) The images are now read in dark subtracted[1] and stacked in an array, once they have all been read in, the rounded mean value of each pixel in the stack is calculated in a separate 1024x1024 integer array**.**

4) The shutter image is now read in, dark subtracted and subtracted from the average dark subtracted flat frame formed in step (3).

5) The final integer flat is then saved as a 1024x1024 headerless binary, along with a stretched jpeg for easy viewing. The standard deviation of the pixel values in the central 1004x1024 area is also printed out to tip off the operator to any problems. These integer flats are located on shell.lpl.arizona.edu in: /home/mars/Phoenix/SSI/Calibration_reports/Flat_Fileds/flats with the extension .img.

Master Flat Generation:

1) The master flats are generated using master_flats.pro. The code first prompts the user for the directory to be used and then reads in all of the .img files present one by one.

2) For each .img found, the minimum, maximum, mean and median pixel values of the image are reported to the user and then the integer image is recast as double precision and divided by the mean of the central 256x256 area. The minimum, maximum, mean and median pixel values of the resulting double precision frame are reported and it is written to a header-less binary 1024x1024 double precision image file with the extension .master_flat instead of the .img of the original integer flat. These files can be found in the same location as the integer flats.

3) An annotated histogram of the master flat-field is generated and saved alongside.

Reference Documents:

1. [1]415640-1151_RevA_FM_SSI_Dark_Model_Generation.doc
2. See "FM_SSI_Calibration_Data.doc" for image correction and dark model info, written by Adam Shaw, /home/mars/Phoenix/IDL/FMSSI_Cal/
3. See "SSI FRD V&V" for list of FRD requirements to be met.

Uncertainty Equations and Analysis:

$$\mathrm{Im}\ age\ \_\ Uncertiaty\ = \left(\frac{\left[\frac{\sqrt{Mean\ \_\ DN * Gain\ \_(e^{-}/DN, eye)}}{\sqrt{Number\ \_\ of\ \mathrm{Im}\ ages}} \right]}{Mean\ \_\ DN\ \_\ Level} \right)$$

$$Dark\ \_\ Uncertiaty\ = \left(\frac{\left[\frac{\sqrt{Mean\ \_\ DN * Gain\ \_(e^{-}/DN, eye)}}{\sqrt{Number\ \_\ of\ \mathrm{Im}\ ages}} \right]}{Mean\ \_\ DN\ \_\ Level} \right)$$

$$Shutter\ \_\ Light\ \_\ Uncertiaty\ = \left(\frac{\left[\frac{\sqrt{Mean\ \_\ DN * Gain\ \_(e^{-}/DN, eye)}}{\sqrt{Number\ \_\ of\ \mathrm{Im}\ ages}} \right]}{Mean\ \_\ DN\ \_\ Level} \right)$$

$$SL\ \_\ Dark\ \_\ Uncertiaty\ = \left(\frac{\left[\frac{\sqrt{Mean\ \_\ DN * Gain\ \_(e^{-}/DN, eye)}}{\sqrt{Number\ \_\ of\ \mathrm{Im}\ ages}} \right]}{Mean\ \_\ DN\ \_\ Level} \right)$$

$$Gain = (47.5318, Left) = (51.9546, Right)$$

$$Final\ \_\ Uncerta\ \mathrm{int}\ y\ = \sqrt{(\mathrm{Im}\ age)^2 + (I\ \_\ Dark)^2 + (SL)^2 + (SL\ \_\ Dark)^2}\ = RSS$$

Image Analysis:

The images below were generated using the IDL program "fmssi_makeflat_wdarkmodel_wSlmodel.pro" which takes five flat field images removes the dark and bias error by use of the dark model, averages them on the pixel-by-pixel basis, subtracts the shutter light (0 integration time image) after its been dark and bias corrected and generates a final flat field image. The last step in the IDL process is for the code to deliver the mean DN values for the image stack, dark, shutter light and dark shutter light for uncertainty calculations. Figures B-4 and B-5 are example of the images that would be processed together into the final product.

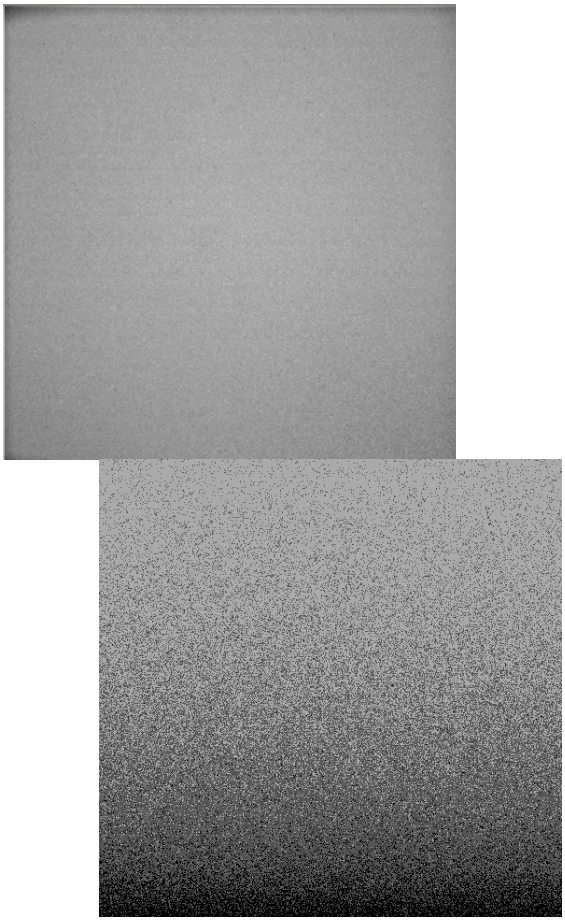

Figure B-4. One of 5 flat field images used to construct a flat field stack (left) and shutter light image which is a 0 itm exposure taken at the same time as the flat field images (right).

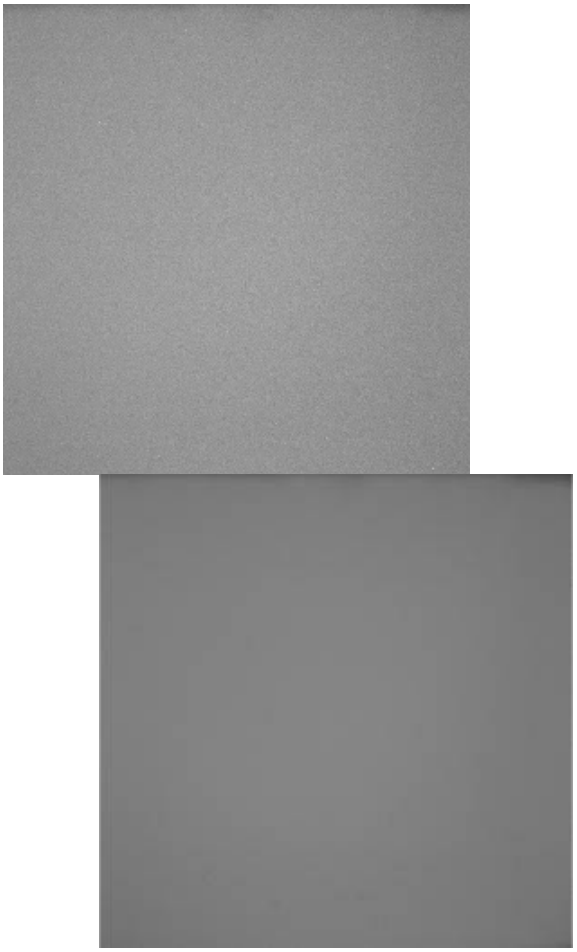

Figure B-5. Examples of Flat Field images with both dark and shutter light subtracted for R2 at -15 C^o and R12 at 5 C^o

The images below were generated using the IDL program "Phoenix_Viewer_v1_02" found on home/mars/Phoenix/IDL/viewer and are example of the type image and histogram that are typical for the flat fields.

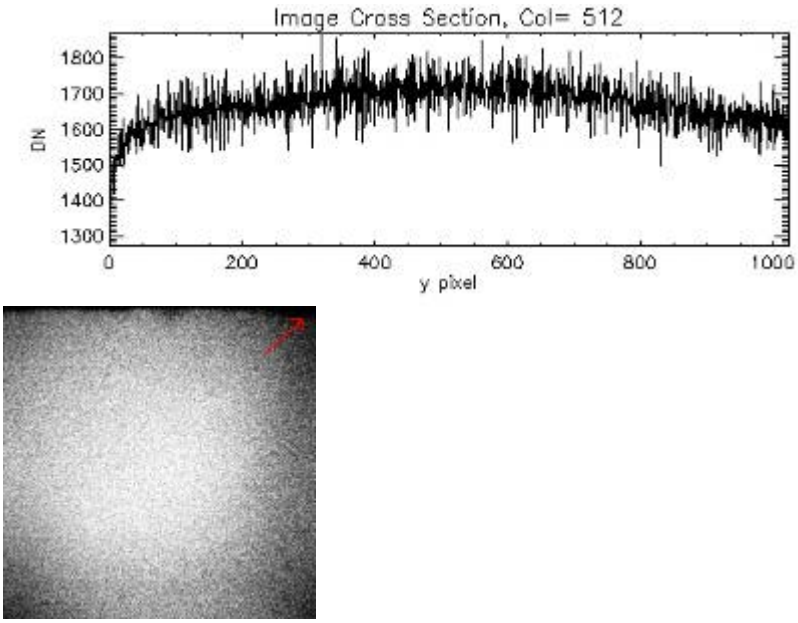

Figure B-6. Histogram in the x-axis of DN values verse pixel location on R2 at -15C^{o} (Left) and a image of the R2 flat field with DN vignetting at the edges (right).

Generate Master flat:

The second stage is to normalize the stacked flats that were generated previously into the final master flats. The procedure is to take the center 256 x 256 area of the stacked flat field, average the DN level and then divide the entire 1024 x 1024 flat field images by the floating point average of the 256 x 256 (described in section B.2). This will be used as the final image correction, using IDL program 'master_flats.pro'.

Radiometric fall off:

If the flat field level is plotted verses the angle off axis, you will see a $\cos^4(x)$ fall off in DN as you move off axis. Figure B-7 is a graph of the DN values as you move radially out from the center of the flat field image. The curve below does not completely match the expected radiometric curve at the corners, (pixels > 650), due to the fold mirror mount vignetting, which was a known minor problem. The effects of the fold mirror mounting will show as a tapered triangle in the two of the corners of the image.

The graph below shows the radiometry falloff plot that was generated using "radial_cosine_plot" available on home/mars/Phoenix/Flat fields/IDL code. The IDL code takes the DN level of the pixels in an expanding radius outward from the center of the flat field image and plot them against the $\cos^4(x)$ fall off curves from the center of the image to the edge. The additional departure comes from image vignetting that is a known constant

inside the geometry of the SSI camera itself and a pixel number jump when reaching the sides of the 1024 x1024 image. This is due to the right and left most columns which have pixel values significantly different than the adjacent columns. This effect can be seen at 512 pixel point.

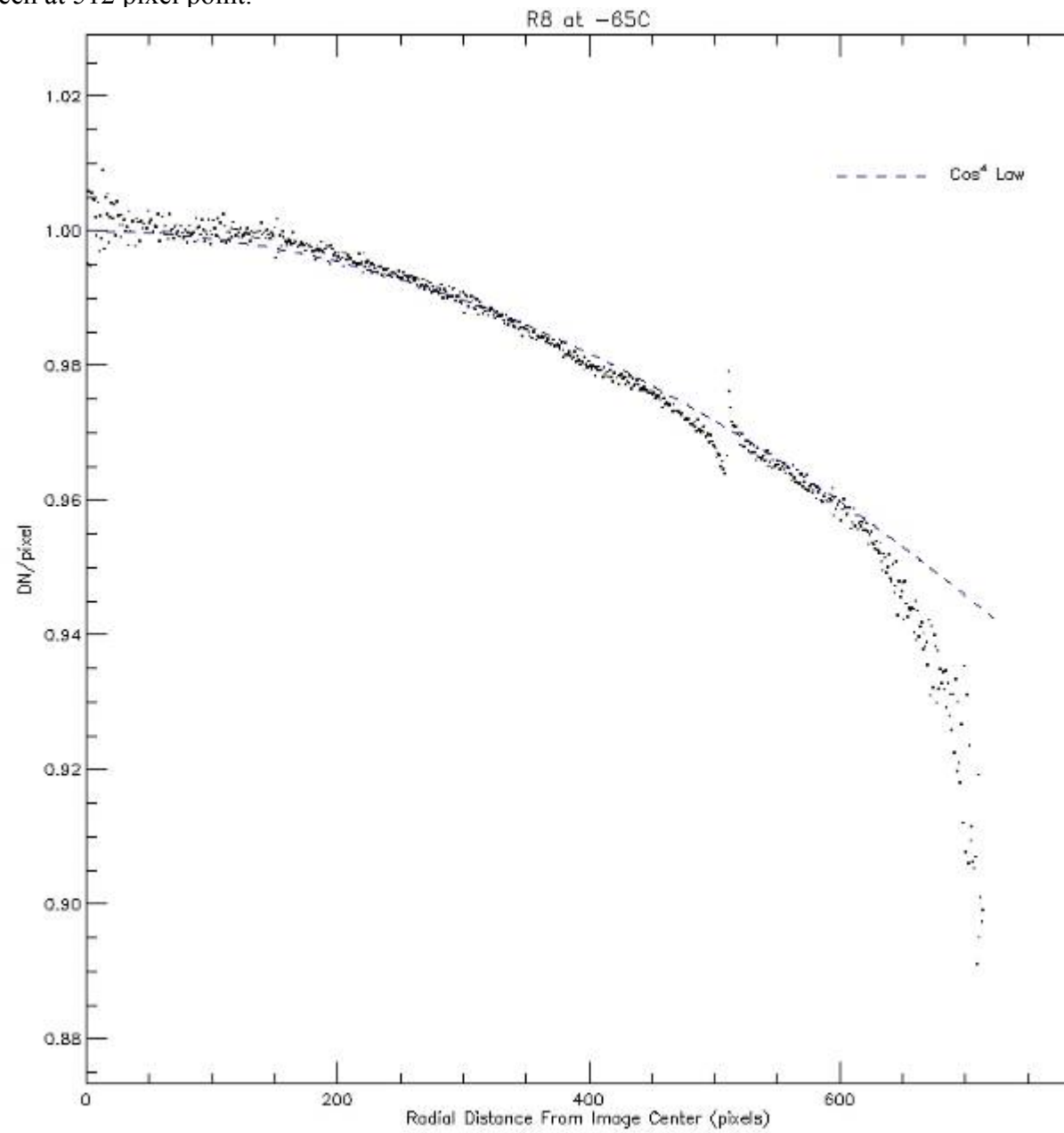

Figure B-7. The DN values in the R8 (-65C^{0}) flat field <u>master</u> fall off when observed from center to edge, this fall off in DN is consistent with the cos^{4}(x) radiometric

B.4 Master Flats - Geology Filters

Table B-3 and B-4 show the correlation of the CCD, Optical Bench and chamber temperatures per SSI filter. In Table B-IV is the percent uncertainty per filter for the left eye of the SSI and in Table B-V is the percent uncertainty per filter for the right eye of the SSI

Table B-3 Uncertainty Percentage for SSI Left Eye

Filter #	CCD T(C^o)	Optical Bench T(C^o)	Chamber T(C^o)	% error	Filter #	CCD T(C^o)	Optical Bench T(C^o)	Chamber T(C^o)	% error
1	25.6	22.3	23	0.16	1	-36.9	-39.3	-40	0.13
2	25.6	22.3	23	0.23	2	-34.9	-38.7	-40	0.16
6	24.3	22.3	23	0.15	6	-38.6	-42.7	-40	0.13
7	24.1	21.8	23	0.16	7	-34.7	-37.8	-40	0.14
8	24.2	22.0	23	0.15	8	-39.2	-41.8	-40	0.13
9	24.4	22.0	23	0.15	9	-38.9	-41.3	-40	0.14
10	24.6	22.2	23	0.13	10	-34.5	-37.3	-40	0.13
11	24.7	22.3	23	0.13	11	-34.2	-37.2	-40	0.14
12	24.9	22.3	23	0.13	12	-34.0	-37.0	-40	0.14
1	2.3	0.4	5	0.14	1	-56.9	-61.1	-65	0.13
2	4.1	1.0	5	0.14	2	-57.3	-61.2	-65	0.15
6	4.7	1.6	5	0.14	3	-58.8	-62.3	-65	0.13
7	4.4	2.0	5	0.13	3	-58.1	-63.5	-65	0.14
8	4.4	2.2	5	0.13	4	-57.7	-62.0	-65	0.68
9	4.5	2.4	5	0.14	4	-58.5	-63.4	-65	0.15
10	4.7	2.6	5	0.12	5	-59.9	-63.2	-65	0.15
11	5.0	2.7	5	0.12	5	-58.7	-62.1	-65	0.12
12	5.2	2.8	5	0.13	6	-58.1	-61.1	-65	0.16
1	-17.8	-20.7	-15	0.13	7	-58.2	-61.4	-65	0.14
2	-16.4	-20.7	-15	0.15	8	-58.0	-61.1	-65	0.17
6	-17.1	-20.8	-15	0.13	9	-57.9	-61.1	-65	0.14
7	-17.7	-20.9	-15	0.14	10	-57.7	-61.1	-65	0.13
8	-18.2	-21.1	-15	0.13	11	-57.7	-61.0	-65	0.16
9	-18.2	-21.3	-15	0.14	12	-57.3	-61.3	-65	0.13
10	-18.5	-21.4	-15	0.13					
11	-18.4	-21.5	-15	0.13					
12	-18.3	-21.6	-15	0.14					

Table B-3 Results of the flat field stacking and dark subtraction for the SSI left eye.

Table B-4 Uncertainty Percentage for SSI Right Eye

Filter #	CCD T(C°)	Optical Bench T(C°)	Chamber T(C°)	% error	Filter #	CCD T(C°)	Optical Bench T(C°)	Chamber T(C°)	% error
1	25.1	21.7	23	0.16	1	-28.3	-33.5	-30	0.14
2	25.3	21.2	23	0.23	2	-27.7	-33.9	-30	0.17
6	23.5	20.4	23	0.22	6	-30.4	-34.9	-30	0.16
7	25.0	22.5	23	0.16	7	-29.5	-33.2	-30	0.14
8	25.0	22.5	23	0.16	8	-29.5	-33.2	-30	0.14
9	25.1	22.5	23	0.15	9	-29.4	-33.3	-30	0.14
10	25.1	22.5	23	0.16	10	-28.4	-32.8	-30	0.15
11	25.3	22.3	23	0.15	11	-27.5	-32.4	-30	0.15
12	25.2	22.0	23	0.13	12	-28.7	-33.6	-30	0.15
1	4.6	2.4	5	0.15	1	-34.5	-39.3	-40	0.14
2	6.8	2.8	5	0.14	2	-34.9	-40.3	-40	0.16
6	8.4	3.5	5	0.14	6	-37.2	-41.5	-40	0.17
7	8.0	4.0	5	0.15	7	-33.5	-36.8	-40	0.14
8	7.3	4.2	5	0.15	8	-33.6	-37.0	-40	0.14
9	7.3	4.3	5	0.15	9	-33.7	-37.3	-40	0.14
10	7.5	4.5	5	0.16	10	-33.9	-37.7	-40	0.14
11	7.7	4.6	5	0.16	11	-34.0	-38.1	-40	0.15
12	8.4	4.8	5	0.15	12	-34.4	-38.7	-40	0.15
1	-14.7	-19.8	-15	0.14	1	-58.6	-63.6	-65	0.13
2	-14.3	-20.2	-15	0.17	2	-57.9	-64.1	-65	0.14
6	-16.2	-20.5	-15	0.21	3	-58.1	-63.5	-65	0.13
7	-15.8	-19.2	-15	0.14	4	-58.5	-63.4	-65	0.21
8	-15.7	-19.2	-15	0.14	5	-58.7	-62.1	-65	0.21
9	-15.5	-19.3	-15	0.14	6	-58.8	-63.8	-65	0.17
10	-15.4	-19.4	-15	0.15	7	-62.5	-65.2	-65	0.13
11	-15.0	-19.5	-15	0.16	8	-61.9	-65.0	-65	0.12
12	-15.0	-19.6	-15	0.16	9	-61.3	-64.7	-65	0.13
					10	-60.6	-64.3	-65	0.14
					11	-59.6	-64.1	-65	0.14
					12	-58.4	-64.0	-65	0.14

Table B-4 Results of the flat field stacking and dark subtraction for the SSI right eye.

Uncertainty Graphs:

The plots in figures B-8 & B-9 show the uncertainty calculation of the left and right eye of the SSI per filter. The plots show the raw uncertainty of the SSI camera, the uncertainty of the integration spheres used and the 1% uncertainty line that every flat field resides below. Flat fields generated from the images for solar filters R3, R5, and L3 showed high uncertainties due to low signal levels and the resulting shot noise in these images. These filters will use the most similar filter for flat fielding. Most of the effects being compensated for with a flat field are not related to the filter, but are camera related. These are vignetting in side the camera, radiometric fall off in the lens illumination of the CCD, and, pixel

by pixel variation in QE. Filters R3, R5 and L3 were plotted using the filter most closely associated center wavelength and adopts their uncertainty. The flat field substitution for filter R3 (671 nm) is filter R1 (672 nm), for filter R5 (935 nm) is filter R4 (935 nm) and finally for filter L3 (451) is filter L2 (445).

Integration sphere:

The integration sphere itself contributes to the uncertainty calculation of the final flat fields. Based on the information obtained from the manufacture the flatness uniformity of the output window is on the order of 0.49%. Therefore the final uncertainty per filter per temperature must be RSS added to the camera uncertainty and is plotted in figures B-8 & B-9.

The graphs below are a composite of the uncertainty error calculated in the flat field stack images, plus the uncertainty in the integration sphere illumination based on calibration data from the manufacturer. The graphs display the raw image error, then the image plus integration sphere error and finally the 1% uncertainty line that the requirements state all filters must reside under.

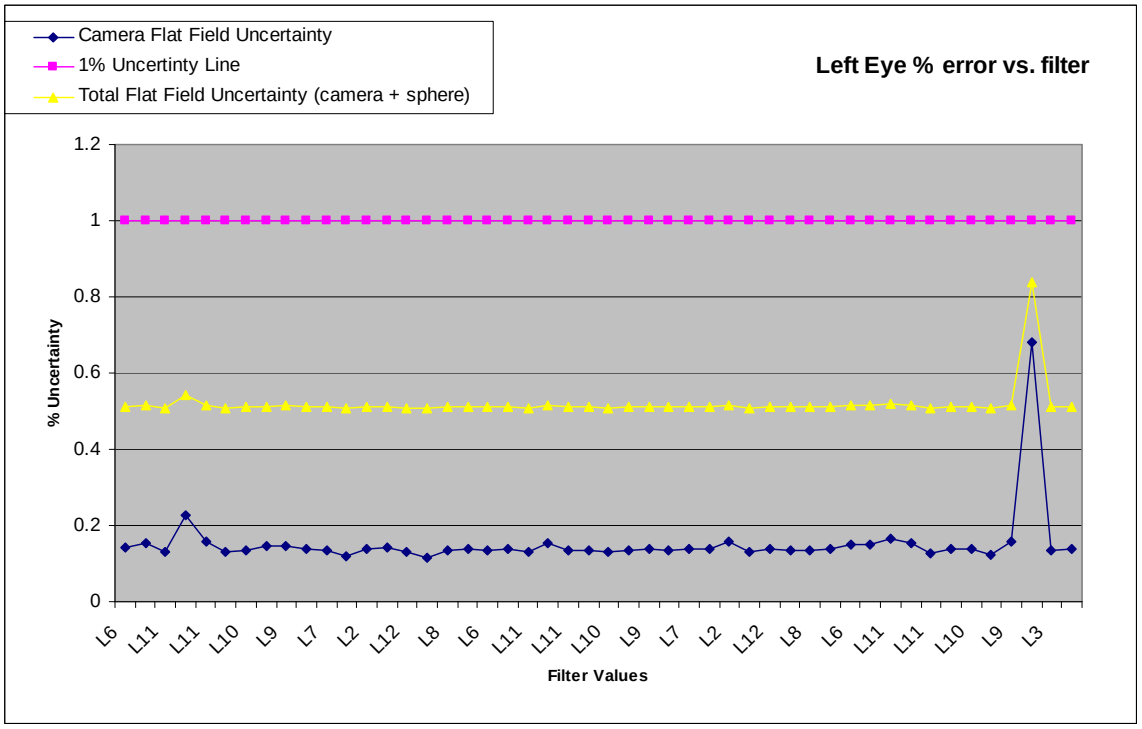

Figure B-8. Shows the final uncertainty values for all (Left Eye) filters across the 23C^{o} to -65C^{o} temperature range.

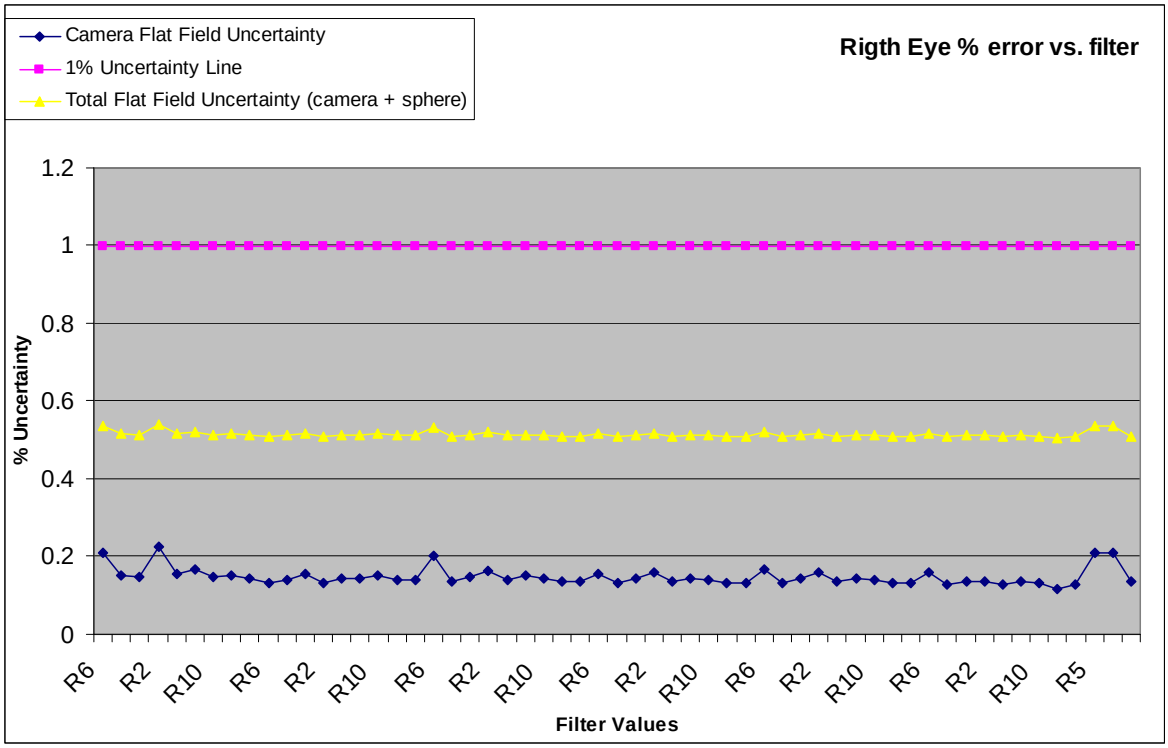

Figure B-9. Shows the final uncertainty values for all (Right Eye) filters across the 23C^{o} to -65C^{o} temperature range.

Conclusion from the Uncertainty plots:

The data shown in figure B-8 & B-9 outline the results of the imaging analysis and errors inherent in the integration sphere. It can be concluded from these graphs that the summation of errors for each flat field has an uncertainty of less than 1%.

B.5 Master Flats - Solar Filter Substitution

R3, R5 and L4 Flat Fields:

Flat fields generated for the R3, R5 and L4 filters at minus 65 C do not meet the specified requirement, due to limitation in the testing setup. The high uncertainty is due to the low DN values that were achieved through the filter at the time of testing. The maximum integration time of 65535 itm or 5.4 minutes was used; however the filter did not transmit more than a few tens of DN. The uncertainty rises with the fall in DN over the standard 2000 DN count. The final result is high uncertainty in the L4 filter. The images had a mean DN value around 30 and with 1 DN of RSS noise, give an uncertainty of ~1/30 or ~3%. There are similar problems with both the R3 & R5 filter. This is an expected effect of the low light level in the test setup and having a low transmission of the solar filter; it is not a problem with the filters or

system itself. The data in the R3, R5 and L4 filters was only taken at -65 C^o

As mentioned above, the flat fields for R3, R5 and L4 solar filters will use the flat field from a filter with similar wavelength and in the same eye. As a verification of our process, the original unacceptable flat field image is divided by the substitution flat field image to inspect for structure. If the composite looks pretty gray and no visual structure is seen, then there is a good substitution.

This image was generated using the standard flat field process described in this document and then dividing one flat field by the other on a pixel-by-pixel basis. The circle seen in the bottom right hand area of the ratio image is a ghost image caused by scattered light or back reflections in the SSI. The circle is only a relative increase in 10 to 30 DN over the background, which has been stretched to between 800 and 900 DN. Shown below are an example of the image division method used for anaylsis.

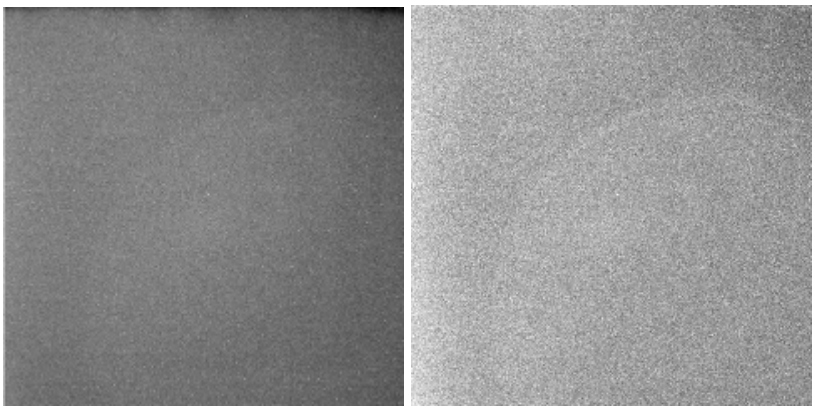

Figure B-10. Original R3 flat field at -65 C^o (left) and test image generated by dividing the R3 (671 nm) flat field by the R1 (672 nm) flat field.

Replacement Flats Field

A replacement table was generated in order to cover the entire temperature/filter range with valid flat fields; this table lays out suitable flats that will be used in place of unsatisfactory flats. This is necessary because several of the solar did not meeting the general specification for the SSI, there was also missing data and a few of the flats having been generate from image data outside the linear QE response of the CCD, invalidating them

During the imaging comparison described above it was uncovered that not all of the filters were displaying acceptable comparisons over similar wavelengths. As a result the same comparison shown in the next section was run on the same filter but at different

temperatures. Examples of a bad flat and the replacement flat of it can be seen in figure B-11 and B-12.

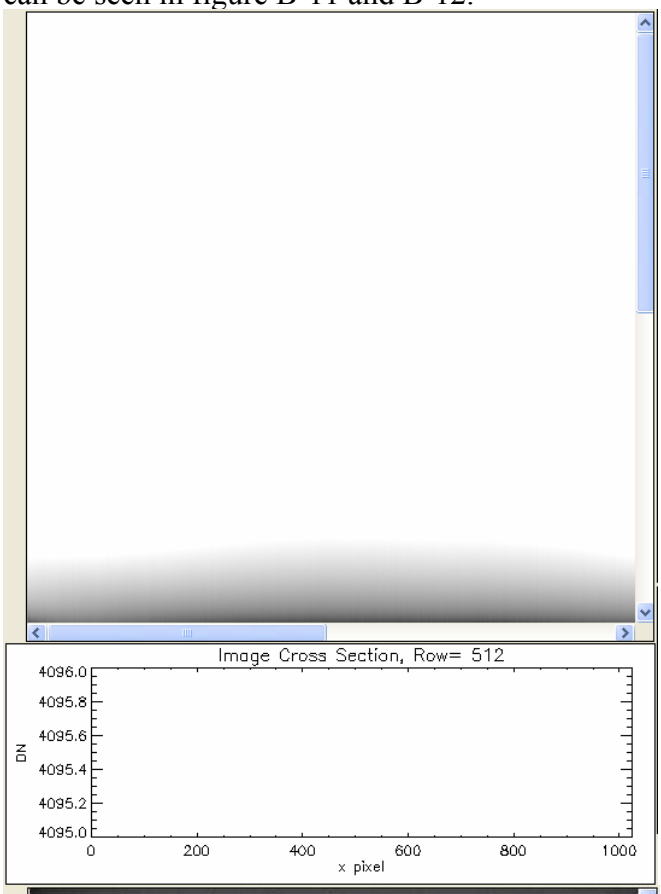

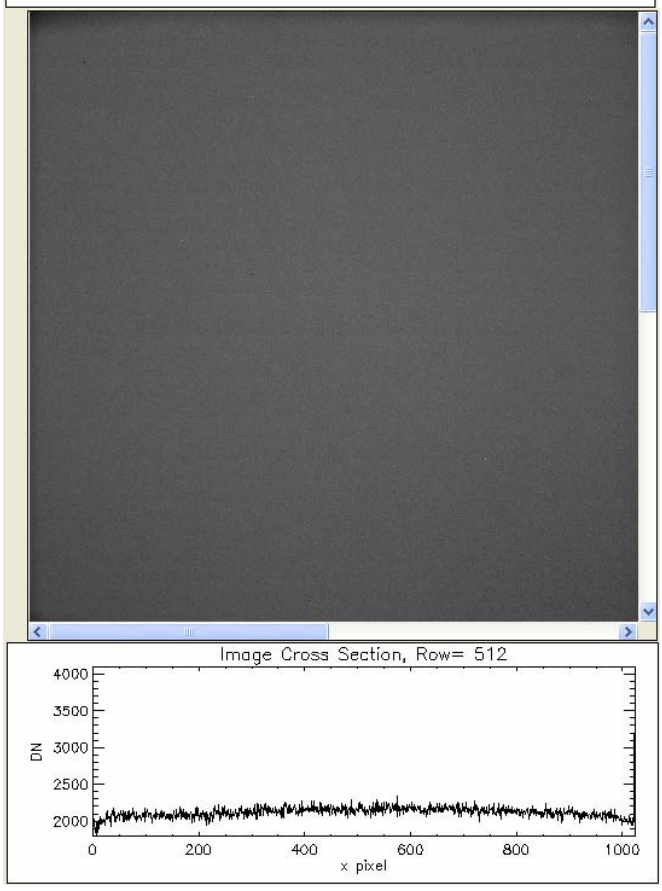

Figure B-11. Saturated L2 at 23 C^{o} (left) and the replacement L2 at -15 C^{o}.

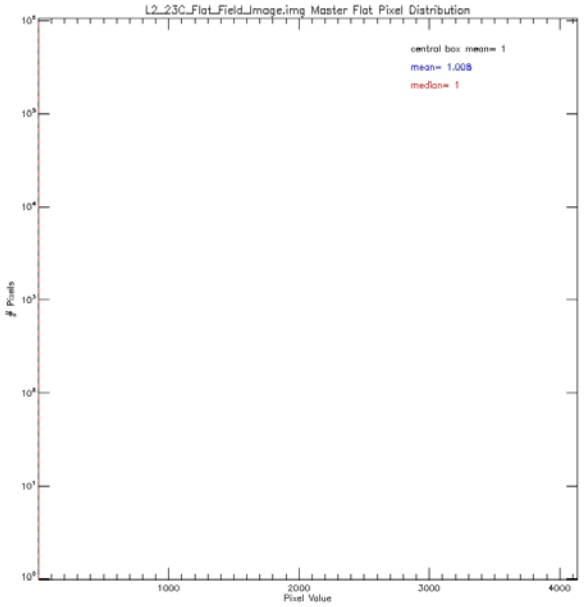

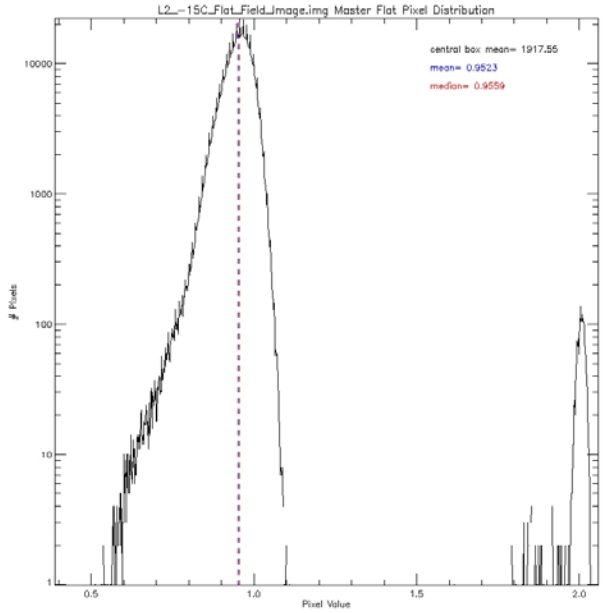

Figure B-12. Histogram of saturated L2 at 23 C^{o} (left) and histogram of the replacement L2 at -15 C^{o}.

Table B-5 Replacement flat field List

Temp ©	Original Filter	Replace With	Temp ©	Original Filter	Replace With
23	L2	L2 at -15C	23	R2	R2 at -15C
23	L3	L2 at -15C	23	R3	R1 at 23C
23	L4	L11 at 5C	23	R4	R4 at -65C
23	L5	L9 at 23C	23	R5	R5 at -65C
23	L10	L10 at -15C	23	R6	R6 at -15C
23	L11	L11 at -15C	23	R12	R12 at 5C
23	L12	L12 at 5C	5	R2	R2 at -15C
5	L2	L2 at -15C	5	R3	R1 at 5C
5	L3	L2 at -15C	5	R4	R4 at -65C
5	L4	L11 at 5C	5	R5	R5 at -65C
5	L5	L9 at 5C	5	R6	R6 at -15C
5	L11	L11 at -15C	-15	R3	R1 at -15C
-15	L3	L2 at -15C	-15	R4	R4 at -65C
-15	L4	L11 at -15C	-15	R5	R5 at -65C
-15	L5	L9 at -15C	-30	R3	R1 at -30C
-40	L3	L2 at -40C	-30	R4	R4 at -65C
-40	L4	L11 at -40C	-30	R5	R5 at -65C
-40	L5	L9 at -40C	-40	R3	R1 at -40C
-65	L3	L2 at -65C	-40	R4	R4 at -65C
-66	L4	L11 at -65C	-40	R5	R5 at -65C
-67	L5	L9 at -65C	-65	R3	R1 at -65C
			-65	R4	R4 at -65C
			-65	R5	R5 at -65C

B.6 Temperature sensitivity

Analyzing flat fields over temperature is all about relative DN/sec changes between pixels: correcting for pixel to pixel differences, illumination fall off and vignetting. In order to uncover these deviations, normalized flat fields of one temperature will be divided by a normalized flat of another temperature in order to check for pixel to pixel variations. The purpose of this comparison is to be able to conclude whether a given flat can be used universally for that filter at any temperature or whether flats will need to be swapped out at different temperatures. Seen below are the L1/R1 results of the variable temperature comparison test.

L1

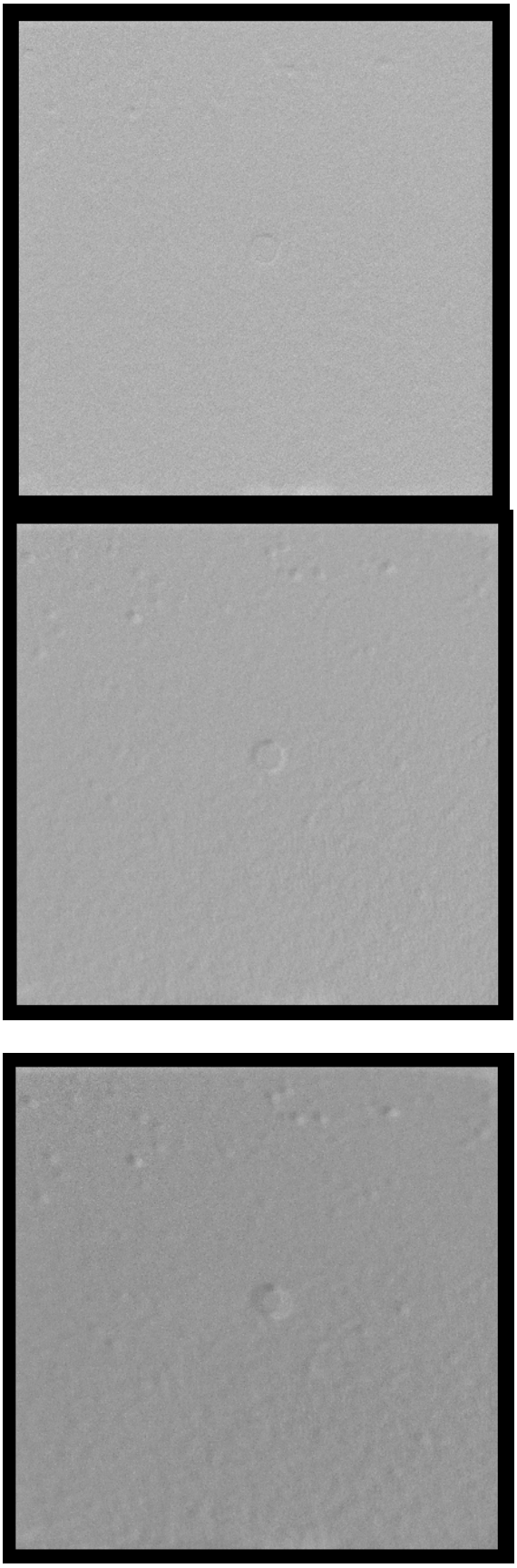

Figure B-11. L1 filter data comparing 5C to -5C, 5C to -40C and 5C to -65C

R1

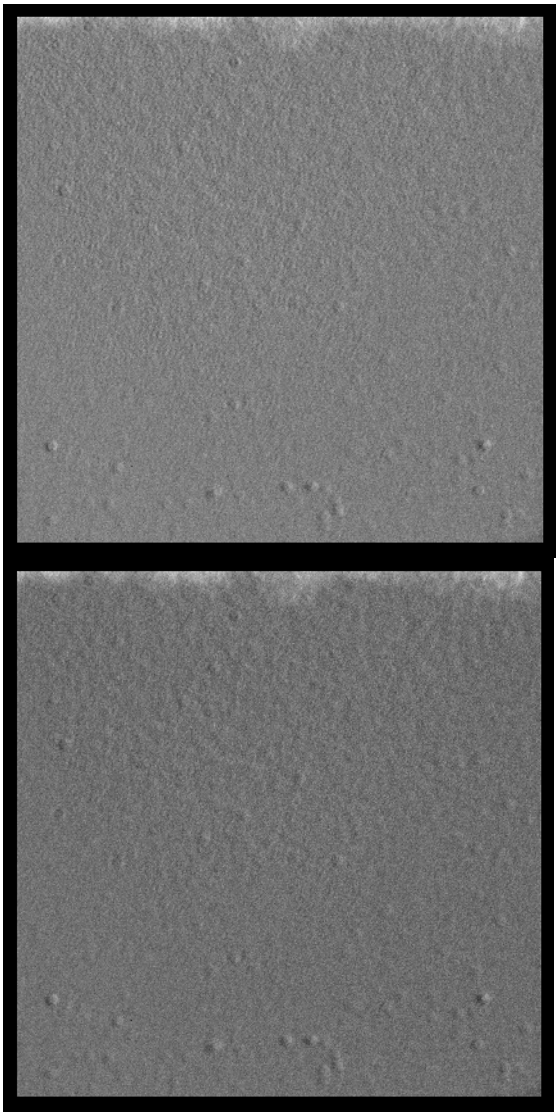

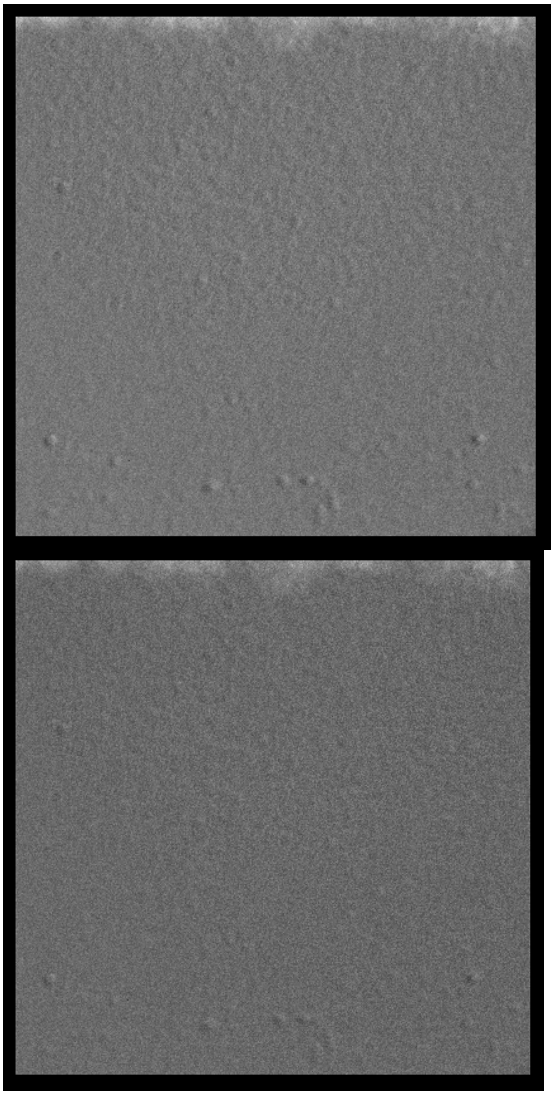

Figure B-12. R1 filter data comparing 5C to -5C, 5C to -30C 5C to -40C and 5C to -65C

Final Summary:

The result of this final analysis showed observable temperature tends once the replacement filter table was used, it was this analysis that uncover several of the bad flat fields in the first place. The image below shows the ~9 pixel shift in the relative location of object in the field from 5C^{o} data to -65C^{o} data. This is not the intended result of having a flat field with generally no temperature dependence and from this we can conclude that temperature is in fact a factor. Shown below is the change in the comparison images of the L1 and R1 filters over there individual ranges of L(5C,-15C, -40C and -65C) and R(5C,-15C, -30C -40C and -65C). For the best flat field correction result the individual flat fields that were generated from 5C to -65C will be substituted depending on the temperature of the SSI that most closely matches the temperature that the flat field was taken at.

C - Absolute radiometry –

C.1 Background

The responsivity testing involves using the SSI inside the Thermal Vacuum Chamber (TVC) to image a Spectralon target inside an isolating Black Box, in order to differentiate the responsivity of each filter inside the SSI. In order to measure the various responsivity of the SSI, a known Spectralon target with high reflectivity in the SSI spectral range relays light from Oriel standard lamp. There will be three types of data needed to measure, analyze and generate responsivity coefficients for the camera head.

1. Averaged Spectralon Image (ASI) is an average set of multiple images that has been corrected for dark and bias errors.
2. Shutter Light Image (SLI) is zero integration time image of the ASI scene
3. Background Scatter Image (BSI) is a image of the scattered light in the scene

The ASI data is a good contrast unsaturated image generally with all pixel below 3200 DN. The SLI data of the Spectralon will have an integration time of zero to capture the inherent camera shutter errors that is then subtracted from the ASI. The BSI data of the Spectralon with the same integration time as ASI will be a measurement of the scattered light level of the scene. This is accomplished by blocking the direct emitted radiance from the Oriel standard lamp, allowing imaging of only the scattered light bouncing around the inside of the Black Box. Using these three data sets and the division of the master flat from this filter will produce a final Corrected Spectralon Image (CSI). From the final CSI data the responsivity coefficient will be calculated by deriving the $W/m^2/nm/Sr.$ reflecting off the Spectralon from the spectral band pass profile of each filter. Finally the images radiance per filter per temperature is then divided by the metric of the corrected image (DN/sec), resulting in a final responsivity coefficient in units of

$$R = \left(\frac{W / m^2 / nm / Sr.}{DN / \sec} \right).$$

C.2 Test Setup and Data Acquisition

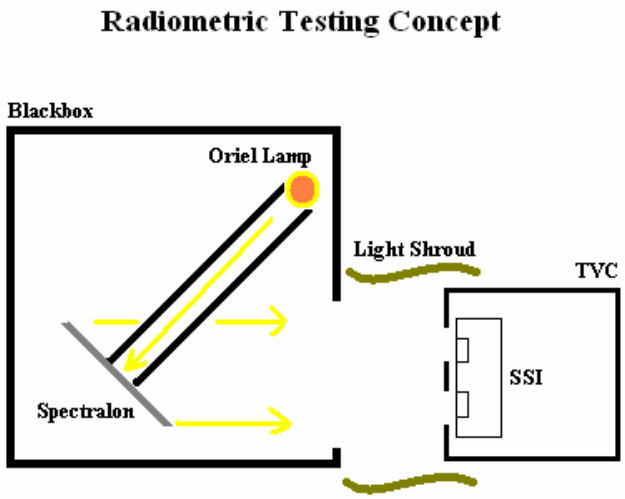

Figure. C-1 Responsivity test setup schematic.

Figure. C-2 Open TVC chamber (left), SSI looking through the cold baffle ports in the TVC (center) and full responsivity setup with the TVC draped to the Black Box where the Spectralon resides.

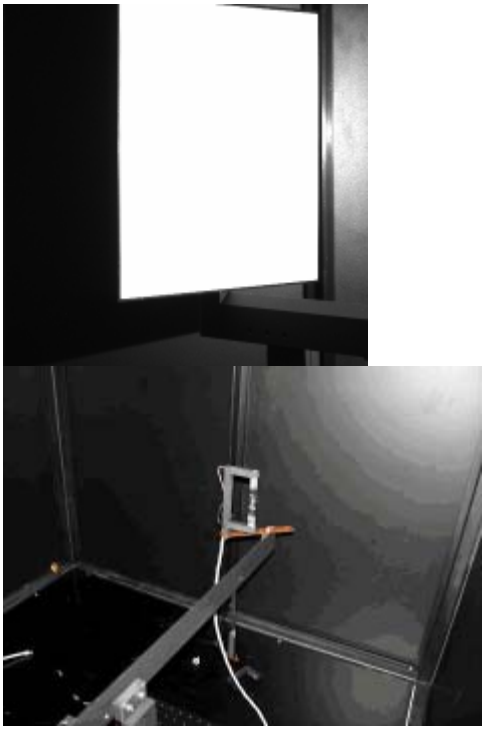

Figure. C-3 A SSI Image Spectralon calibration target (left) and the standard Oriel calibration lamp (right) inside the Black Box.

Software:
There were primarily two software programs used to do the analysis in this report; IDL programs listed below and Microsoft Excel. The IDL programs were used to do image manipulation and measure DN values. Excel was used to collect the data form IDL and to calculate, manipulate and plot the different effect and results of the analysis.

Image Files:

Listed below is the path location to the imaging data used the analysis process.

Raw data:
1. /support_files_for_responsivity/Resp_test
2. /support_files_for_responsivity/Solar_test

Processed radiometry images:
/support_files_for_responsivity/New_Radiometric_Images

Spreadsheet:

List below is the path location of the spreadsheets used to calculate the unknown coefficients and store measured data.

/support_files_for_responsivity

1. Radiometric_Coefficients.xls (calculating coefficients)
2. SN5-139-140_calibration_comparison_plus.xls (source data)
3. Scatter_light_vs_Direct_light_ratio.xls (scattered light analysis)

Log files:

List below is the path location of the log file used in the image correction and temperature mapping.
/support_files_for_responsivity

SEQ_FLAT_FIELD_FM_TESTING_06-17-06.log

Absolute Responsivity IDL Programs:

List below is the path location of the IDL tools used to analyze the responsivity data.
/support_files_for_responsivity/IDL_Code

1. apply_master_flat.pro (program)
2. image_sample.pro (program)
3. box_script.txt (command script)
4. fmssi_makeflat_wdarkmodel_wSlmodel.pro (program)

Absolute Responsivity IDL Tool
All IDL code used is located under
/support_files_for_responsivity/IDL_Code

The primary tool is an IDL script (box_script.txt in the IDL_Code directory) that does the following:
1) The user edits the name and path of the file to be examined and the double precision master flat file to be used on it.
2) The image file is read in, and the median pixel DN value reported.
3) The master flat is then applied using apply_master_flat.pro. This program reads in the floating point flat field array, reads in the images (ASI & SLI) and converts it to floating point. Then the program divided the image by the flat field and converts the result back to integer format. Any pixels having a DN>4095 are reset to 4095.
4) The flat-fielded CSI is displayed on the screen using image_sample.pro, overlaid with 100x100 box. The user will move the box around until the brightest part of the image is inside the box. Then a right click will print out the lower left coordinates of the box along with the mean pixel DN in the box.

Step by Step procedure:

1. Read the measured values for the filter CW and bandwidth from the Filter report, 415640-1140 FM SSI Filter Profiles over Temperature.
2. Using data set "SN5-139_calibration_comparison_plus.xls", calculate the spectral irradiances at the center wavelength of each filter using linear interpolation to determine the spectral irradiance at the center wavelength.
3. Convert new calculated irradiance ($mW/m^2/nm$) to the radiance ($W/m^2/nm/Sr.$) dividing irradiance by $1000*\pi$ steradians.
4. Place radiance data per filter in spreadsheet
5. Download Log file in preparation for image processing to find the temperature data for each image.
6. Open IDL command script "box_script.txt" which will require the ASI, SLI, log file and the master flat files for that temperature and filter.
7. Running the program will produce mean DN values of the ASI dark, SLI and SLI dark along with generating the mean DN of the center of the Spectralon.
8. Place all values in spreadsheet for later manipulation
9. Using imaging data, calculate the window transmission using image corrected "Closed TVC" files divided by "Open TVC" files, record in spreadsheet
10. Using the second data set taken on July 9^{th}, 2006 with the spare lamp, calculate the scattered light ratio of (ASL-SLI) divided by the [(ASI-SLI)-BSI]. Record in spreadsheet
11. Using the manufactures data, calculate the reflectivity of the Spectralon at the 45^o exitance angle the testing was done at and taking into account the change in reflectivity verse wavelength. Record in spreadsheet
12. Using the spreadsheet data calculate the (W/m2/nm/Sr.)/(DN/sec) with the CSI and step 3 for each temperature and filter. Once complete divide by the conversion factor, which is a multiplication the steps 9-11.
13. Calculate the uncertainty using error bounds in the filter profiles, image DN, DN dark, SLI, SLI dark and error in radiance curve
14. Collect and plot the responsivity coefficients verse temperature for all filter
15. Fit polynomial line to data points and record the coefficients for the fit curve of responsivity over temperature.
16. Compile errors in test setup, images and source to generate absolute and relative uncertainty.
17. Add profiling errors to test setup, image and source errors to generate final responsivity profile uncertainty.

C.3 Data Processing

Deriving the DN/sec quantity:

In figure C-4 are examples of the three main images that were be used to generate the mean (DN/sec) portion of the responsivity coefficient R is calculated. The ALI and SLI are used directly in this section when coupled with the master flat to find the DN/sec level of the CSI, where as the BSI image is used later as part of the conversion factor. The 2 to 3 raw images have an average on the order of 2500 DN and will be stack averaged after they have been bias and dark corrected. The second level of correction coming from the shutter light image and will be corrected for both bias and dark, before it is subtracted from the corrected ALI. The resulting image produced has the effects from bias, dark and shutter removed, leaving the nearly ideal DN/sec radiance reflecting off the Spectralon. The final DN/sec level will later be used to calculate after the conversion factor has been applied to the DN/sec from the CSI. Examples of the ASI, SLI and BSI images are shown below in figure C-4.

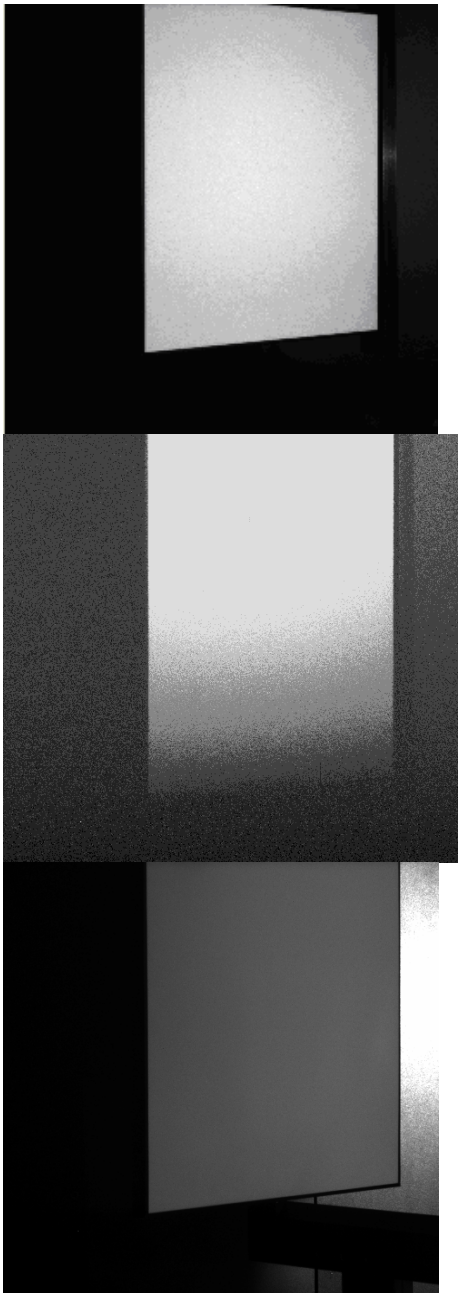

Figure C-4 Is 1 of 2 Spectralon images used to make the ASI (left), SLI shutter light image (center) and BSI scatter light image (right).

The second stage of the image analysis is using the normalized master flats to divide out some the radiometric falloff effects in all the SSI images. This process will produce the final CSI image that will be used to generate the DN/sec level of the scene.

$CSI = \frac{(ASI - SLI)}{Master\_Flat}$ Example of the normalized flat field and the histogram profile can be seen in figure C-5 and C-6

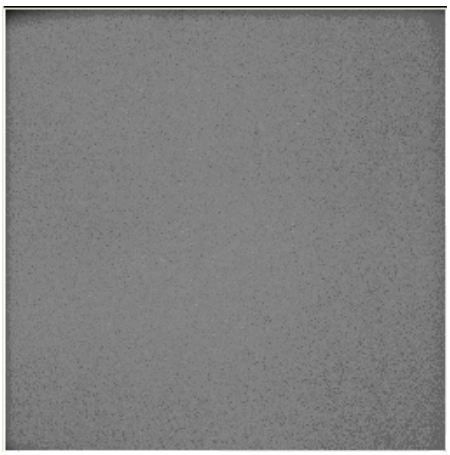

Figure. C-5 FM SSI L1 at -65 C is the original flat field to be normalized.

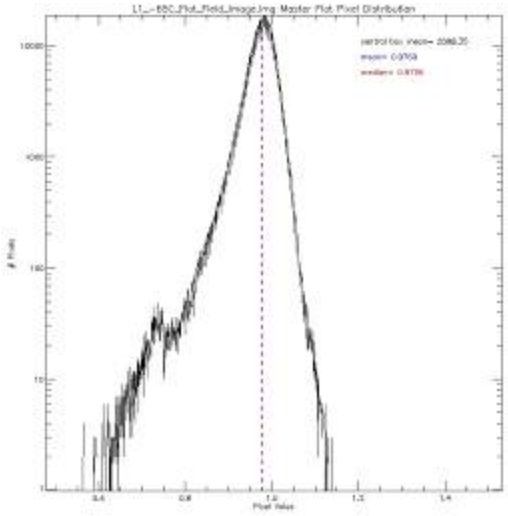

Figure. C-6 Histogram plot of normalized master flat

The DN/sec measurement is achieved after the master flat division, dark, bias and shutter corrected are all complete. This will bring uniformity to the image and remove field effects of the CCD. With all image manipulation complete it is now possible to derive and the DN/sec flux that the camera is seeing. The next step in the process is to choose an area of the Spectralon in the image to analyze, with the end goal of a direct reading of the source.

The key is to choose a section in the center of the Spectralon that has a uniform DN distribution that is a closest to the source and not effected by $\cos^4(x)$ radiometric fall off. The mean DN reading is achieved by using IDL command “box_script.txt” taking an average of DN values over a 100 x 100 box in the center of the Spectralon. Then the average DN reading per filter per temperature is recorded in a spreadsheet. This value is modified by the conversion factor that is a multiplicative grouping of the window

transmission, reflectivity and BSI correction from another data set. The final result is a DN/sec value that has be compensated for all effects other then a radiometry fall off.

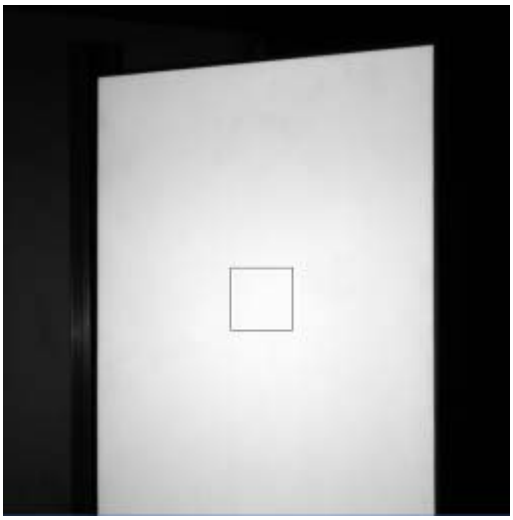

Figure. C-7 Final CSI after correction for dark current, bias, shutter effect and flattened with the master flat.

Deriving the W/m^2/nm/Sr:

The second step of responsivity analysis process is to derive the filter modified output of the of the Oriel lamp source, to determine the irradiance output per nanometer over the pi (π) solid angle.

The Oriel irradiance standard lamp was recently calibrated to allowing for the filter profile to weight the output. There are two main uncertainty errors in the lamp itself, the error in the profile over wavelength and the variation in temperature of the source producing an error in output. The error uncertainty in the profile of the irradiance itself is on the order of ~3%, where as there is an estimated variation in the source temperature of ~1.55%, that translates to a variation in output of ~1.55E^4 = ~6%. This data indicates that the profiling of the source is the largest uncertainty error in the entire report.

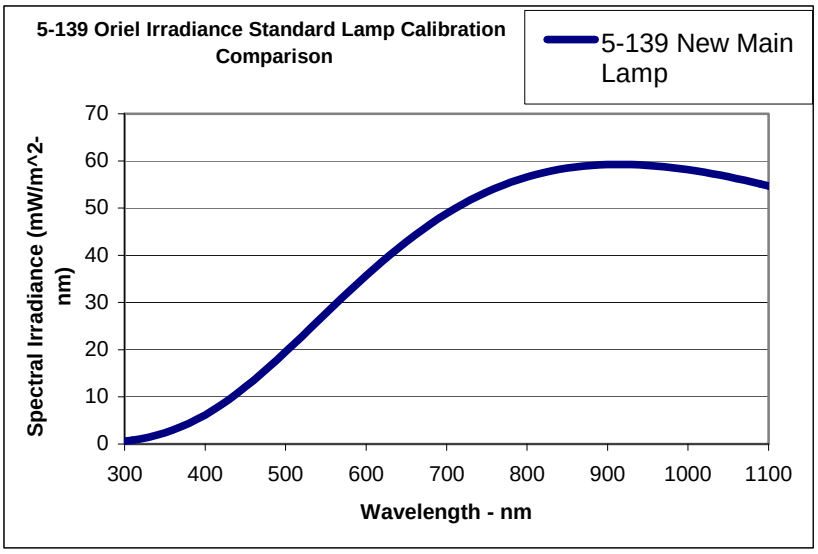

Figure. C-8 Is the measured output of the Oriel standard lamp.

The graph below shows where in the Oriel irradiance curve the filters in the SSI head fall. This center wavelength location along with the measured bandwidth of the filter themselves are used to calculate the W/m^2 coming out of the source.

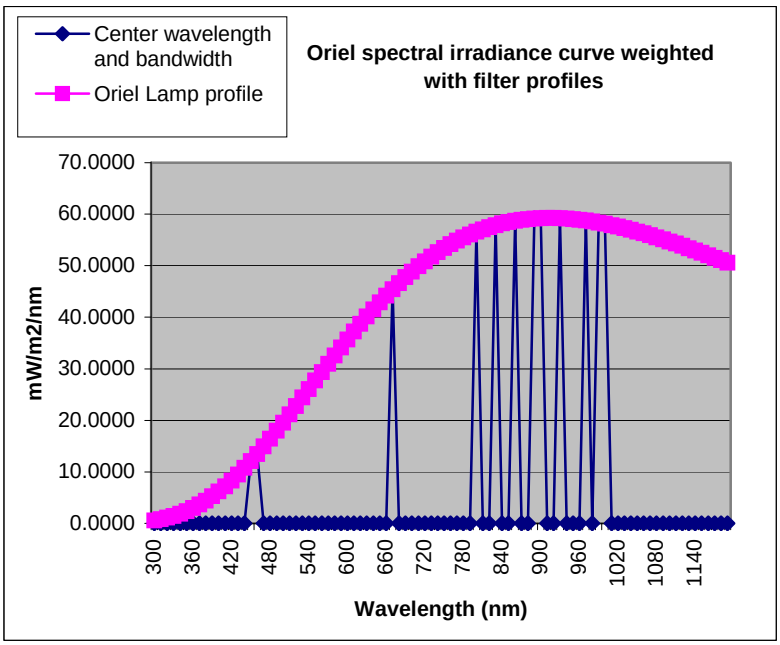

Figure. C-9 Plot of the weighted filter profile data for the SSI multiplied with the irradiance curve of the Oriel source to calculate the in band irradiance per filter.

Table C-1 Spectral irradiance per wavelength ($mW/m^2/nm$)

	irradiance ($mW/m^2/nm$) at-65 C^o	
	Left Eye	**Right Eye**

1	45.7	45.7
2	11.6	11.4
3	12.2	45.5
4	58.3	59.1
5	59.1	59.1
6	56.1	11.4
7	56.6	53.6
8	58.7	53.6
9	59.2	53.6
10	59.2	36.3
11	58.0	24.9
12	58.7	17.2

Table C-1 Results of the weighted multiplication in figure C-9, displays irradiance per nm (spectral irradiance) that was been calculated using the measured filter center wavelength and the Oriel irradiance curve at -65 degrees Celsius.

Scattered Light:

There is inherent scattered light in any test setup that does not block the energy coming out of the unused 3π emittance area of the source. In order to subtract the unwanted scatter light that makes it into the direct image of the Spectralon, the source is blocked and a second set of images is taken, the BSI. The second set of data is an image of the scattered light itself and can be subtracting from the direct plus scattered light image (ASI-SLI) to give the ratio of direct to direct + stray.

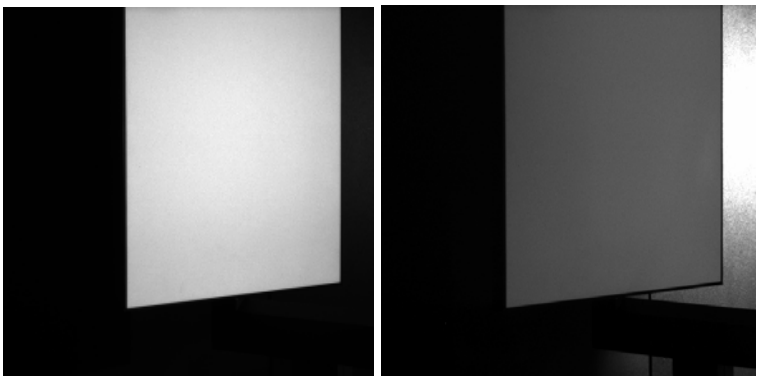

Figure C-10. L1 (ASI-SLI) image of the direct + scatter light (left) and BSI L1 image of just the scattered light (right). The two images have different image stretches for display.

Evaluation of the background scattered light in the BSI blocked verse the direct imaging data is then used to compensate for the extra DN levels in the unblocked CSI images. The measurements

done with the solar filters gave anomalous error bounds due to the low DN levels in the images taken. Therefore the conversion factor for the filters L3, L4, L5, R3, R4, and R5 were replaced by the other non-solar filters that closely match the center wavelength of solar filter. The graph below shows the final values of the conversion factor plotted verses wavelength. It shows that the scattered light is from 3 to 6% of the total DN energy in the CSI image. This correction factor will be included into the conversion factor in C-3 to remove the scattered light bias in the responsivity.

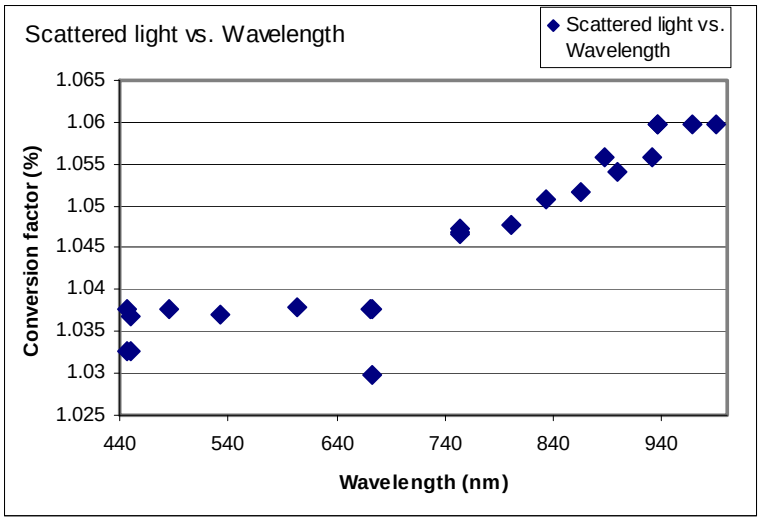

Figure. C-11 Plot shows the ratio comparison of the direct plus scattered image data divided by direct image data. The graph also shows the scattered light level increasing as the wavelength ranges into the IR.

Spectralon:

A Spectralon targets reflectivity is constant at 99% over the spectral band of the SSI between 450 to 1000 nm. The Spectralon target itself is almost perfectly Lambertian and therefore has little to no irradiance drop off with angle. Table "Sample SRS-99" shown below gives the error in the Spectralon target as you rotate that target off axis. Reference documentation: /support_files_for_responsivity /A Guide to Reflectance Coatings and Materials.pdf

Table C-2 Correction factor generation from manufactures data

Wavelength (nm)	Spectralon (reflectivity vs. wavelength)	Spectralon delta reflectivity at 45°	Correction factor
450	0.99	+0.009	0.999
500	0.99	+0.009	0.999
550	0.99	-0.006	0.984
600	0.99	-0.006	0.984
650	0.99	-0.006	0.984

700	0.99	-0.006	0.984
750	0.99	-0.006	0.984
800	0.99	-0.002	0.988
850	0.99	-0.002	0.988
900	0.99	-0.002	0.988
950	0.99	-0.002	0.988
1000	0.99	-0.002	0.988

Table C-2 is the multiplicative results of using the two manufactures data sets below for Spectralon SRS-99

WAVELENGTH (nm)	SPECTRALON
250	0.96
300	0.98
350	0.99
400	0.99
450	0.99
500	0.99
550	0.99
600	0.99
650	0.99
700	0.99
750	0.99
800	0.99
850	0.99
900	0.99
950	0.99
1000	0.99

Figure. C-12 Data tables of the conversion factor used in the responsivity calculation and measured data from the manufacture on reflectivity vs. wavelength and reflectivity departure from Lambertian viewed at 45 degree exitance from the Spectralon SRS-99.

Window Transmission:

In order to calculate the amount of energy that is being lost over the spectral band of the SSI because of imaging through the twin BK7 windows in the TVC. A set of imaging was taken of the Spectralon before the responsivity test began, first with the TVC open and on windows in the path. For comparison the lid was then closed on the TVC, and the image to image DN values drop in response to the BK7 windows the light is passing through. The two sets of image were then compared after dark, bias and shutter correct was completed, a roughly 0.5 to 3% transmission loss depending on the filter. The solar filters transmission values were replaced with there most closely matching center wavelength non-

solar in order to remove anomalous measurements do to extremely low DN level that create larger error bounds.

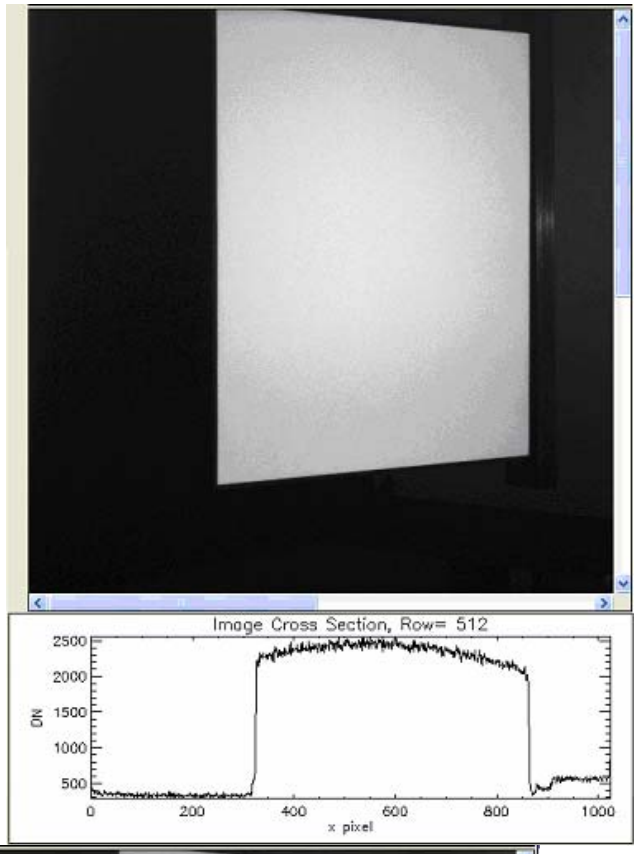

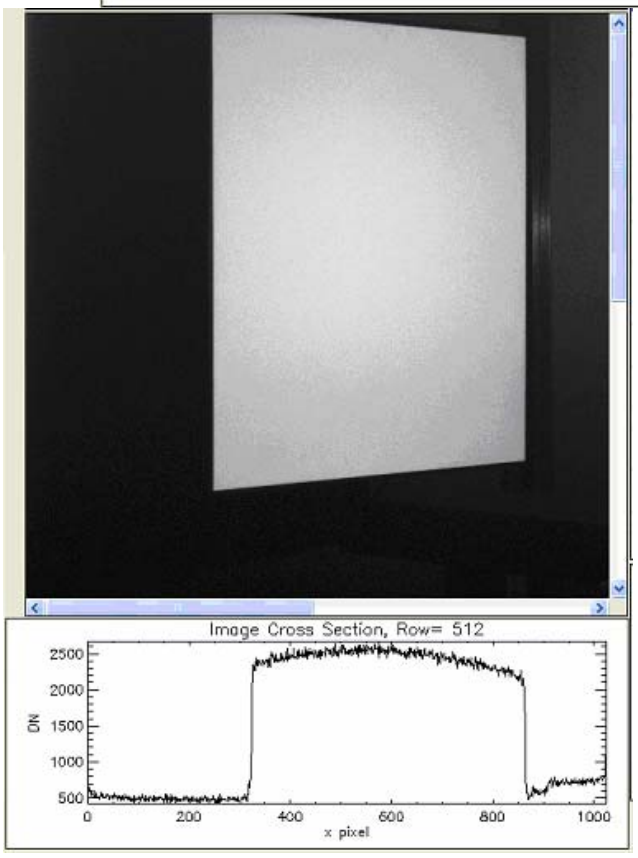

Figure. C-13 For the L1 filter the open DN level is 794.055 (left) and the closed DN level is 806.977 (right).

The window transmission over the SSI spectral band is shown in the graph C-14, there is a notable variation of about 1.2% in the transmission of different filters at the same wavelength. This is most likely because of small responsivity changes do to temperature variation during testing of the SSI.

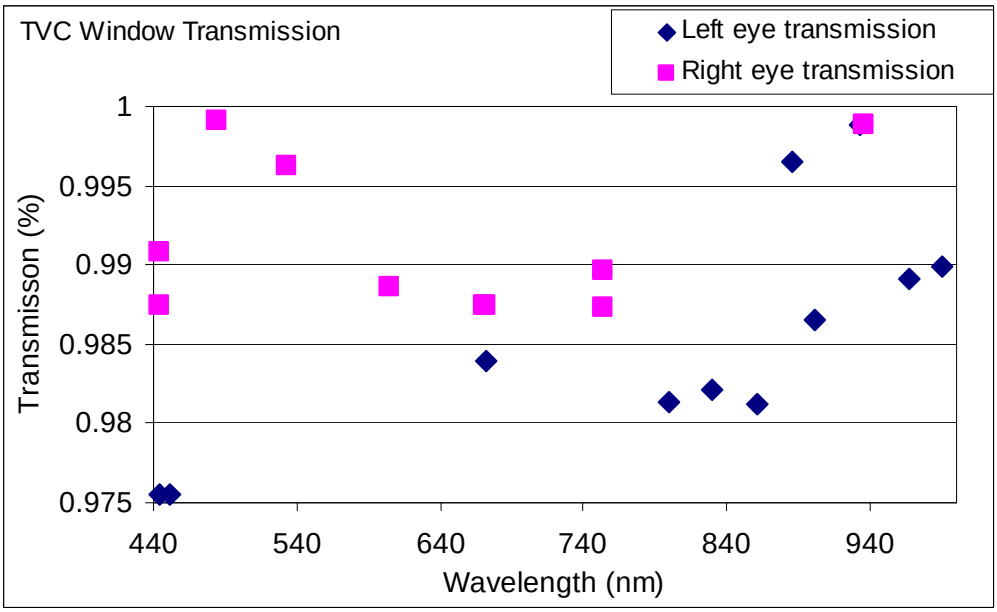

Figure. C-14 Plot of the window transmission of the SSI left and right eye through the BK7 windows.

Image processing steps:

There was a 5 step process used to correct and validate the three image sets taken during the testing at LPL. This process corrects for all non-direct radiance effect in the SSI images of the Spectralon and allows for a pure sampling of the radiance to DN level to be measured. The step by step process below describes how the images are corrected and in what order.

Step 1:

Flat = (ASI-SLI) = [(5 stacked flat images – dark – bias) – (Shutter light flat image – dark – bias)]

Step 2:

$$Master\_Flat(double\_precision\_ratio) = \left(\frac{Flat}{AvgDN\_value\_of\_center\_256x256}\right)$$

Step 3.

$$Scattered\_light\_conversion = \left[\frac{(ASI - SLI) - BSI}{(ASI - SLI)}\right] = \frac{(\mathrm{Im}age\_direct + scatter) - (\mathrm{Im}age\_s}{(\mathrm{Im}age\_direct + scatter)}$$

Step 4.

$$Conversion\_window\_transmission = \left(\frac{Open\_TVC\_\mathrm{Im}age}{Closed\_TVC\_\mathrm{Im}age}\right)$$

$$Conversion\_reflectivity = \frac{1}{(\mathrm{Re}flectivity\_per\_filter)}$$

Step 5:

$$Complete\_image = \frac{ASI - SLI}{Master\_flat} = \left(\frac{[(\mathrm{Im}age - dark - bias) - (shutter\_image - dark - bias)}{Master\_Flat(double\_preciesion\_ratio)}\right.$$

$$Correction\_factor = \left(Corr\_window\_transmission * Corr\_reflectivity * Scattered\_light\_c\right.$$

$$Corrected\_Spectralon\_\mathrm{Im}age = CSI = \left(Complete\_image * Correction\_factor\right)$$

The correction factor shown in Table C-III is the multiplicative correction needed in order to compensate for the loss in energy from window transmission and the energy gain due to the scattered light and the energy that never arrived do the reflectivity. The correction factor is used to correct all responsivity coefficients regardless of the temperature.

Table C-3 Overall Correction Factor

Filter #	Spectralon Reflectivity (45°)	Window Transmission ratio (23C°)	Background ratio	Overall Correction Factor
L1	1.016260163	1.016	0.971	1.003
L2	1.001001001	1.025	0.968	0.994
L3	1.001001001	1.025	0.968	0.994
L4	1.012145749	1.010	0.944	0.965
L5	1.012145749	1.004	0.947	0.962
L6	1.016260163	1.018	0.952	0.985
L7	1.016260163	1.019	0.954	0.988
L8	1.016260163	1.019	0.951	0.985
L9	1.012145749	1.014	0.949	0.973
L10	1.012145749	1.001	0.947	0.960
L11	1.012145749	1.031	0.944	0.985
L12	1.012145749	1.011	0.944	0.966
R1	1.016260163	1.013	0.964	0.992
R2	1.001001001	1.013	0.964	0.977
R3	1.016260163	1.013	0.964	0.992
R4	1.012145749	1.001	0.944	0.956
R5	1.012145749	1.001	0.944	0.956
R6	1.001001001	1.009	0.964	0.974
R7	1.012145749	1.010	0.955	0.977
R8	1.012145749	1.013	0.955	0.979
R9	1.012145749	1.013	0.955	0.979
R10	1.016260163	1.012	0.963	0.990
R11	1.016260163	1.004	0.964	0.984
R12	1.001001001	1.001	0.964	0.965

C.4 Responsivity

With the imaging analysis completed and the radiance calculated, using the measured filter profiles and measured Oriel standard lamp curve, the responsivity coefficients R are completed. The next step in the process is to repeat the responsivity calculation for the nominal temperature range of 5, -15, 40 and -65C° that imaging data is available for. An extension of calculating the responsivity with temperature is to derive a quadratic fit to the responsivity data over temperature to allow for a profiling over ranges not cover by measured data. The final step of the process is to calculate the uncertainty in the individual response coefficients R themselves, which is a RSS summation of individual errors.

The RSS total uncertainty per RC comes from several individual variation errors like dark, shutter, center wavelength, bandwidth, and the output of the Oriel standard lamp.

Table C-4 Responsivity coefficients (R)

Filter	R at -65 C^o $\frac{(W/m^2/nm/Sr.)}{(DN/\sec)}$	R(T), T in C^o $\frac{(W/m^2/nm/Sr.)}{(DN/\sec)}(T)$	~ Uncertainty from Image DN and Filter profile (%)
L1	7.301E-06	$-5.93E^{-11}(T^2)-9.87561E^{-10}(T)+9.80253E-06$	0.002
L2	3.691E-05	$4.81E^{-10}(T^2)+1.97407E^{-07}(T)+4.70887E^{-05}$	0.009
L3	4.733E-04	$-1.07E^{-08}(T^2)+4.82103E^{-07}(T)+0.000544883$	0.010
L4	5.388E-04	$3.48E^{-08}(T^2)-2.70929E^{-07}(T)+0.000375352$	0.019
L5	2.962E-05	$8.11E^{-10}(T^2)+1.08081E^{-08}(T)+2.64798E-05$	0.007
L6	6.743E-06	$6.29E^{-12}(T^2)-5.02864E^{-09}(T)+6.30278E^{-06}$	0.005
L7	7.501E-06	$2.94E^{-11}(T^2)-7.34077E^{-10}(T)+7.33416E^{-06}$	0.004
L8	6.259E-06	$3.36E^{-11}(T^2)-7.27515E^{-09}(T)+5.62761E^{-06}$	0.005
L9	5.887E-06	$2.47E^{-11}(T^2)-1.23446E^{-08}(T)+4.99017E^{-06}$	0.006
L10	1.544E-05	$1.20E^{-10}(T^2)-4.3235E^{-08}(T)+1.21863E^{-05}$	0.007
L11	4.899E-05	$2.03E^{-09}(T^2)-1.68386E^{-07}(T)+2.98188E^{-05}$	0.000
L12	2.863E-05	$7.79E^{-10}(T^2)-8.37898E^{-08}(T)+1.98952E^{-05}$	0.011
R1	8.749E-06	$4.99E^{-11}(T^2)+1.99528E^{-08}(T)+9.87165E^{-06}$	0.003
R2	3.732E-05	$9.97E^{-10}(T^2)+2.2438E^{-07}(T)+4.86256E^{-05}$	0.009
R3	1.629E-04	$-1.46E^{-09}(T^2)+3.83255E^{-07}(T)+0.000188233$	0.004
R4	1.366E-04	$5.73E^{-09}(T^2)-2.29099E^{-08}(T)+0.000113003$	0.008
R5	1.382E-04	$4.64E^{-09}(T^2)+9.2778E^{-08}(T)+0.00011363$	0.008
R6	4.174E-05	$4.39E^{-10}(T^2)+2.13925E^{-07}(T)+5.38541E^{-05}$	0.009
R7	6.215E-06	$5.82E^{-11}(T^2)+6.46177E^{-09}(T)+6.41783E^{-06}$	0.003
R8	6.113E-06	$-1.86E^{-11}(T^2)+2.48439E^{-10}(T)+6.21968E^{-06}$	0.003
R9	1.560E-05	$1.45E^{-10}(T^2)+1.61095E^{-08}(T)+1.60145E^{-05}$	0.003
R10	1.354E-05	$1.59E^{-10}(T^2)+4.28981E^{-08}(T)+1.56387E^{-05}$	0.002
R11	1.044E-05	$1.24E^{-10}(T^2)+3.47298E^{-08}(T)+1.22175E^{-05}$	0.003
R12	2.103E-05	$2.61E^{-10}(T^2)+9.14789E^{-08}(T)+2.5669E^{-05}$	0.004

In table C-4 are several of the key radiometric coefficients needed on Mars to calibrate to the sunlight modulated by the reflectivity of the Martian surface.

C.5 Responsivity change with temperature

In order to compensate for the effects of the responsivity changing as the SSI camera head cycles through many different temperatures, the responsivity is plotted from $5C^{o}$ to $-65C^{o}$ The results of the analysis on the change in responsivity over temperature render the general trend of a decrease in response in the UV to visible wavelength, remained fairly constant in the visible to near infrared and increase in infrared filters.

The graphs and fitted data is broken up between left and right eye, also the data for the geo filters verse the solar filter has been separated.

Radiometric Responsivity coefficients over the temperature range of $5\ C^{o}$ to $-65\ C^{o}$

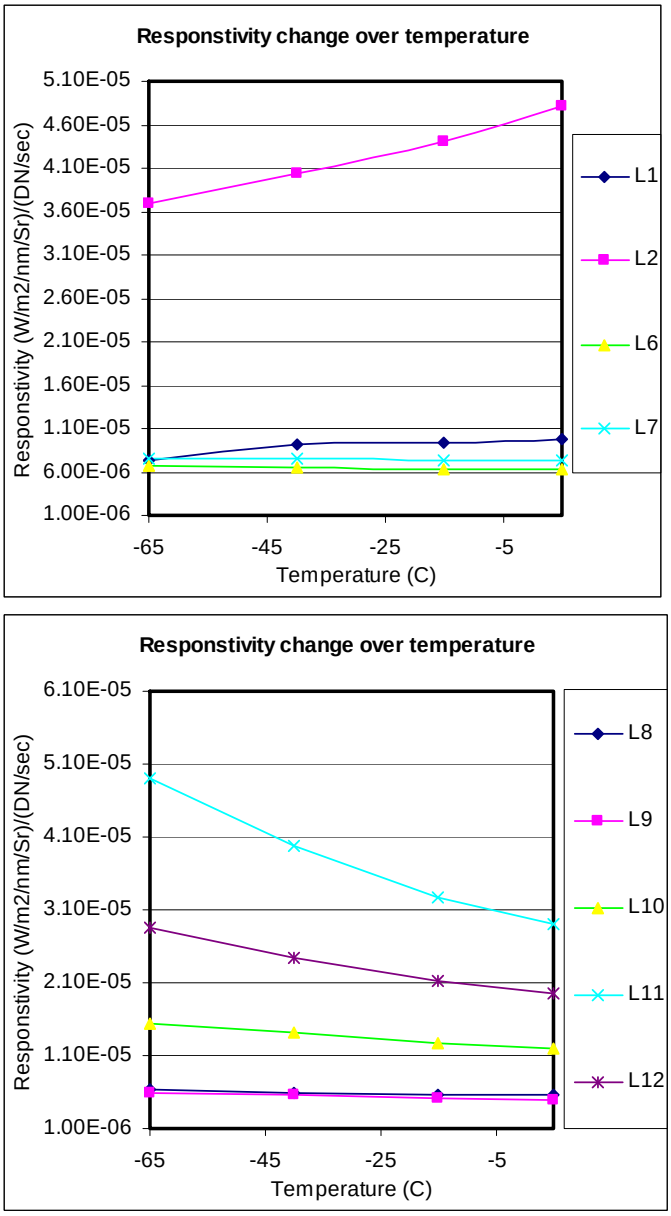

Fig C-15. Plots of the change in responsivity over temperature in L1, L2, L6, L7, L8, L9, L10, L11 and L12

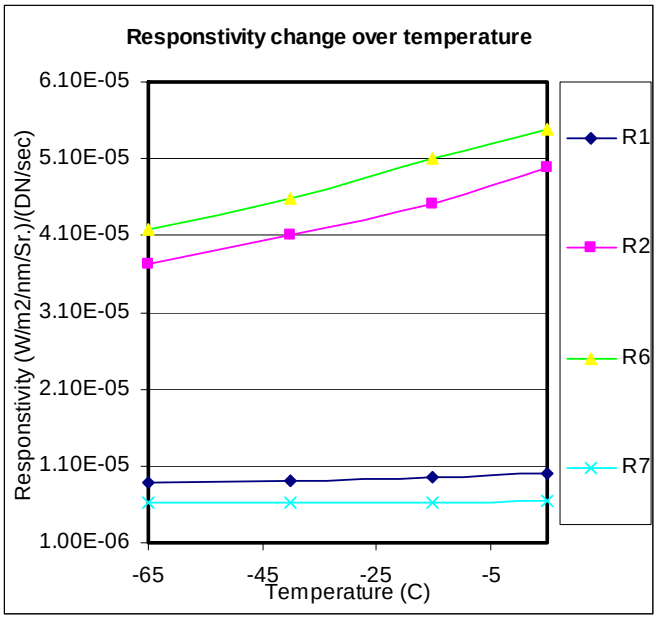

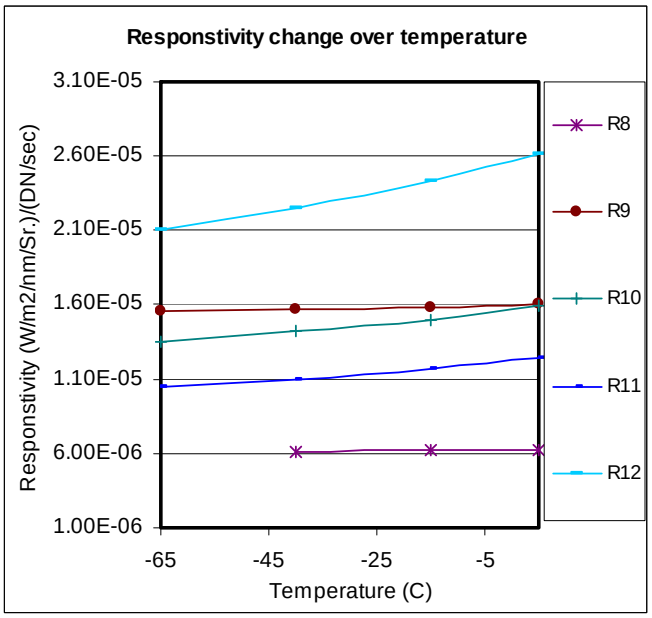

Fig C-16. Plots of the change in responsivity over temperature in R1, R2, R6, R7, R8, R9, R10, R11 and R12.

The profiling for the solar was done separately do to the typical scale factor differences in the solar filter verse the other SSI filters. The result of the plotting was the same as previous filter plotting, showing about the same trend with wavelength.

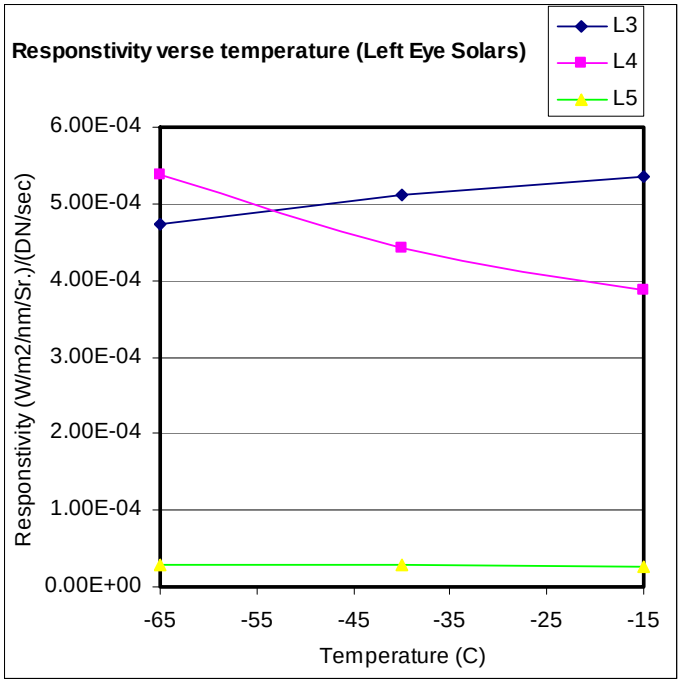

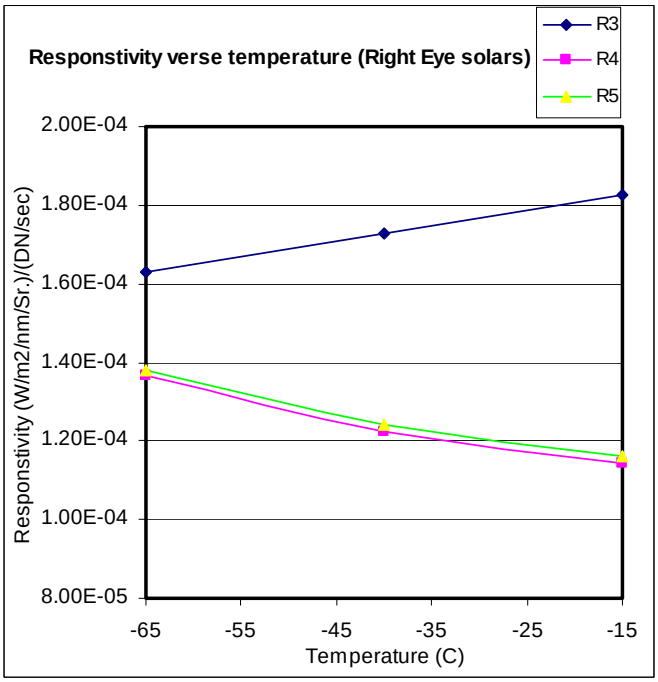

Fig C-17. Plots of the change in responsivity over temperature in L3, L4, L5, R3, R4 and R5.

Results of profiling:

The profiling of the responsivity with temperature will be done in two parts; first the data will be scaled to easily show % change in responsivity with temperature and second a polynomial trend line will be fitted and displayed. After normalizing the results of the $\Delta R(T)$ plot shows that there is a maximum of 70% change in response over temperature at the extreme ends of the filter spectrum and only a couple percent in the mid band.

Collection of all left eye filter normalized at 5 C^o to 1

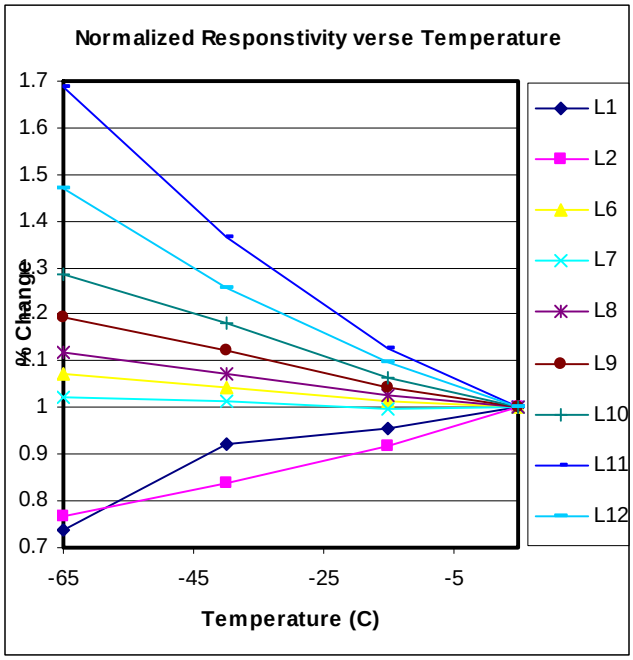

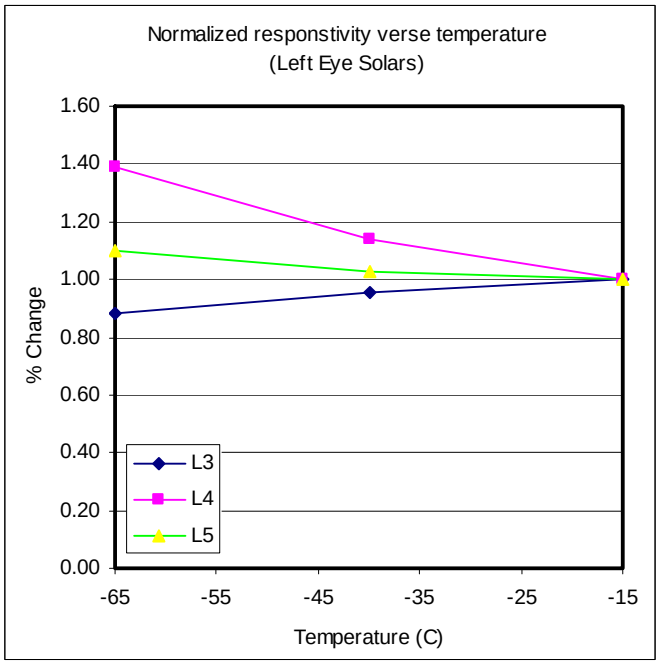

Figure C-18. Normalized plots of the geological and solar filter over temperature (Left Eye).

L1&L2 normalized and profile fitted

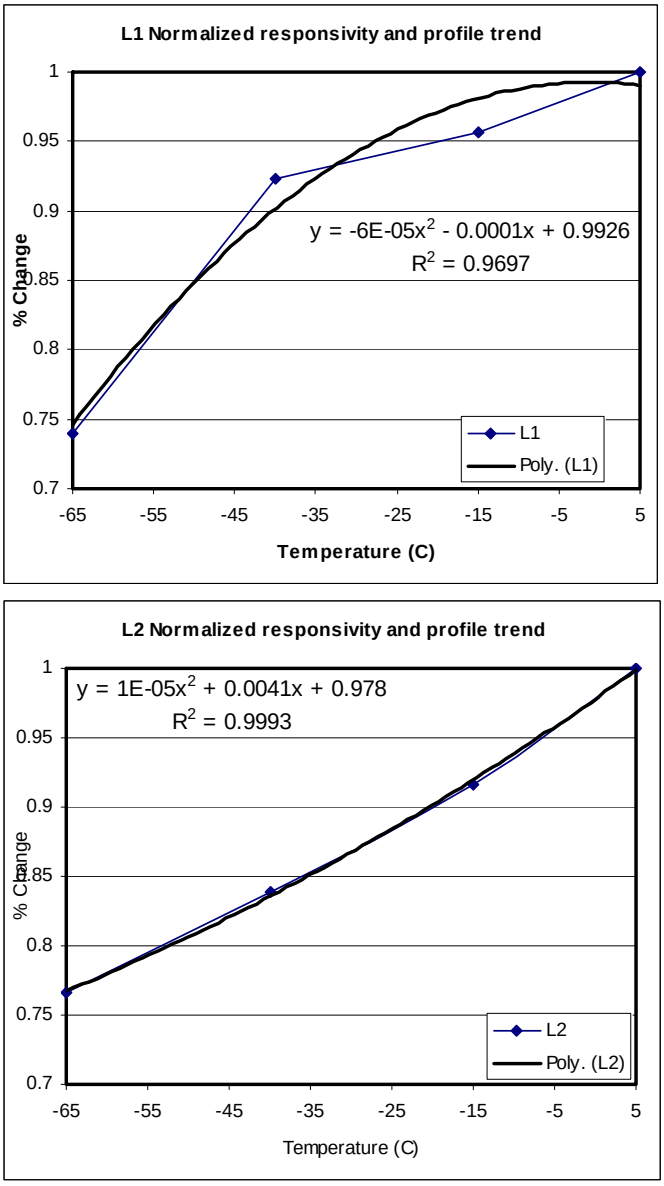

Figure C-19. Normalized plots of the L1 and L2 filter over temperature, with the polynomial fitted profile.

L3&L4 normalized and profile fitted

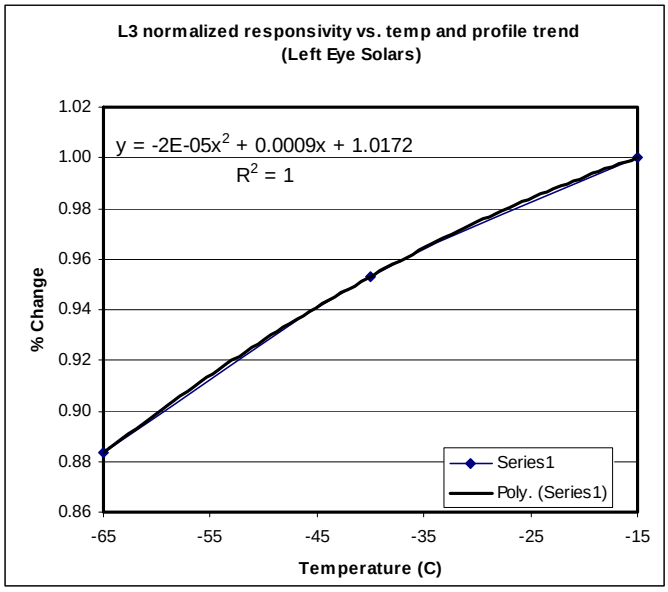

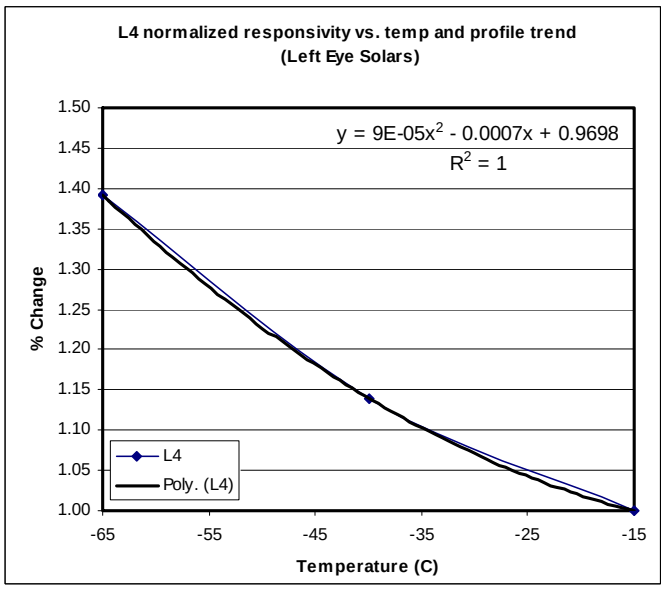

Figure C-20. Normalized plots of the L3 and L4 filter over temperature, with the polynomial fitted profile.

L5&L6 normalized and profile fitted

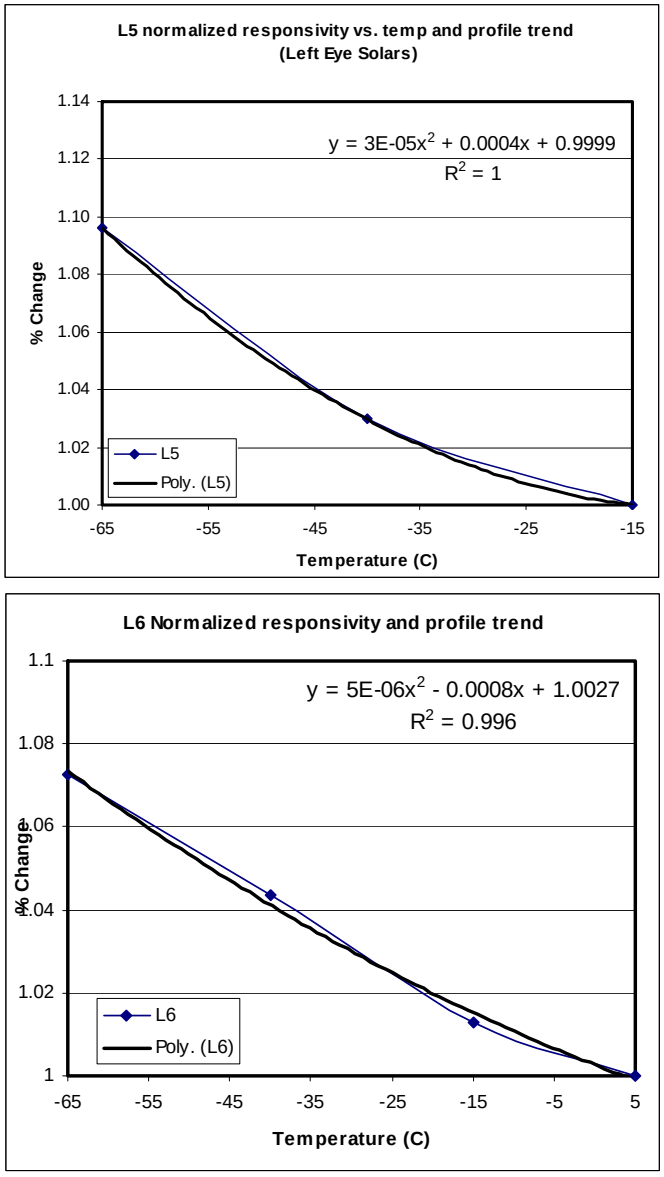

Figure C-21. Normalized plots of the L5 and L6 filter over temperature, with the polynomial fitted profile.

L7&L8 normalized and profile fitted

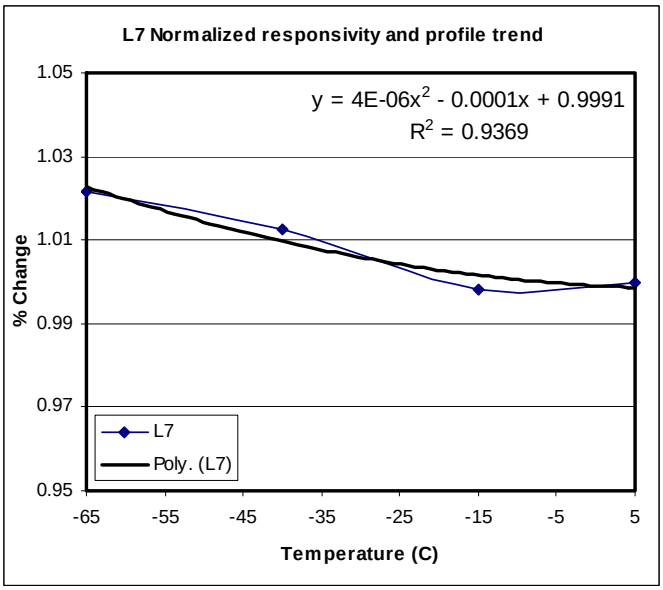

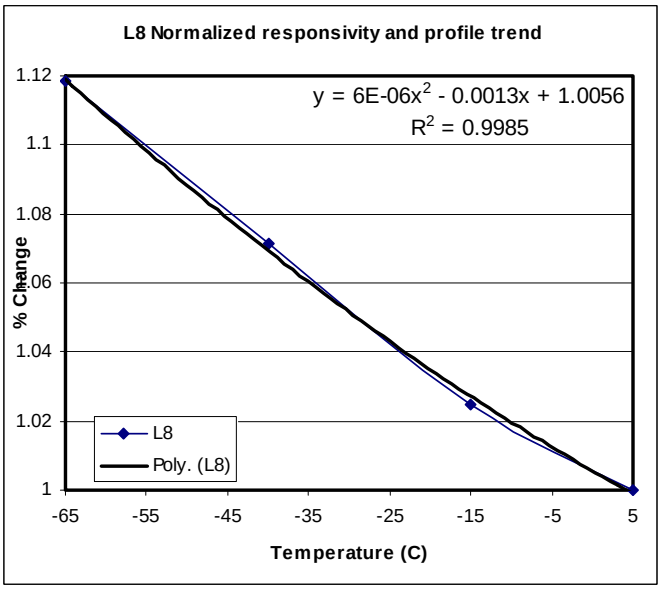

Figure C-22. Normalized plots of the L7 and L8 filter over temperature, with the polynomial fitted profile.

L9&L10 normalized and profile fitted

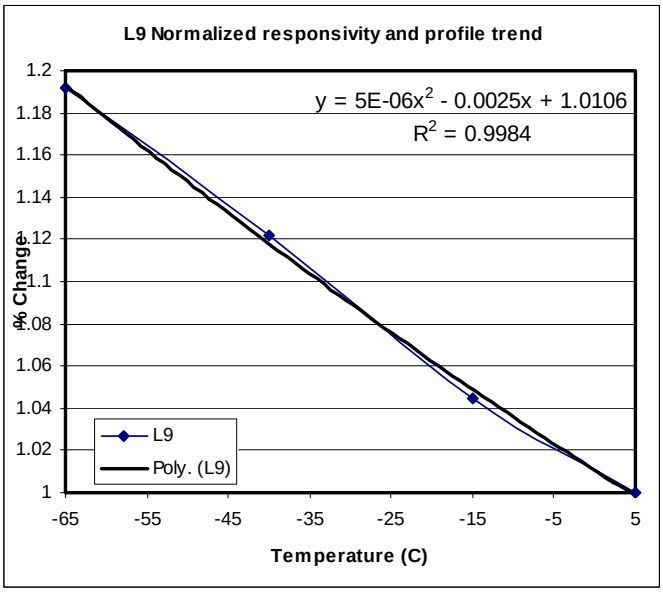

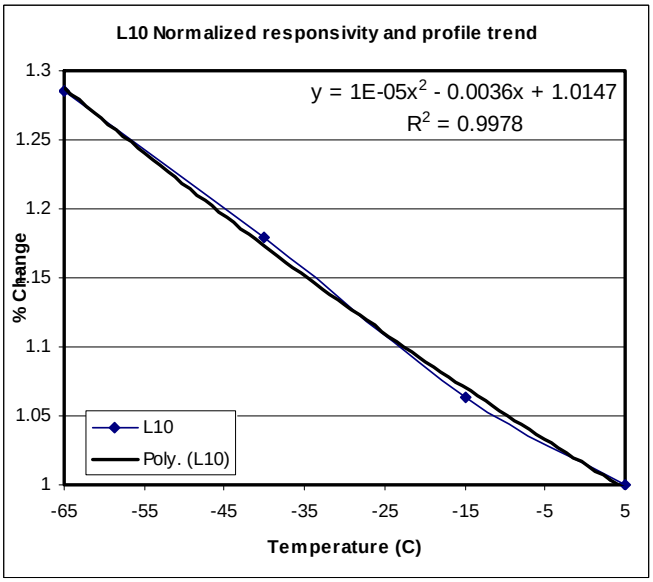

Figure C-23. Normalized plots of the L9 and L10 filter over temperature, with the polynomial fitted profile.

L11&L12 normalized and profile fitted

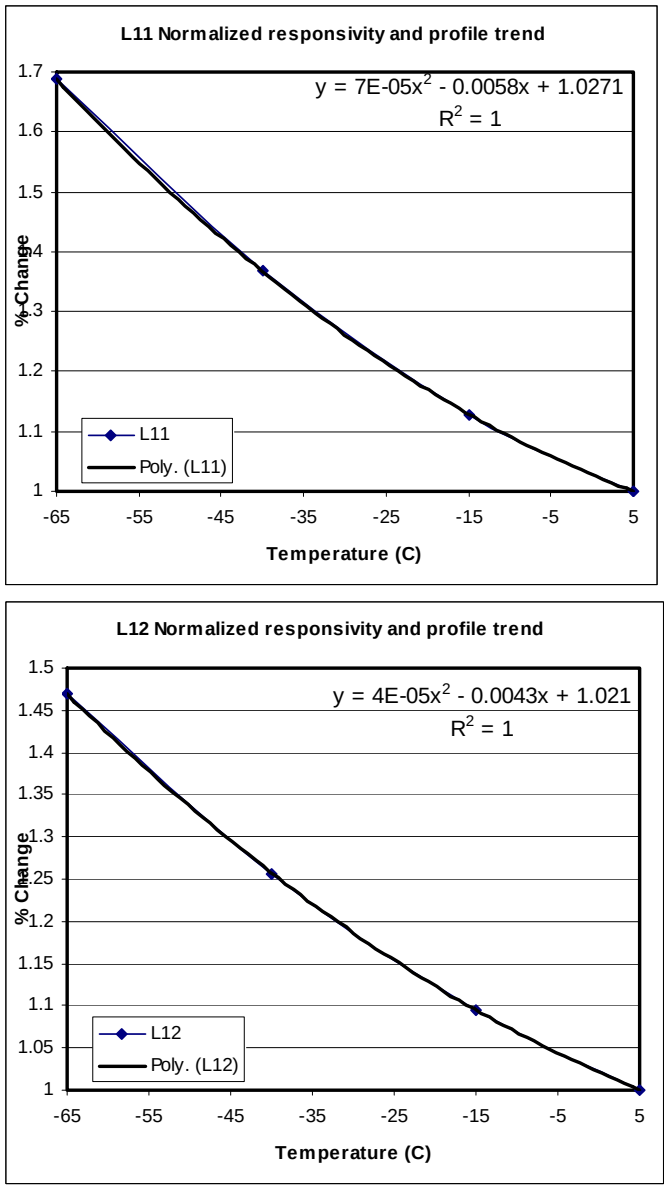

Figure C-24. Normalized plots of the L11 and L12 filter over temperature, with the polynomial fitted profile.

Collection of all right eye filter normalized at 5 C^{o} to 1

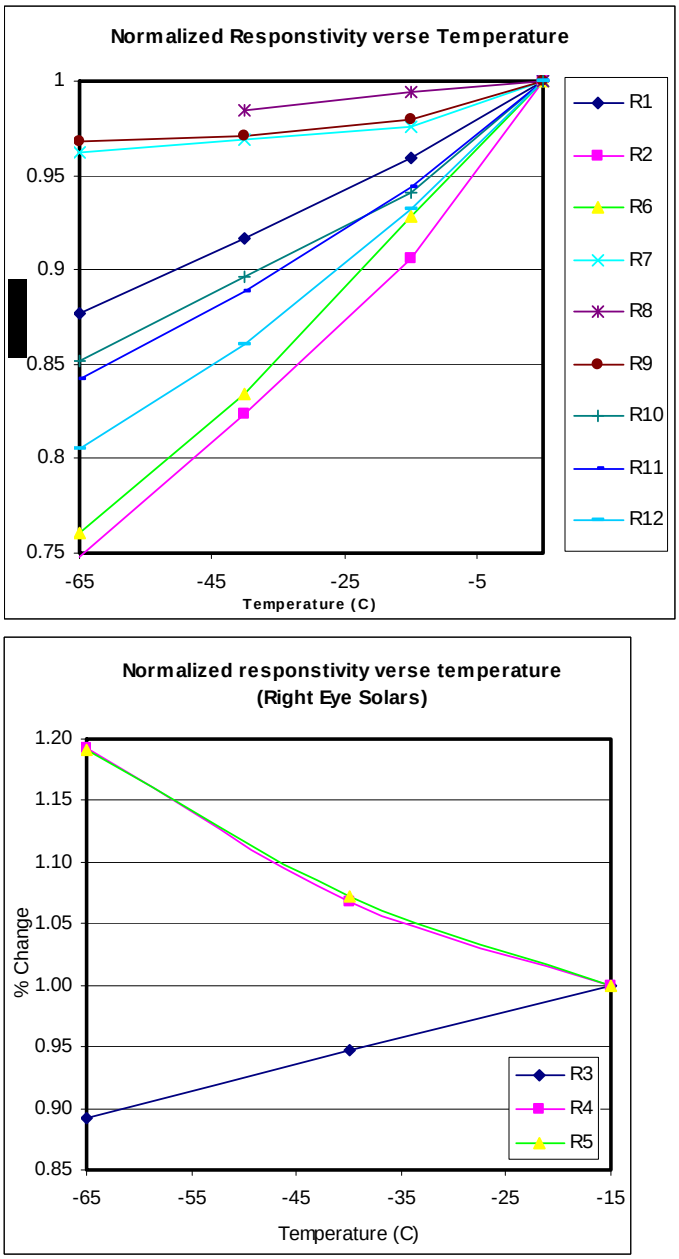

Figure C-25. Normalized plots of the geological and solar filter over temperature (Right eye).

R1&R2 normalized and profile fitted

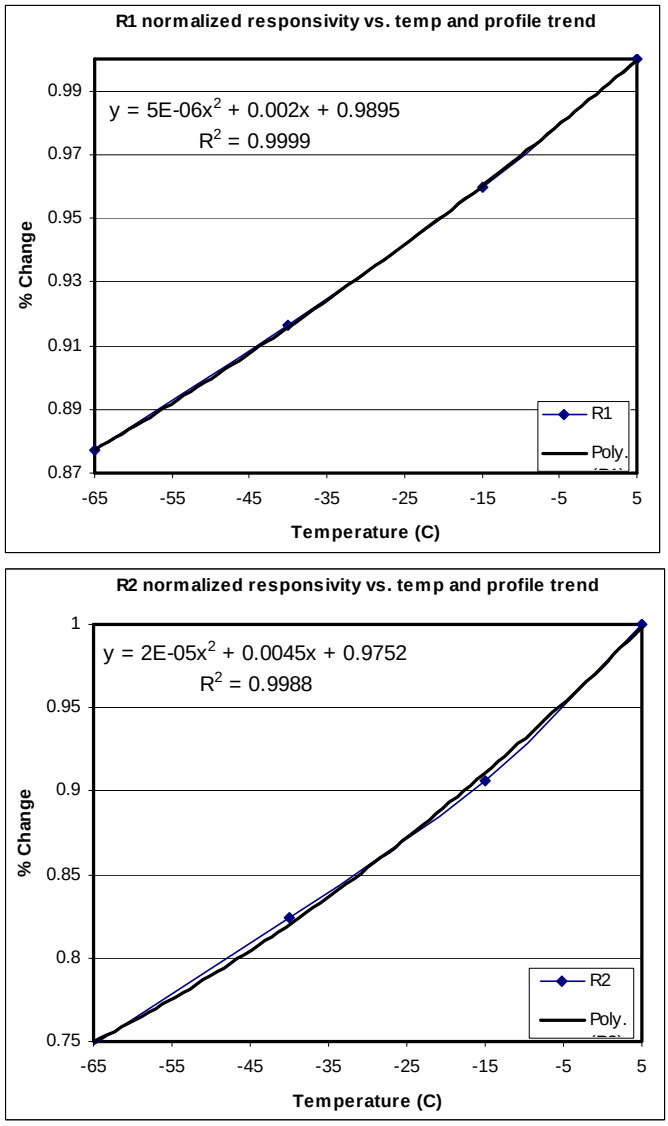

Figure C-26. Normalized plots of the R1 and R2 filter over temperature, with the polynomial fitted profile.

R3&R4 normalized and profile fitted

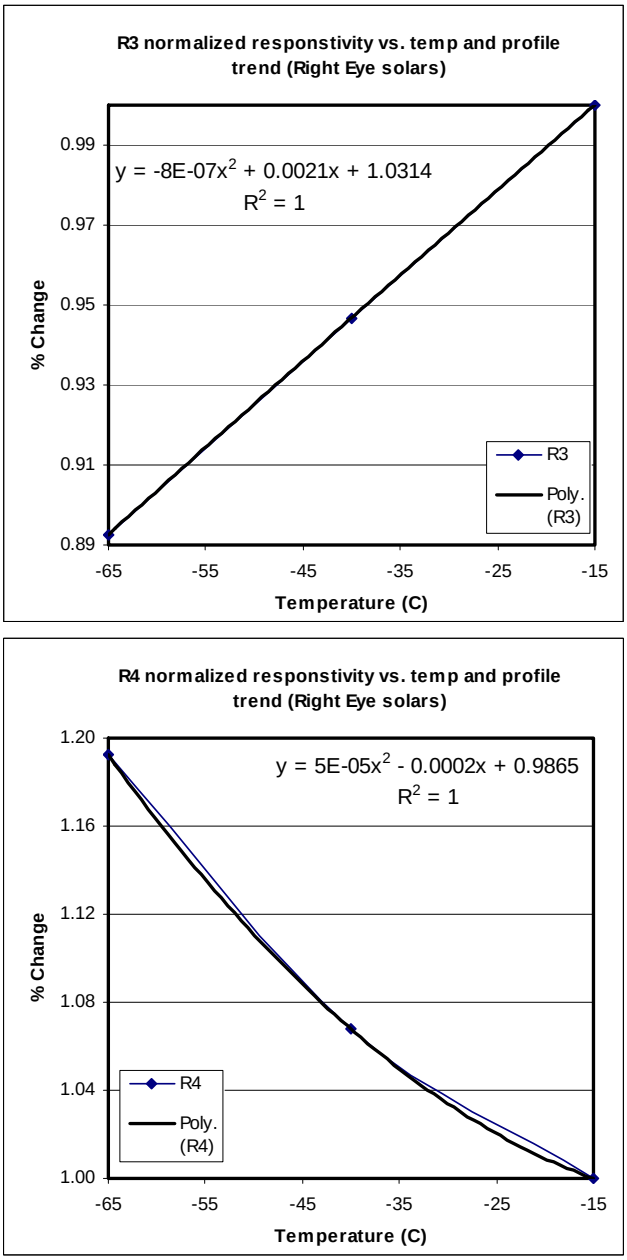

Figure C-27. Normalized plots of the R3 and R4 filter over temperature, with the polynomial fitted profile.

R5&R6 normalized and profile fitted

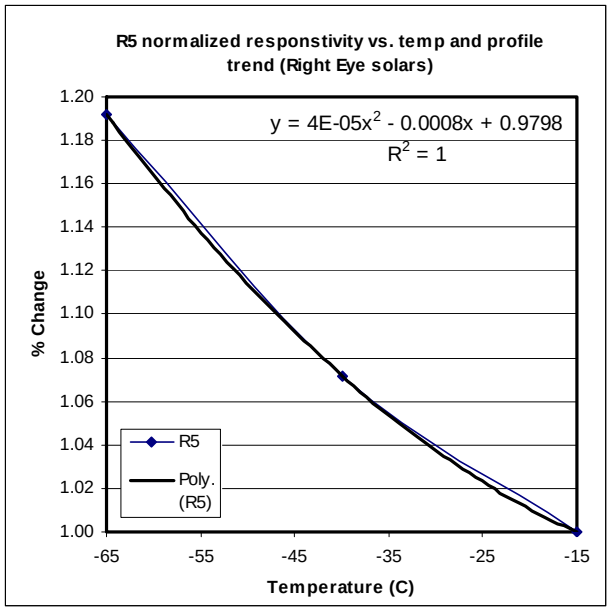

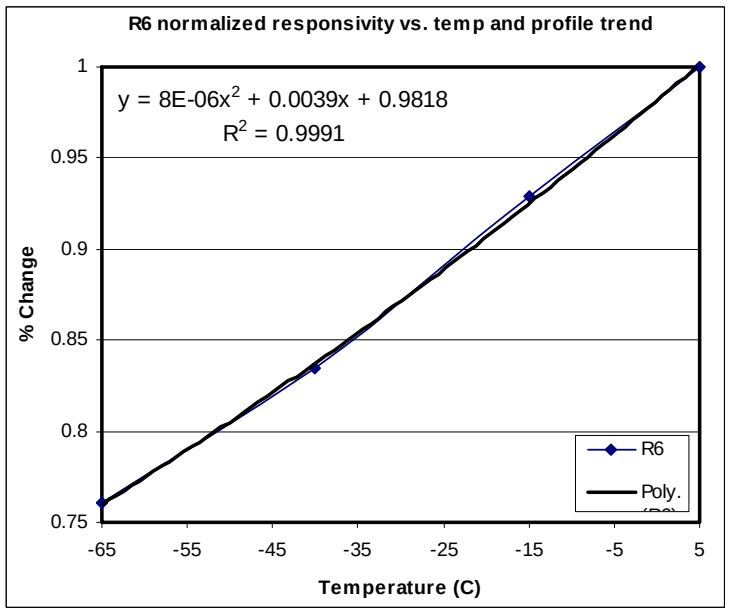

Figure C-38. Normalized plots of the R5 and R6 filter over temperature, with the polynomial fitted profile.

R7&R8 normalized and profile fitted

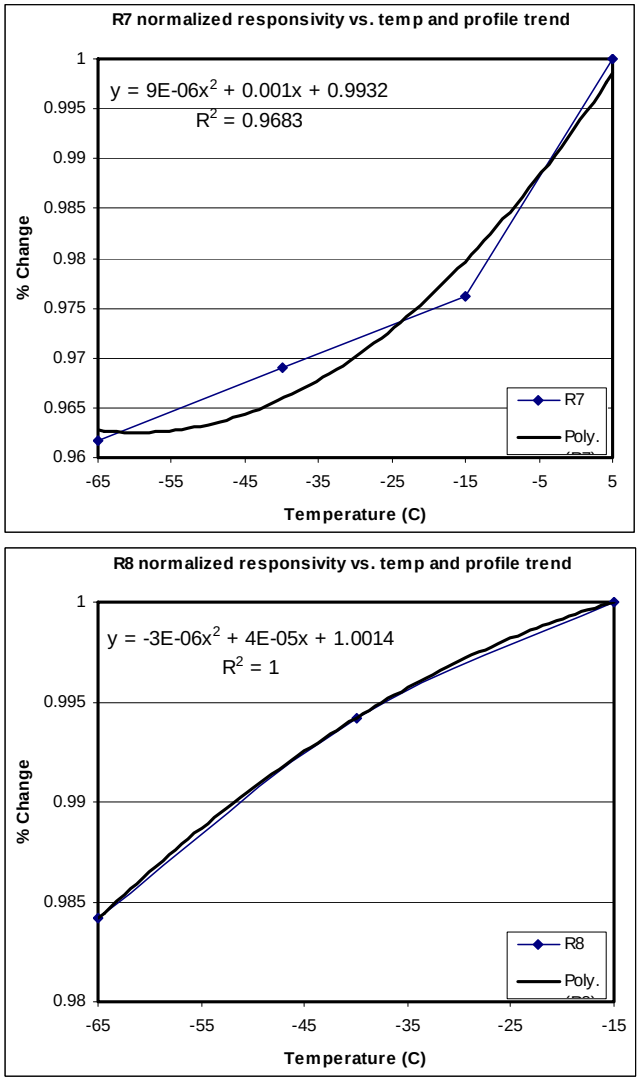

Figure C-29. Normalized plots of the R7 and R8 filter over temperature, with the polynomial fitted profile.

R9&R10 normalized and profile fitted

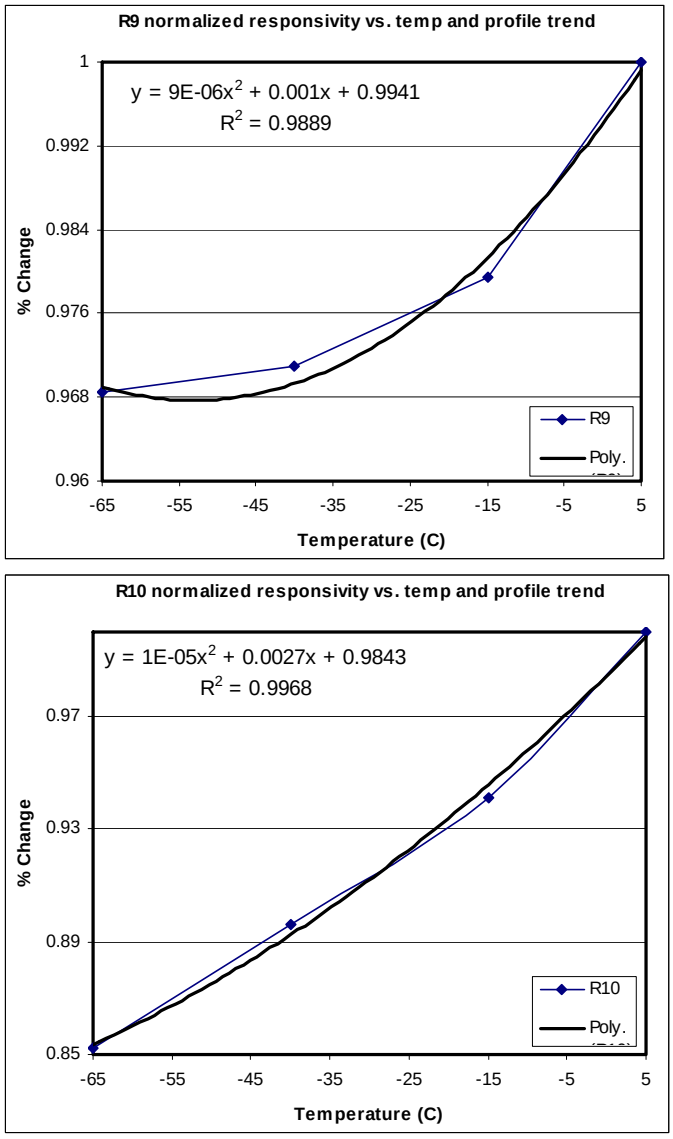

Figure C-30. Normalized plots of the R9 and R10 filter over temperature, with the polynomial fitted profile.

R11&R12 normalized and profile fitted

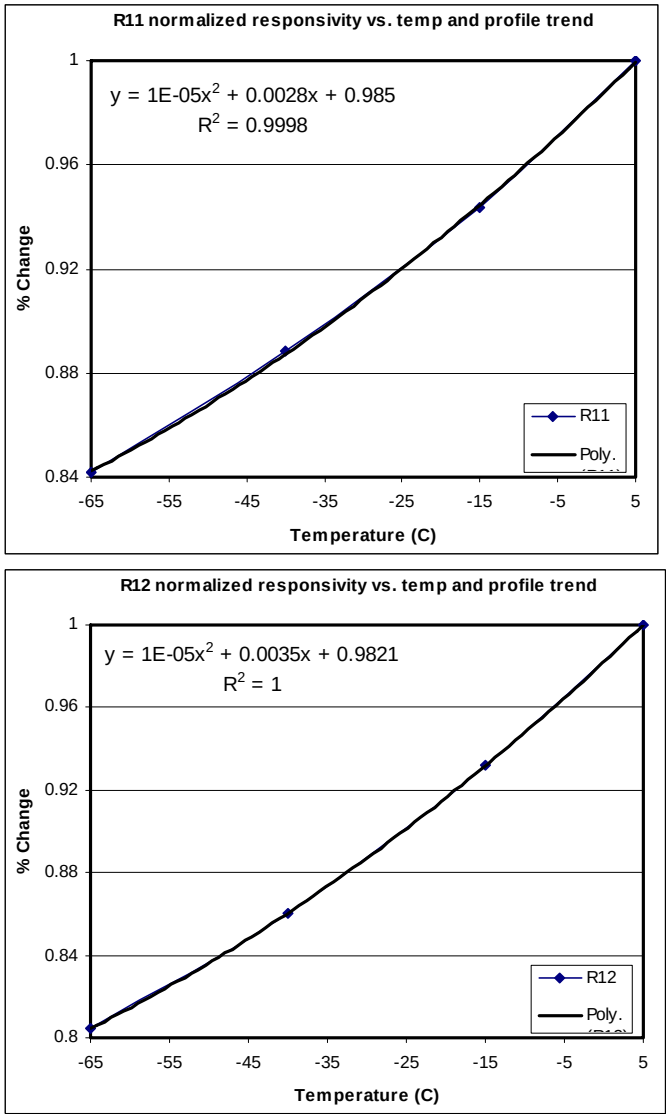

Figure C-31. Normalized plots of the R11 and R12 filter over temperature, with the polynomial fitted profile.

Final summary:

The absolute and relative uncertainty calculation are derived by taking into account the error in images, error in the test setup, the errors in the material that are used, error in our ability to measure things like temperature and final error in image processing tools previously generated. The main different between the absolute and relative uncertainty comes from dropping the knowledge of where geometrically everything is and comparing in relative geometry and filter to filter profiling. This shift from bounded geometry coordinates to a relative frame reduces the error by a factor of two.

Table C-5 Absolute and Relative Uncertainties:

	Absolute Calibration	Relative, filter to filter calibration
Contributors to Uncertainty in Radiometric Calibration.	Est value - %	Est value - %
shot noise in light image	0.017	0.017
read noise in light image	0.047	0.047
shutter shot noise in light image	0.052	0.052
shutter read noise in light image	0.052	0.052
shot noise in blocked image	0.008	0.008
read noise in blocked image.	0.057	0.057
Uncertainty in transmission of TVC windows.	1.183	1.183
uncertainty in temperature of CCD	0.079	0.079
uncertainty in temperature of PCB	0.076	0.076
uncertainty in distance to Spectralon	0.5	0
uncertainty in reflectance of Spectralon	0.5	0.25
Uncertainty in temperature of the irradiance lamp	6.013	0
Uncertainty in irradiance of lamp.	2.857	2.084
uncertainty in BW of filter	0.33	0.33
Uncertainty in CWL of filter.	0.602	0.602
Uncertainty in shape of filter.	0.466	0.466
Uncertainty in where lamp is closest to Spectralon, i.e., where is center of Spectralon illumination.	0.5	0
uncertainty in flat field	0.57	0.57
RMS sum	**6.9**	**2.6**

Table C-5 shows an absolute responsivity uncertainty of 10% and a relative uncertainty of 3%

The uncertainty in the responsivity profiles is the final step in the characterization of the CCD response in the 24 filters inside the SSI head. The table below lays out all the errors that contribute to the uncertainty in the profile, with the exception of the uncertainty in the fitted polynomial curve to the calculated data. The fitted data is seen in figure C-18 to C-34 and shows the polynomial fit and the equation for that fit in table C.IV. The average uncertainty for the fit being used in figure C-18 to C-34 and table C-IV give an uncertainty of ~0.6%, however this is easily reducible by the use of a quadratic fit. The final determination for this report was to follow the MER Pancam calibration report and keep the fit simple unless otherwise specified. Table C-VI shows that the profiling of the responsivity in both the mean case and worst case both meet the 2% specification.

Table C-6 Responsivity uncertainty calibration over Temperature

Uncertainty over temperature		
Contributors to Uncertainty in Radiometric Calibration.	**Average Est value - %**	**Worst Case Est value - %**
shot noise in light image	0.017	0.076
read noise in light image	0.052	0.076
shutter shot noise in light image	0.047	0.081
shutter read noise in light image	0.052	0.076
shot noise in blocked image	0.008	0.005
read noise in blocked image.	0.057	0.055
Uncertainty in transmission of TVC windows.	1.183	1.183
uncertainty in temperature of CCD	0.079	0.079
uncertainty in temperature of PCB	0.076	0.076
uncertainty in reflectance of Spectralon	0.25	0.25
uncertainty in BW of filter	0.33	0.505
Uncertainty in CWL of filter.	0.602	1.011
Uncertainty in shape of filter.	0.466	0.758
uncertainty in flat field	0.516	0.839
Fitted profile	N/A	N/A
RMS Sum	***1.6***	***2.0***

Table C-6 shows a 2% uncertainty in the profiling

D - Stray Light –

D.1 Background

The stray light testing used a high intensity semi-collimated light source to simulate the angular extent of the sun to the SSI, isolated

for all external light contamination. This measurement was accomplished with the goal of comparing the light levels as a function of stray light verse distance from the center of the SSI Field of View (FOV). The data was acquired imaging the source at various stages off axis, giving the simulated effect of the sun moving from on axis to greater than 14 degrees outside the FOV. The analysis for this section uses both saturated and unsaturated images in several different filters to interpolate stray level. The unsaturated images are all in solar filters that can run long integration time without saturating the data, forming the basis for the interpolation later. With the known responsivity coefficient for each filter and the unsaturated image data in hand, a fitted plot of the radiance profile curve is established for the source. From the fitted plot an interpolated set of quantity for the saturated images can be generate and fitted to the profile curve, the saturated images gain an extremely high image sensitivity that is capable discerning >1E-5 radiance effects. The final result of this test setup was the successful measurement of the inherent stray light levels in the FOV of the SSI, analyzed radially outward from a bright source such as the Sun.

D.2 Test Setup and Data Acquisition

The radiance of the source is generated and plotted using data from the solar filter images of the simulated sun and by comparison measurement of the unsaturated DN values inside the pixels of the sun source. Using the responsivity coefficient to convert the DN/sec to radiance allows for the non solar filters with there saturated image of the source to be interpolated. This fitting of non-solar data based on a linear fit of the blackbody allows for a DN/sec conversion that increases the SSI ability to detect the small input from the scattered light. Once the radiance for the saturated images is calculated, the DN summation of the source over its ~530 pixel extent will be used to measure the amount of energy that enters the camera when the Sun is 4 degrees or 298 pixels off axis from the source. The over all stray light level is determined using the ratio comparison between the DN summation of the source and the DN level of individual pixels at ~300 pixels off axis. The final result of this measure showed that the SSI has a stray light level of >1E-5 the radiance of the source when the sun is at least 4 degree outside the SSI FOV.

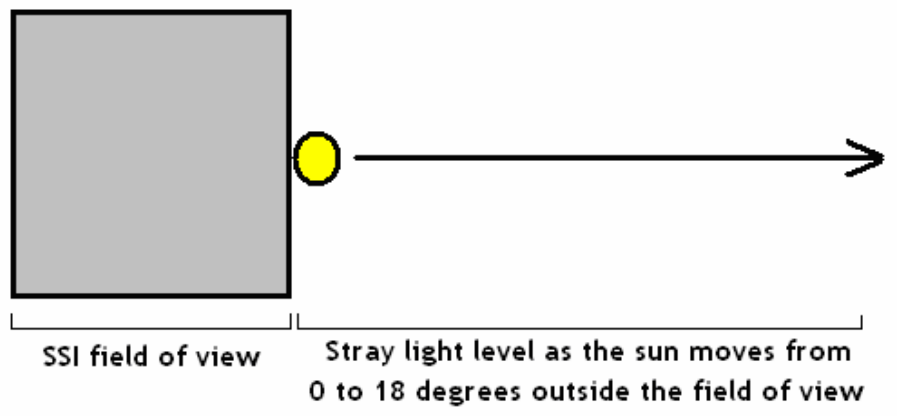

Figure D-1. Pictorial concept of how the stray light radiances drop as the Sun moves off axis.

All images that were used in the stray light analysis were taken using the FM SSI inside the LPL cleanroom using the MAGI Blackbox, a collimated slide projector and the TVC. The images were taken in a specific way to give a complete picture of the SSI field of view and what happens as the sun move from the center to far outside the FOV. There are four types of images necessary to complete the stray light analysis; the first is the unsaturated images of the source which look dark with a circular source in the field. Second, the saturated images that resembles the set of unsaturated images with the addition of a large amount of bleeding in the area near the source. The third item of the analysis is a set of off axis images that measure only the stray light and has no source in the field of view. The last type of image taken is a shutter light, which is an image with an identical scene as the other three image types, but with no integration time, giving a direct measurement of the cameras shutter effect. Figure D-2 shows an example of the two types of stray light imaging data that were acquired for this test.

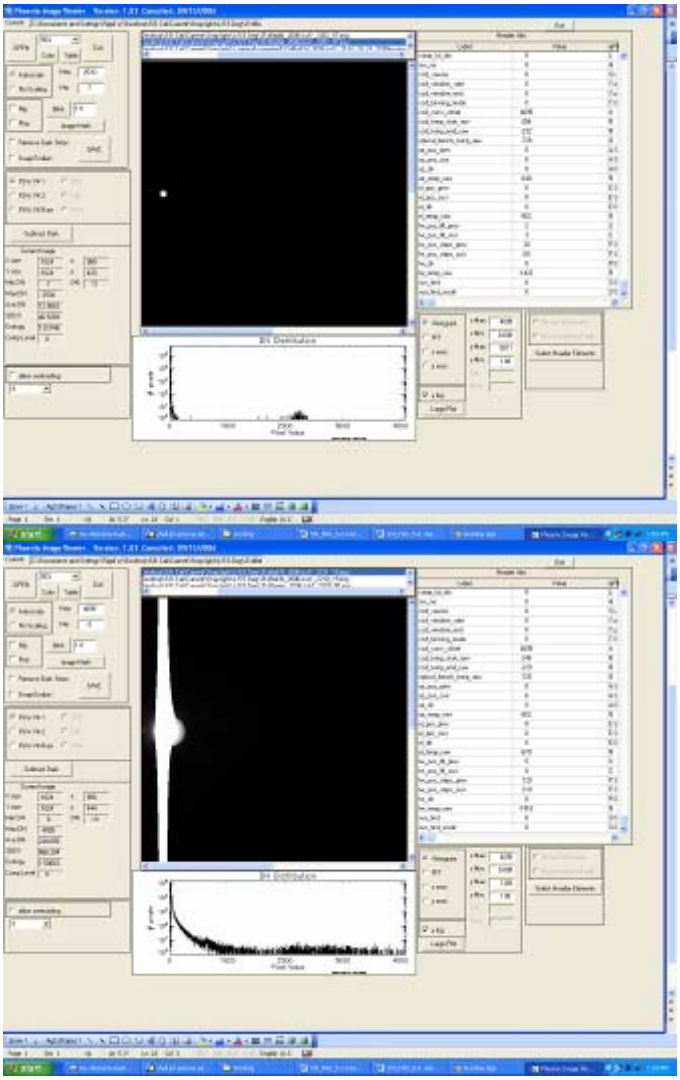

Figure D-2. Unsaturated image in the L3 filter verse saturated image in the L8 filter.

Table D-1 Absolute radiometric responsivity coefficients

Filter	R(T) at -65C^{o} (W/m^{2}/nm/Sr.)/(DN/sec)
L1	7.301E-06
L2	3.691E-05
L3	4.733E-04
L4	5.388E-04
L5	2.962E-05
L6	6.743E-06
L7	7.501E-06
L8	6.259E-06
L9	5.887E-06
L10	1.544E-05
L11	4.899E-05

L12	2.863E-05
R1	8.749E-06
R2	3.732E-05
R3	1.629E-04
R4	1.366E-04
R5	1.382E-04
R6	4.174E-05
R7	6.215E-06
R8	6.113E-06
R9	1.560E-05
R10	1.354E-05
R11	1.044E-05
R12	2.103E-05

The data in table D-1 will be used to calculate the radiance in saturated images.

D.3 Data Processing

The unsaturated images are useful themselves, but are more useful to fill in the radiance curves for the rest of the filters. The saturated images will be used to extent the sensitivity of the SSI pass the normal 4095 DN level and into the larger resolution DN/sec level. The off axis images will be used to track the stray light levels, simulating an increase in the angle between the SSI and the Sun. The shutter light images will be used to correct the images of the capture effect inherent in all CCD based images systems.

The underexposed images L3, L4, L5, R3, R4 and R5 were used to calculate the radiance in $W/m^2/nm/Sr$. of the image. These images were used to plot the radiance verse wavelength for the known filter to calculate the radiance of the saturated images. Using the plots to fit the unknown values in the other 8 filters and the responsivity coefficient of the other 8 filters, the scaled source summation DN values of the saturated images is calculated. Once the all image corrections are completed the average DN value at 4 degrees from the source is measured and used in ratio over the new calculated summized DN level.

Procedure:

1. Correct images for dark, bias and subtract shutter.
2. Sum the DN level per second over the source of the unsaturated images. This is typically 530 pixels and for this analysis was used as a standard.
3. Using the responsivity coefficients of the unsaturated filters calculate the radiance
4. Plot the radiance verse wavelength in the unsaturated filters

5. Use the rough radiance curve of the source generated in step 4 to interpolate the new radiance values at the wavelengths of the non solar filter images.
6. Add radiance values from step 5 to spreadsheet for each non solar filter.
7. Using the responsivity coefficients in the non solar filters to calculate the DN/sec of the source using ratio of non solar to solar filter radiance
8. Measure the DN/sec level of the area ~300 pixels out side the source for all filter, insert into spreadsheet.
9. Ratio the DN/sec of the stray light over the DN/sec summation of the source in each filter.
10. Use IDL program "fmssi_stray_light_plot.pro" to generated plots of the stray light level verse angle, using the DN/sec level of source calculated earlier.

Software:

Image directory:
There is a large amount of imaging data that is stored on home/mars for this test. The images are broken down per eye, per test angle and each folder contains the filter and shutter images.
/support_files_for_polarization/StrayLight_data

Spreadsheet:
The spreadsheet contains the DN, integration times, filter numbers, wavelength, radiance plot slope and other coefficient used to calculate the stray light constants.
/support_files_for_polarization

1. "Straylight.xls"

Log files:
The log files are used to monitor and track the temperatures of the different component inside the SSI. The log files are used to calculate the DN correction in dark model which is subtracted for the images.
/support_files_for_polarization

1. "SEQ_geo_target_testing_060630.log"

IDL Code:
The IDL code has two purposes; the first is to analyze individual images and also analyze a set of four images plus there shutter lights. The purpose of the program is to correct the images and then calculate the DN/sec level of the horizontal axis of the images as move away from the source.

/support_files_for_stray_light/IDL_Code/

1. "fmssi_stray_light_plot.pro" (Radiance vs. Angle analysis program)

Stray Light Code:
All IDL code used is located under
/support_files_for_stray_light/IDL_Code/

To produce the plot illustrating the change in stray light level versus angle off-center the following steps were followed:
1) The main code is fmssi_stray_light_plot.pro. It must be modified each run for master flat file to be used, shutter and images frame paths and filenames, and also for the DN/sec value of the source.
2) For each off-center angle tested the corrected versions of the exposure and shutter images are read in and stored in an array. CCD temperature, exposure time and eye are read from the header and stored in an array.
3) The flight software SEQ file is then parsed for the CCD electronics temperature reading taken at the time closest to each individual image exposure, this is stored with the other temperatures and exposure time.
4) The master flat specified in (1) is read in.
5) For each image/shutter pair for a specific off angle axis the $dark^2$ is then subtracted and the two are differenced if the CCD electronics temperature is above -45°C, otherwise they are simply differenced on the basis that individual dark subtraction here will introduce more error.
6) For the first two off axis angles only the image is now displayed and the user is prompted to left click on the image until the center of the solar disk has been located, to aid in this the mean of the DN values in 3x3 box centered on the pixel selected is displayed along with the DN value of the selected pixel. This is done in order that the code can consider only off axis locations in one direction, and the first two images cover a range of angles that include both the on axis disk and both off axis directions.
7) Each image is assumed to contain a certain range of off axis angles in the direction being analyzed: The first from 0-6°; the second from 0-12°; the third from 2.5-16° and the fourth from 4.2-18°. The angle corresponding to each column from either the respective center selected in (6) (First two images) or edge-to-edge is thus assigned an off-axis angle value. For each of these columns the mean DN of a single pixel wide strip extending 5 rows above and below the row selected in (6) is also calculated and divided by the exposure time multiplied by DN/sec value of the source.
8) The off-axis angles are then plotted versus the DN/sec value of the source for all of the off-axis angles from all images on the same plot.

There are two set of images that can be used to measure the source verse the stray light ratios. The images with the source in the center and the images with the source 5.5^{o} off axis both have areas that are 300 pixels away from the source that can be used to analyze the stray light level. The idea behind this test requirement is that the science team would like to be able to image the sky with the Sun only 4 degrees outside the SSI FOV. As a result this requirement was born to ensure the random scatter light that will make it into the SSI even with the Sun off axis would be of a level that would not affect the science team. The images with the SSI centered, and the source at 11^{o} off axis are truly representative images of what the SSI will be required to do, how ever the any data that has a measurable area 300 pixel away from the source is also valid data. In this case images for all data set were examined and the set with the lowest general DN level at 300 pixels out was used to measure the average DN/sec level per filter shown in table D-3. Below is an example image with the projector source in the center of the SSI FOV.

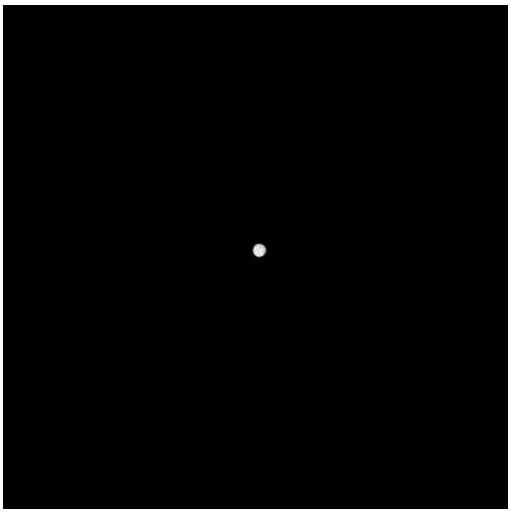

Figure D-3. Shows the center source being measured by integrating the DN in the 530 pixel area of the source and then dividing by the image integration.

The image below shows the source structure and the extent of the source which is about 530 pixels in general with an average DN of 2500 per pixel. The result of which is with a 1.6 second exposure time for a final DN/sec of ~2.2E6.

Figure D-4. Zoomed image of Sun source is approximately 26 pixels wide and extends 530 pixels total.

Graphs of fitting radiance values:

In order to calculate the DN level of the source in the stray light images that were taken over the whole filter set, it will require both measurement and interpolation of the radiance. The method of fitting the saturate radiance values to the unsaturated radiance values will be used to generate the radiance curve of the source in unit of $W/m^2/nm/Sr$. to work directly with our responsivity coefficients. Plotting the known L3, L4, L5, R3, R4 and R5 radiance verse wavelength, which then is used to fit a linearly trend and calculation of the unknown filter radiances from the trend. With the interpolated radiance, integration time of the individual filter images and the filter responsivity coefficients, the summized DN level in the on-axis images is derived. There is a known drop in the radiance in the IR seen at about 900 nm do to a glass window that is in the projector, blocking the IR transmission out past 900nm.

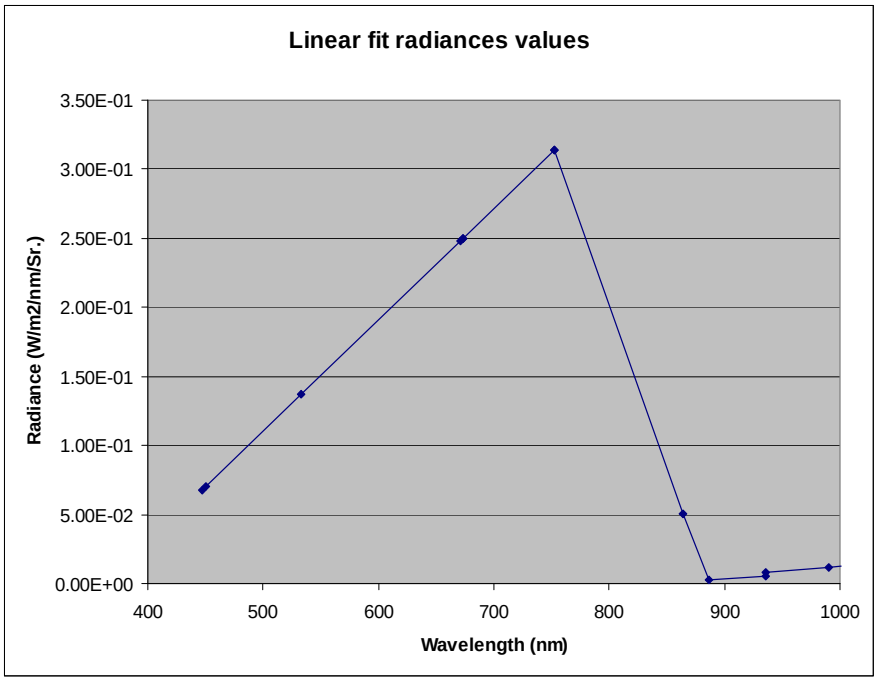

Figure D-4. Measured and interpolated radiance values following the upward curve of the source. The saturated filter radiance values are linearly fitted to the unsaturated filter radiance values to complete the curve.

D.4 Stray Light Performance

Table D-2 Calculated DN, Requirements and Results

CW (nm)	Filter #	Measured DN	Itm	Response @ -65C	Radiance	Derived avg DN per pixel	DN at 4° off axis	# of pixels in source	Final ratio	Accuracy
446.8	L2	N/A	2000	3.69E-05	7.24E-02	1.83E+04	70.98	530.92	7.13E-06	7.13E-07
450.7	L3	2294.39	3000	4.73E-04	7.55E-02	2.29E+03	0.27	530.92	2.20E-07	2.20E-08
533	R11	saturated	2000	1.04E-05	1.42E-01	1.32E+05	282.17	530.92	3.95E-06	3.95E-07
671	R3	3901.36	500	1.63E-04	2.54E-01	3.90E+03	0.31	530.92	1.50E-07	1.50E-08
672.8	L1	saturated	2000	7.30E-06	2.55E-01	2.87E+05	318.87	530.92	1.71E-06	1.71E-07
672.8	R1	saturated	2000	8.75E-06	2.55E-01	2.86E+05	297.34	530.92	1.92E-06	1.92E-07
753	R8	saturated	2000	6.11E-06	3.20E-01	5.35E+05	17.79	530.92	6.36E-08	6.36E-09
753	R9	saturated	2000	1.56E-05	3.20E-01	2.11E+05	12.41	530.92	1.13E-07	1.13E-08
864.2	L8	saturated	2000	6.26E-06	5.08E-02	8.71E+04	19.79	530.92	4.49E-07	4.49E-08
886.9	L5	1604.28	4000	2.96E-05	2.14E-03	1.60E+03	0.50	530.92	5.92E-07	5.92E-08
935.9	R4	1076.71	5000	1.37E-04	5.00E-03	1.08E+03	1.65	530.92	2.88E-06	2.88E-07
935.9	R5	1215.37	4000	1.38E-04	7.07E-03	1.22E+03	1.20	530.92	1.86E-06	1.86E-07
990.7	L4	492.47	12000	5.39E-04	1.09E-02	1.57E+03	3.15	530.92	4.41E-06	4.41E-07
1001	L11	saturated	2000	4.90E-05	1.17E-02	3.02E+03	3.44	530.92	2.48E-06	2.48E-07

The results show that at 4° off-axis from the edge of the projector source, the stray light is measured on the 2.1E-6 radiance scale or less, which is less that 1E-5. All measures taken and interpolated values were measured to accuracy of 1% to 10%, therefore giving a general accuracy in the stray light of 1.1E-7 or 5% after RSS the individual parts together.

Stray light plot over testing field of view:

There are four filters for which a full set of data is available from 0° to 18° off-axis where the source is moved from the center of the SSI FOV to 18° out from the center of the SSI FOV. The SSI stray light plots below layout verification of the functional requirements by plotting relative DN level over the summation of the Sun source DN level as a function of degrees away from the SSI field of view.

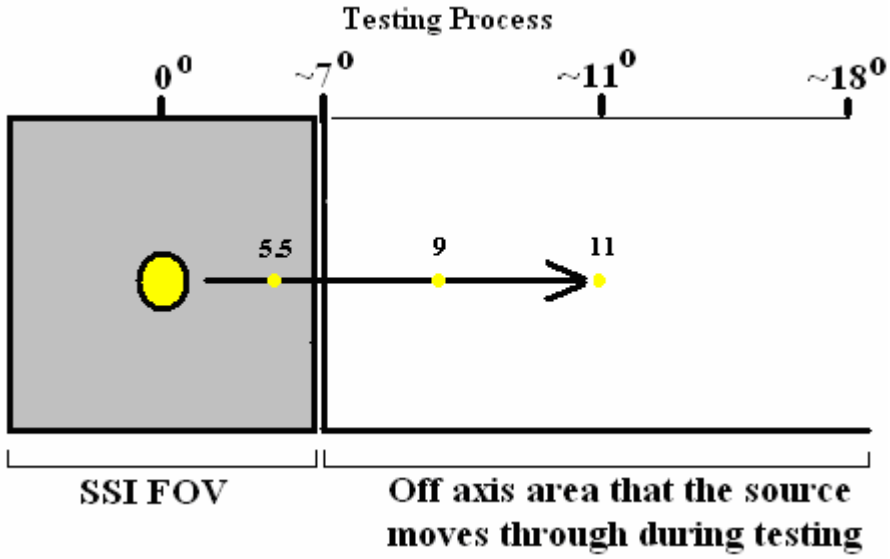

Figure D-6. Pictorial concept of how the source moves during testing

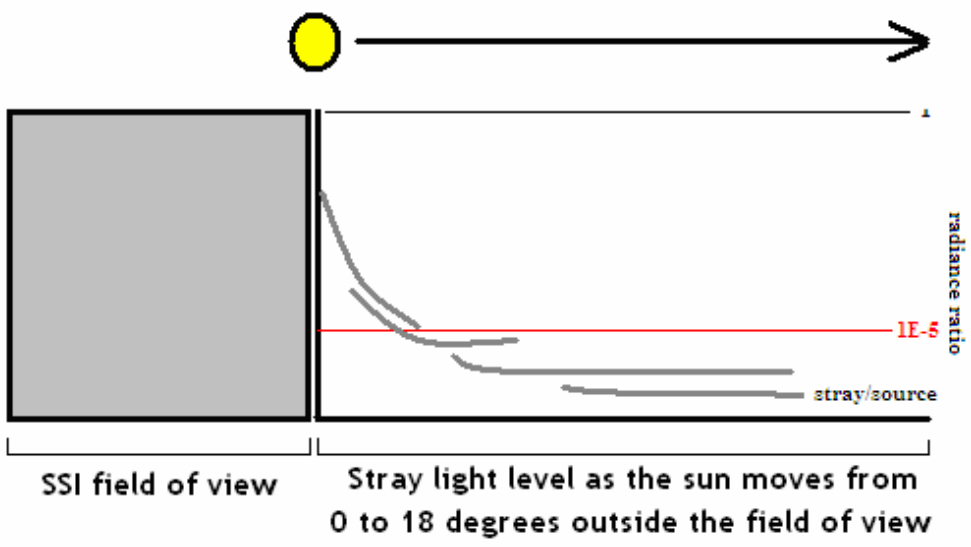

Figure D-5. Pictorial concept of the stray/source plots verse degrees off axis.

SSI Analysis of the Stray Light:

Using imaging data on-axis, with the source 5.5^{o} off, 9^{o} off and 11^{o} off-axis a plot per filter was generated to represent the average DN/sec level scanning away from edge of the SSI eye field of view, divided by the summations of the DN over the Sun source.

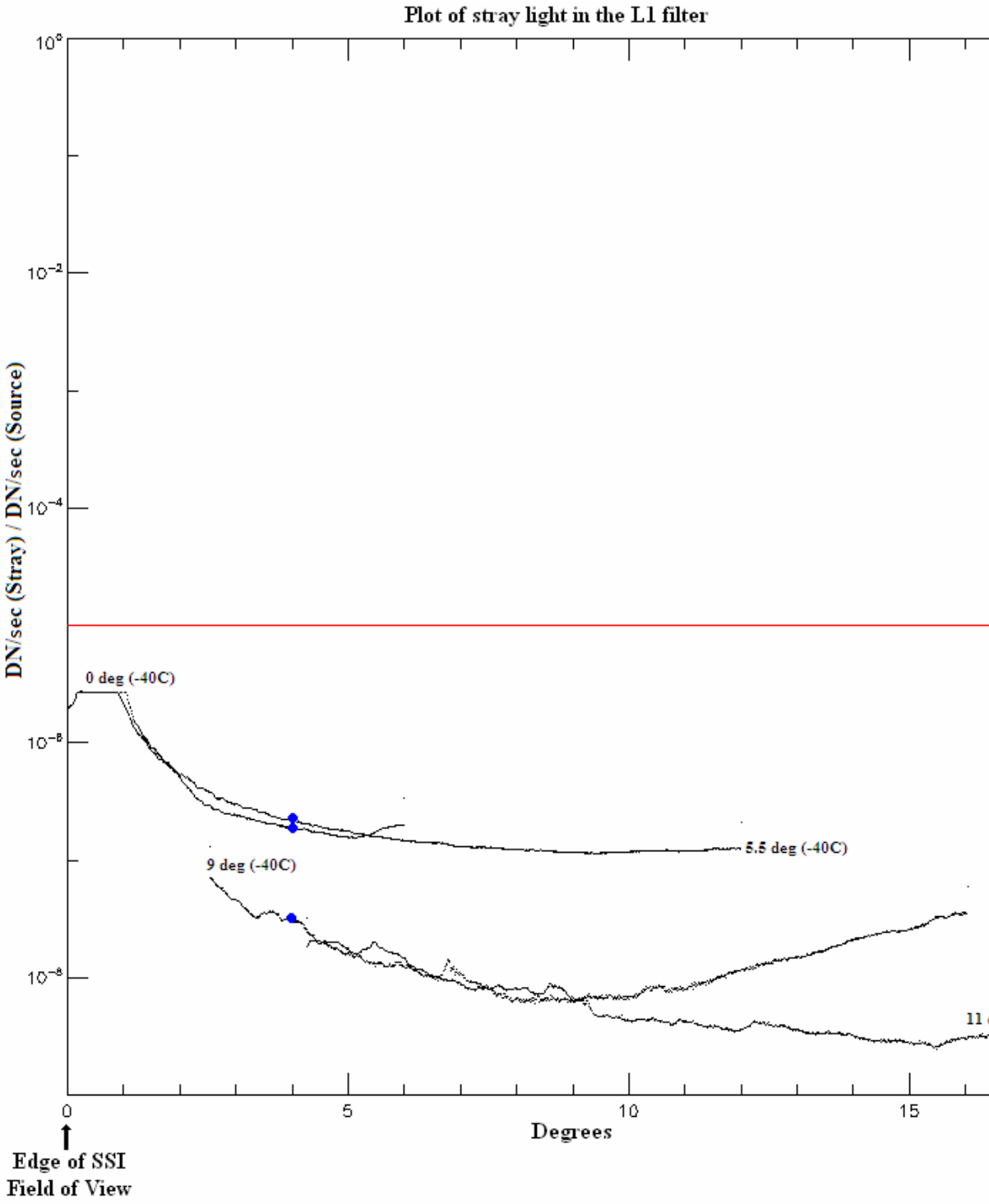

Figure D-6. Plot of the 4 stray light images over an 18 degree field of view (1E-5 radiance spec is met over the total 18 degrees)

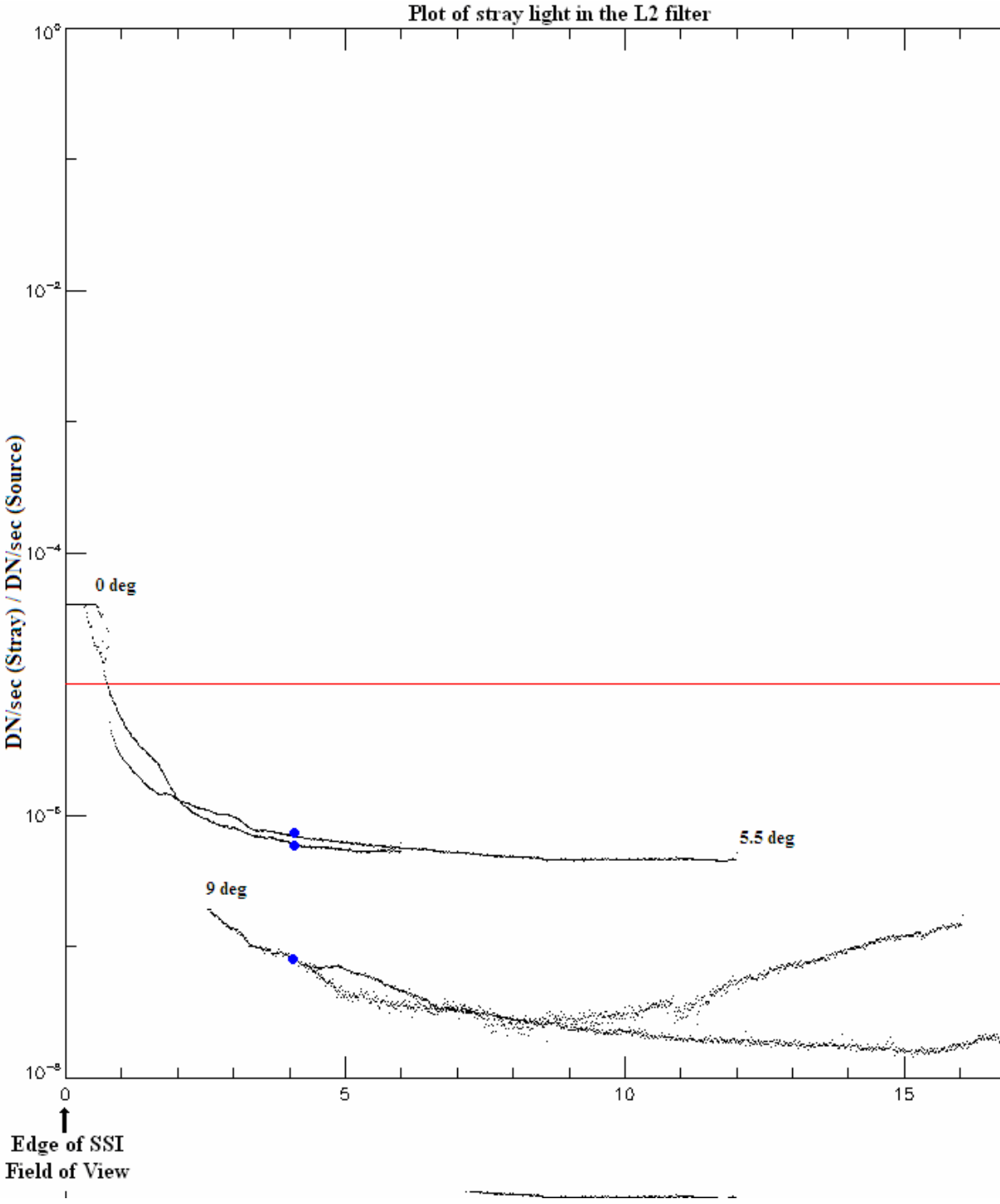

Figure D-7. Plot of the 4 stray light images over an 18 degree field of view (1E-5 radiance spec is met from 1 to 18 degrees).

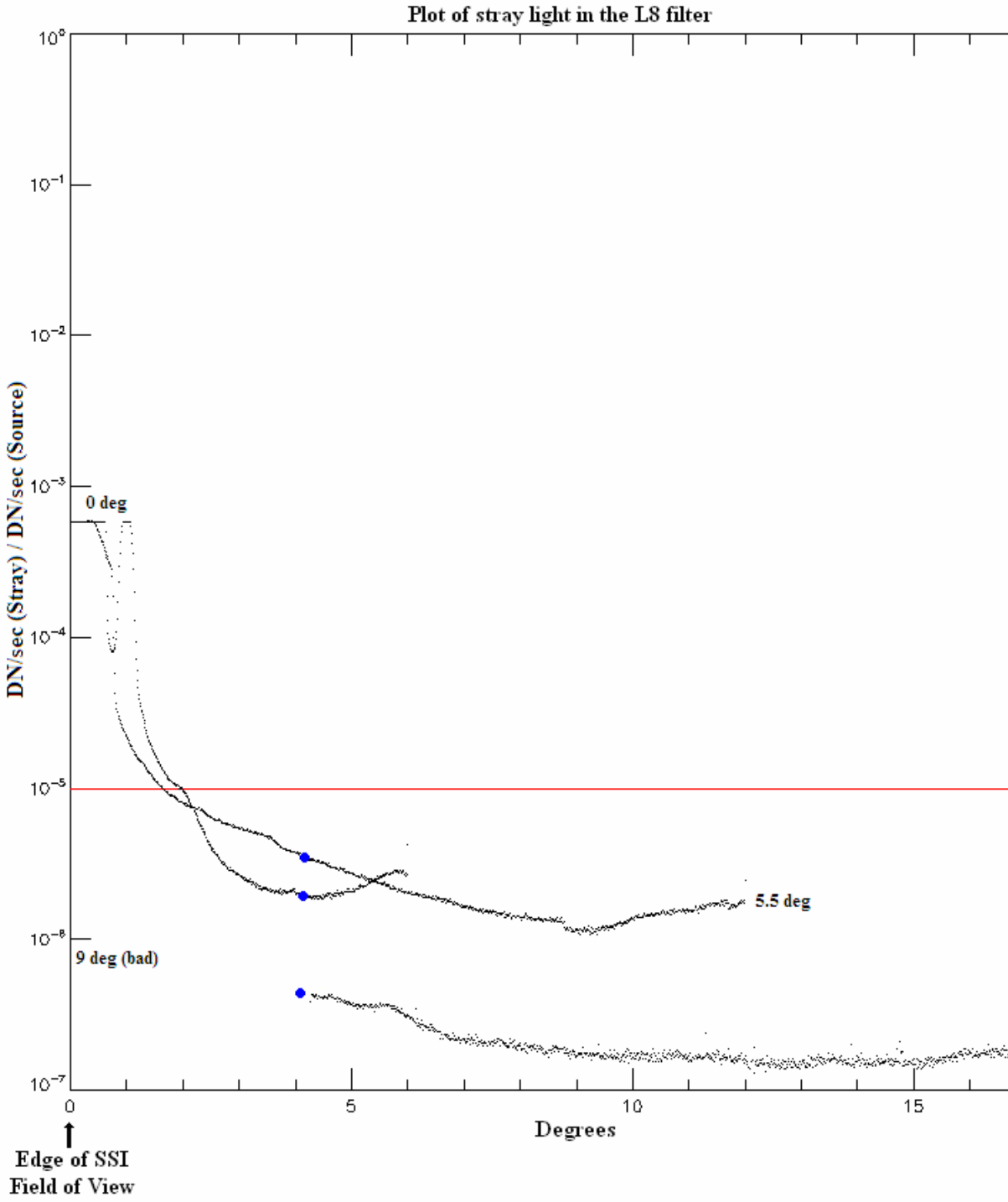

Figure D-8. Plot of the 3 stray light images over an 18 degree field of view (1E-5 radiance spec is met from 2 to 18 degrees).

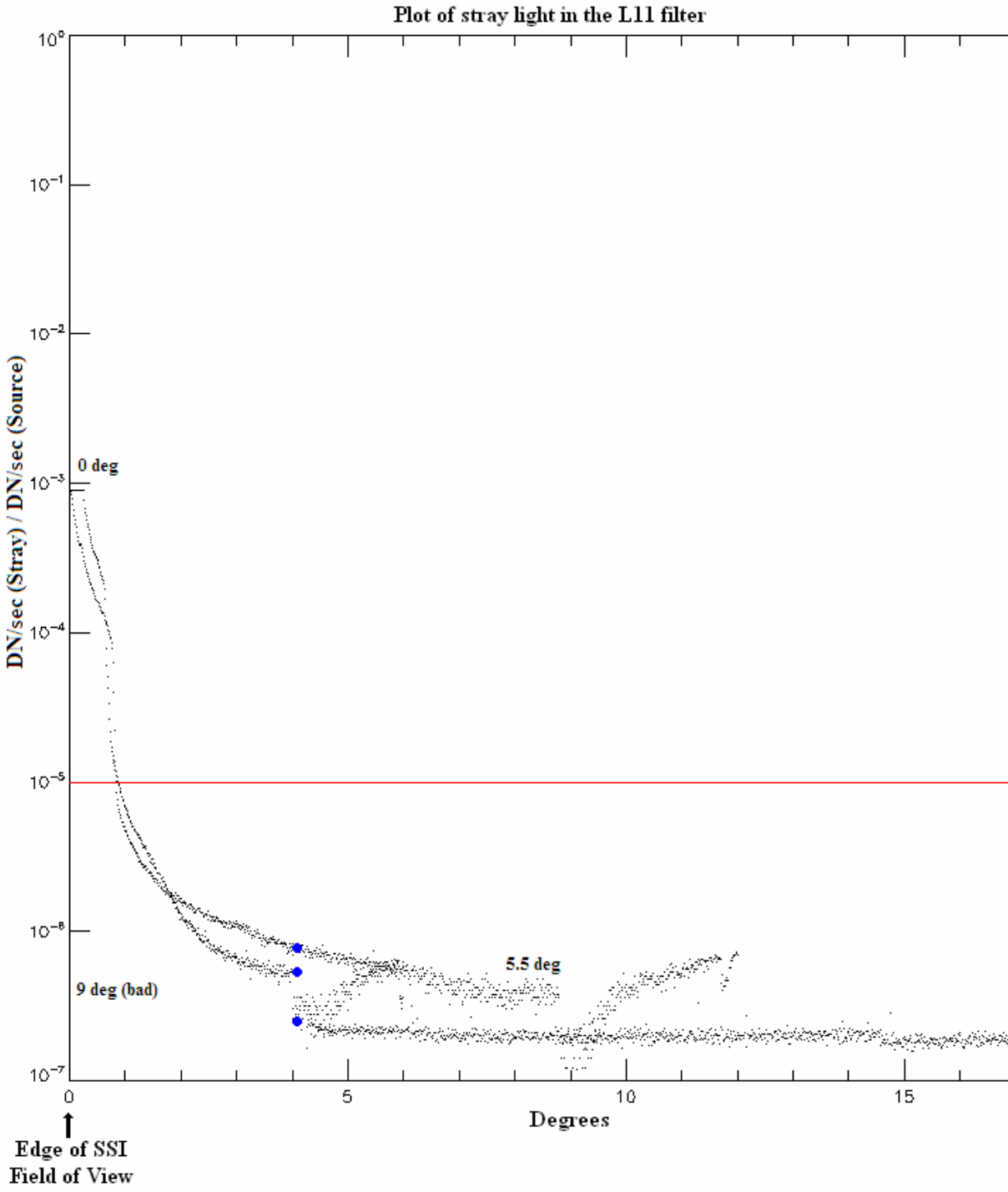

Figure D-9. Plot of the 3 stray light images over an 18 degree field of view (1E-5 radiance spec is met from 1 to 18 degrees).

Final Summary:

The final results in this section conclude that all the measured filters meet the requirements of having a 1E-5 radiance or better stray light level, when the source is at least 4 degrees outside the SSI field of view. There were two methods of verification used; the first involved integrating the DN values inside the Sun source used to measure the stray light. The DN level is then measured at 300 pixels off axis of the source, then the stray light DN/sec level 4^{o} off was divided by the summed DN level of the source. The second method involves plotting the DN/sec level of the 4 data sets across their field and then dividing that level by the summed DN level of the Sun source. The relative radiance is then plotted as a function of moving the Sun off axis from the edge of the SSI field of view, out to 18 degrees outside the edge of the SSI field of view. Both methods of analyzing the stray light level were successful and proved that every filter measured meets the functional requirements and to the specified accuracy of as least 10%.

E - Linearity, Gain, Read Noise - ML

- **E.1 Test Setup and Data Acquisition**
- **E.2 Data Processing**
- **E.3 Video Offset**
- **E.4 Linearity**
  - **Gain**
  - **Read Noise**
  - **SNR vs. DN**

F - Bad and Hot Pixel Map - AS

F.1 Test Setup and Data Acquisition

The hot and bad pixel maps were generated from photon transfer and linearity data acquired on 06/15/2007 for the Left Eye and 06/18/2007 for the right eye while The FM SSI camera was installed in the Magi Group, Lunar and Planetary Lab, UofA (MAGI) Thermal Vacuum Chamber, at a nominal CCD temperature of about -20°C. Multiple images were taken while exposed to a constant source of illumination using an integrating sphere (Figure F - 1, Figure F - 2) at each of a range of integration times, all the way to saturation.

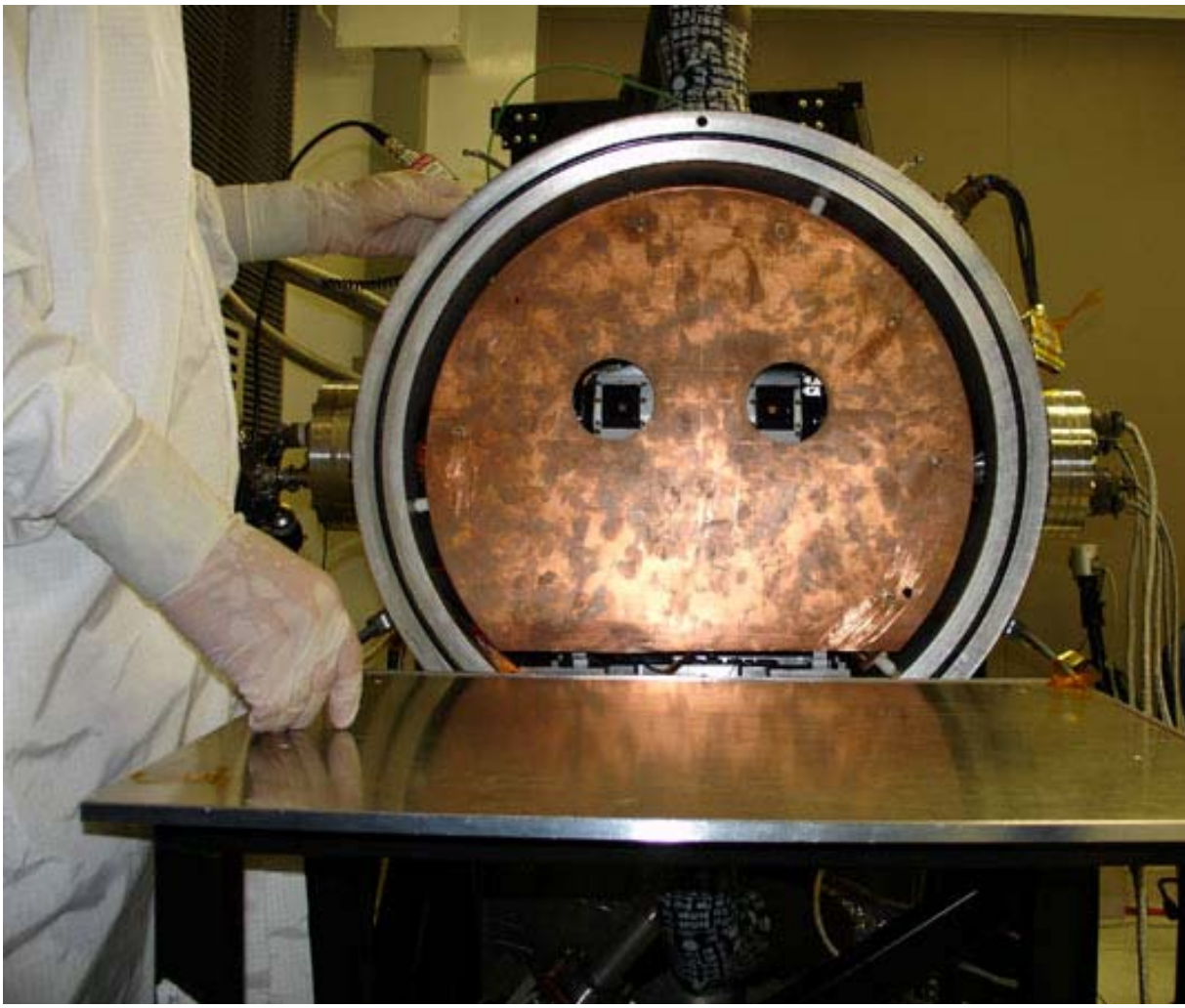

Figure F - 1: FM SSI Camera inside the Thermal Vacuum Chamber During Test Setup Prior to Door Installation

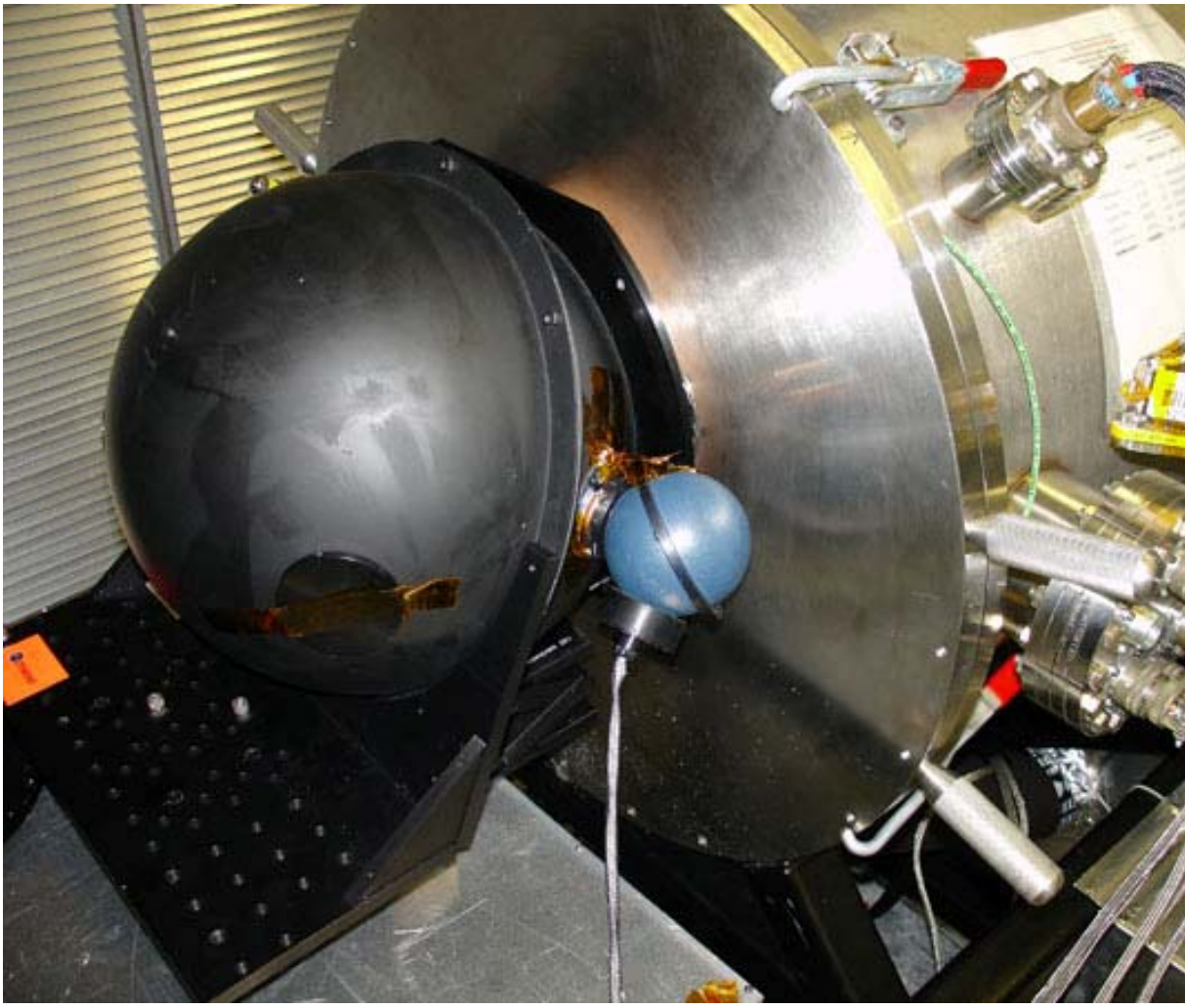

Figure F - 2: Integrating Sphere in Front of Thermal Vacuum Chamber Window During Testing

F.2 Hot Bad Pixel Table Implementation

Prior to detailing the processing and analysis that resulted in the hot and bad pixel tables included with the flight software it is best to understand their implementation. The flight software can support two tables for each eye called the hot and bad pixel correction tables[3] of up to 4096 entries each. Not all of the correction types are supported by each table, the correction types are:

1) Scaling (Hot only)

The scaling option of the hot pixel correction allows a floating-point value to be applied as a multiplier (or divisor, if it's a fractional value n such that $0 < n < 1$). This is useful for linear pixels that have somewhat higher or lower responsiveness than the local average.

2) Replacement (Hot and Bad)

The replacement option simply substitutes a value from the correction table for the pixel value at the specified coordinates.

3) Averaging (Hot and Bad)

Averaging is done using the target pixel's nearest neighbors.

Hot pixel correction is performed first, followed by bad pixel correction. The implementation being such that the table is simply stepped through and the requested operation performed. This leads to some workarounds being necessary to achieve the desired results.

a) Firstly the extreme left and right columns on the SSI CCD are much more responsive than any of the others; this means that they are always higher than their surroundings and often saturated in a perfectly good image. Since there is no option to replace one pixel with whatever value is seen in another pixel, the approach that will be taken here is to replace alternating sections of both columns with a low value in the hot table and then use nearest neighbor replacement multiple times throughout both tables in order to bring these two columns into line with the average level of the rest of the image. As a direct result of this, the FM SSI correction tables supplied with the flight software should be both be applied, or neither should be applied.

b) Secondly, if you have a block of hot/bad pixels which you wish to replace, nearest neighbor average replacement will, if done blindly, tend to keep dragging uncorrected pixels into the average, resulting in very ineffective correction. In this case it is best to first get the edges such that very few uncorrected and yet affected pixels are brought into the mean, and then to spiral into the affected area propagating the correction as you go. If the block is quite large then a couple of iterations ought to be quite effective.

c) Thirdly the most effective correction that can be achieved with this framework would seem to be to scale the pixel whenever possible, and to this end a lot of the development outlined below goes into the identification of as many close to linear anomalous pixels as possible, with the other methods used mainly on the two outlying columns.

F.3 Data Processing and Table Development

The images were first reunited with their dark/null strips and corrected for the ifsw pixel shift problem using reattach_dark_strips_new.sav. The main analysis code was pixel_by_pixel_map_2L.pro and pixel_by_pixel_map_2R.pro for the left and right eyes respectively.

1) The images were first read in and their integration times recorded along with the mean of a centered 256x256 box and the image itself (Figure F - 3).

2) Then for each pixel within the image frame for each integration time, provided pixel response in the frame is over 100DN and the mean box value for the integration time is less than 3500DN, a comparison is done to the local (Figure F - 4) median pixel response. Percentage difference of the pixel response from the local median response is recorded and added in quadrature to those of the same pixels in the other frames to give total percentage deviation of a given pixel from the local median across the

integration times, $\Delta_{TOT\%}$ (Equation F - 1). The first and last columns are ignored throughout because of their abnormally high response and are added to the final table automatically.

$$\Delta_{\%}^{i,j,itime} = 100 \times \frac{\left|DN_{i,j} - \text{median}(\text{nearest neighbors})\right|}{0.5 \times \left(DN_{i,j} + \text{median}(\text{nearest neighbors})\right)}$$

$$\Delta_{TOT\%} = 100 \times \sum_{itime} \sqrt{\left(\left(\Delta_{\%}^{i,j,itime} / 100\right)^2\right)}$$

Equation F - 1: total percentage deviation of pixel i,j from the local median across the integration times

3) For each pixel across the different frames, integration time vs. pixel response (where the response is less than 3000DN) is then fitted to a straight line (Figure F - 5) and the offset/slope fit parameters and their uncertainties are recorded, along with the χ^2 goodness of fit.

4) The median of the offset, slope and χ^2 along with the standard deviation of the slope and offset are calculated across all pixels. Then the standard deviation of the χ^2 values for those pixels having $\chi^2 < 30000$.

5) For each pixel and its linearity fit the following checks are then carried out in this order; following an assignment, the rest of the possible assignments are then skipped over and the next pixel selected. The first and last column are not included in the analysis:

a) If the offset of the fit is not finite then the pixel is labeled Bad, with Average of nearest neighbors specified.

b) If the slope of the fit is not finite then the pixel is labeled Bad, with Average of nearest neighbors specified.

c) If χ^2 goodness of fit is not finite then the pixel is labeled Bad, with Average of nearest neighbors specified.

d) If the slope of the fit is greater than 120% or less than 80% but greater than 20% of the median slope of the nearest neighbors then the pixel is labeled Hot, with Scale by median slope/pixel slope specified.

e) If the slope of the fit is less than or equal to 20% of the median slope of the nearest neighbors then the pixel is labeled Bad, with Average of nearest neighbors specified.

f) If the pixel is not immediately adjacent to the 1-pixel wide hot strip at the left or right hand side, and the cumulative percentage deviation of the pixel value from its neighbors is greater than 55% and the pixel slope is between 30% and 70% of that of the nearest neighbors then it is labeled Hot, with scale by median slope/pixel slope specified.

g) If the pixel is not immediately adjacent to the 1-pixel wide hot strip at the left or right hand side, and the cumulative percentage deviation of the pixel value from its neighbors is greater than 55% and the pixel slope is less than 30% or greater

than 70% of that of the nearest neighbors, then the pixel is labeled Bad, with Average of nearest neighbors specified.

6) The top row of the image is considered separately, and provided the fit coefficients are finite it is labeled Hot, with scale by median slope/pixel slope specified.

7) Entries are made in the Hot correction table to replace the entirety of the first and last column with a nearest neighbor average, then in the Bad correction table to firstly replace every other vertical pair with a value of 100, and then to replace all of them with the average of the nearest neighbor.

The determination of a pixel's inclusion in either the hot or bad pixel correction table was first approached in terms of limits on the fit parameters (Figure F - 6), but was largely replaced by a more flexible and reliable approach – looking at the median value of the quantity amongst the nearest neighbors (Figure F - 7). The first advantage of this approach was a more obvious cutoff point that seemed to, in conjunction with pixel response slope, include all of the pixels that appeared defective at first glance, without including too many of the borderline cases. The second advantage was the reduction in the amount of limits to be fine tuned.

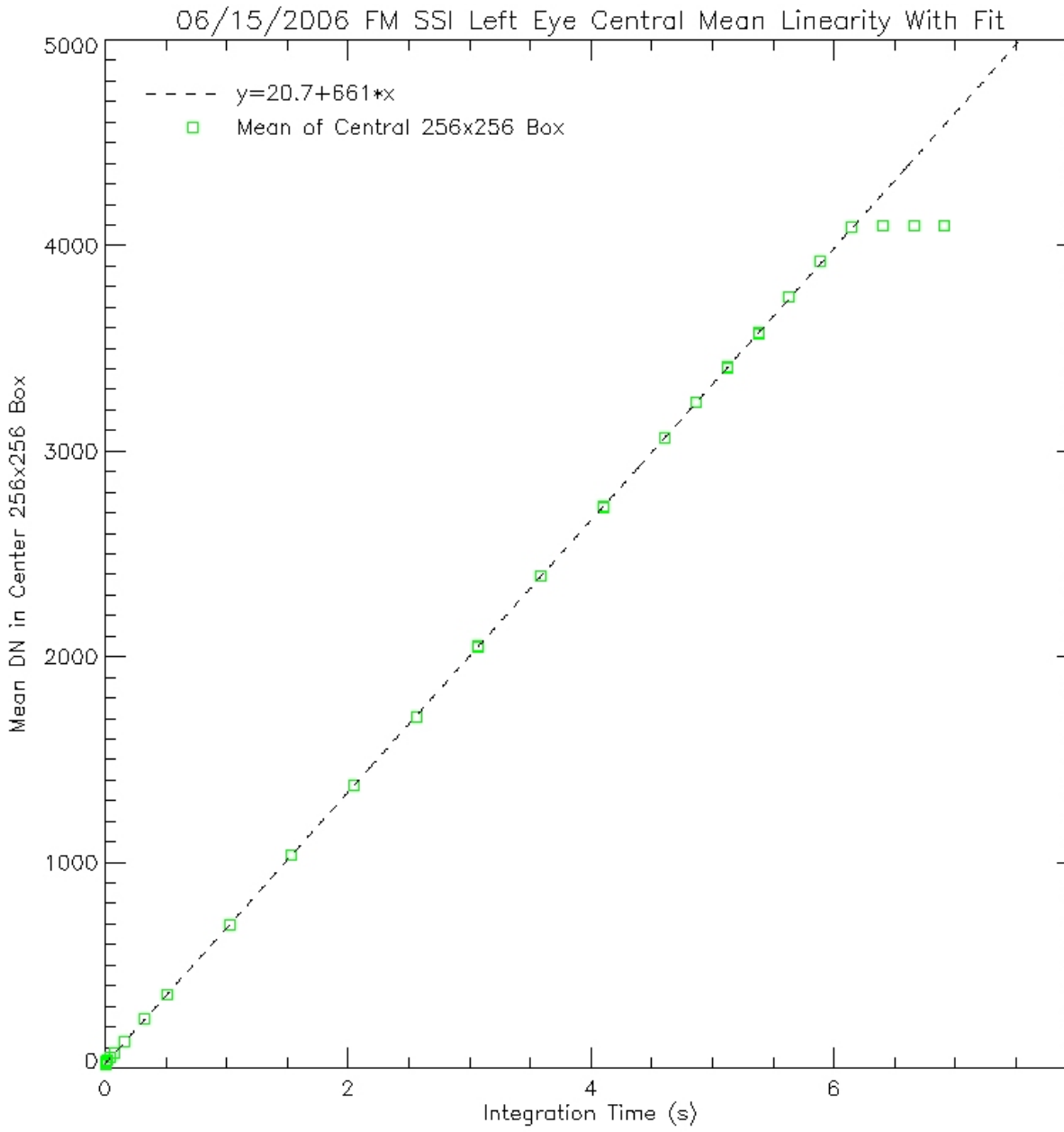

Figure F - 3: Left Eye Central Mean Showing Saturation

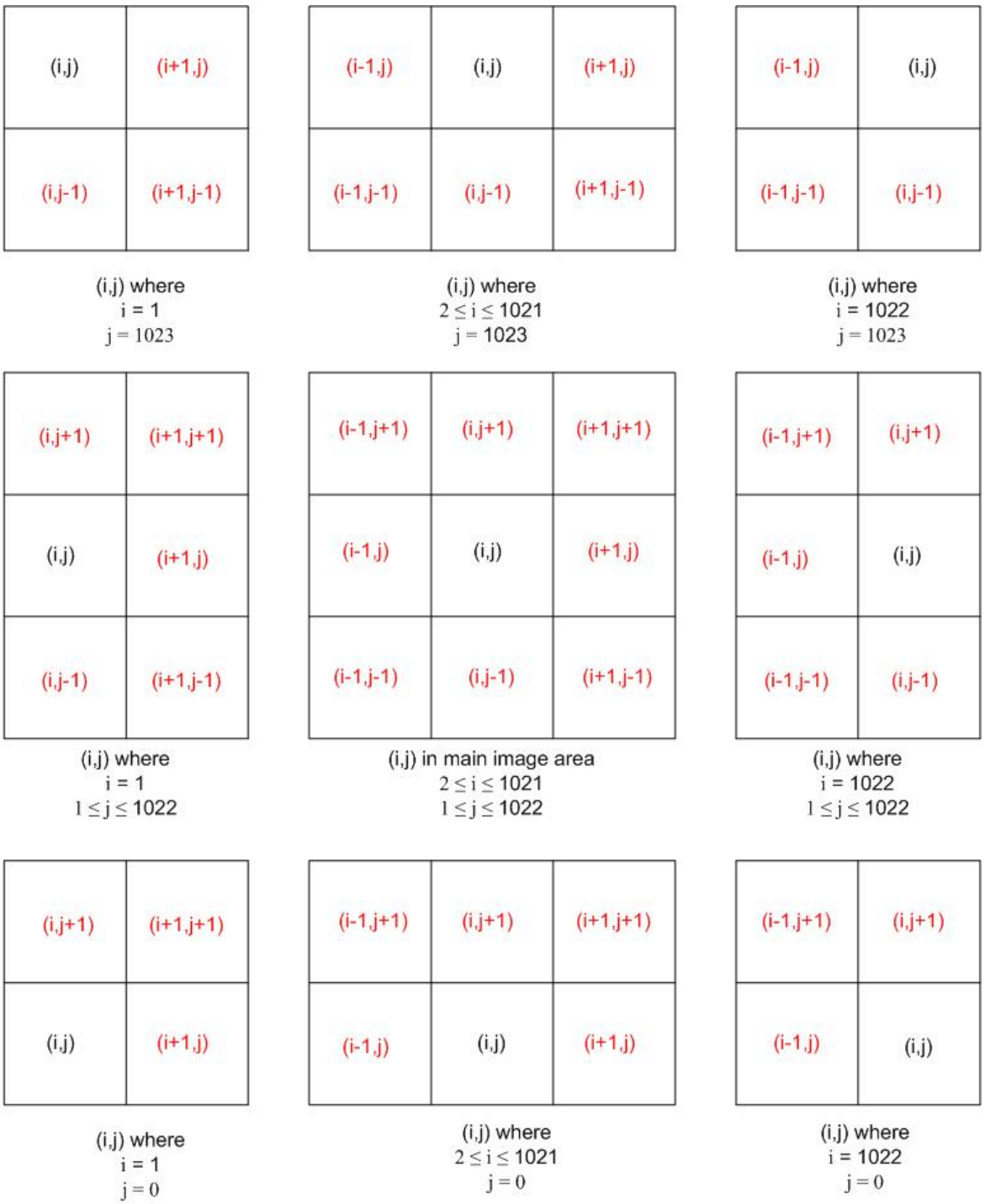

Figure F - 4: Nearest Neighbor Definitions. Nearest Neighbors Denoted in Red

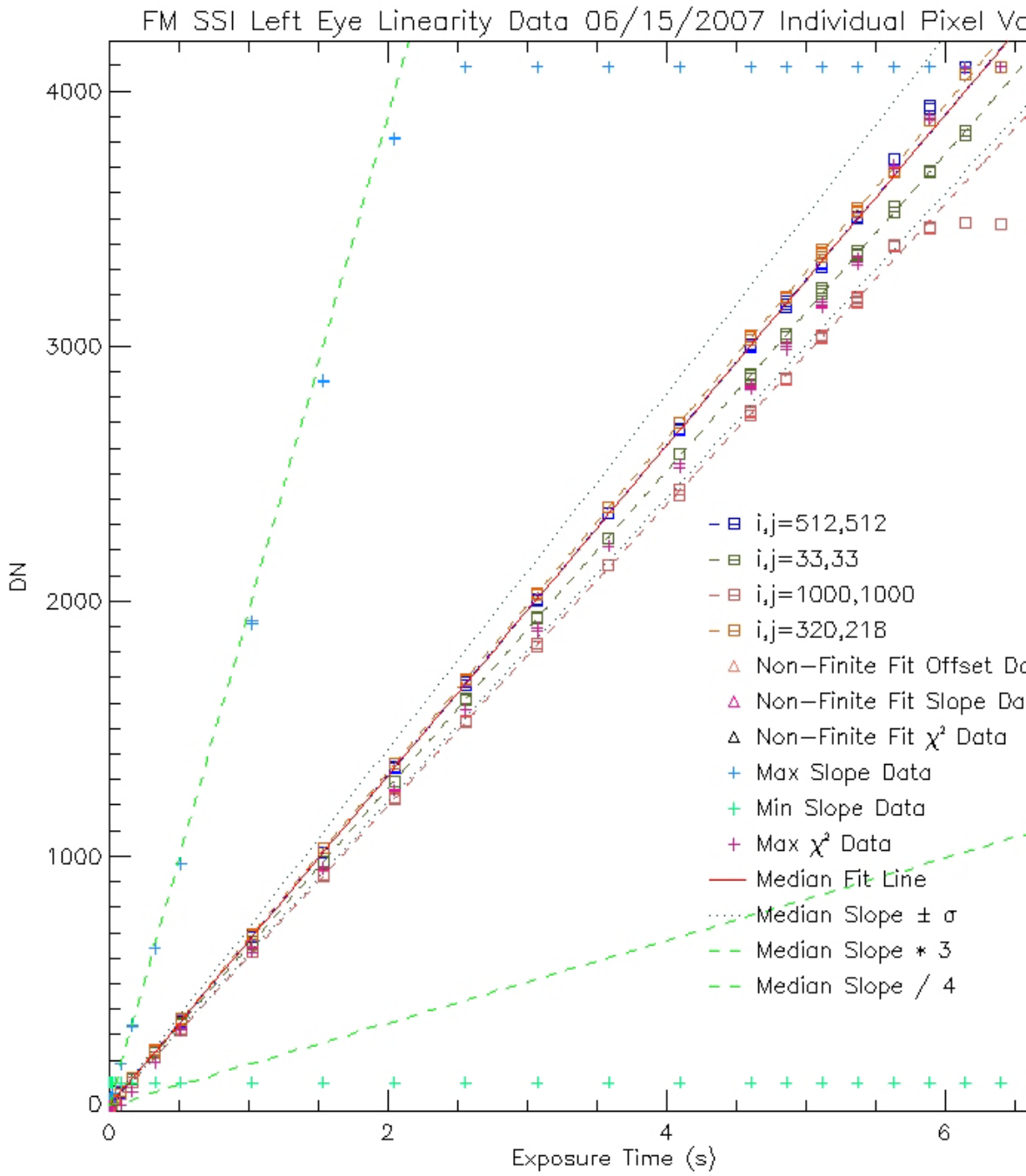

Figure F - 5: FM SSI Pixel Linearity Data

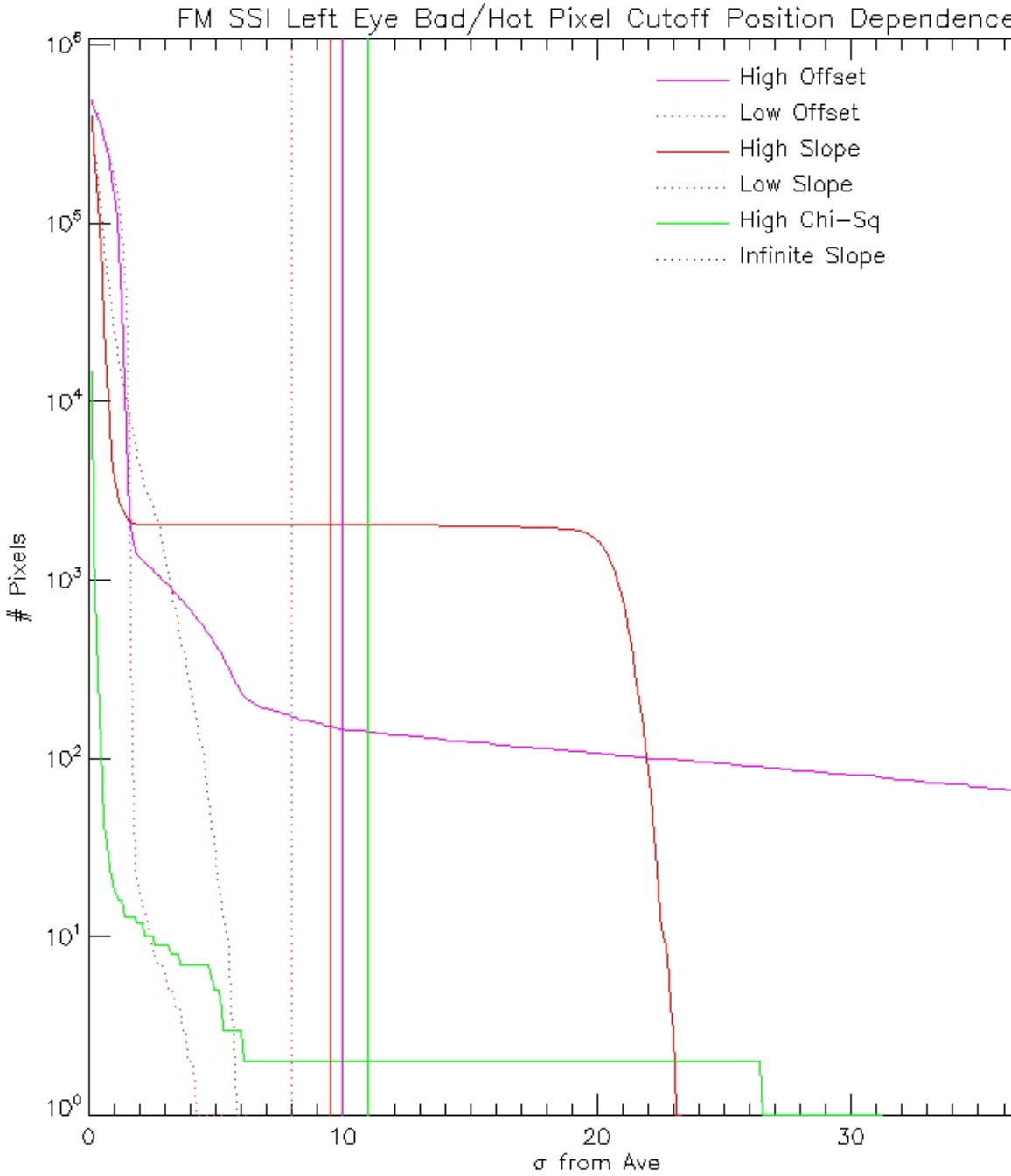

Figure F - 6: A limit based approach to inclusion in the hot/bad pixel tables

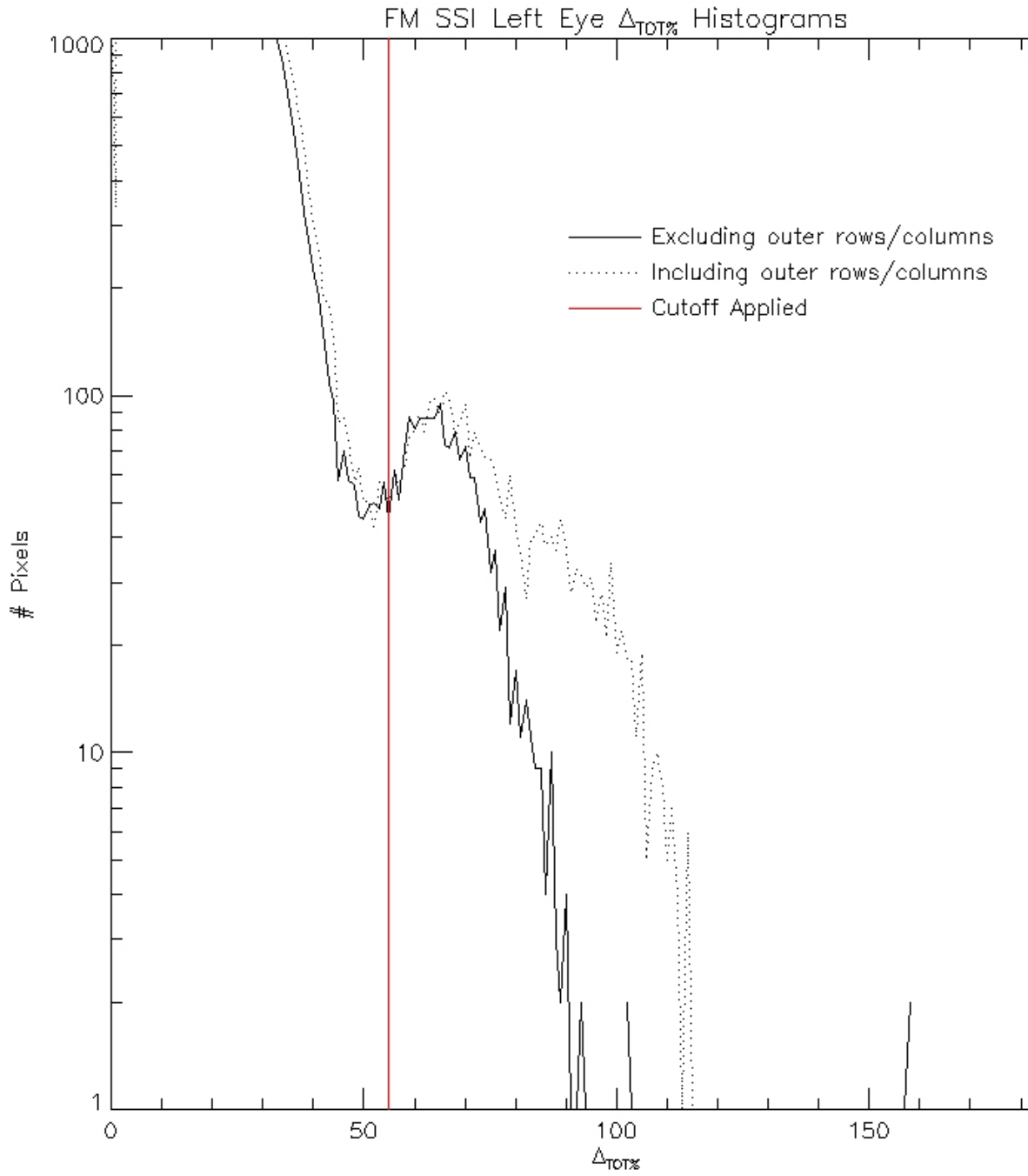

Figure F - 7: Histogram of $\Delta_{TOT\%}$ Across the FM SSI Left Eye Data

F.4. Hot pixel map

The hot pixel map has the following form prior to compilation for the flight software:
x-pos, y-pos, mode, scaling

where modes available are: -2=scale using supplied coefficient, -1=replace with average of nearest neighbors, and ≥0=replace with this value. The following tables with edge pixels omitted were generated by the method above:

Left Eye

x	y	mode	scaling
88	87	-2	1.40987
91	82	-2	1.26079
92	82	-2	2.01105
92	83	-2	1.55294
93	82	-2	1.35863
93	83	-2	1.43151
94	417	-2	1.27327
370	434	-2	1.35839
399	584	-2	1.28849
728	735	-2	1.35345

Right Eye

x	y	mode	scaling
222	875	-2	1.67291
223	875	-2	1.71196
223	876	-2	1.25824
331	615	-2	1.27388
908	66	-2	0.612378
1017	772	-2	1.51062
1017	773	-2	1.95746
1017	774	-2	1.50633

Which were then hand edited to help remove pixel groupings and remove duplicates to:

Left Eye

x	y	mode	scaling
88	87	-2	1.4
91	82	-2	1.26
92	82	-2	2.01
92	83	-2	1.55
93	82	-2	1.35
93	83	-2	1.43
94	417	-2	1.27
370	434	-2	1.35
399	584	-2	1.28
728	735	-2	1.35
88	87	-1	0
91	82	-1	0
92	82	-1	0
92	83	-1	0
93	82	-1	0
93	83	-1	0

Right Eye

x	y	mode	scaling
222	875	-2	1.67
223	875	-2	1.71
223	876	-2	1.25
222	875	-1	0
223	875	-1	0
223	876	-1	0
331	615	-2	1.27
1017	772	-2	1.51
1017	773	-2	1.95
1017	774	-2	1.5
1017	772	-1	0
1017	773	-1	0
1017	774	-1	0
1016	773	-1	0

F.5 Bad pixel map

The bad pixel map has the following form prior to compilation for the flight software:
x-pos, y-pos, mode

where modes available are: -1=replace with average of nearest neighbors, and ≥0=replace with this value. The following tables with edge pixels omitted were generated by the method above:

Left Eye

x	y	mode	
2	421	-1	0
84	677	-1	0
93	84	-1	0
98	515	-1	0

Right Eye

x	y	mode	
222	874	-1	0
907	66	-1	0

174	856	-1	0
219	326	-1	0
254	432	-1	0
302	385	-1	0
373	945	-1	0
373	946	-1	0
381	946	-1	0
399	583	-1	0
486	369	-1	0
489	223	-1	0
497	265	-1	0
500	4	-1	0
580	937	-1	0
654	50	-1	0
670	94	-1	0
695	336	-1	0
712	243	-1	0
821	107	-1	0
877	882	-1	0
894	979	-1	0
957	997	-1	0
973	699	-1	0
974	699	-1	0
975	346	-1	0

Which were then hand edited to help remove pixel groupings and remove duplicates to:

Left Eye

x	y	mode
2	421	-1
84	677	-1
93	84	-1
98	515	-1
174	856	-1
219	326	-1
254	432	-1
302	385	-1
373	945	-1
373	946	-1
381	946	-1
373	945	-1
373	946	-1
381	946	-1
399	583	-1
486	369	-1
489	223	-1
497	265	-1
500	4	-1

Right Eye

x	y	mode
222	874	-1
907	66	-1
908	66	-1
907	66	-1
908	66	-1

580	937	-1
654	50	-1
670	94	-1
695	336	-1
712	243	-1
821	107	-1
877	882	-1
894	979	-1
957	997	-1
973	699	-1
974	699	-1
973	699	-1
974	699	-1
975	346	-1

The complete as generated Hot and Bad pixel tables can be found in:
FMSSI_L_Hot_Pixels.dat
FMSSI_L_Bad_Pixels.dat
FMSSI_R_Hot_Pixels.dat
FMSSI_R_Bad_Pixels.dat

The complete as implemented Hot and Bad pixel tables can be found in:
FMSSI_L_Hot_Pixels_final.dat
FMSSI_L_Bad_Pixels_final.dat
FMSSI_R_Hot_Pixels_final.dat
FMSSI_R_Bad_Pixels_final.dat

G - Polarization –

G.1 Background

In order to verify the performance of the polarization filter in the SSI head for later use on Mars, a set of requirements were specified to measure not only the R9 polarization filter but also compare those results to other filters (for this test R8 was used) in the wheel. This report focuses on the measurement of the R9 and R8 filters inside the SSI camera head and comparing there polarization sensitivity to each other. The requirements of the test were to align an external non-polarized light source and attenuate the income light with a Wolfstan prism whose polarization axis is rotationally adjustable. The SSI is then used to take images of the polarized light passing through the Wolfstan, the filters and finally falling on the right CCD. Using this test setup allowed for a comparative measurement to be made between the match wavelength filters R9/R8 allowing for tracking of the degree of polarization in the SSI, orthogonally relative to boresite optical axis coming out of the camera head. The final objective of this section was to measure the variation of the DN/sec in the SSI

images as the Wolfstan prism attenuates the incoming light from full intensity to extinction, thereby measuring the cross polarization effect of an external source verse angle.

Table G-1 Filter specifications

Filter #	Center Wavelength	Application	**Filter #**	Center Wavelength	Application
L1	672 nm	Stereo Pair	R1	672 nm	Stereo Pair
L2	445 nm	Stereo Pair	R2	445 nm	Stereo Pair
L3	451 nm	Atmospheric	R3	671 nm	Atmospheric
L4	990 nm	Water	R4	935 nm	Water
L5	886 nm	Water	R5	935 nm	Water
L6	830 nm	Surface	R6	445 nm	Diopter
L7	802 nm	Surface	R7	753 nm	Diopter
L8	861 nm	Surface	R8	753 nm	Surface
L9	901 nm	Surface	R9	753 nm	Polarizer
L10	932 nm	Surface	R10	604 nm	Surface
L11	1001 nm	Surface	R11	533 nm	Surface
L12	967 nm	Surface	R12	485 nm	Surface

G.2 Test Setup and Data Acquisition

Procedure:

1. Measurement of vertical optical polarization axis to ½ degree accuracy

2. Image throughput light extinguishment on the polarizer over 180 degrees of travel, in 10 degree steps. (See fig. G-3)

3. Compare and contrast the Digital Number (DN) (computer converted intensity) throughput of the R9 polarized filter to R8 filter.

4. Image throughput light extinguishment on the R9 and R8 over 180 degrees of travel, in 30 degree steps.

5. Image throughput light extinguishment on the L1, L2 and L10 over 180 degrees of travel, in 30 degree steps.

6. The test will be done at approximately -45^{o}C and at a vacuum of at least ~10^{-4} torr, it will also comply with all NASA JPL ESD and ERD requirements.

Configuration:

The configuration of the thermal test and the associated equipment and computer control setup are laid out in the functional schematic below in Fig. G-2 Where as the light path of the polarization test setup for the SSI will be laid out in the section below in Fig. G-3.The Thermal Vacuum Chamber (TVC) which is a hot and cold controllable vacuum chamber capable of 10^{-7} torr and +/- temperatures of -120^{o}Cto 65^{o}C, was used for the entire polarization test. The temperature and vacuum of the TVC was continuously monitored and controlled while being simultaneously logged by a LabView base software program. Throughout the polarization testing procedure the chamber was held a constant vacuum between 10^{-6} torr and 10^{-4} torr and testing condition called for the temperature to be held at -45^{o}C. The SSI and its electronics were mated to the TVC by a vacuum feed through plate to the Payload Software Testbed (PST) and finally controlled by the Instrument Flight control Soft Ware (IFSW). Where as the systems are interlinked for monitoring, the TVC is controlled separately from the SSI.

Procedure:

The SSI is horizontally mounted inside the TVC chamber and held at a constants temperature of -45^{o}C throughout the polarization test. Conductive cooling was done with thermal with copper foil straps connecting the SSI camera head to the cold plate. In addition; radiant cooling to a cooled shroud is used to transfer the heat away from the camera head. The TVC has direct control over two systems to control the temperature; the first is a hollowed out solid thermal plate that has a solenoid controlled Liquid Nitrogen (LN2) supply for cooling and the second is a series of resistive heating patches attached to the thermal plate and radiant cooling shroud to balance the LN2. Temperature measurement for the control is done by reading the temperature in the chamber with 6 RTD thermal couples that are plotted and logged through the LabView control software. Finally, the environment around the test setup controlled to minimize the uncertainty in the measurement of the polarization. The room lights were turned off, because of which a shroud was not necessary.

Schematics of the System and Setup:

Computer Network

The computer network diagram below in Fig. G-2 shows the SSI control setup necessary to keep the acquisition of the SSI imaging data flight representative. Also shown is the stand alone

control of the TVC separate from the control of the SSI head. The 28V power supply is powering the SSI head, CCD and SSI onboard electronics. The PST is a stand alone system taking the place and representative a flight Phoenix Lander onboard computer. The FSW is networked to the PST and thereby is used to control and acquire images from the SSI. With these systems in place the TVC computer keeps the temperature constant simulating, while the networked FSW acquires the test images using the flight representative setup.

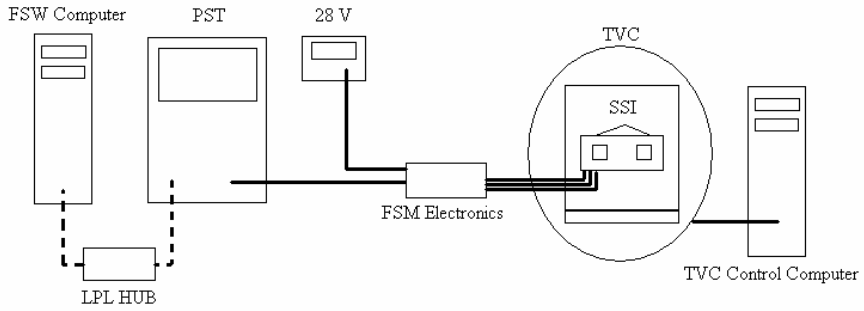

Figure G-2. Functional Schematic

Optical Path

With the electronic and environmental controls in place the external optical setup is used to supply the external lighting needed for the polarization testing. A high power light source is used to give a maximum 2500 DN level signal to the SSI over a medium to short integration time. A diffuser and aperture are placed near the source and before the SSI input window to homogenize the light signal, giving a fairly uniform intensity over the 50 by 50 pixel area were the light is falling. The final step is to place a Wolfstan prism between the diffuser and the aperture to allow for adjustment of the input polarization axis of the light entering the SSI. The test involves rotating the Wolfstan prism in steps of 0.25^{o} to 10^{o} to cross the two polarizer's polarization axis's to go from 100% throughput to 0%. This will allow for calibration of where the polarization axis is located relative to the SSI head and will later be used for measurement of the degree of polarization atmospheric comparisons of Mars.[5]

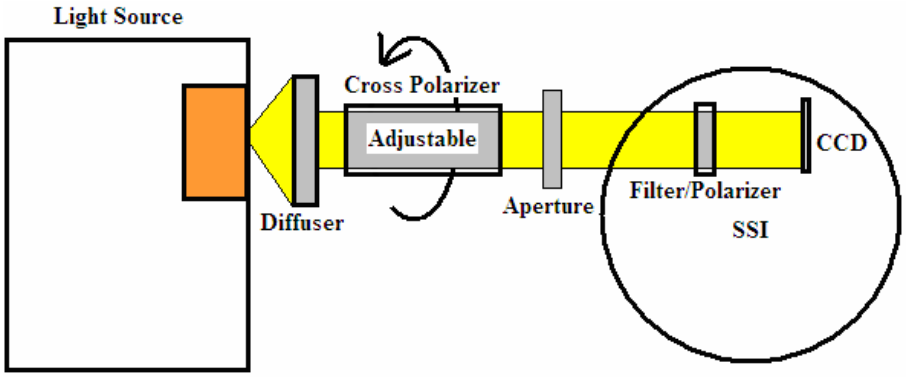

Figure G-3. Axis adjustable polarization test setup.

Software:

There were several sets of images taken to measure the change in DN level as the Wolfstan cross polarizer is rotated. The Excel spreadsheet was used to track the constant coefficients, DN measurements and calculated stray light levels. Finally an IDL software program was used to correct the images take and measure the needed values.

Raw Data:
The raw data that was use to do the DN/sec analysis is located.
/support_files_for_polarization/Polarization_data/

Images:
The images of the Wolfstan polarizer are located on home mars and are filed by testing angles.
/support_files_for_polarization

Spreadsheet:
The spreadsheet is used to track the polarization coefficients.
/support_files_for_polarization

1. Polarization.xls (data sheet)

IDL software:
The IDL program is used to correct the image and measure the mean DN levels
/support_files_for_polarization/IDL_Code

1. shutter_dark_box_select.pro (image correction)

Log files:

List below is the path location of the log file used in the image correction and temperature mapping.
/support_files_for_responsivity

1. SEQ_geo_target_testing_060630.log

The SSI FSW Operations:

Below shown in Fig. G-4 is the side profile of the test setup done at the University of Arizona in the class 1000 clean room at LPL. The images show the high intensity light source being directed into the front window of the TVC chamber, through the Wolfstan prism and a series of stray light baffles.

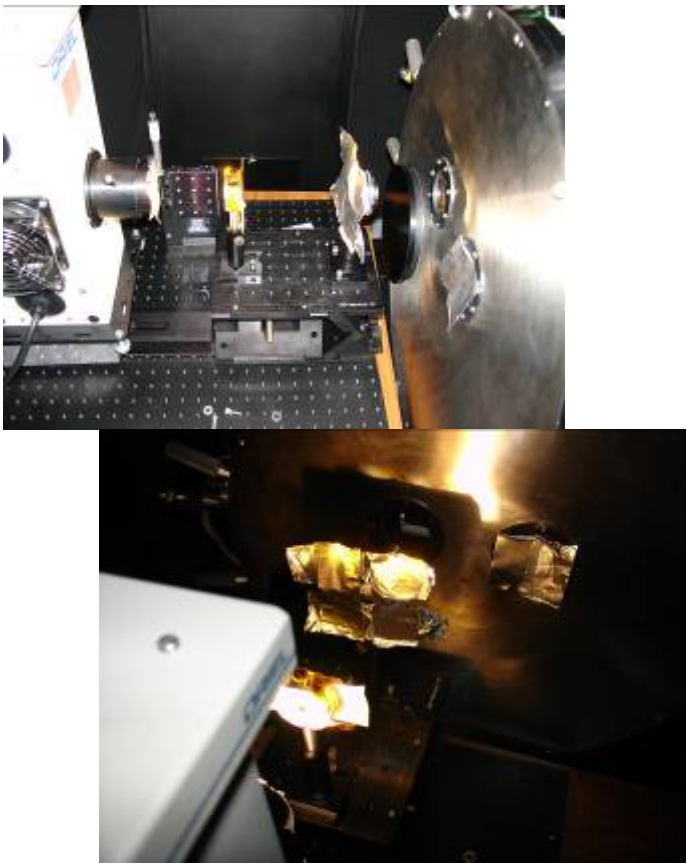

Figure G-4. Test setup; light source diffuser, cross polarizer, aperture, TVC window into the SSI.

Figure G-5 shown the two front windows of the TVC aligned with the stereo eye's of the SSI camera head, this allows for imaging testing to be completed while the SSI is held at Mars environmental conditions.

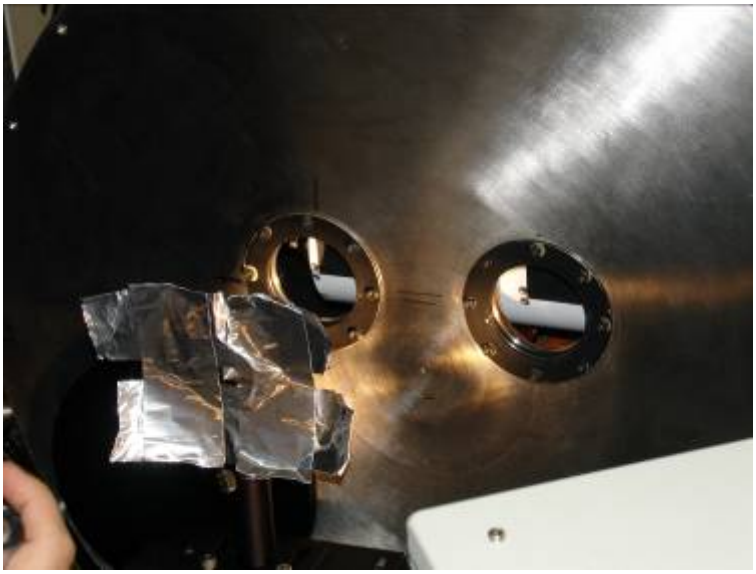

Figure G-5. Imaging aperture in front of the TVC chamber.

In order to calibrate the relative polarization measurements, several images of the front window of the SSI were taken through the Wolfstan prism, along the same path as the test. The images seen in figure G-6 were used to analyze the angular orientation of the SSI window to be approximated and therein the filters within the SSI head, compared to the Wolfstan prism orientation. Using the two screws visible through the Wolfstan prism in the center of the left image of figure G-6, a centroiding was applied and from there an angular comparison of the image was done. If the centroiding of the two screws is connected and represents the reference line and then the edge of the Wolfstan in the image is taken as a second line the angular separation of the two where they overlap is 3.1^{o} +/- 1. From this it can be determined that when the Wolfstan degree indicator is set to 0^{0} the SSI is rotated 3.1 degrees off vertical.

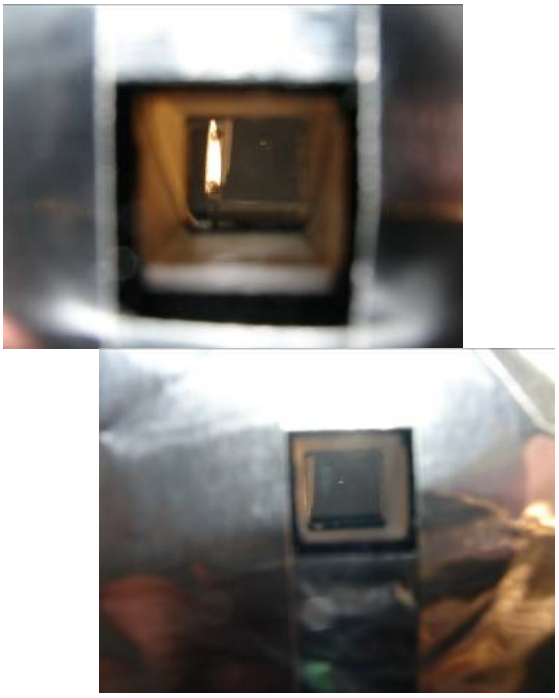

Figure G-6. Images of the front of the SSI window taken through the cross polarizer to give angular comparison between the SSI and the Wolfstan orientation.

Thermal Cycling:

TVC control system monitored several camera temperatures during the test, along with archiving and recording the temperature cycling of the flight component. Figure G-7 shows the chamber being taken from room temperature down to the -45°C specified in the testing requirements.

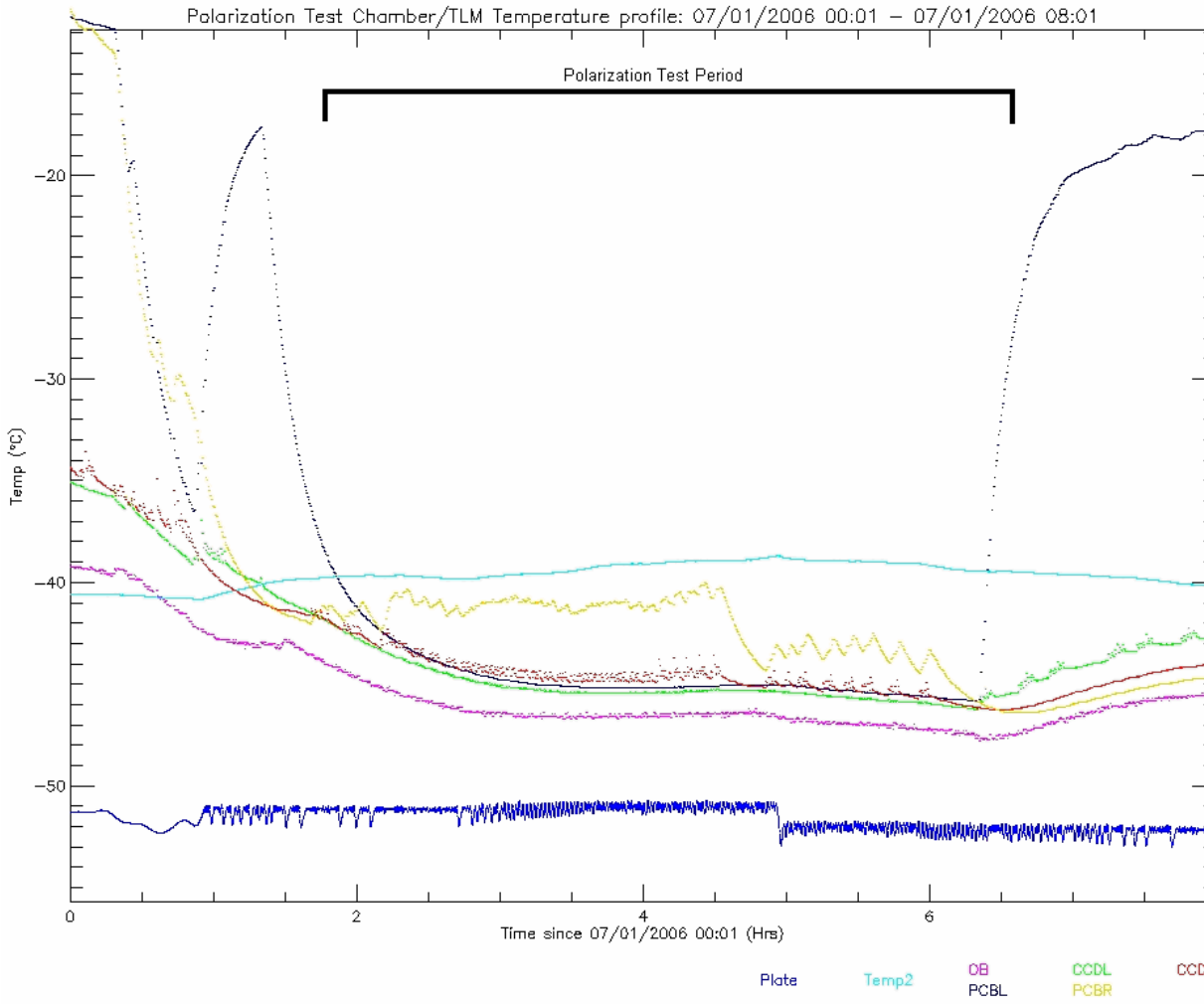

Figure G-7. Test specific thermal log of the temperature cycle inside the TVC chamber during the polarization test.

G.3 Data Processing

The data being analyzed contains image of a high intensity light source at various DN levels, allowing for measurement of the degree of polarization. The two key components in this process are the rotation of the Wolfstan polarizer and the measurement of the extinction level by the SSI.

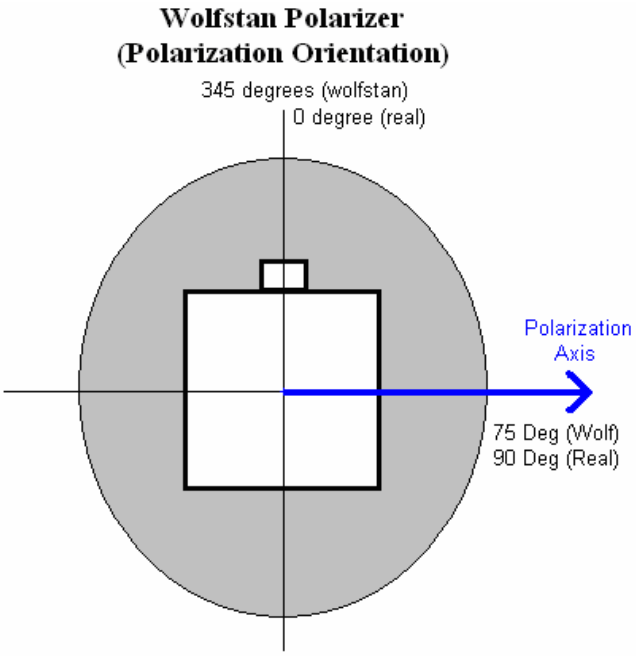

Figure G-8. Wolfstan cross polarizer diagram of polarization and orientation axes looking down the optical axis

The results of the testing were a profiling of the inherent polarization characteristics of two critical atmospheric flight filters, the R9 polarizer and R8 filter. Do to the design of the Wolfstan mount and the optical railing being used, the prism was oriented in such a way that the 345^{o} indicator on the mount itself is really 0^{o} for the test setup. Therefore the readings recorded in the SSI handbook and log files are relative and were converted to absolute angles after testing was complete.

Figure G-9 shows the comparison of the extinguished DN levels of the R9 polarizer verse the R8 filter, as the Wolfstan prism was transitioned through an 180^{o} test rotation. The first 180^{o} rotation was completed in 10^{o} steps, in order to map the overall extinction curve of the two filters, varying the cross polarizing Wolfstan between 180^{o} and 360^{o}. In the second test the Wolfstan rotation was narrowed between 341^{o} and 345^{o} in order to evaluate the closest cross polarization axis. The results showed that the point of maximum extinction lies at 342.5^{o} (relative) and that the final polarization axis for the R9 filter was 90^{o} off or 72.5^{o}. Whereas the

R8 filter did not have the same level of extinction as the R9 filter, it did show polarization sensitivity of about 4% along the same axis as the R9 filter.

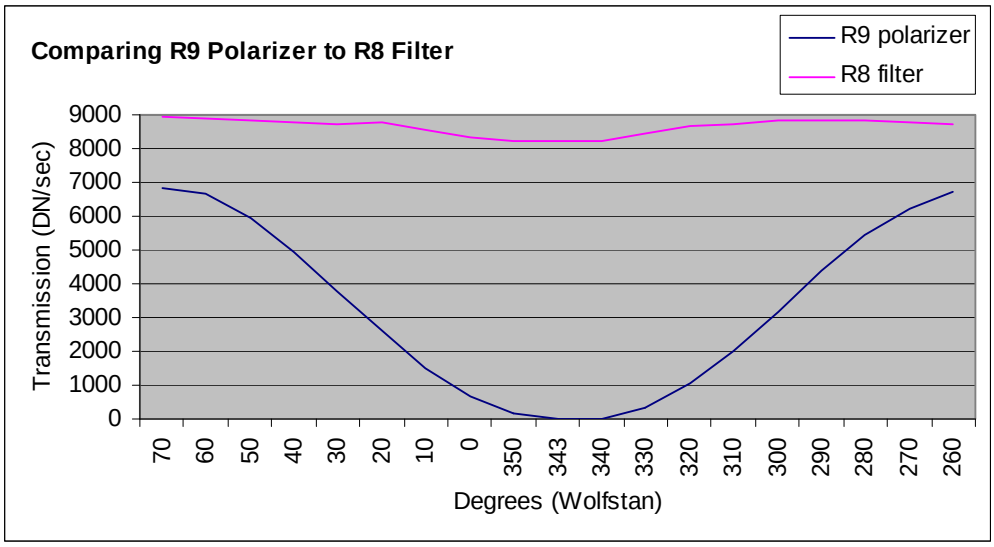

Figure G-9. Shows the polarization extinction level comparison between R8 and R9

The R8 and R9 DN/sec results were then scaled in order to display the percent change or degree of polarization in the polarizer itself verse the R8 filter. The R8 filter does not having any polarization effect. However, the mirrors inside the SSI camera head will have some degree of polarization. The R8 filter measurement is fundamentally a reading on the SSI camera degree of polarization.

The real orientation angle to the SSI was be calculated using the data shown in figure G-9 and then correcting for the 15^{o} off set in the Wolfstan prism degree wheel and 3.1^{o} rotation in the SSI/Wolfstan alignment. The result of which is a diagram of the polarization extinction of the SSI showing the polarization axis of the SSI residing just off vertical at a 0.6^{o} rotational offset. However the error bounds of the measurement resolution for both the Wolfstan mount scale and the alignment between the SSI/Wolfstan are on the order of 0.5^{o}, concluding that the SSI polarization axis lies between 0.1^{o} and 1.1^{o}.

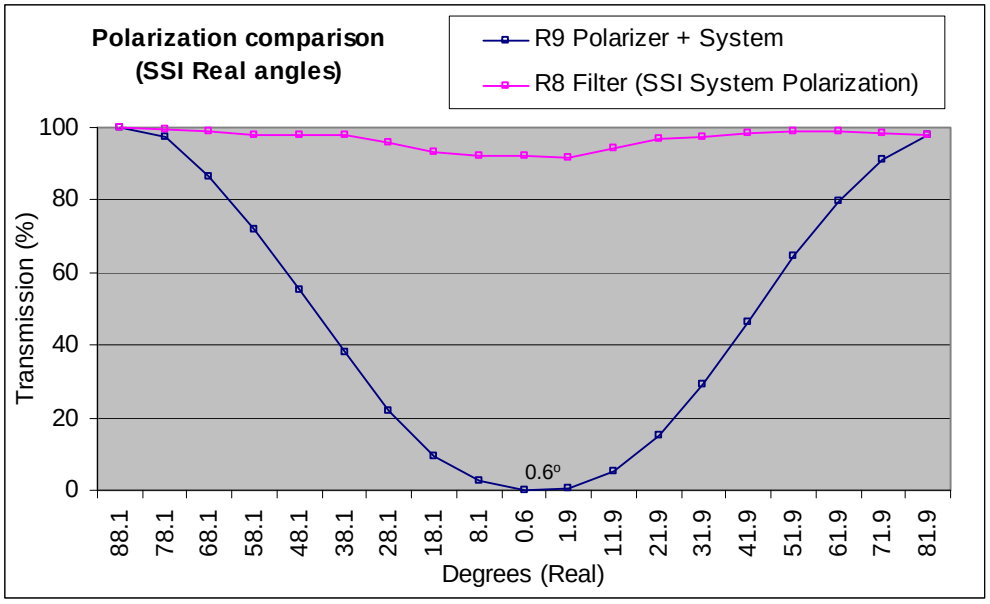

Figure G-10. Shows a detailed measurement with angular correction to the SSI.

A enter set of images were taken in order to evaluate the polarization extinction level of the SSI R9 filter. Below is a DN scaled image that represents the type of data that was taken in the R8 & R9 filters. The center cube is the Wolfstan prism that was used as a cross polarizer to periodically measure the DN drop with angle. The final of the data set is seen in figures G-9 and G-10 where that data was been graphed to show the extinction of the light coming from the Wolfstan and block by the cross polarized R9 filter.

Figure G-11. Polarization image scaled between 200 and 12 DN.

The set of images below shows the extinction levels between the different filters, shown at the two extremes. The goal of this set of testing was mainly to show the R8 polarization axis inside the SSI camera head The images below show the “Brightest” image,

representing that both the polarization axes of the filter and cross polarizer overlap, minimizing extinction effects. The second set of images shows the “Dimmest” image, representing that the two polarization axes are orthogonal to each other, causing various level of irradiant extinction.

Shown below in Fig. G-12 and G-13 are the two main filter that had the most detailed level of analysis for there polarization axis.

Brightest **Dimmest**

R9-Polarizer

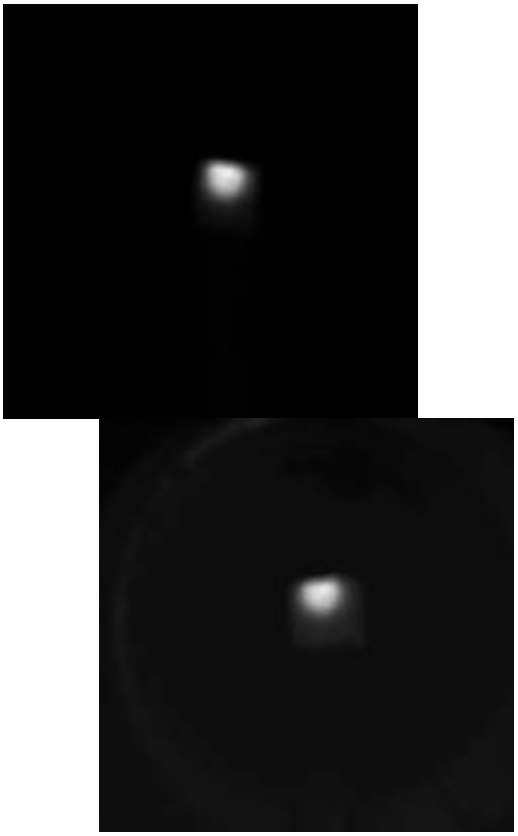

-88.1^{o} 0.6^{o}

Figure G-12. Shows the R9 polarizer and its polarization axis at 0.6 degrees.

R8-Comparison Filter

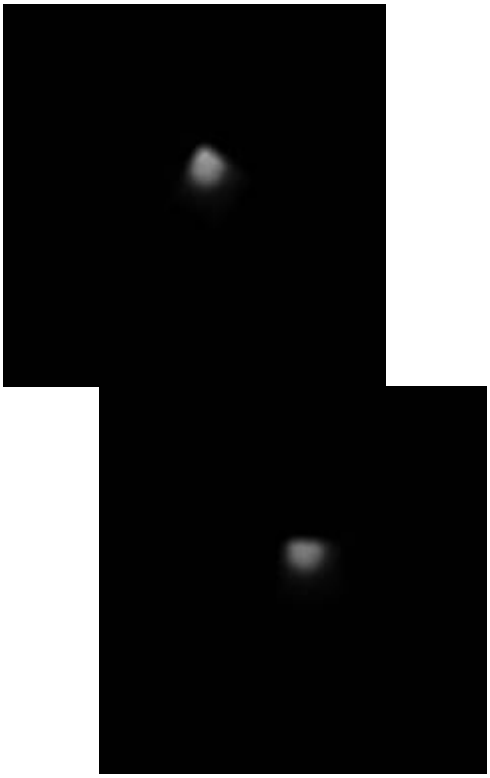

Figure G-13. Shows the R8 filter and its polarization axis at -88.1 degrees.

Imaging Analysis:

The histograms shown below represent a cross section of the DN level along the y-axis of the SSI images for both bright and dim image.

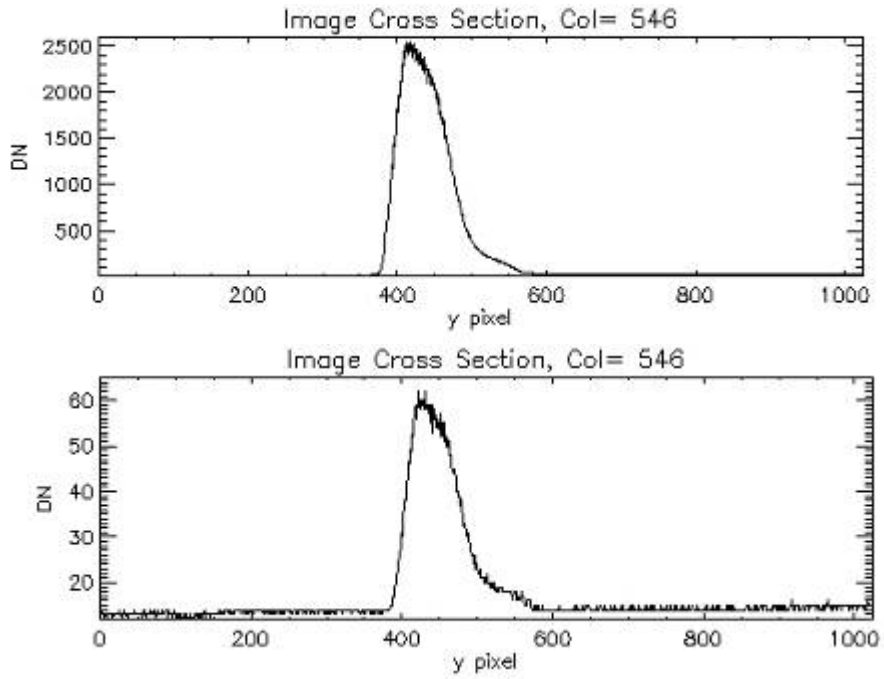

Figure G-15. Shows the histogram comparison between the R9 images "brightest" and "dimmest" (image correction not complete).

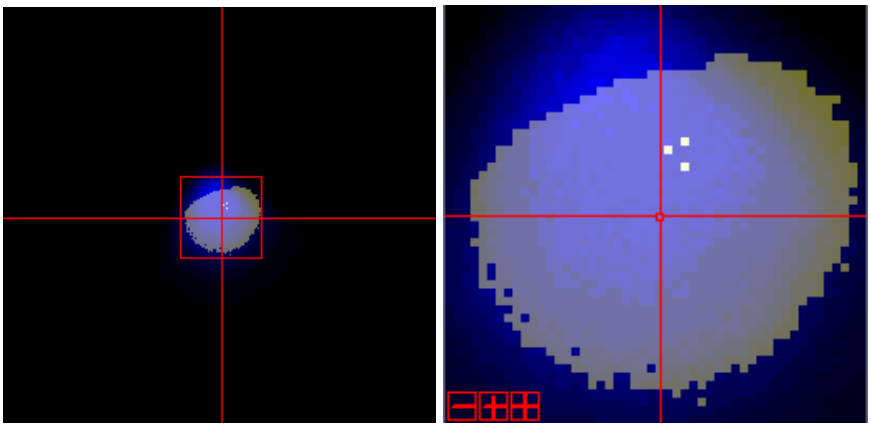

Figure G-16. Shows a composite of the two images "brightest/dimmest" and there relative location and DN levels.

G.4 Polarization Performance.

Table G-2 Comparison chart between the SSI images and polarization

Transmission (%)	Separation between Wolfstan/SSI polarization angles (degrees)	DN/sec
0.0	90	18.38

5.0	85.5	359.46
10.0	81	700.54
15.0	76.5	1041.63
20.0	72	1382.71
25.0	67.5	1723.79
30.0	63	2064.87
35.0	58.5	2405.95
40.0	54	2747.04
45.0	49.5	3088.12
50.0	45	3429.20
55.0	40.5	3770.28
60.0	36	4111.36
65.0	31.5	4452.45
70.0	27	4793.53
75.0	22.5	5134.61
80.0	18	5475.69
85.0	13.5	5816.77
90.0	9	6157.86
95.0	4.5	6498.94
100.0	0	6840.02

Table G-2 shows the mean measured DN/sec values over 150x150 pixels area in the polarization images and compares the DN/sec values to polarization angle represented by them.

Final Summary:

This section outlines the successful measurement of the polarization axis of the R9 polarizing filter and the R8 comparison filter. The analysis of the data shows the relative polarization axis of the system measured with the R8 filter is aligned with polarization axis of the R9 polarizing filter. There are two key imaging measurement needed to finish the calculation of the R9 polarization filter in the SSI head, the maximum extinction of 342.5^{o} (Wolfstan) and the alignment error of the SSI/Wolfstan pair of 3.1^{o}, seen in Fig. G-6. The DN verse angle and percent change verses angle graphs shows that the Wolfstan polarizer reaches full extinction at 342.5^{o} (Wolfstan). When we correct for the alignment error between the SSI/Wolfstan, correct for the relative Wolfstan numbering verse SSI frame and then taking into account that the SSI polarization is 90 degrees off from the Wolfstan the final polarization axis is generated. From the previous steps can conclude the final polarization axis for the SSI is 0.6^{o} plus + or - a 0.5^{o} in the Y-axis rotated clockwise, relative the front window of the SSI.

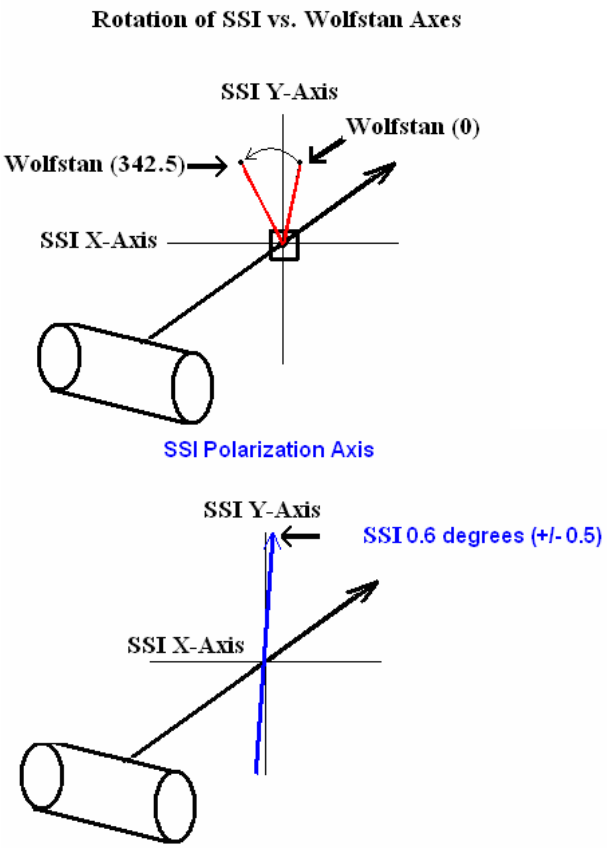

Figure G-17. Wolfstan rotation axis compared to SSI axis.

The polarization calibration measures show that filter R9 is installed correctly and will allow for effective polarization imagery to be taken on Mars. From this we can conclude that the SSI has extinction ratio of 0.13% (1/(770-2)) per DN of image exposure which correlates to a polarization angular deviation of 0.00204 radians per DN.

H - Filters - AS

H.1 Filter In-Band Test Setup and Data Acquisition

The FM SSI filters were made by Barr Associates to UA specifications and were supplied along with room temperature measurements of their profile. Further room temperature measurements were made at the UA prior to their mounting inside the flight filter wheel and camera head. Following completion of the camera more measurements were made over a range of temperatures by imaging monochrometer output. This third set of measurements will be the primary dataset for analysis given its system wide scope and range in temperature; however, supporting data from the other two datasets will be invoked when necessary due to certain limitations in the third dataset.

The FM SSI camera was located in the Magi Group, Lunar and Planetary Lab, UofA (MAGI) Thermal Vacuum Chamber. The camera was pointed at a polished 2" circle of Spectralon illuminated by an Acton SP150 monochrometer (Figure H - 1). Both the camera and monochrometer were controlled using TMV2 via scripts and the resulting images and log-files archived.

Data was taken between 6/25/2006 and 6/30/2006 at nominal temperatures of -65°C, -15°C and a couple of temperatures in between for the solar filters (Table H - 1). The monochrometer slit width and pre-filter were varied as necessary. The slit width controlled the bandwidth of the output light, but a narrower slit width also reduced the output light intensity. The pre-filter removed the possibility of aliasing at unwanted wavelengths.

Date	Start Time	End Time	Filter	In Band/ Solar InB	Notes	Nominal Temp
25-Jun	9:55	10:15	R1	InB		-65
	10:31	11:30	R2	InB		-65
	12:41	14:00	R6	InB		-65
26-Jun	11:00	11:18	R7	TInB	Bad?	-65
	14:10	14:37	R7	InB		-65
	14:41	15:07	R8	InB		-65
	15:11	15:42	R9	InB		-65
	15:46	16:08	R10	InB		-65
	16:14	17:01	R11	InB		-65
	17:06	18:22	R12	InB		-65
	20:00	21:00	R3	SInB	Bad	-65
	21:15	22:10	R4	SInB	Bad	-65
27-Jun	3:00	4:00	R3	InB		-65
	4:13	5:08	R4	SInB		-65
	5:20	6:15	R5	InB		-65
	10:57	12:58	R5	SInB		-53

	15:12	16:07	R5	SInB	dt3 ?	-40
	16:22	17:23	R5	SInB		-40
	17:33	18:28	R4	SInB		-40
	22:37	23:34	R4	SInB	Too Warm	-15
28-Jun	23:43	0:39	R5	SInB	Too Warm	-15
	1:03	1:59	R3	SInB	Too Warm	-15
	8:36	9:35	R4	SInB		-20
	9:45	11:27	R5	SInB		-20
	11:46	12:34	R3	SInB	Wrong Log	-20
	13:19	13:45	R1	InB		-15
	13:51	14:49	R2	InB		-15
	15:48	17:06	R6	InB		-15
	17:11	17:38	R7	InB		-15
	17:43	18:12	R8	InB		-15
	18:16	18:44	R9	InB		-15
	18:46	19:23	R10	InB		-15
	19:27	20:09	R11	InB		-15
	20:43	21:21	R12	InB		-15
	22:16	22:42	L1	InB		-15
29-Jun	23:36	0:38	L2	InB		-15
	0:48	1:12	L6	InB		-15
	1:28	1:53	L7	InB		-15
	2:01	2:47	L8	InB		-15
	2:59	4:01	L9	InB		-15
	4:09	4:48	L10	InB		-15
	5:55	5:45	L11	InB	incomplete	-15
	5:59	6:46	L12	InB		-15
	6:56	7:44	L11	InB		-15
	8:07	9:52	L3	SInB	Bad	-15
	10:02	10:29	L4	SinB	Blank	-15
	10:48	11:44	L4	SInB	Look Dodgy…	-15
	12:05	13:08	L5	SInB		-15
	13:17	14:12	L3	SInBa	Look Dodgy…	-15
	18:54	19:49	L3	SInBa		-40
	20:46	21:51	L4	SinB		-40
	22:08	23:03	L5	SinB		-40
30-Jun	5:41	6:06	L6	InB		-65
	6:10	6:35	L7	InB		-65
	6:39	7:24	L8	InB		-65
	7:28	8:27	L9	InB		-65
	8:32	9:09	L10	InB		-65
	9:14	10:02	L11	InB	Some Missing	-65
	10:07	10:59	L12	InB		-65
	11:03	11:29	L1	InB		-65
	11:35	12:37	L2	InB		-65
	13:51	14:48	L4	SInB		-65
	14:58	16:20	L5	SInB		-65
	16:34	17:37	L3	SInBa	Faint	-65

Table H - 1: Complete List of In Band Filter Profile Measurement Collected in Thermal Vacuum Temperature, including Bad Data-sets

Figure H - 1: Experimental Setup for TVC Filter Profile Testing

H.2 In Band Analysis Procedure

The following datasets were used in the following analysis, all can be found at /home/mars/Phoenix/Testing Data/ FM_SSI_Filter_In_Band_Out_Of_Band_Complete along with the analysis software used:

80ms spectra of the Oceans Optics LS-1-Cal-Int tungsten halogen light source obtained on 03/11/2006 using the Oceans Optics USB 2000 spectrometer with associated darks.
Spectra taken on 08/16/2006 by the Oceans Optics USB 2000 spectrometer of the output from the Acton SP 150 Monochrometer reflected off of a piece of polished Spectralon. The monochrometer was run at 5nm intervals across the entire wavelength range of the FM SSI filter set, multiple spectra were obtained at each wavelength either without a pre-filter or through pre-filters 2,3 in their areas of transmission.
Images taken by the FM SSI between 06/24/2006 08:00 and 06/30/2006 17:40 while inside the TVC (Thermal Vacuum Chamber), using the TMV2 software for acquisition, of a piece of

polished Spectralon illuminated by the Acton SP 150 monochrometer with various settings as outlined below. Spectra of atomic line sources reflected off of a piece of polished Spectralon obtained with the Oceans Optics USB 2000 spectrometer on 08/16/2006.

The first step in the analysis was to ensure a clean calibration of the monochrometer output; this was obtained via measurements made with the Oceans Optics spectrometer.

The spectrometer was calibrated first in wavelength[4] and then in spectral response. In order to calibrate the spectrometer in wavelength, the central wavelength of several atomic emission lines were measured and compared with their known central wavelengths. The difference over wavelength was fit with a cubic polynomial. This constitutes the spectrometer wavelength calibration. The accuracy of this calibration should be about ±0.1nm. Details of this calibration can be found in /home/mars/ Phoenix/Testing Data/060731_Monochromator_Calibration.

For the spectral response the spectra taken of the LS-1-Cal-Int tungsten halogen light were averaged and the average dark subtracted (Figure H - 2). Standard deviations of each spectral pixel value were calculated across the set for both the spectrum and the dark and propagated through from here until the end of the filter profile determination process. This observed spectrum was divided into the calibration spectrum provided by the lamp manufacturer (Figure H - 2) to give the spectral responsiveness of the Oceans Optics USB 2000 spectrometer (Figure H - 3). The code used for this step can be found in calibrate_oceans_spectrometer_ls1calint.pro.

Following the spectrometer calibration, the spectral output of the monochrometer could be assessed. Multiple spectra taken of the monochrometer output when commanded at 5nm intervals were taken through either pre-filter# 2 or pre-filter# 3 or with no pre-filter; these were then averaged and examined to isolate the observed spectral peak. The observed peak central wavelength as seen on the spectrometer was compared to the nominal commanded wavelength in order to generate a table of commanded versus actual wavelength. The peak was integrated under and this value taken to be proportional to the monochrometer output intensity at this wavelength, modulated by the spectrometer response. The spectrometer response was divided out and once normalized, the result taken to be the output efficiency of the monochrometer with wavelength (Figure H - 4,Figure H - 5 ,Figure H - 6). The code for this can be found in monochrometer_cal.pro.

Once the monochrometer output had been quantified the images taken during testing could be subjected to analysis. For each FM SSI filter at a given nominal temperature the following products existed and were used:

Several TMV2 format images of the illuminated Spectralon, each one corresponding to a different commanded wavelength of the monochrometer, which was being incrementally stepped across the band-pass region of the filter.
A TMV log file containing the CCD/PCB/OB temps for each image, along with details of pre-filter, monochrometer slit-width and filenames.

The main In-Band reduction program is fmssi_inband_filter_profiles.pro; the following steps outline its operation.

For each monochrometer wavelength in the set the corresponding image was read in, dark-subtracted using the dark model and cropped slightly along all sides to remove the dark/bias strips and any other edge issues that might be present (e.g. Figure H - 7).

The user is presented with the image from the centermost wavelength tested displayed using a stepped color table to bring out DN countour levels (e.g.Figure H - 8) and places a box that fully contains the entire illuminated region with the aid of vertical and horizontal histograms.
The vertical and horizontal sums of the image are then analyzed to locate the center of the spot within the selected box area (+100 pixels on each side) on each image. If it cannot be determined or falls outside of the selected box area, the mean position of those that could be accurately determined is used, if none of the centers could be accurately located then the center of the box is used as the nominal spot center location. A much smaller sub-box is used to gauge the peak DN level of the spot (usually 21 or 31 pixels in width depending on the brightness) This is initially centered in the nominal spot center and allowed to migrate by up to 12 pixels up, down, and side to side, the center location of the box when the mean of the box is maximized becomes the nominal spot center. The position of nominal centers who's sub-box mean is greater than 20% of the maximum sub-box mean are then fitted via a robust least squares fit, in the event that there are less than 4 of these nominal centers, all of the nominal centers will be used for the fit. All of the nominal centers are then replaced with final centers on the line. This is designed to remove the effect of hot/bad pixels and any noise that is on a par with the signal in dim images.

A 20 pixel wide strip at the outer edge of the box (+100 pixels on each side) is analyzed to determine a mean background level including error estimate taking account of the individual CCD gains. The strip is broken into 4 pieces, one above the box, one below, one to the left and the final one to the right. If we consider one of these pieces, P^k_{ij} where k=1,2,3,4 for the pieces and P^k_{ij} is the DN value of the dark subtracted image in piece k at location (i,j) then the background level is the mean of the medians of the pieces. The variance associated with the median, $\tilde{x}_k$, for piece k is: $\sigma_{\tilde{x}_k}^{\ 2} = \frac{\pi \cdot (2n_k + 1)}{(4n_k)} \sigma_k^{\ 2}$ where n_k is the number if pixels in piece k and σ_k is the standard deviation of the mean of the pixels in piece k[5]. The mean background is the simple mean, $B = \sum_{k=1}^{4} \tilde{x}_k$, and the variance, $\sigma_B^{\ 2} = \sum_{k=1}^{4} \sigma_{\tilde{x}_k}^{\ 2} \Big/ 4$.

The means of these sub-boxes centered on these final boxes are then calculated along with their SNR, they are also displayed on the screen to allow verification of the sub-box size and position as you step through those(e.g. Figure H - 9). SNR is calculated as[6]: Where: I_{ij} is the DN value of the pixel in the image sub-box at position (i,j)

D_{ij} is the DN value of the pixel in the dark current sub-box at position (i,j)

t is the image exposure time in seconds

B is the background level

gain is the CCD gain in e^-/DN (Left: 48.3, Right:50.3)

N_R is the read noise in e^- (Left: 18.7, Right: 24.1)

The spectral point is then calculated as $F(\lambda) = (S - B \cdot \text{gain}) / (\varepsilon_\lambda \cdot \text{gain})$ where, ε_λ, is the monochrometer efficiency at the image wavelength, λ. The uncertainty in this value is calculated as:

$$\sigma_{F_\lambda} = F(\lambda) \cdot \sqrt{\left(\frac{\sigma_{\varepsilon_\lambda}}{\varepsilon_\lambda}\right)^2 + \text{SNR}_\lambda^{\ -2}}$$

Once this is completed the profile needs to be sealed off in the event the lowest or highest wavelength image spectral point is greater than 2% of the highest point. In order to do this a point is simply added to the profile at a wavelength equal to λ_{min}-Δλ and/or λ_{min}+Δλ (where Δλ is the wavelength spacing of the image data

points) with value F=0. The uncertainty in this point being taken as 2% of F_{max}.
Central wavelength of the final profile is calculated as the expectation value of the profile, $\lambda_{cw} = \int_{\lambda_{min}}^{\lambda_{max}} \lambda \frac{F(\lambda)}{\int_{\lambda_{min}}^{\lambda_{max}} F(\lambda) d\lambda} d\lambda$, and the uncertainty in this as $\sigma_{\lambda_{cw}} = \frac{\Delta\lambda}{\lambda_{cw}} \cdot \int_{\lambda_{min}}^{\lambda_{max}} \sigma_{F_\lambda} d\lambda$.
The FWHM of the final profile is calculated by interpolating between profile points to find the wavelengths above and below the central wavelength for which the profile height is half of the maximum height and differencing these. The error in the FWHM is calculated as $\sigma_{FWHM} = \frac{FWHM}{\lambda_{cw}} \cdot \int_{\lambda_{min}}^{\lambda_{max}} \sigma_{F_\lambda} d\lambda$.

Once the in-band data for each temperature had been reduced a combined plot showing all of the filter in-band measurements was made using fmssi_combined_inband_profile_plot.pro (Figure H - 12). Also individual plots for each filter showing the change in central wavelength and bandwidth with temperature (e.g. Figure H - 11).

H.4 In Band Notes

1) Effects of Monochrometer Slit Width on Solar Filters:
The slit-width setting on the monochrometer has a direct effect on the width of the wavelength profile

$$\text{Dispersion [nm/mm]} = \left(\frac{\cos(x + \phi) \cdot 10^6}{G \cdot F \cdot m} \right)$$

Where: $\phi = \arcsin\left(\frac{m \cdot \lambda \cdot G}{2 \cdot 10^6 \cdot \cos(x)} \right)$ is the Grating Rotation Angle [°]

λ = Wavelength [nm]
G = Groove Frequency = 1200 mm^{-1}
m = Grating Order (1)
x = Half Angle = 25.0°
F = Focal Length = 150mm
The slit-width also has an effect on the intensity of the light coming out of the monochrometer. Because the solar filters have very low transmission, it was necessary to widen the monochrometer slit width from 0.68/0.95 mm to between 1.22 and 2.0 mm in order to keep the integration time within reason. The effect of the broader monochrometer profile convolves with the filter transmission profile, both having near equal widths, leading to significant broadening of the observed profile. This effect can be seen in the above results table, and can probably be removed

eventually, but for now we are using the more realistic filter profile bandwidths measured by Barr for the solar filters.

2) Monochrometer and Spectrometer Efficiency Drop-Off in Red:

The efficiency of both the spectrometer and monochrometer drops of rapidly in the red. As a result of this, the calculated efficiency uncertainties are relatively larger at longer wavelengths. This efficiency is usually the main uncertainty source in the CW and FWHM calculations even without this effect, as currently calculated, this leads the uncertainty in CW and FWHM to fall outside of the specified bounds in L4SSI124 and L4SSI125. There is a work around for this, that will be implemented in the calibration report. The values quoted here, being an artifact of the analysis, can be expected to fall within spec.

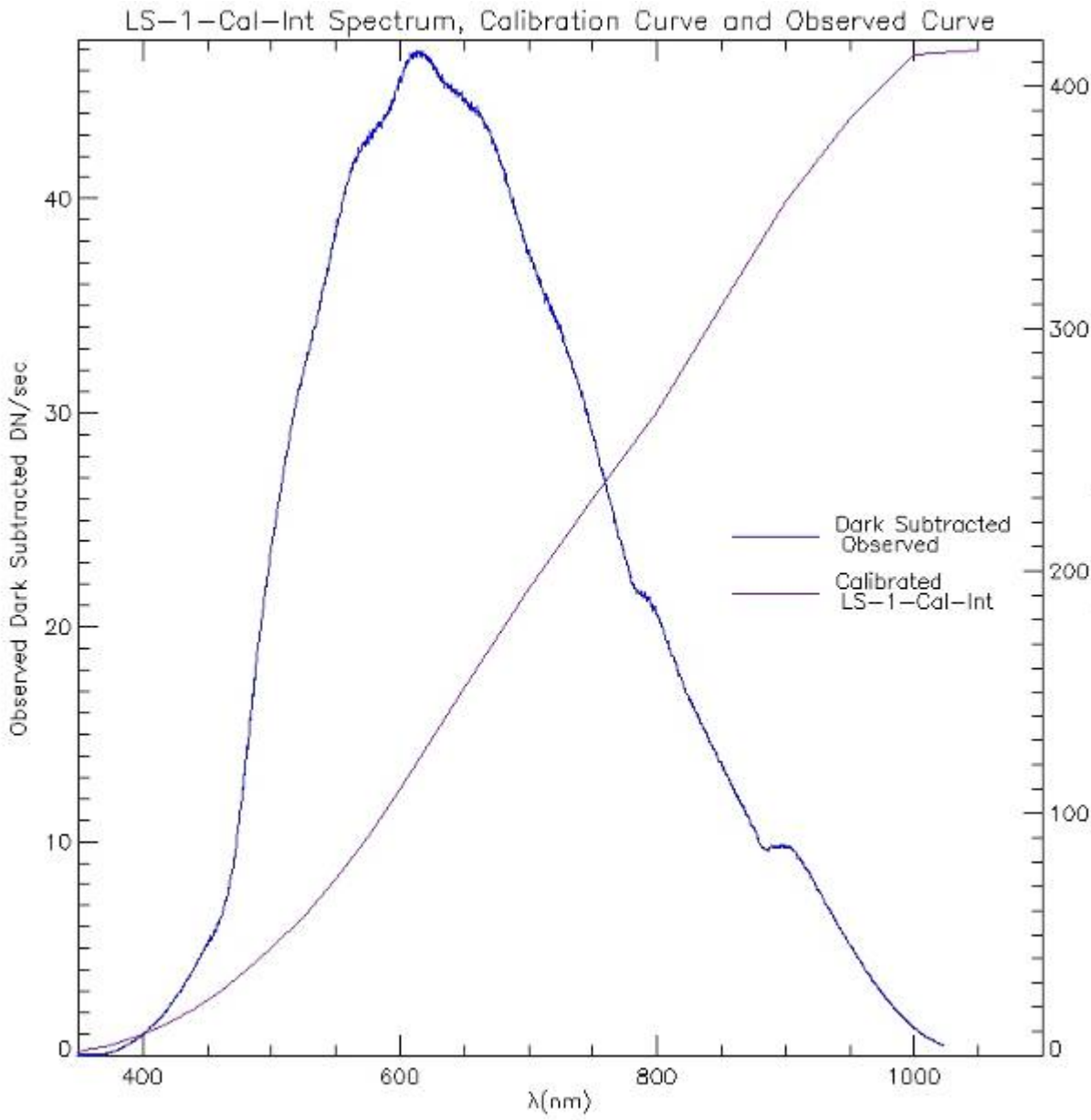

Figure H - 2: Comparison of Oceans Optics LS-1-Cal-Int spectrum as observed with the Oceans Optics USB 2000 spectrometer and as calibrated by the manufacturer

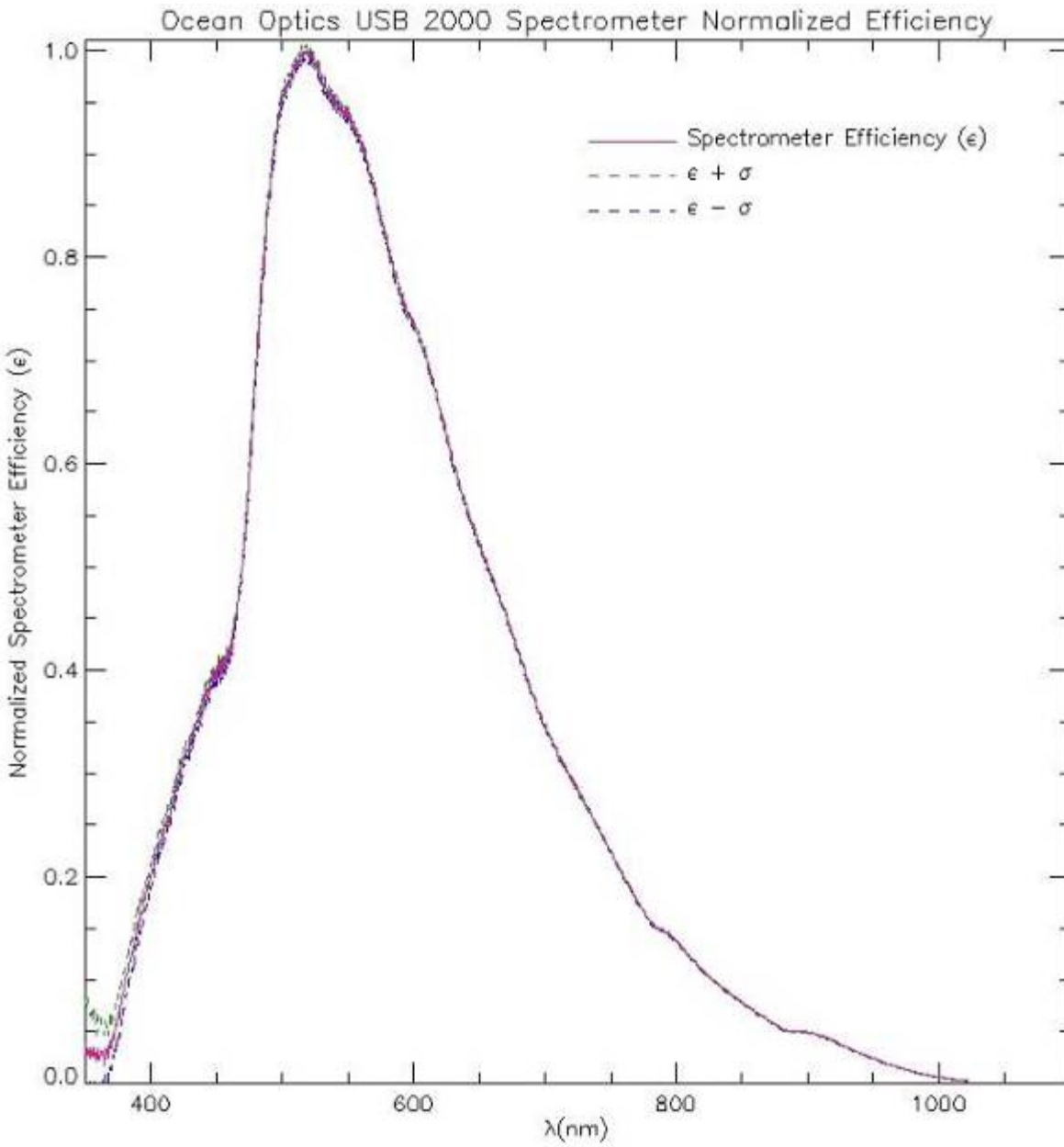

Figure H - 3: Calculated spectral responsiveness of the Oceans Optics USB 2000 spectrometer.

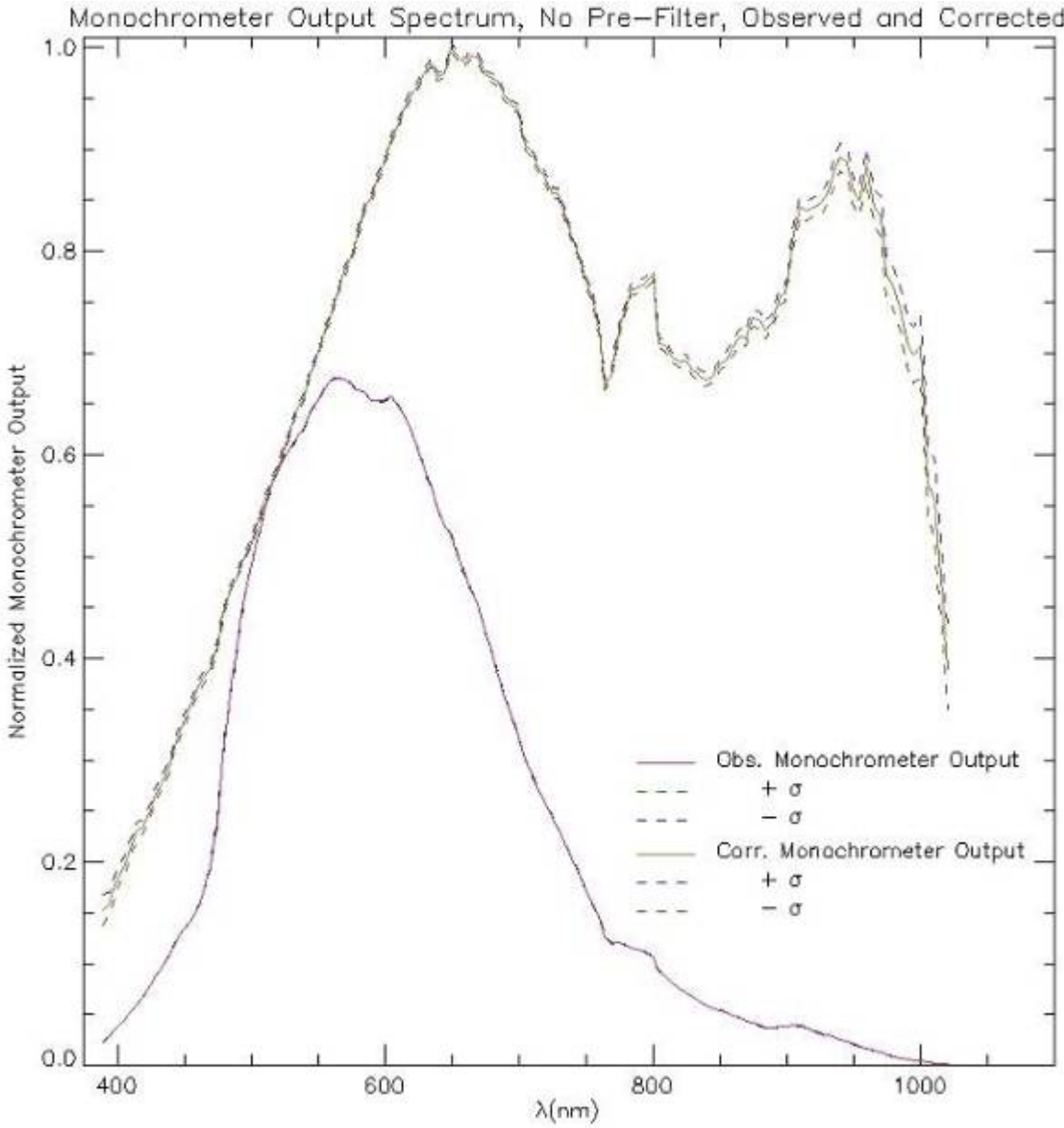

Figure H - 4: Monochrometer output efficiency vs. wavelength with no pre-filter

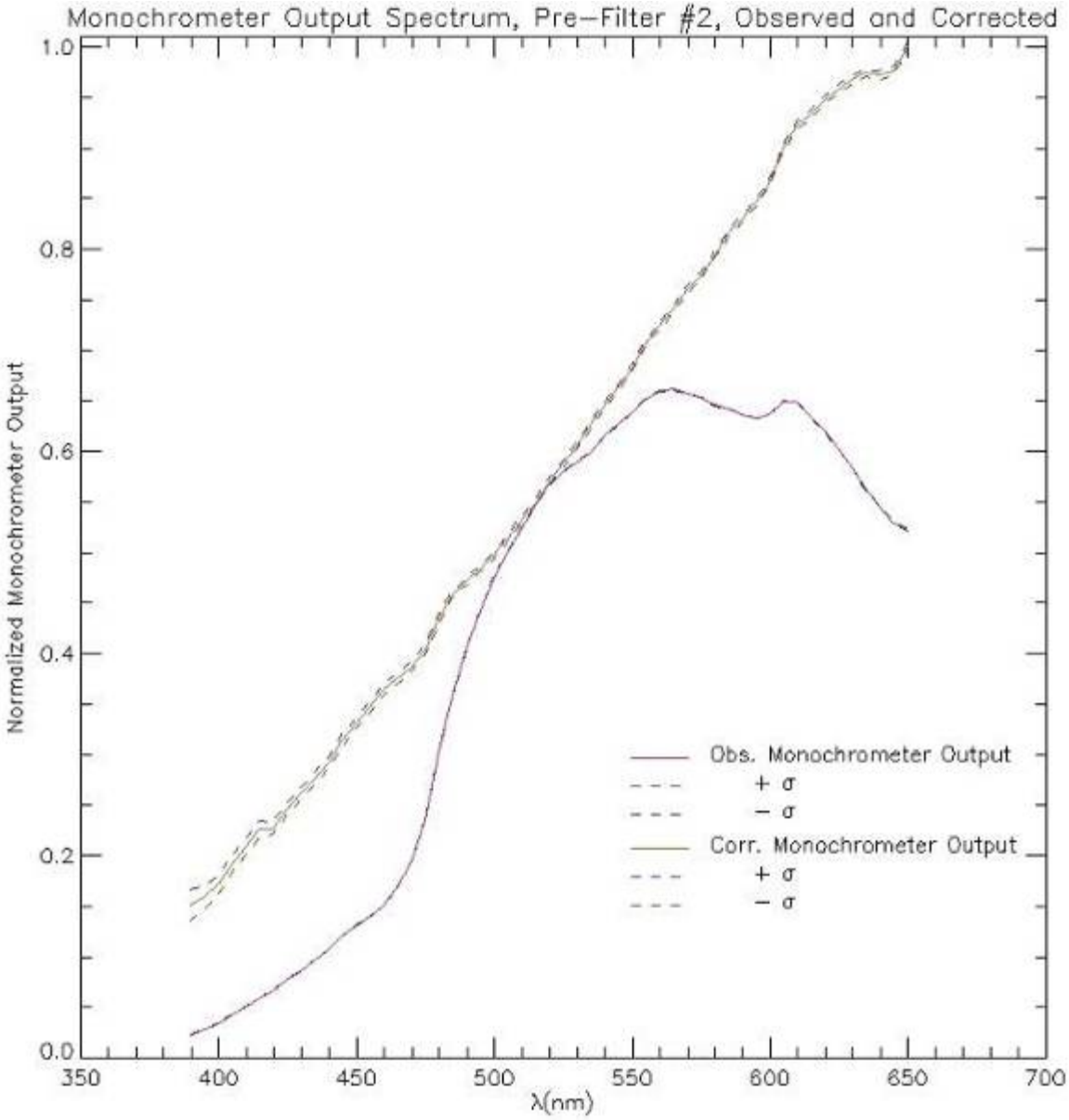

Figure H - 5: Monochrometer output efficiency vs. wavelength with pre-filter# 2

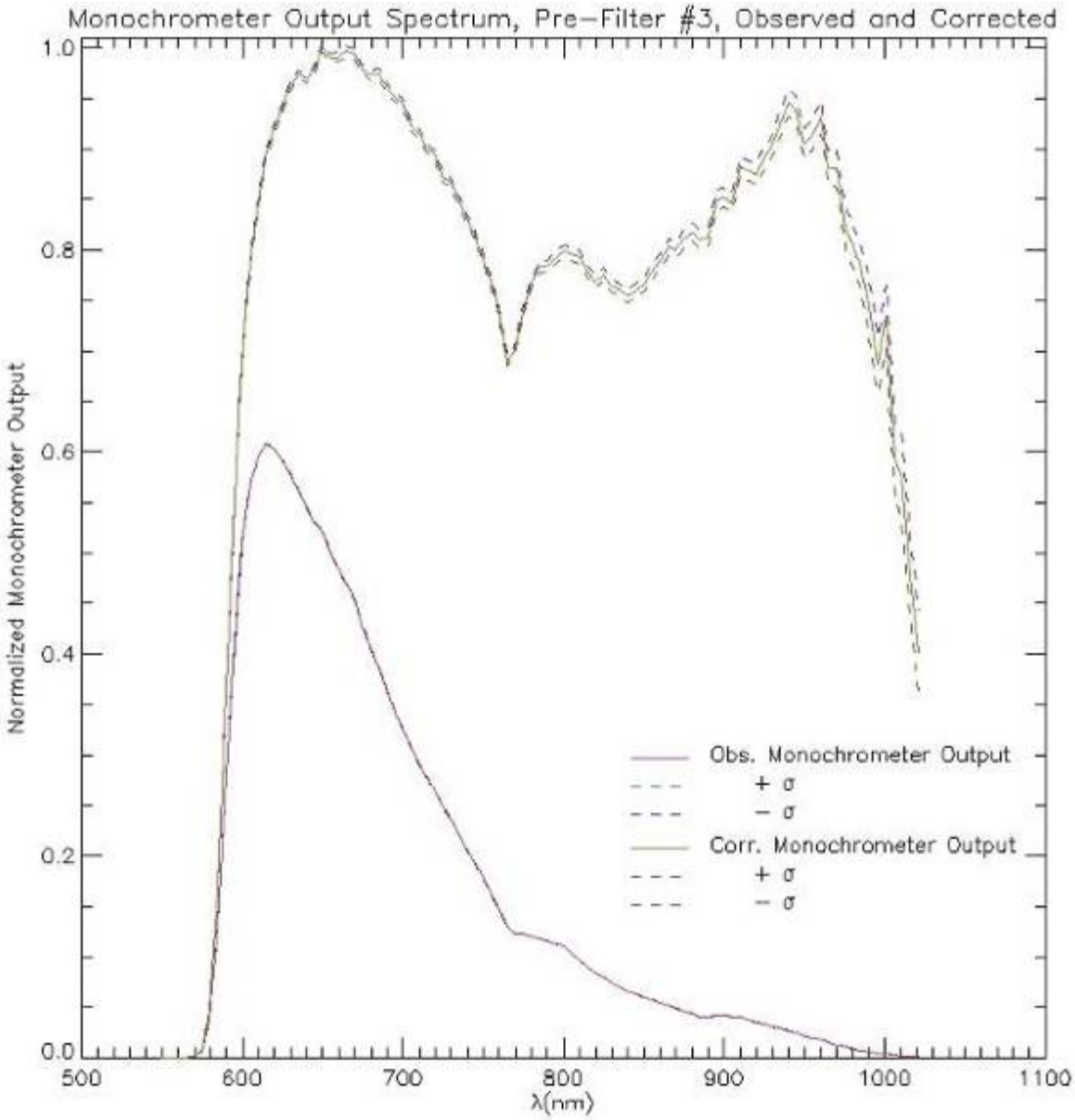

Figure H - 6: Monochrometer output efficiency vs. wavelength with pre-filter#3

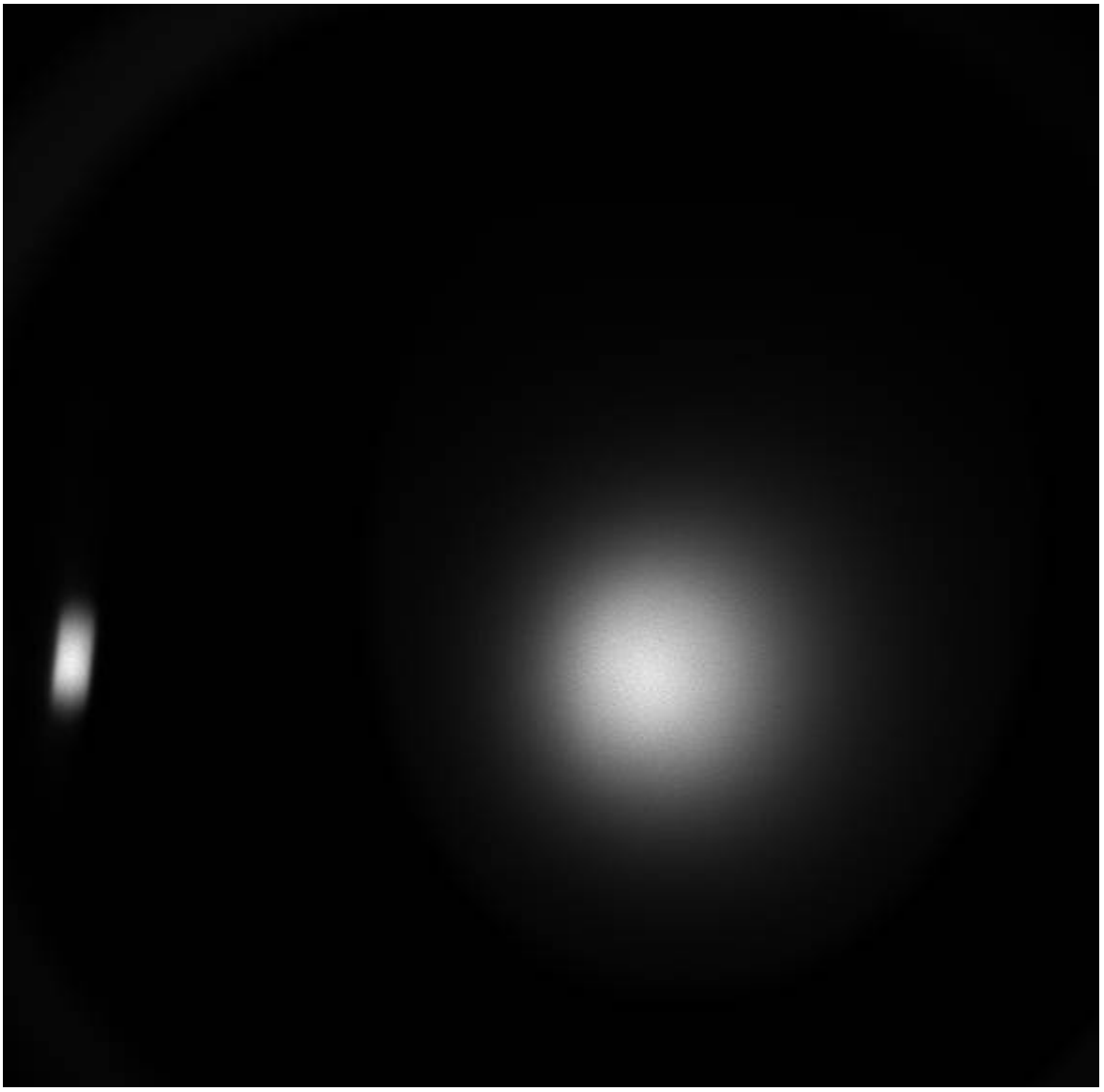

Figure H - 7: Example dark subtracted FM SSI Image of the monochrometer output reflected off of the polished Spectralon. On the L.H.S is a reflection caused by the TVC housing.

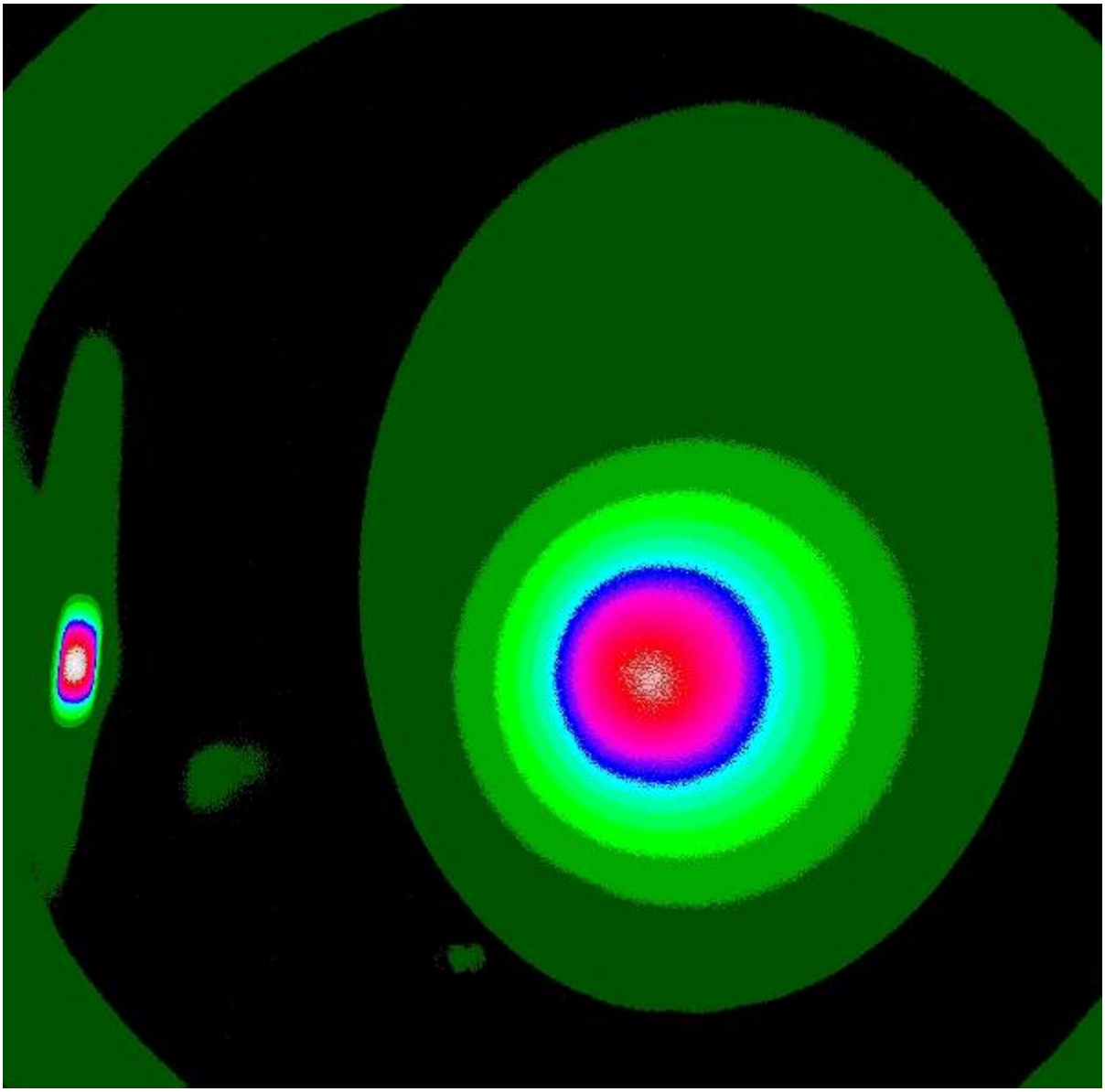

Figure H - 8: Fig. 7 using stepped color table

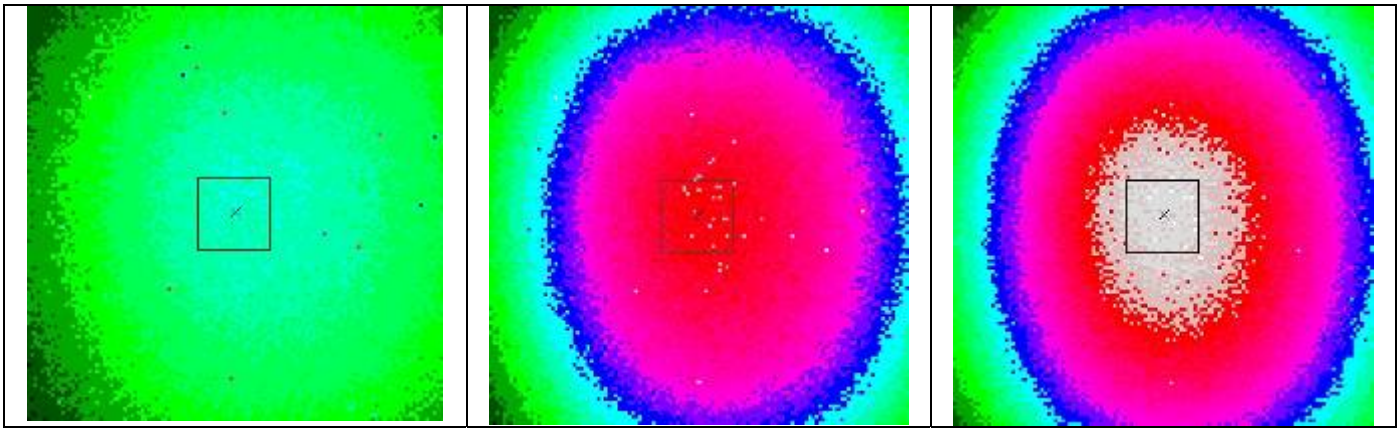

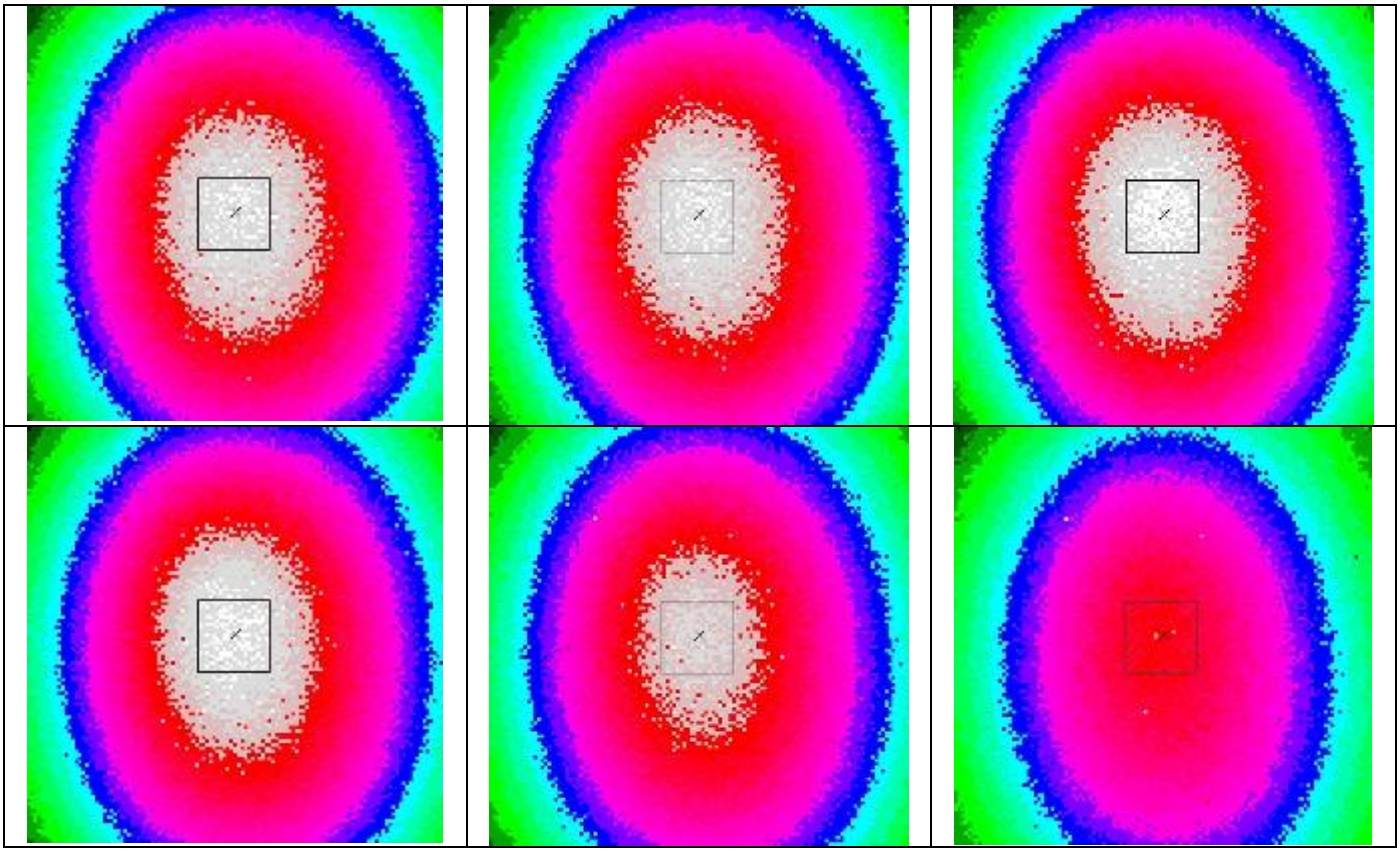

Figure H - 9: Example of Sub-box Positioning in L5 at -65C, X marks center of sub-box, black line shows box size

H.3 In-Band Filter profile Results – CWL and BW with Temperature

L1:

Source	Nominal Temp (°C)	Median OB Temp (°C)	CW (nm)	+/- (nm)	FWHM (nm)	+/- (nm)	Res. (nm)
UA	-65	-66.3	672.85	0.17	19.08	0.09	2.3
UA	-15	-18.2	672.85	0.17	19.04	0.09	
Barr	Room	672.72		18.89		.1	
Nominal			672	2	20	2	

Table H - 2: L1 Results

L2:

Source	Nominal Temp (°C)	Median OB Temp (°C)	CW (nm)	+/- (nm)	FWHM (nm)	+/- (nm)	Res. (nm)
UA	-65	-65.6	446.89	0.77	22.80	0.41	2.4
UA	-15	-19.2	446.55	0.94	22.99	0.45	
Barr	Room		445.86		22.74		.2
Nominal			445	2	23	2	

Table H - 3: L1 Results

L3:

Source	Nominal Temp (°C)	Median OB Temp (°C)	CW (nm)	+/- (nm)	FWHM (nm)	+/- (nm)	Res. (nm)
UA	-65	-65.4	450.76	0.35	13.72[7]	0.27	2.0
Barr	Room		451.02		4.09		.1
Nominal			451	6	5	1	

Table H - 4: L1 Results

L4:

Source	Nominal Temp (°C)	Median OB Temp (°C)	CW (nm)	+/- (nm)	FWHM (nm)	+/- (nm)	Res. (nm)
UA	-65	-65.5	990.72[8]	0.70	11.52[2]	0.44	1.7
UA	-40	-38.5	990.53	0.68	16.67[2]	0.62	
Barr	Room		990.60		4.90		.25
Nominal			990	0.6	5	0.4	

Table H - 5: L1 Results

L5:

Source	Nominal Temp (°C)	Median OB Temp (°C)	CW (nm)	+/- (nm)	FWHM (nm)	+/- (nm)	Res. (nm)
UA	-65	-64.2	886.99	0.25	10.96[2]	0.15	1.7
UA	-40	-39.7	886.81[3]	0.25	11.56[2]	0.16	
UA	-15	-16.6	886.46	0.24	14.06[2]	0.19	
Barr	Room		886.19		5.77		.2
Nominal			886	0.6	6	0 .4	

Table H - 6: L1 Results

L6:

Source	Nominal Temp (°C)	Median OB Temp (°C)	CW (nm)	+/- (nm)	FWHM (nm)	+/- (nm)	Res. (nm)
UA	-65	-65.4	833.31	0.37	28.35	0.26	2.3
UA	-15	-19.7	833.30	0.37	28.39	0.26	
Barr	Room		833.18		29.91		.25
Nominal			830	2	30	2	

Table H - 7: L1 Results

L7:

Source	Nominal Temp (°C)	Median OB Temp (°C)	CW (nm)	+/- (nm)	FWHM (nm)	+/- (nm)	Res. (nm)
UA	-65	-65.6	801.48	0.29	21.68	0.17	2.3
UA	-15	-20.6	801.54	0.29	21.64	0.17	
Barr	Room		802.24		21.34		.2
Nominal			802	2	21	2	

Table H - 8: L1 Results

L8:

Source	Nominal Temp (°C)	Median OB Temp (°C)	CW (nm)	+/- (nm)	FWHM (nm)	+/- (nm)	Res. (nm)
UA	-65	-65.8	864.27	0.71	36.91	0.37	2.4

UA	-15	-20.9	864.28	0.71	36.84	0.37	
Barr	Room		863.73		37.49		.25
Nominal			861	2	36	2	

Table H - 9: L1 Results

L9:

Source	Nominal Temp (°C)	Median OB Temp (°C)	CW (nm)	+/- (nm)	FWHM (nm)	+/- (nm)	Res. (nm)
UA	-65	-66.0	899.52	0.98	44.34	0.50	2.4
UA	-15	-20.9	899.53	0.98	44.79	0.50	
Barr	Room		901.72		46.07[3]		.2
Nominal			901	2	44	2	

Table H - 10: L1 Results

L10:

Source	Nominal Temp (°C)	Median OB Temp (°C)	CW (nm)	+/- (nm)	FWHM (nm)	+/- (nm)	Res. (nm)
UA	-65	-66.2	931.04	0.71	24.57	0.33	2.4
UA	-15	-21.1	930.71	0.70	24.68[3]	0.33	
Barr	Room		931.94		25.22		.25
Nominal			932	2	27	2	

Table H - 11: L1 Results

L11:

Source	Nominal Temp (°C)	Median OB Temp (°C)	CW (nm)	+/- (nm)	FWHM (nm)	+/- (nm)	Res. (nm)
UA	-15	-20.8	1001.04	2.74[9]	25.86	1.34[4]	2.5
Barr	Room		1001.96		27.50		.25
Nominal			1001	2	27	2	

Table H - 12: L1 Results

L12:

Source	Nominal Temp (°C)	Median OB Temp (°C)	CW (nm)	+/- (nm)	FWHM (nm)	+/- (nm)	Res. (nm)
UA	-65	-65.9	968.30	1.32[4]	29.37	0.64	2.4
UA	-15	-21.0	968.50	1.33[4]	29.68	0.65	
Barr	Room		968.87		30.10		.25
Nominal			967	2	31	2	

Table H - 13: L1 Results

R1:

Source	Nominal Temp (°C)	Median OB Temp (°C)	CW (nm)	+/- (nm)	FWHM (nm)	+/- (nm)	Res. (nm)
UA	-65	-72.3	672.41	0.22	19.05	0.11	2.3
UA	-15	-18.2	672.87	0.17	19.04	0.09	
Barr	Room		672.69		18.87		.1
Nominal			672	2	20	2	

Table H - 14: R1 Results

R2:

Source	Nominal Temp (°C)	Median OB Temp (°C)	CW (nm)	+/- (nm)	FWHM (nm)	+/- (nm)	Res. (nm)
UA	-65	-71.6	446.80	0.77	22.85	0.42	2.4
UA	-15	-17.3	446.68	0.93	22.94	0.45	

Barr	Room		445.91		22.74		.2
Nominal			445	2	23	2	

Table H - 15: R1 Results

R3:

Source	Nominal Temp (°C)	Median OB Temp (°C)	CW (nm)	+/- (nm)	FWHM (nm)	+/- (nm)	Res. (nm)
UA	-65	-71.1	671.06	0.13	9.07[2]	0.07	1.5
Barr	Room		671.50		4.93		.2
Nominal			671	6	5	1	

Table H - 16: R1 Results

R4:

Source	Nominal Temp (°C)	Median OB Temp (°C)	CW (nm)	+/- (nm)	FWHM (nm)	+/- (nm)	Res. (nm)
UA	-65	-69.9	935.53	0.24	10.83[2]	0.18	1.4
UA	-40	-33.5	935.70	0.23	12.54[2]	0.20	
UA	-20	-16.7	936.06	0.23	14.06[2]	0.22	
Barr	Room		936.51		5.19		.2
Nominal			935.9	0.6	5	0.4	

Table H - 17: R1 Results

R5:

Source	Nominal Temp (°C)	Median OB Temp (°C)	CW (nm)	+/- (nm)	FWHM (nm)	+/- (nm)	Res. (nm)
UA	-65	-69.0	935.70	0.24	11.02[2]	0.18	1.4
UA	-40	-37.5	935.79	0.23	12.33[2]	0.20	
UA	-40	-34.5	935.80	0.23	12.72[2]	0.21	
UA	-20	-15.9	936.05	0.23	14.09[2]	0.22	
Barr	Room		936.22		5.20		.2
Nominal			935.9	0.6	5	0.4	

Table H - 18: R1 Results

R6:

Source	Nominal Temp (°C)	Median OB Temp (°C)	CW (nm)	+/- (nm)	FWHM (nm)	+/- (nm)	Res. (nm)
UA	-65	-71.6	449.66	1.01	28.74	0.51	2.4
UA	-15	-17.9	449.64	1.19	28.73	0.54	
Barr	Room		448.04		30.01		.2
Nominal			445	3	23	2	

Table H - 19: R1 Results

R7:

Source	Nominal Temp (°C)	Median OB Temp (°C)	CW (nm)	+/- (nm)	FWHM (nm)	+/- (nm)	Res. (nm)
UA	-65	-73.6	752.93	0.23	20.04	0.12	2.3
UA	-15	-16.8	753.12	0.23	20.12	0.12	
Barr	Room		753.02		20.07		.1
Nominal			753	2	19	2	

Table H - 20: R1 Results

R8:

Source	Nominal Temp (°C)	Median OB Temp (°C)	CW (nm)	+/- (nm)	FWHM (nm)	+/- (nm)	Res. (nm)
UA	-65	-73.0	754.15	0.23	20.64	0.13	2.3
UA	-15	-16.8	754.15	0.23	20.64	0.13	
Barr	Room		754.46		20.26		.25
Nominal			753	2	19	2	

Table H - 21: R1 Results

R9:

Source	Nominal Temp (°C)	Median OB Temp (°C)	CW (nm)	+/- (nm)	FWHM (nm)	+/- (nm)	Res. (nm)
UA	-65	-71.8	753.26	0.23	16.79	0.10	2.3
UA	-15	-16.9	753.54	0.23	16.91[3]	0.10	
Barr	Room		753.53		16.92		.2
Nominal			753	2	19	2	

Table H - 22: R1 Results

R10:

Source	Nominal Temp (°C)	Median OB Temp (°C)	CW (nm)	+/- (nm)	FWHM (nm)	+/- (nm)	Res. (nm)
UA	-65	-71.6	603.71	0.12	14.79	0.06	2.3
UA	-15	-16.1	603.78	0.12	14.79	0.06	
Barr	Room		604.06		14.81		.2
Nominal			604	2	16	2	

Table H - 23: R1 Results

R11:

Source	Nominal Temp (°C)	Median OB Temp (°C)	CW (nm)	+/- (nm)	FWHM (nm)	+/- (nm)	Res. (nm)
UA	-65	-71.4	532.03	0.32	28.07	0.16	2.4
UA	-15	-16.3	532.00	0.32	28.07	0.16	
Barr	Room		532.71		28.47		.2
Nominal			533	2	28	2	

Table H - 24: R1 Results

R12:

Source	Nominal Temp (°C)	Median OB Temp (°C)	CW (nm)	+/- (nm)	FWHM (nm)	+/- (nm)	Res. (nm)
UA	-65	-71.0	485.04	0.33	20.87	0.18	2.3
UA	-15	-16.4	485.26	0.38	20.77	0.20	
Barr	Room		484.99		19.60		.25
Nominal			485	2	23	+2/-4	

Table H - 25: R1 Results

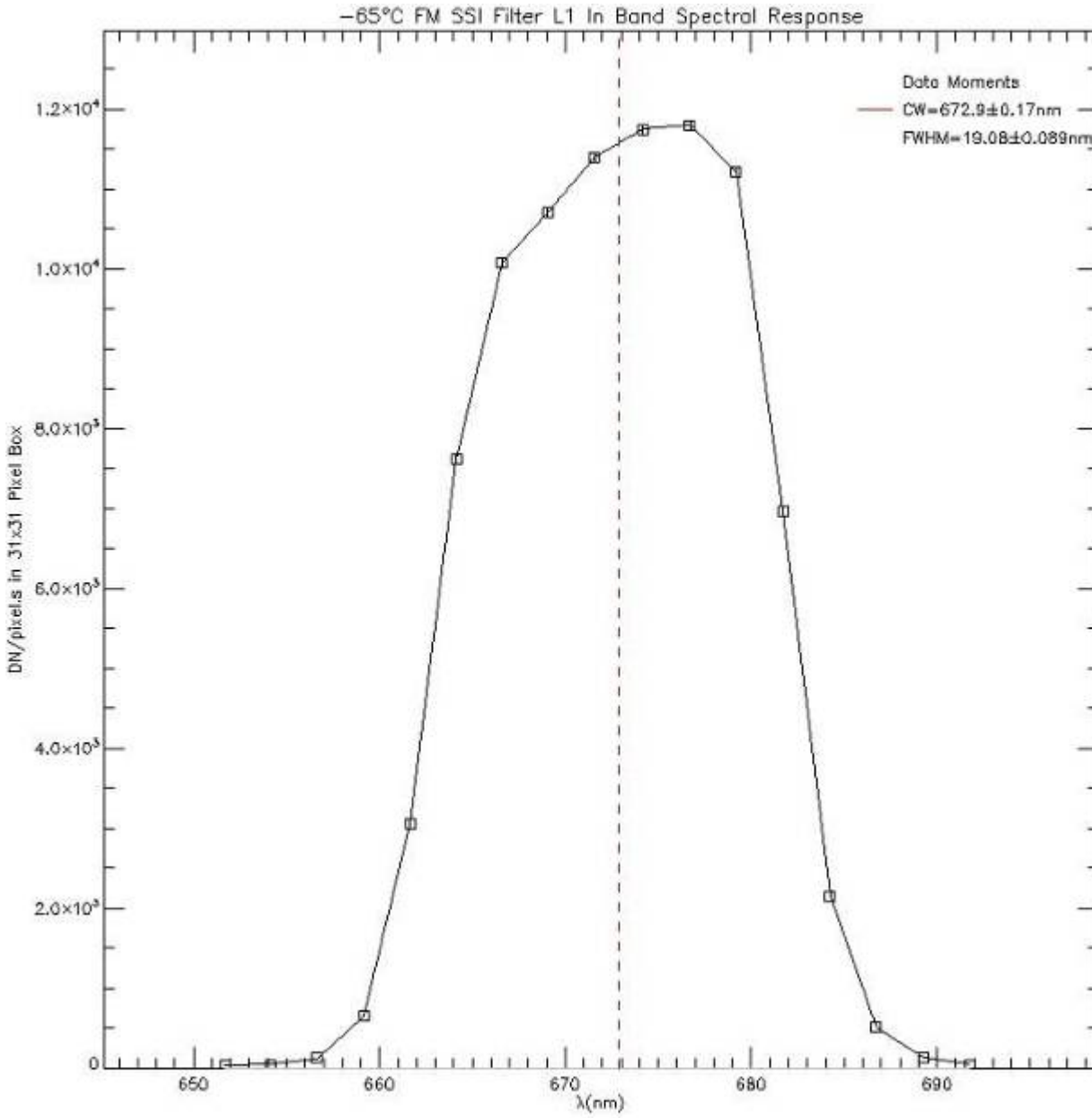

Figure H - 10: L1 -65°C Filter Profile

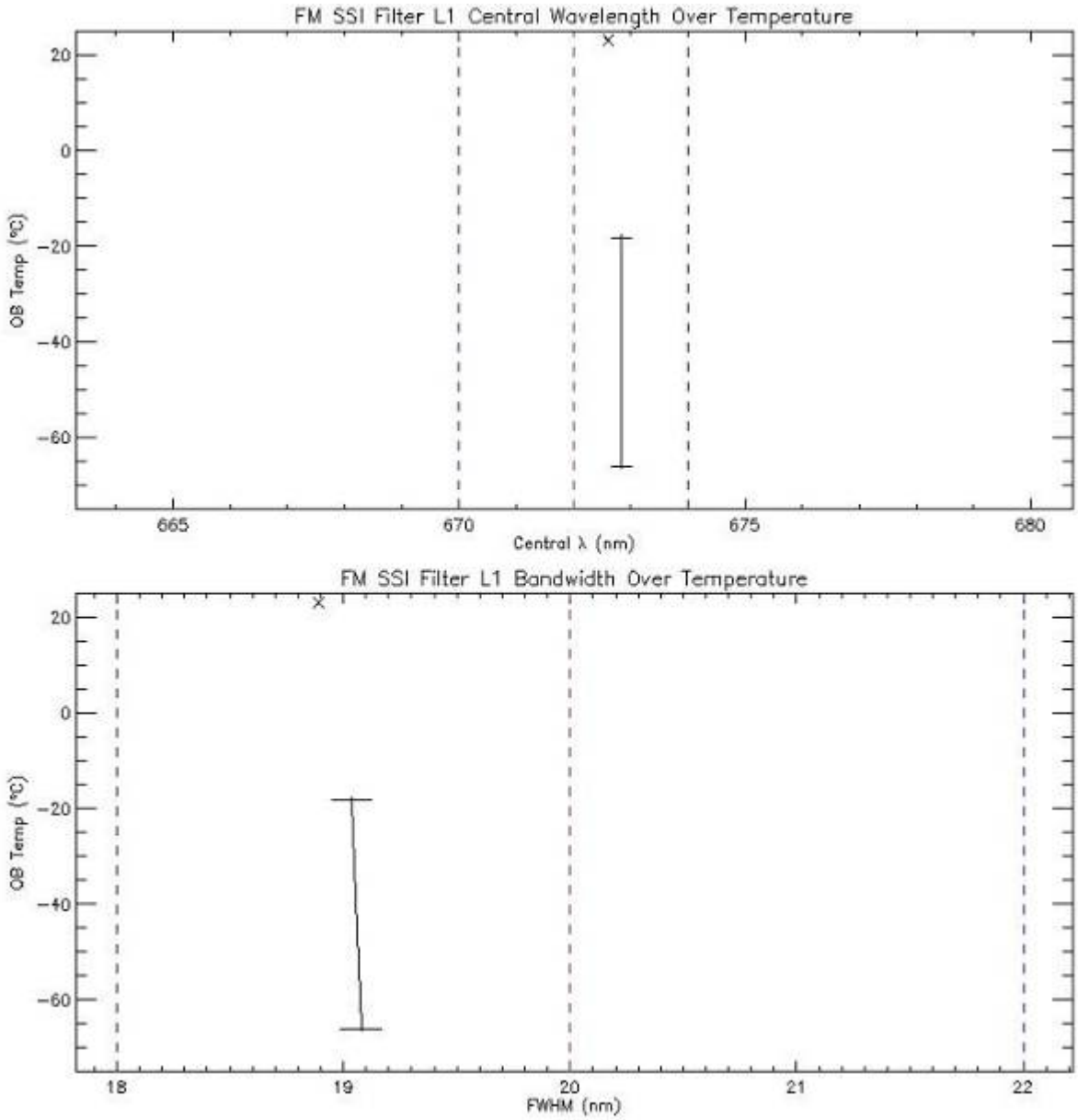

Figure H - 11: L1 Central Wavelength and Bandwidth Over Temperature

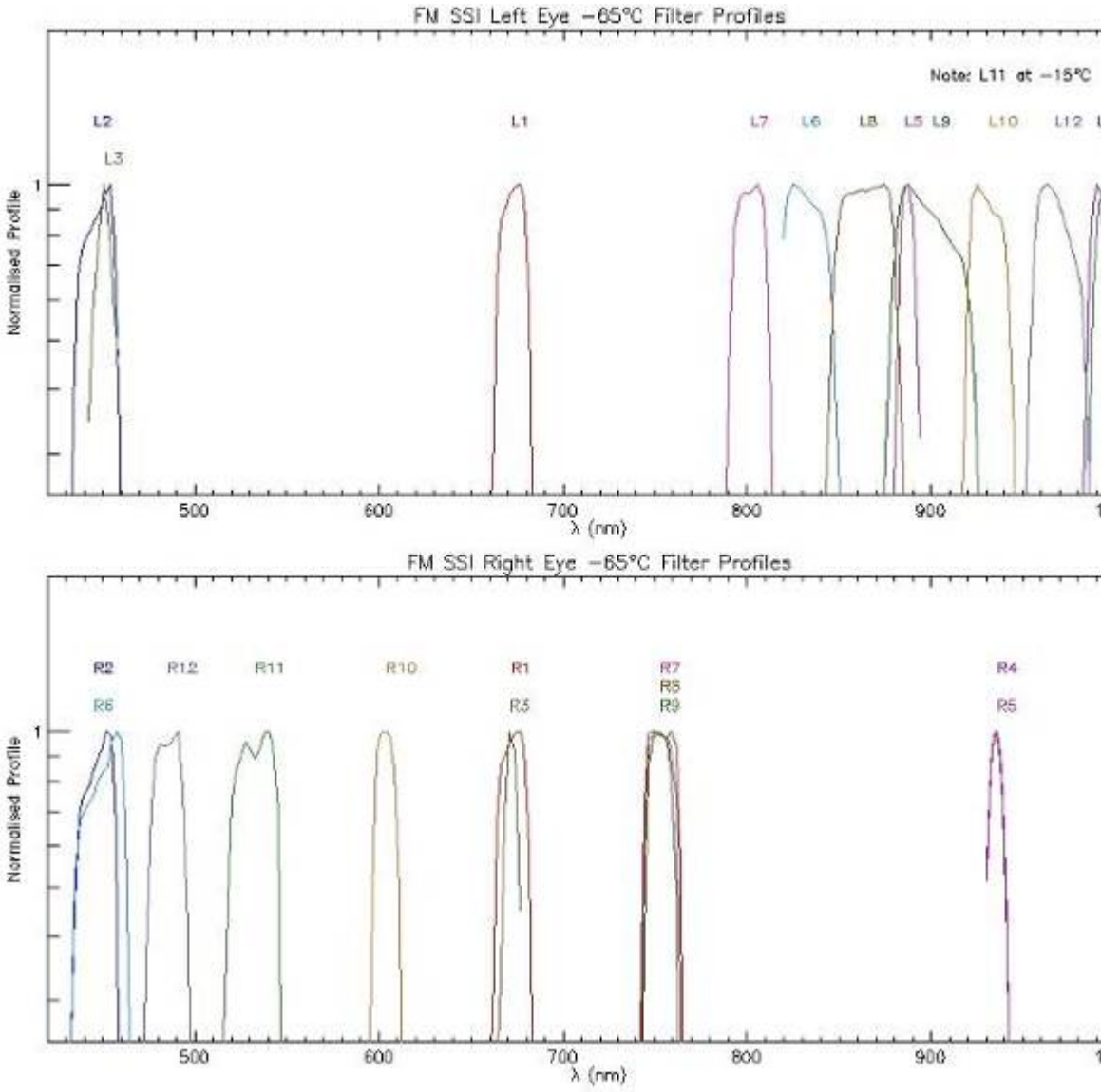

Figure H - 12: All FM SSI UA Filter Profiles

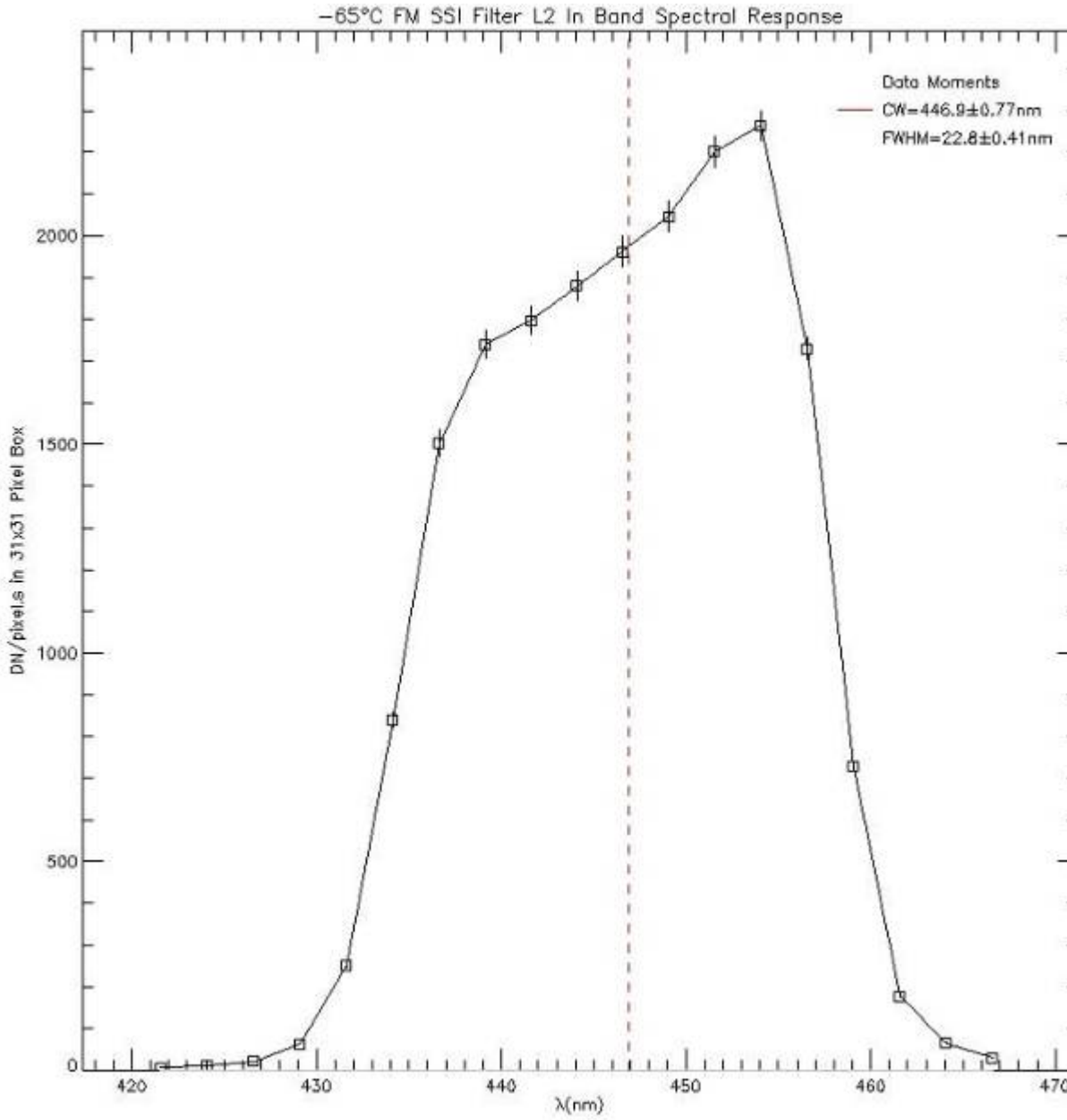

Figure H - 13: L2 -65°C Filter Profile

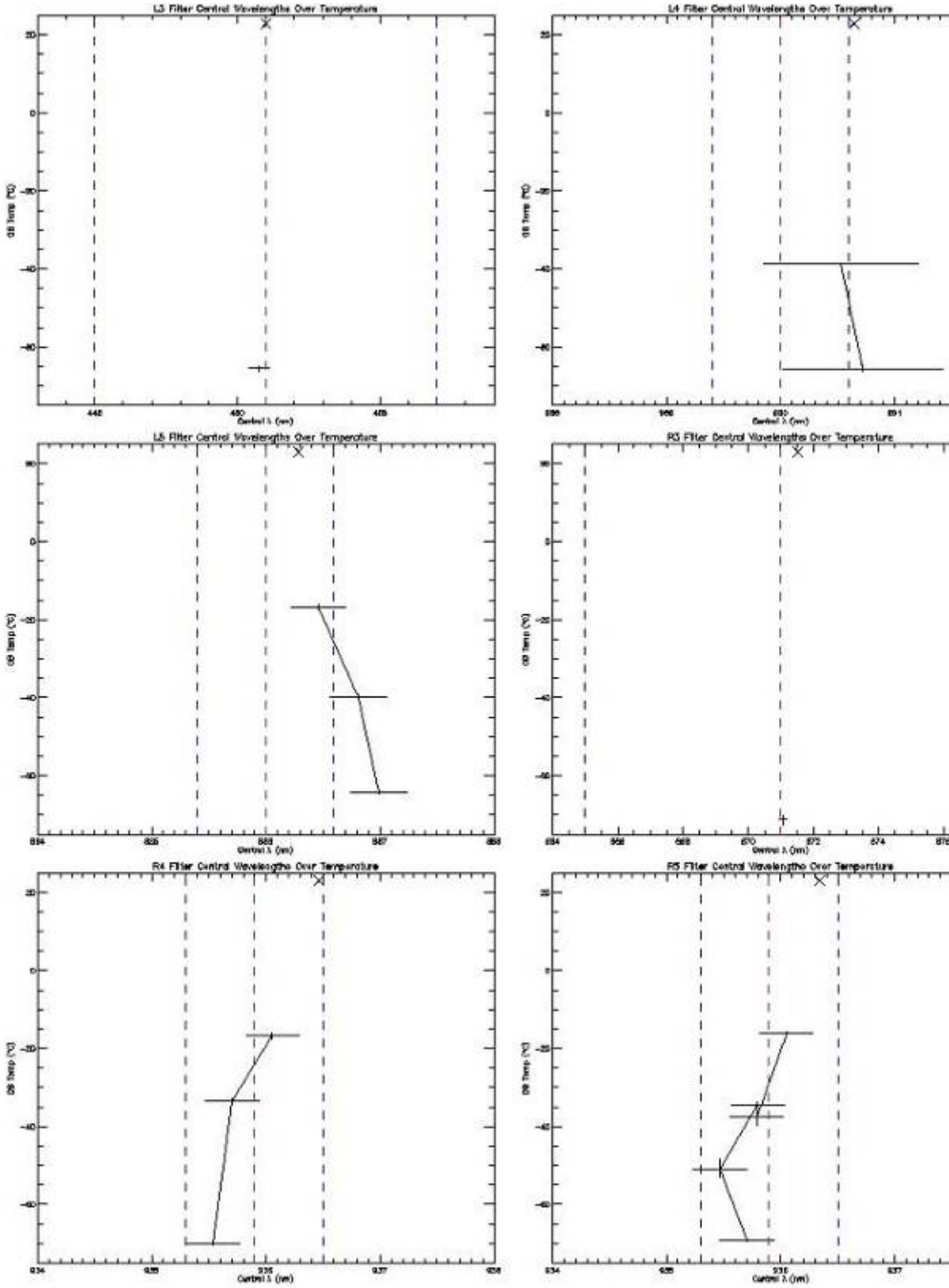

Figure H - 14: Narrow Band Filter CW With Temperature

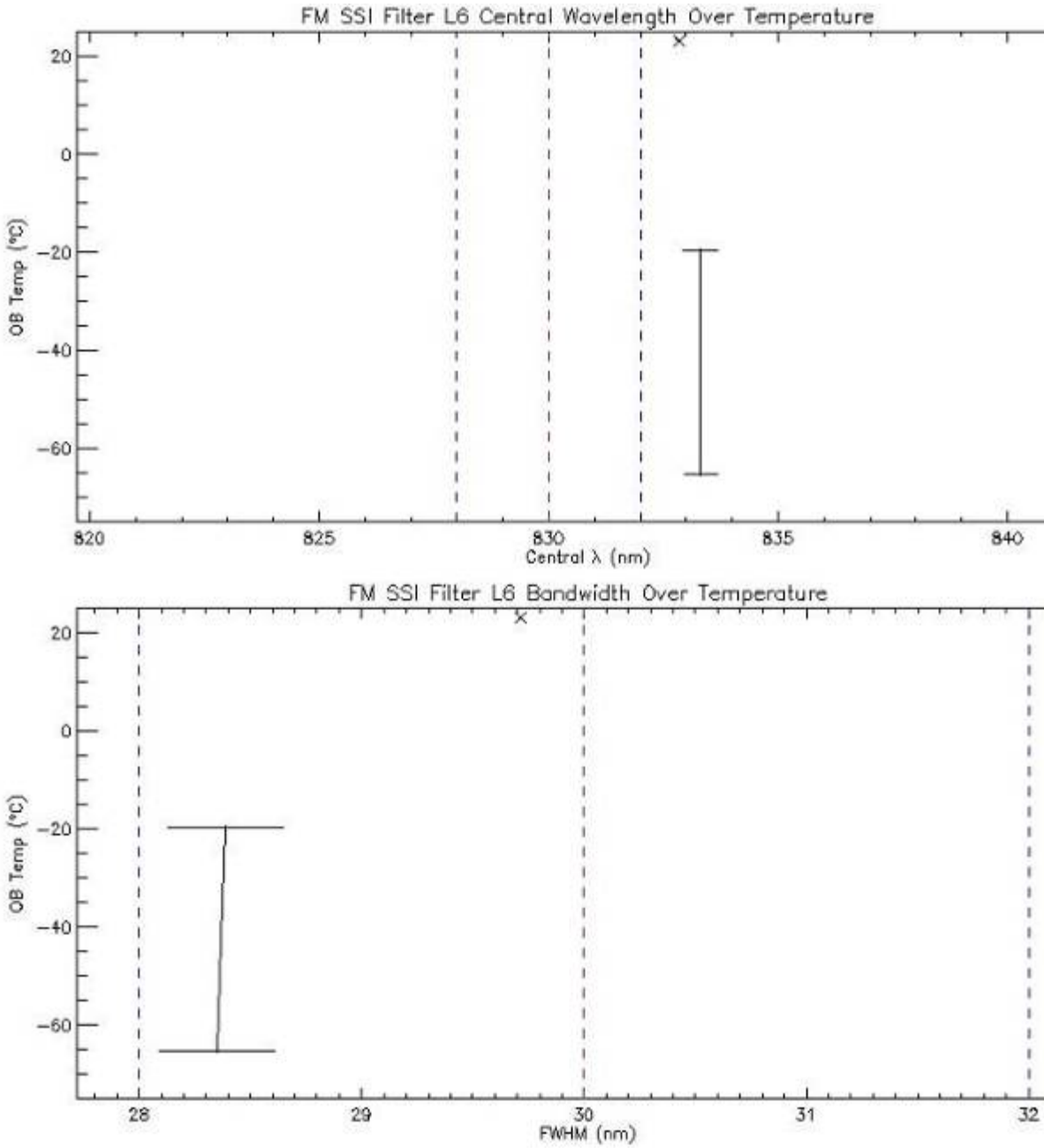

Figure H - 15: L6 Central Wavelength and Bandwidth Over Temperature

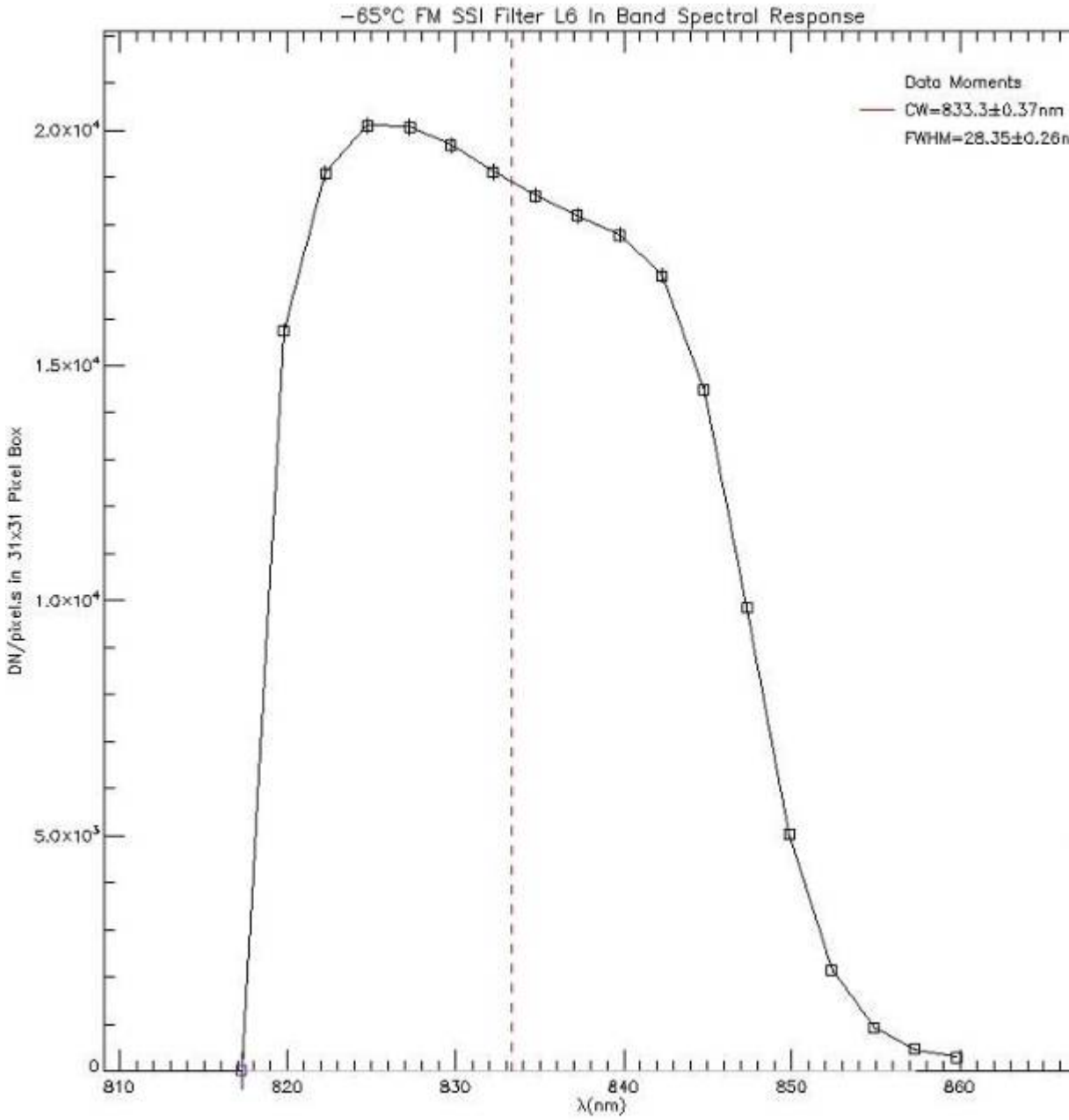

Figure H - 16: L6 -65°C Filter Profile

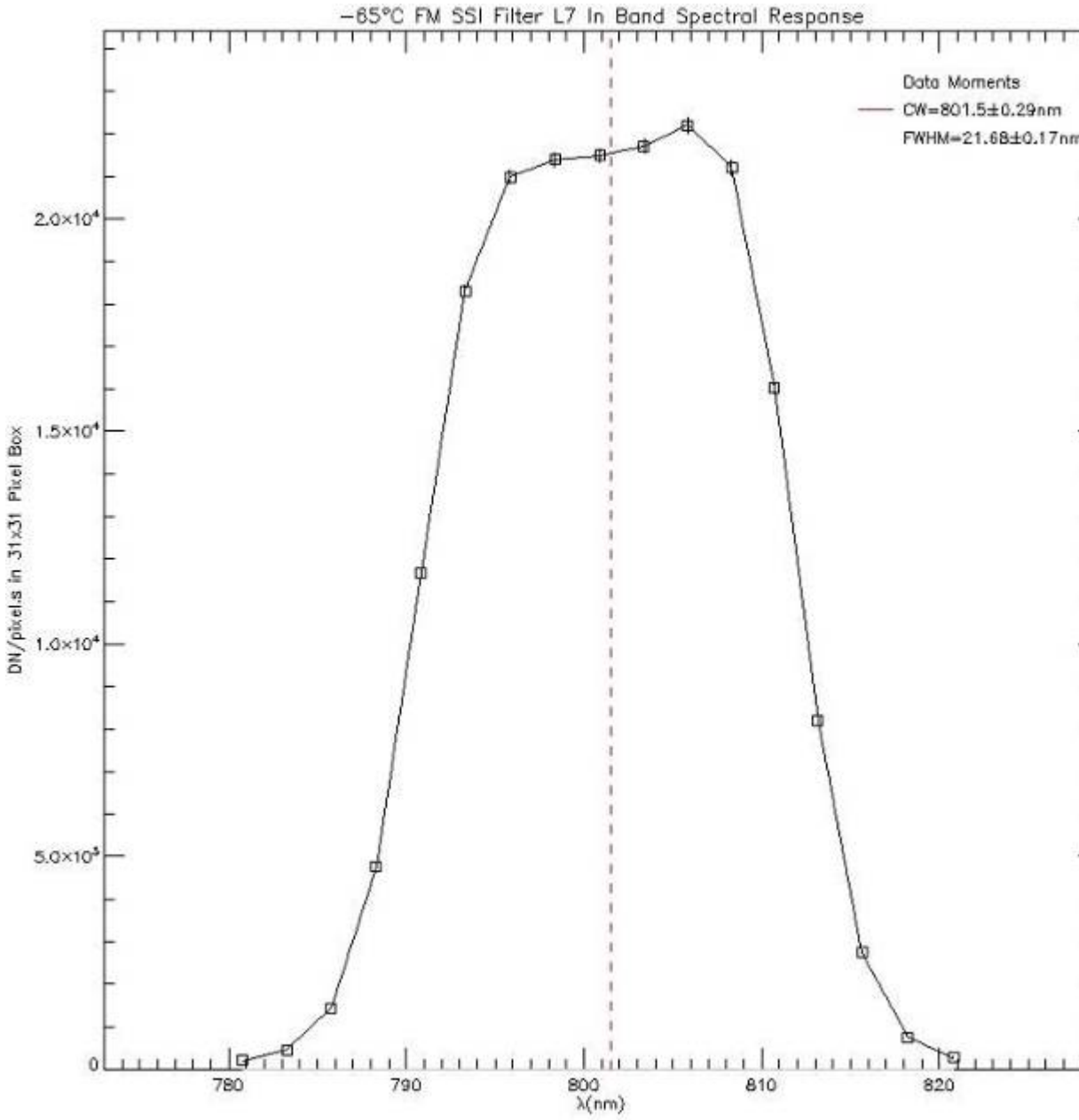

Figure H - 17: L7 -65°C Filter Profile

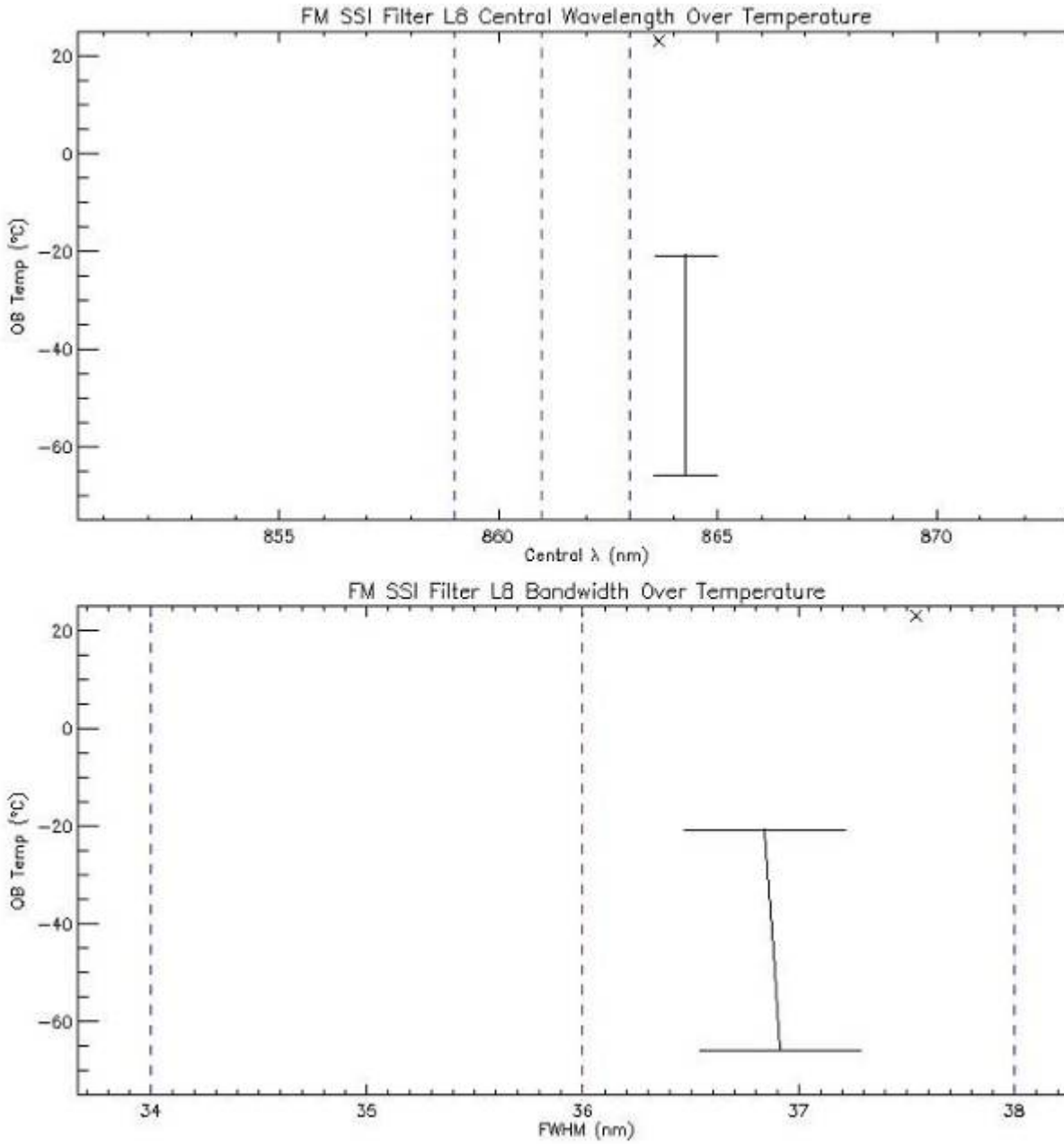

Figure H - 18: L8 Central Wavelength and Bandwidth Over Temperature

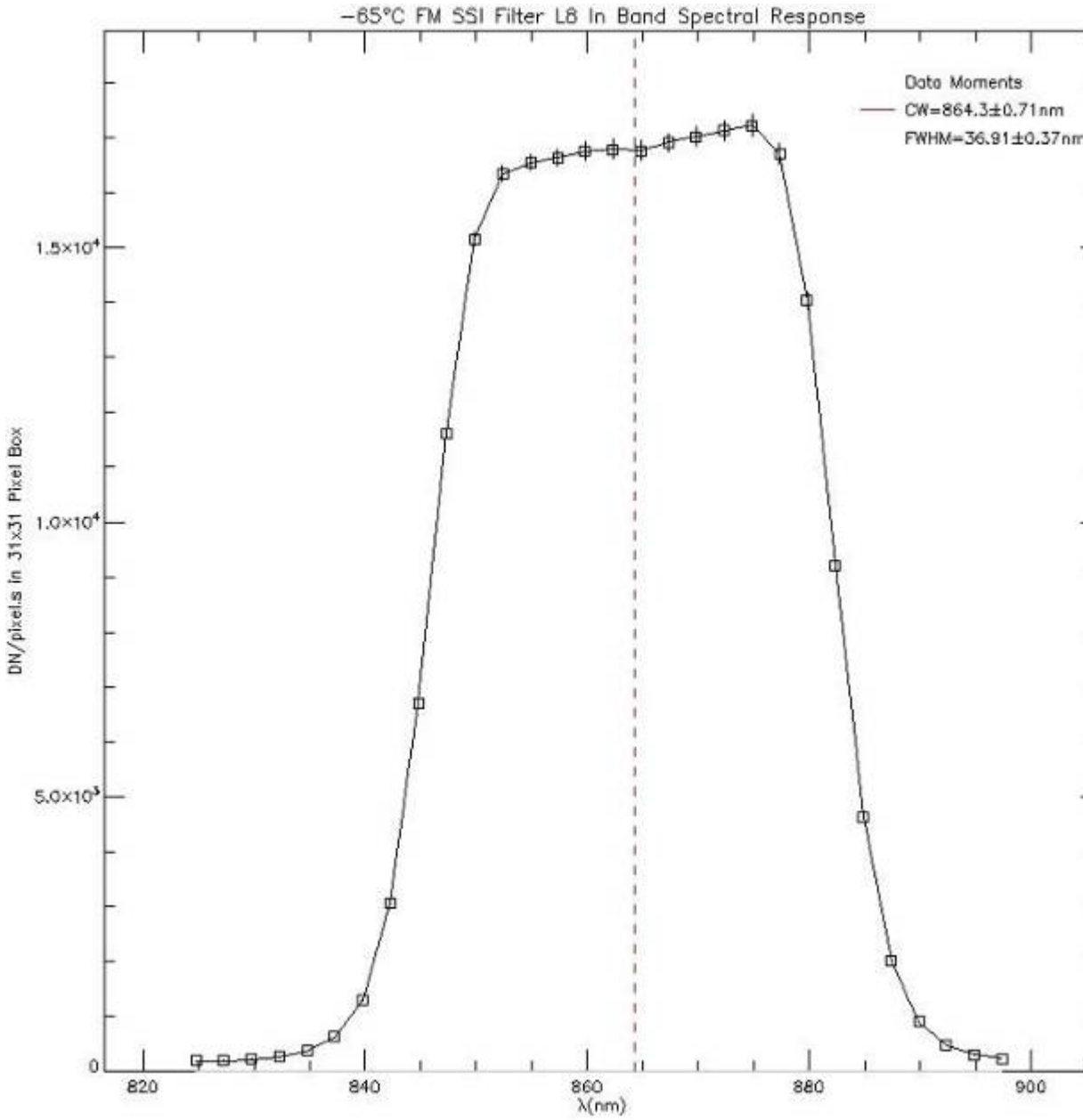

Figure H - 19: L8 -65°C Filter Profile

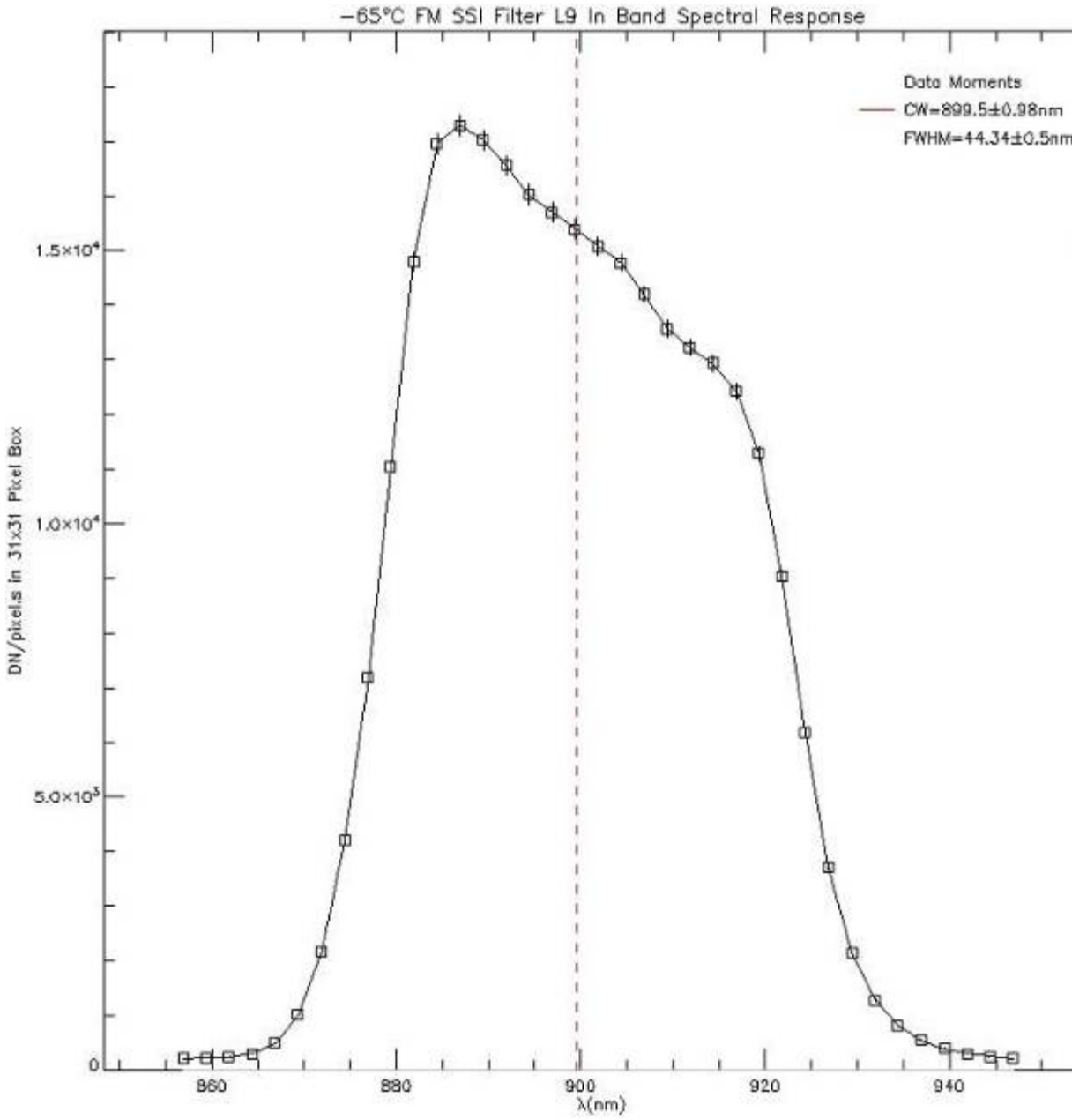

Figure H - 20: L9 -65°C Filter Profile

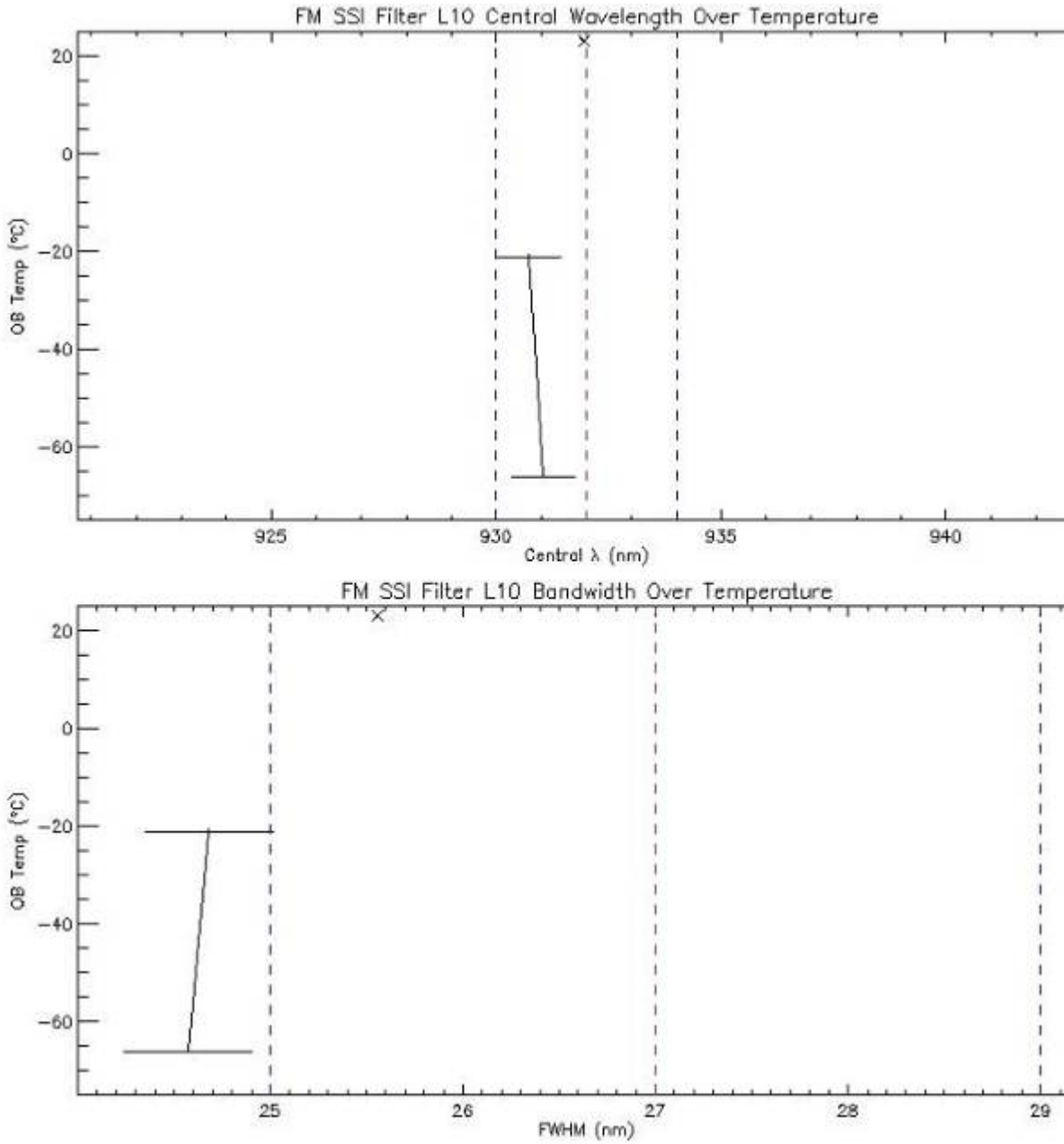

Figure H - 21: L10 Central Wavelength and Bandwidth Over Temperature

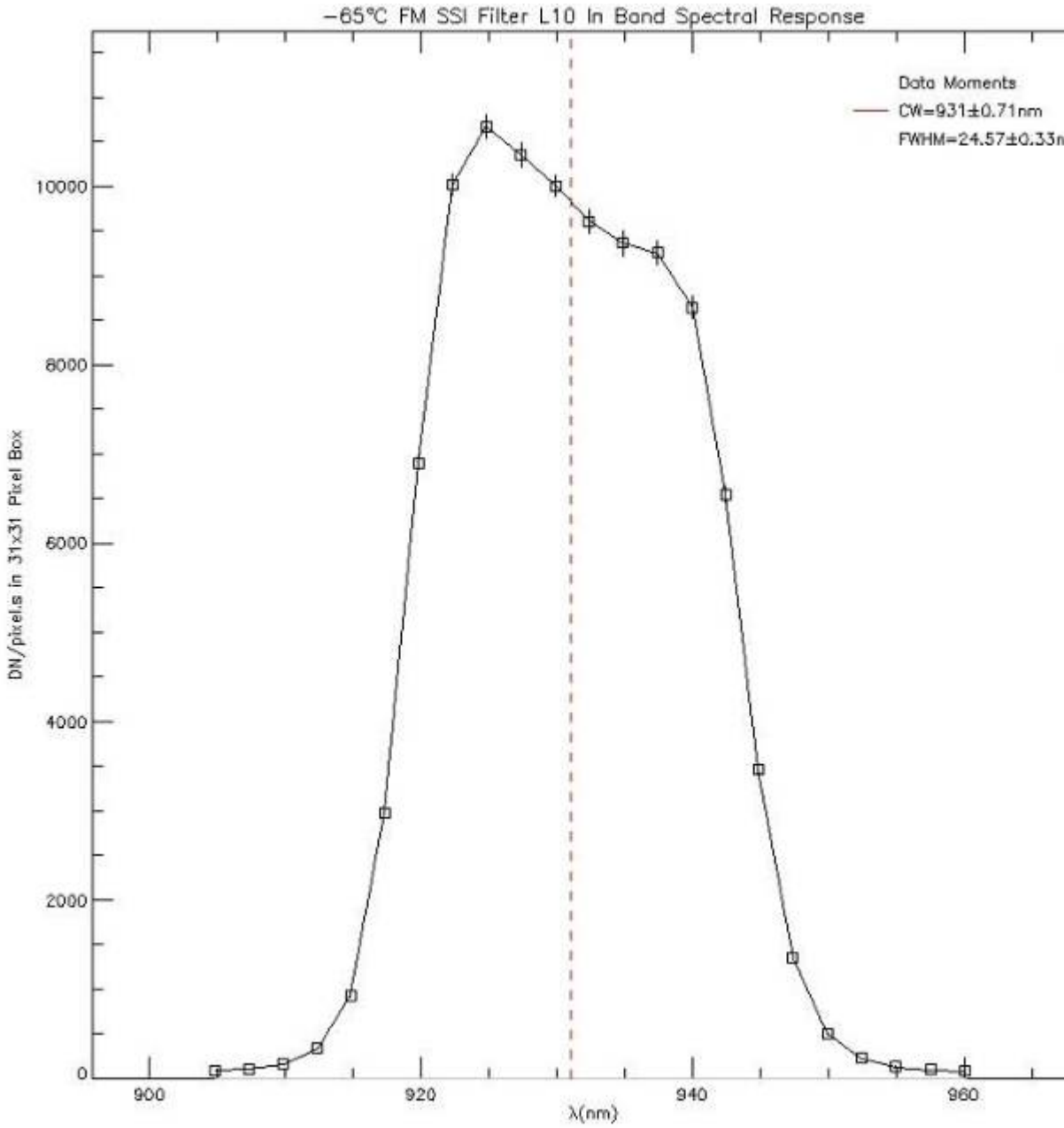

Figure H - 22: L10 -65°C Filter Profile

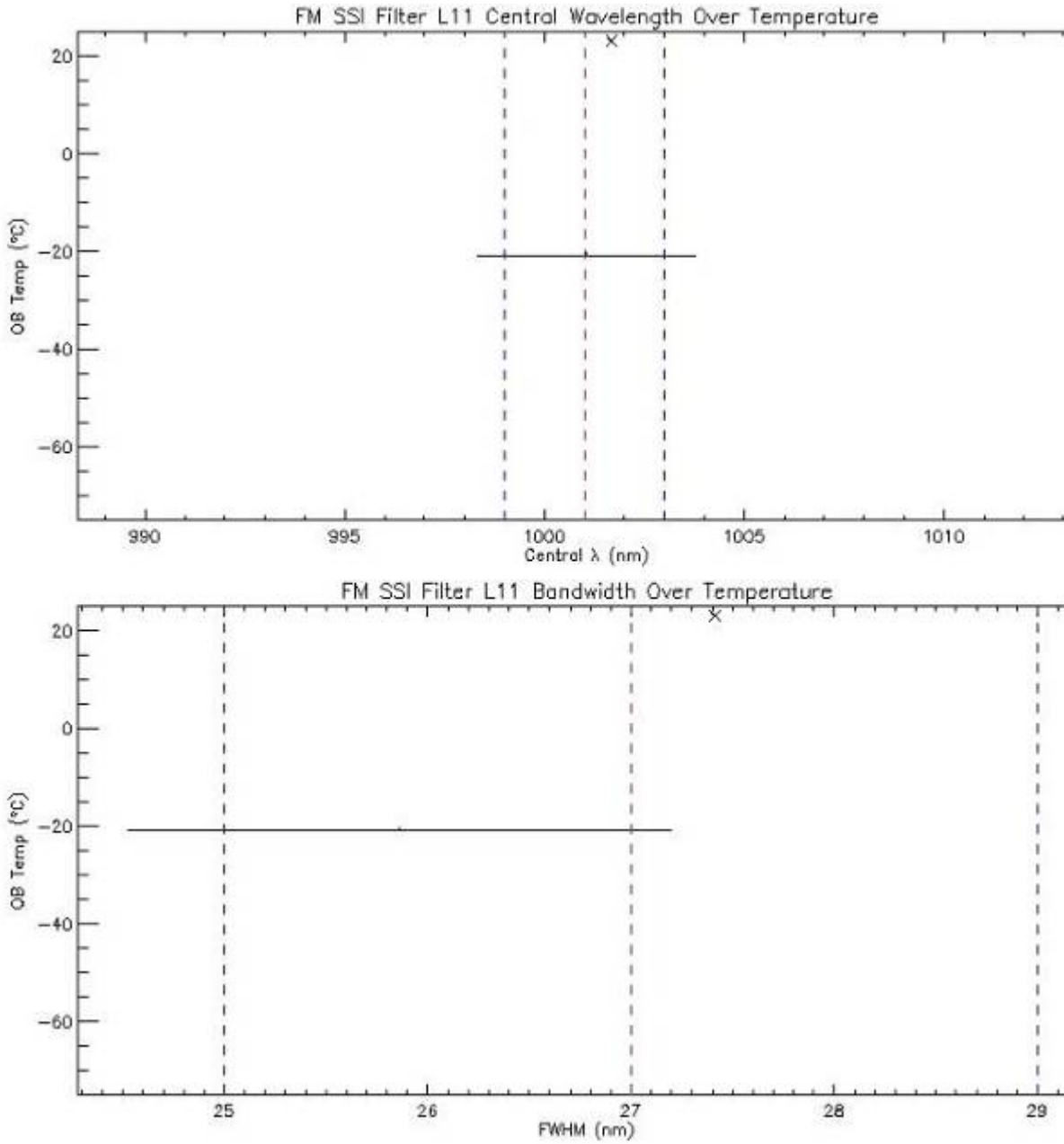

Figure H - 23: L11 Central Wavelength and Bandwidth Over Temperature

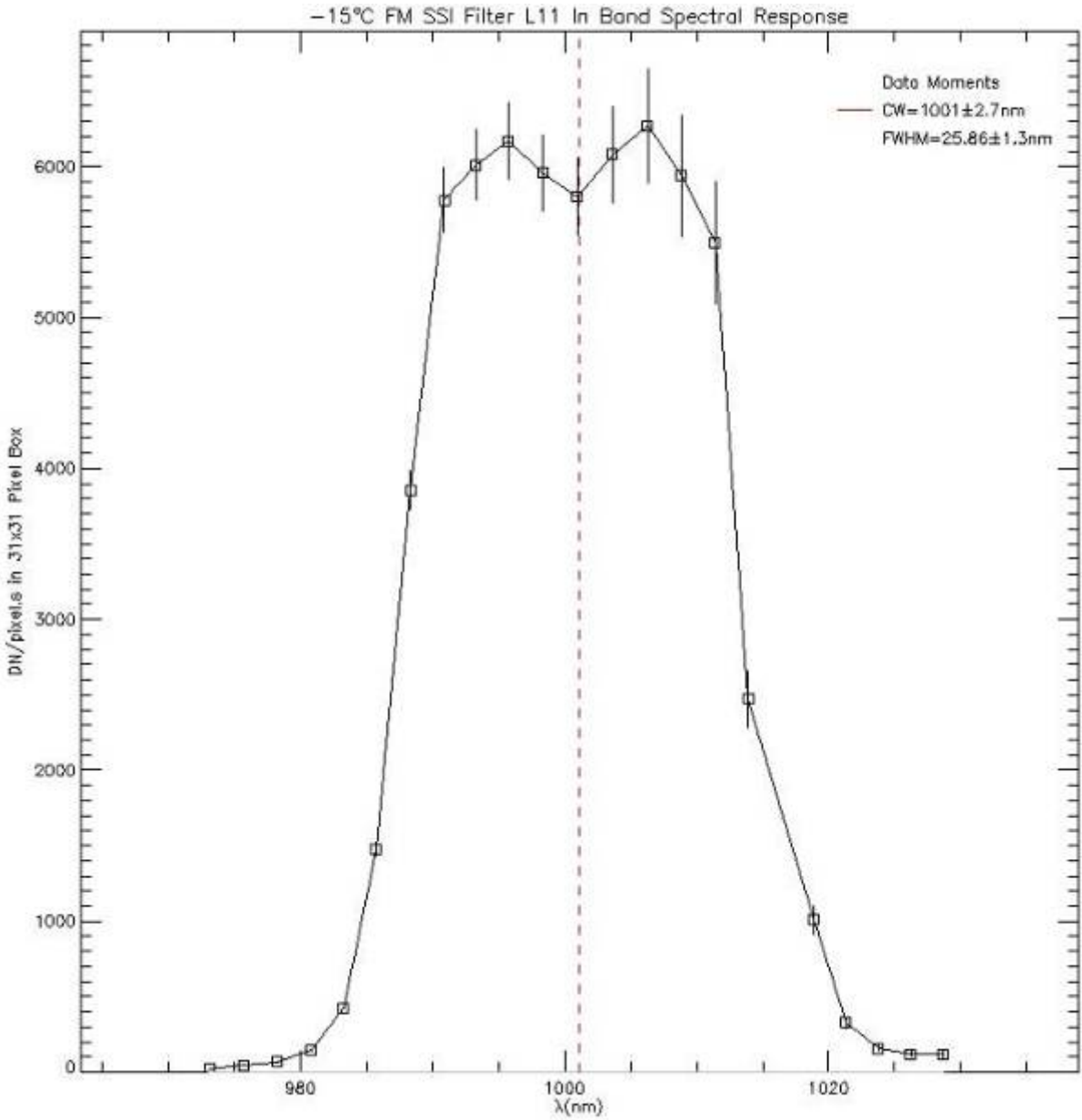

Figure H - 24: L11 -15°C Filter Profile

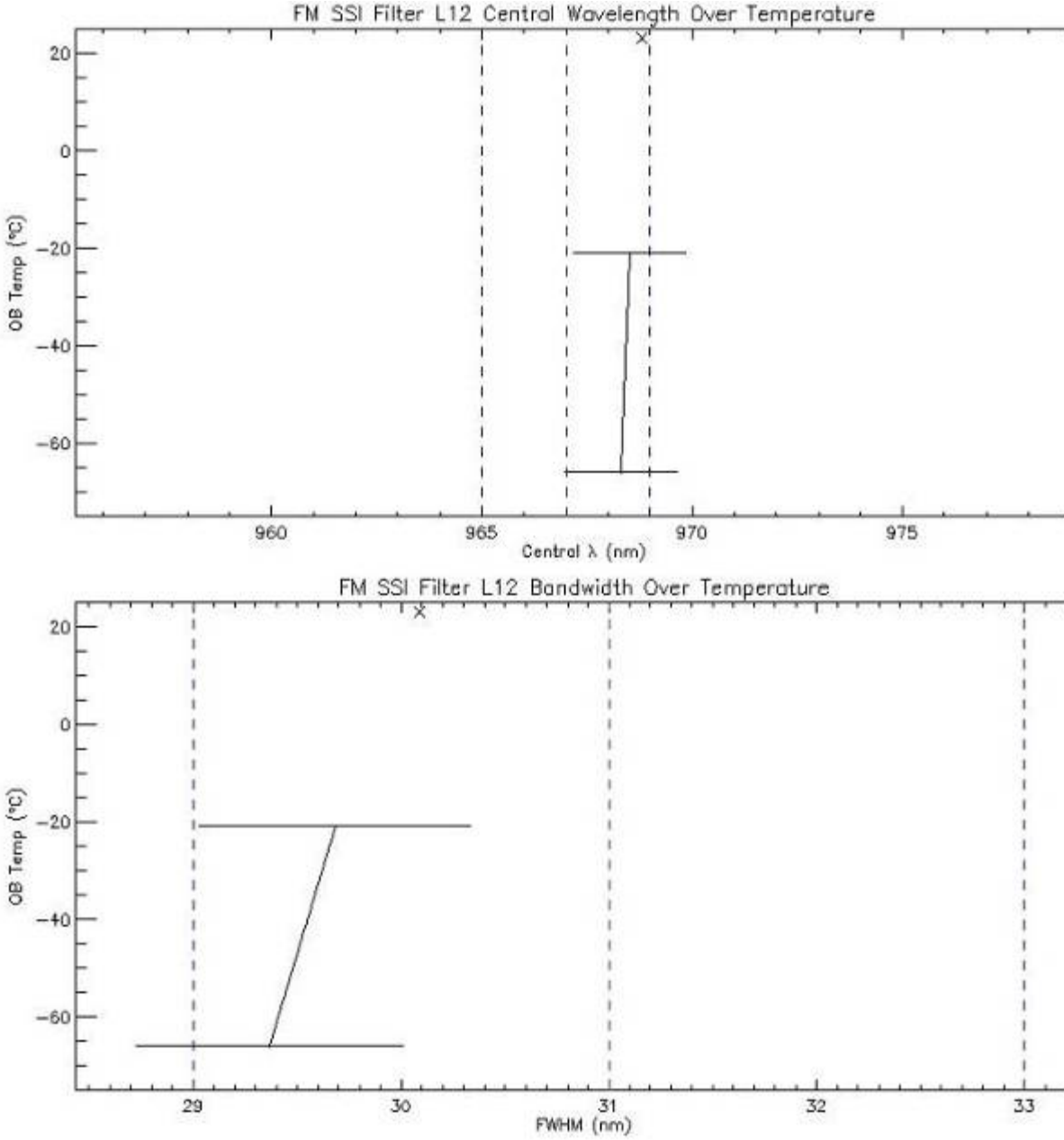

Figure H - 25: L12 Central Wavelength and Bandwidth Over Temperature

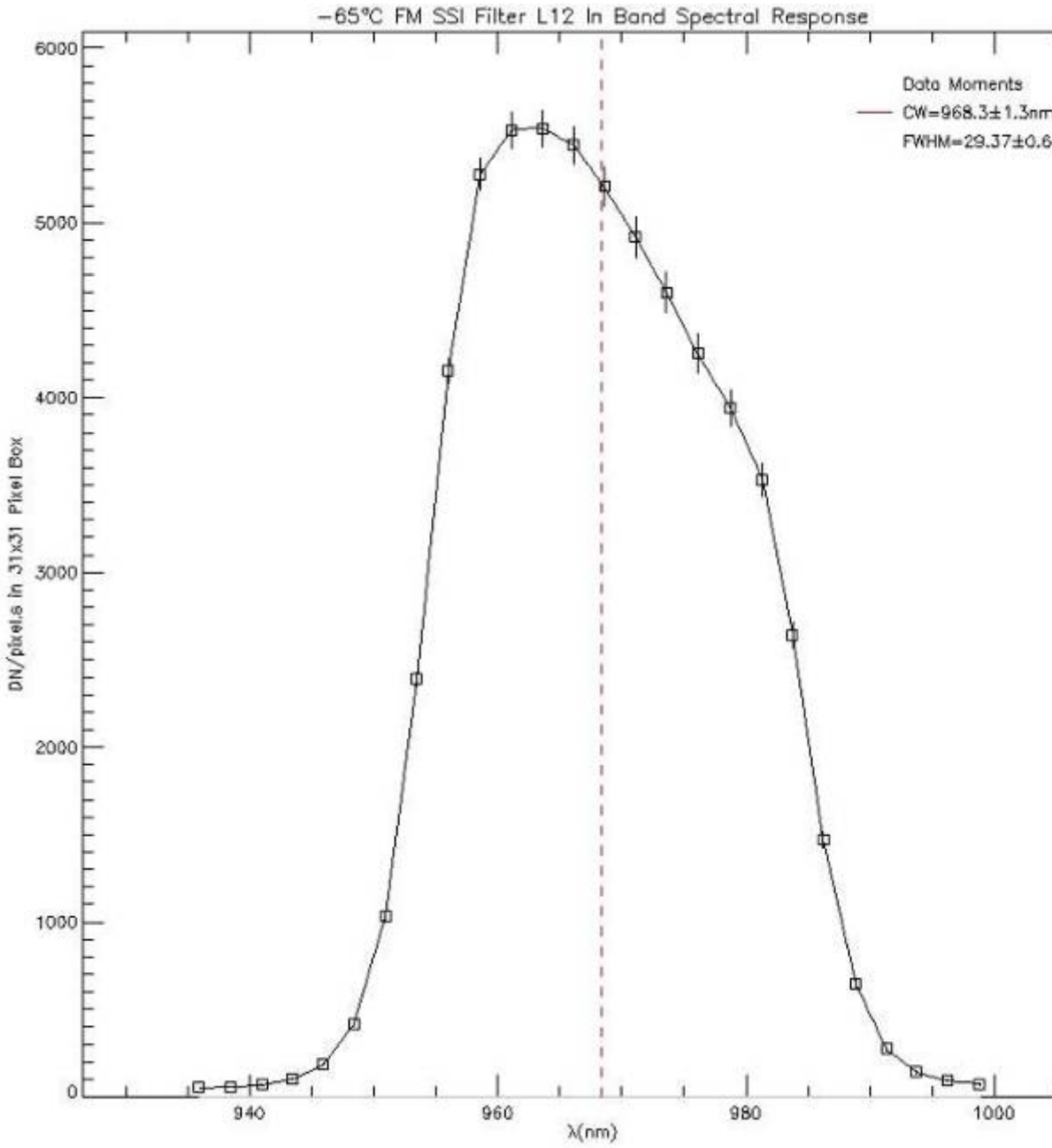

Figure H - 26: L12 -65°C Filter Profile

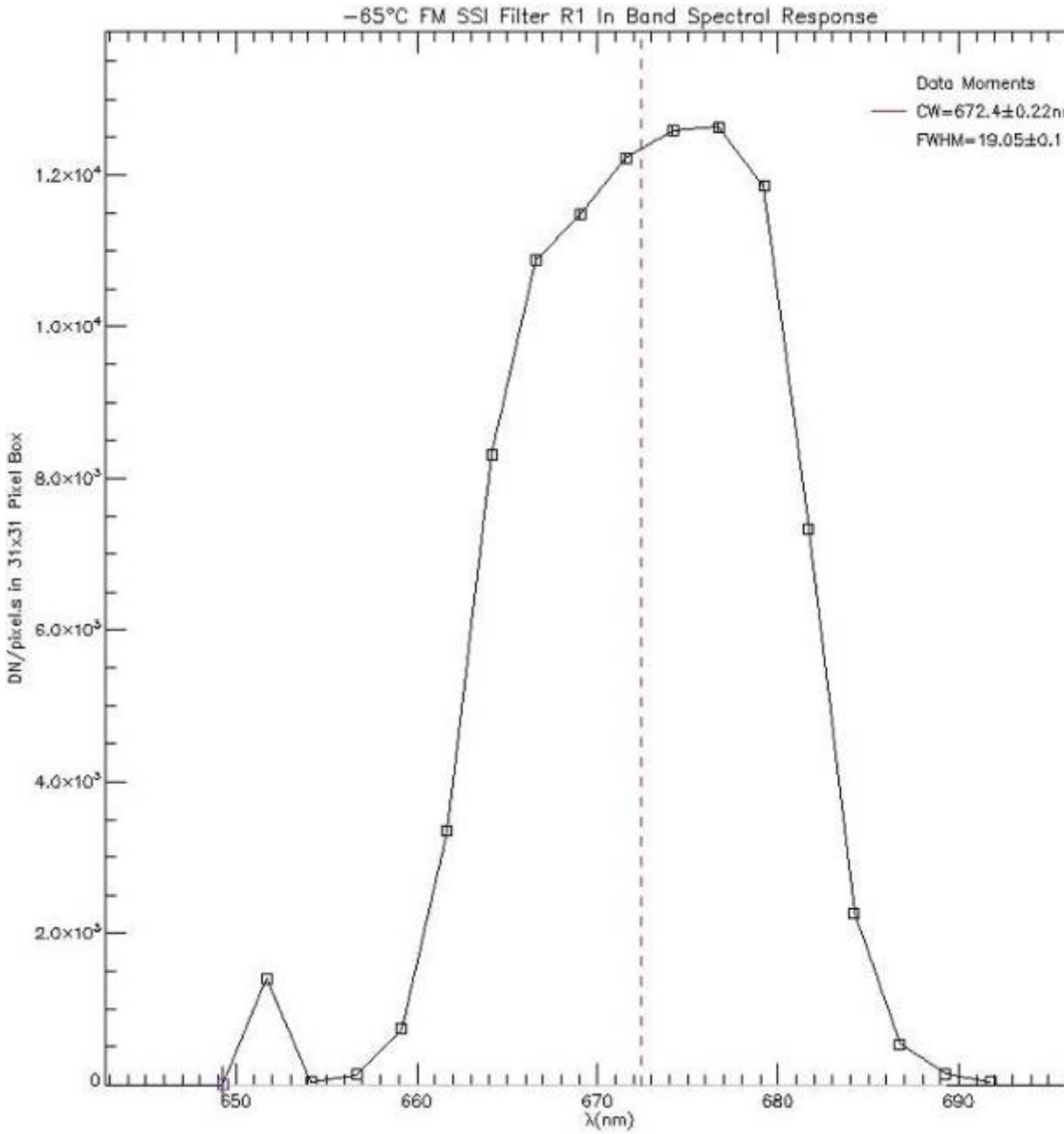

Figure H - 27: R1 -65°C Filter Profile

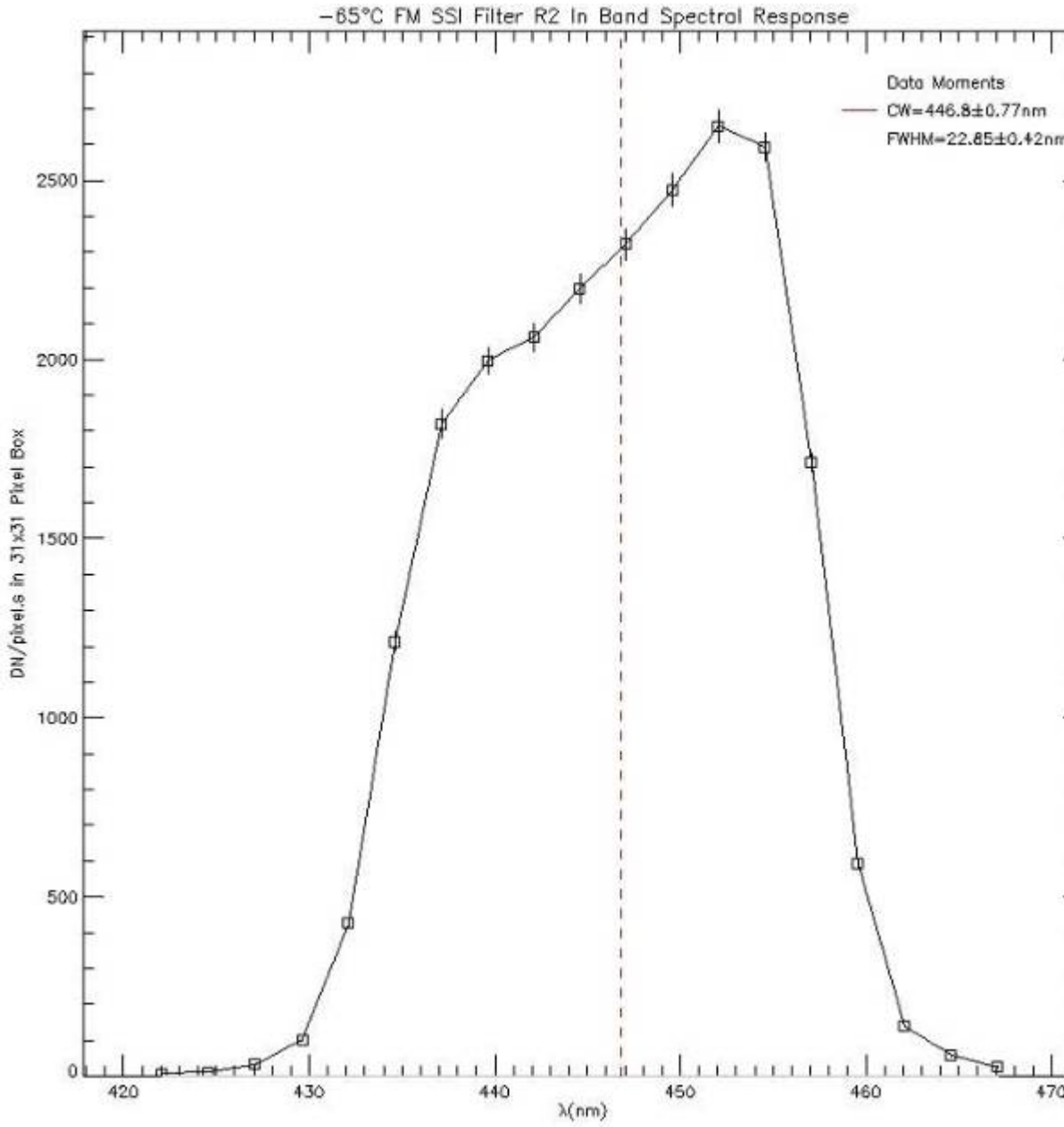

Figure H - 28: R2 -65°C Filter Profile

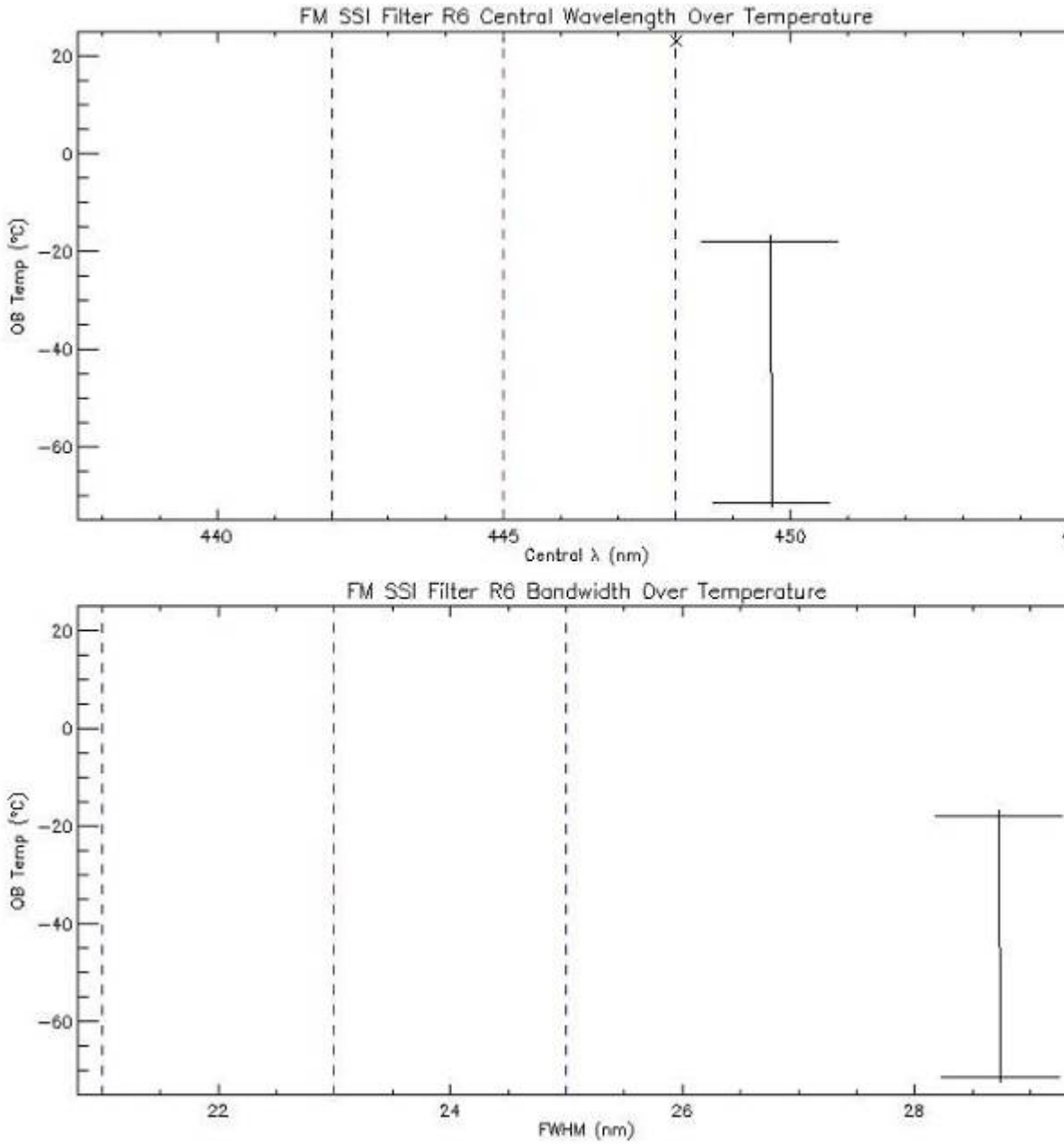

Figure H - 29: R6 Central Wavelength and Bandwidth Over Temperature

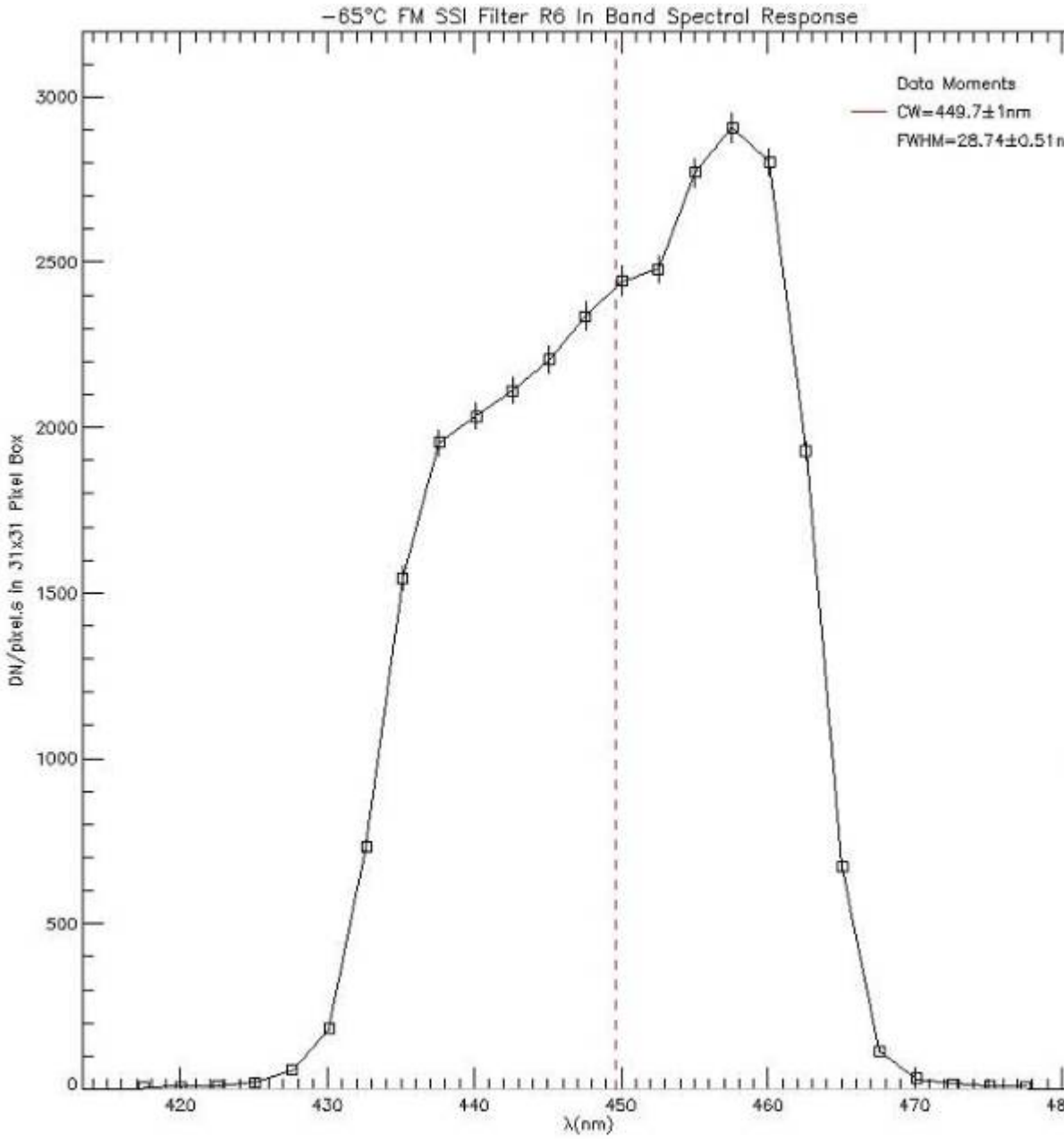

Figure H - 30: R6 -65°C Filter Profile

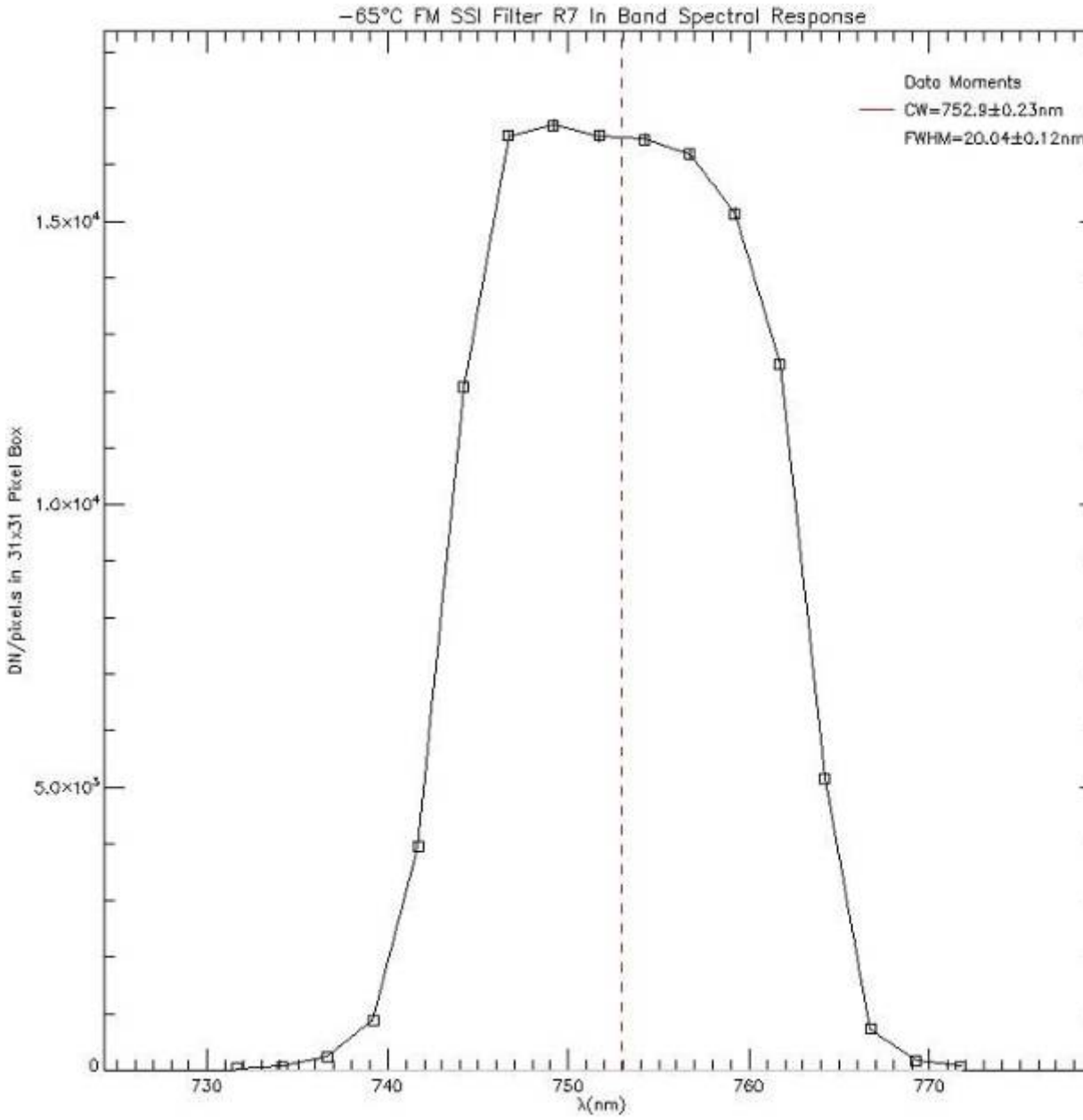

Figure H - 31: R7 -65°C Filter Profile

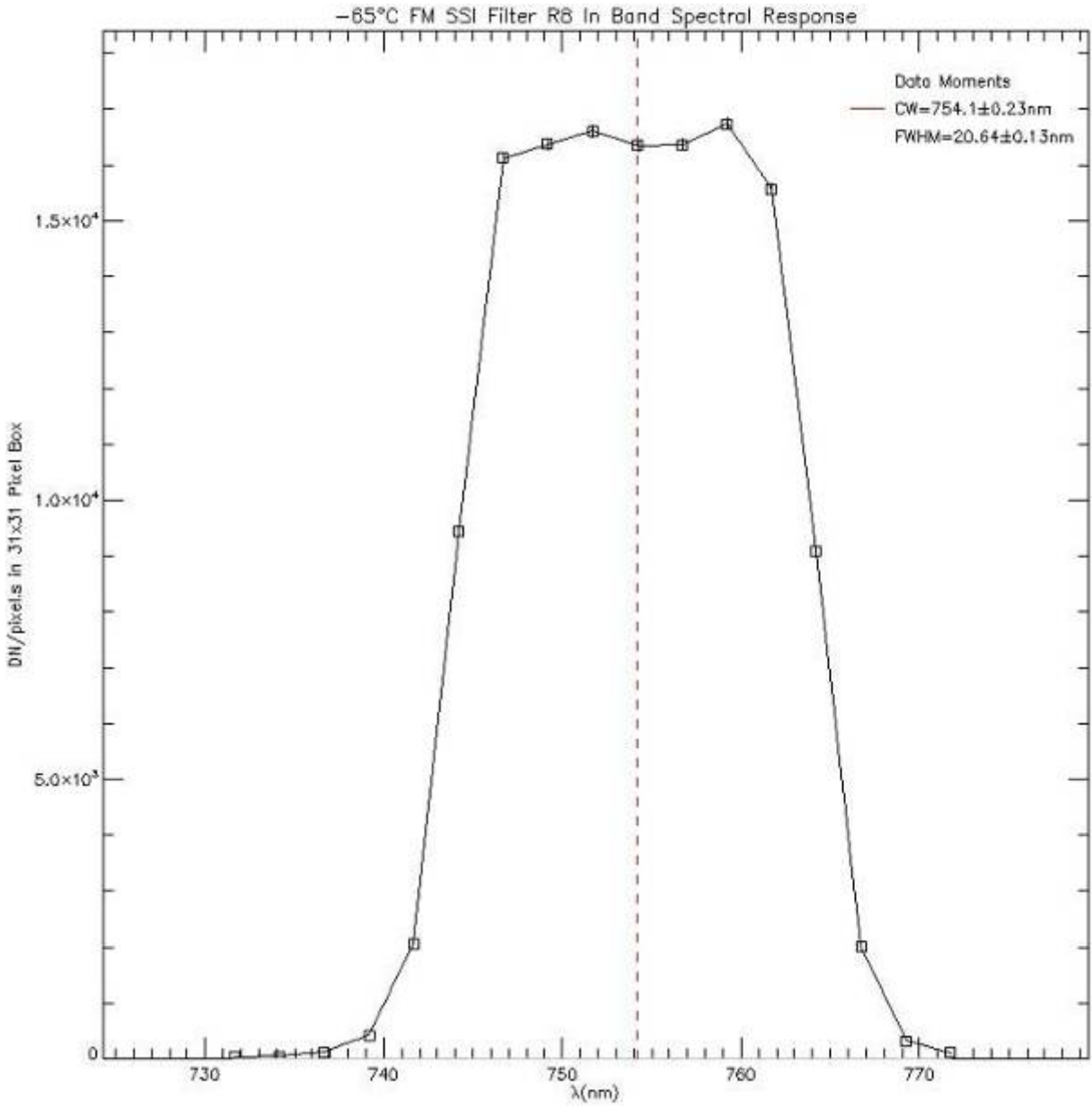

Figure H - 32: R8 -65°C Filter Profile

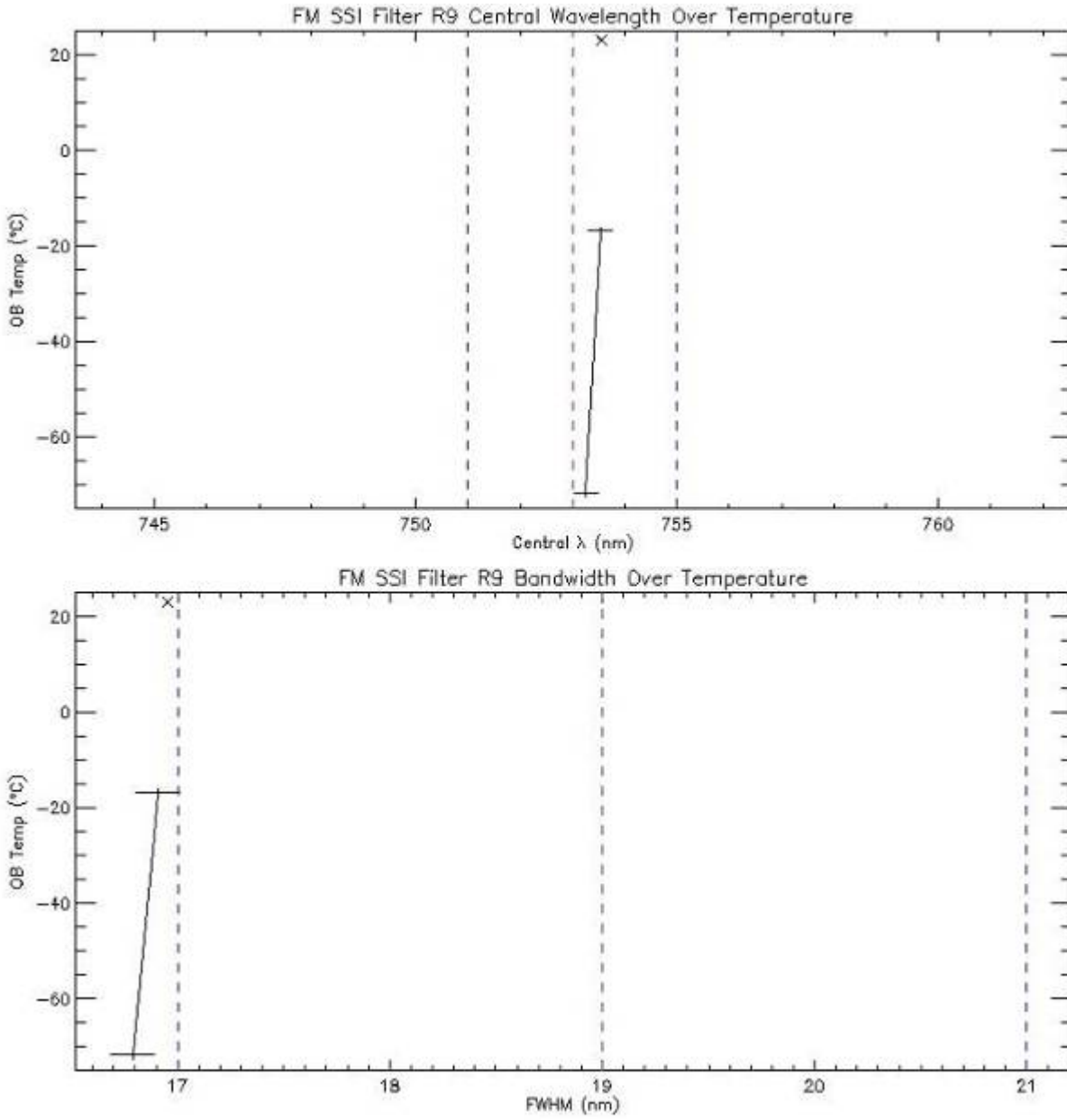

Figure H - 33: R9 Central Wavelength and Bandwidth Over Temperature

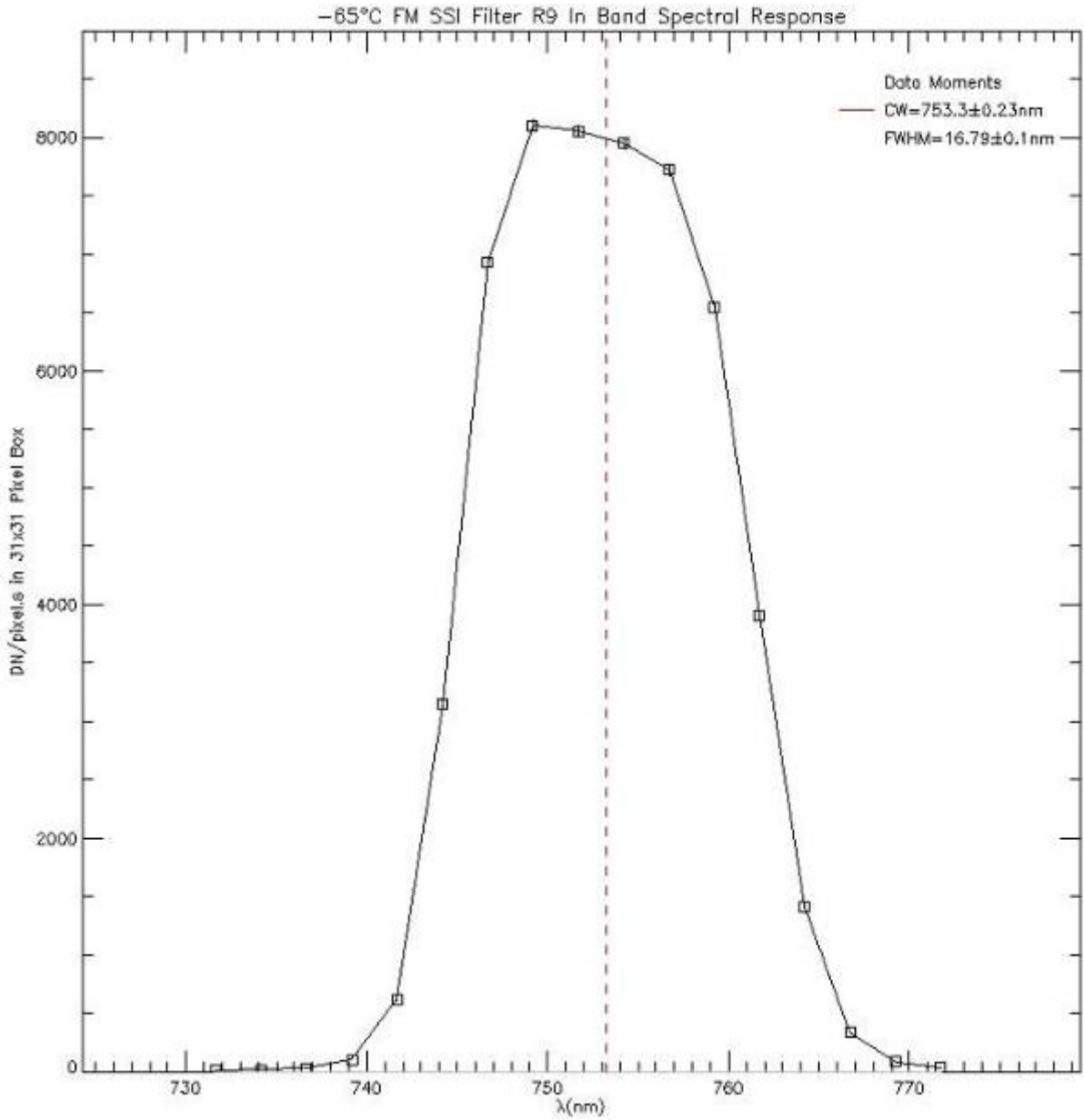

Figure H - 34: R9 -65°C Filter Profile

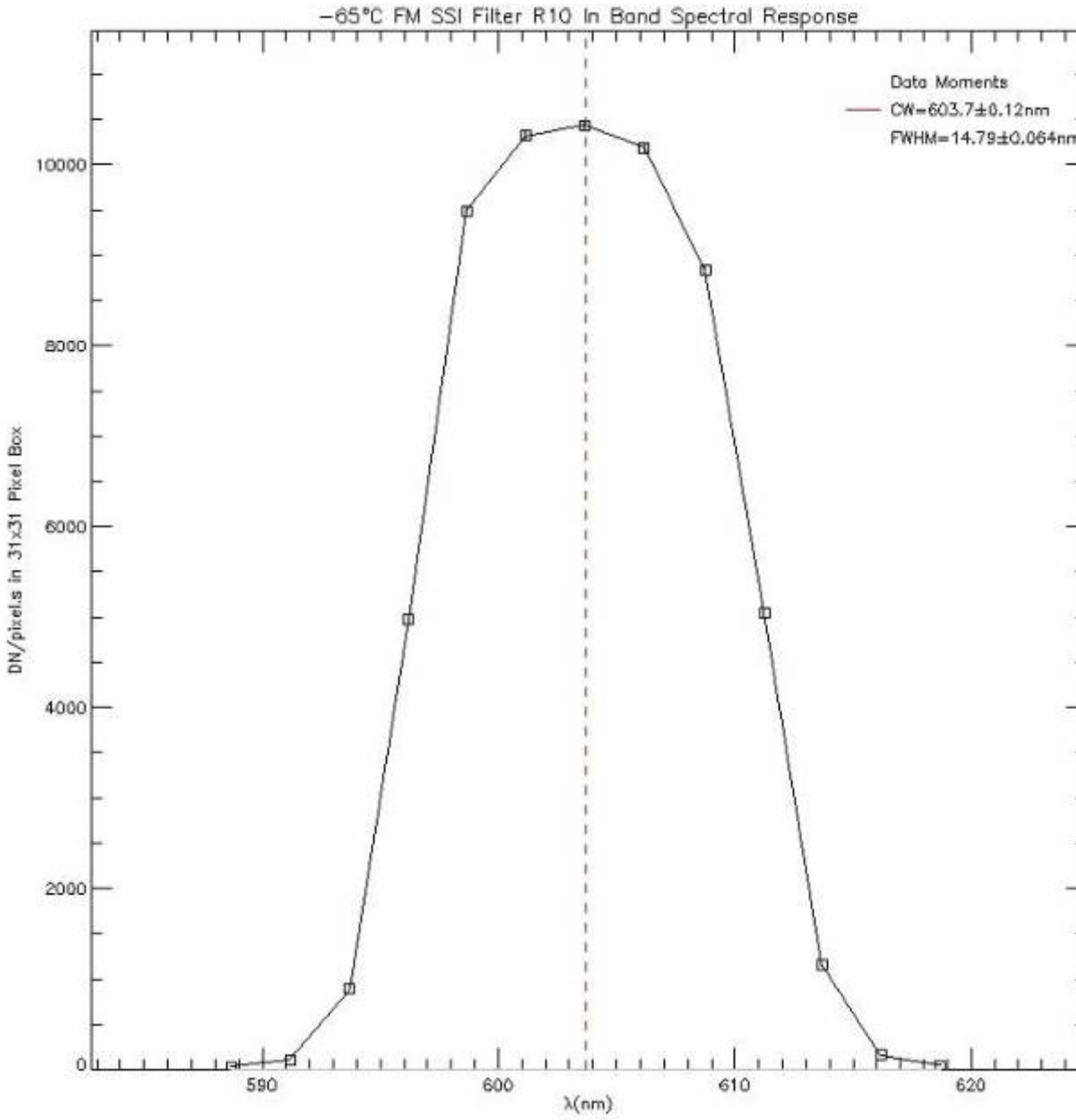

Figure H - 35: R10 -65°C Filter Profile

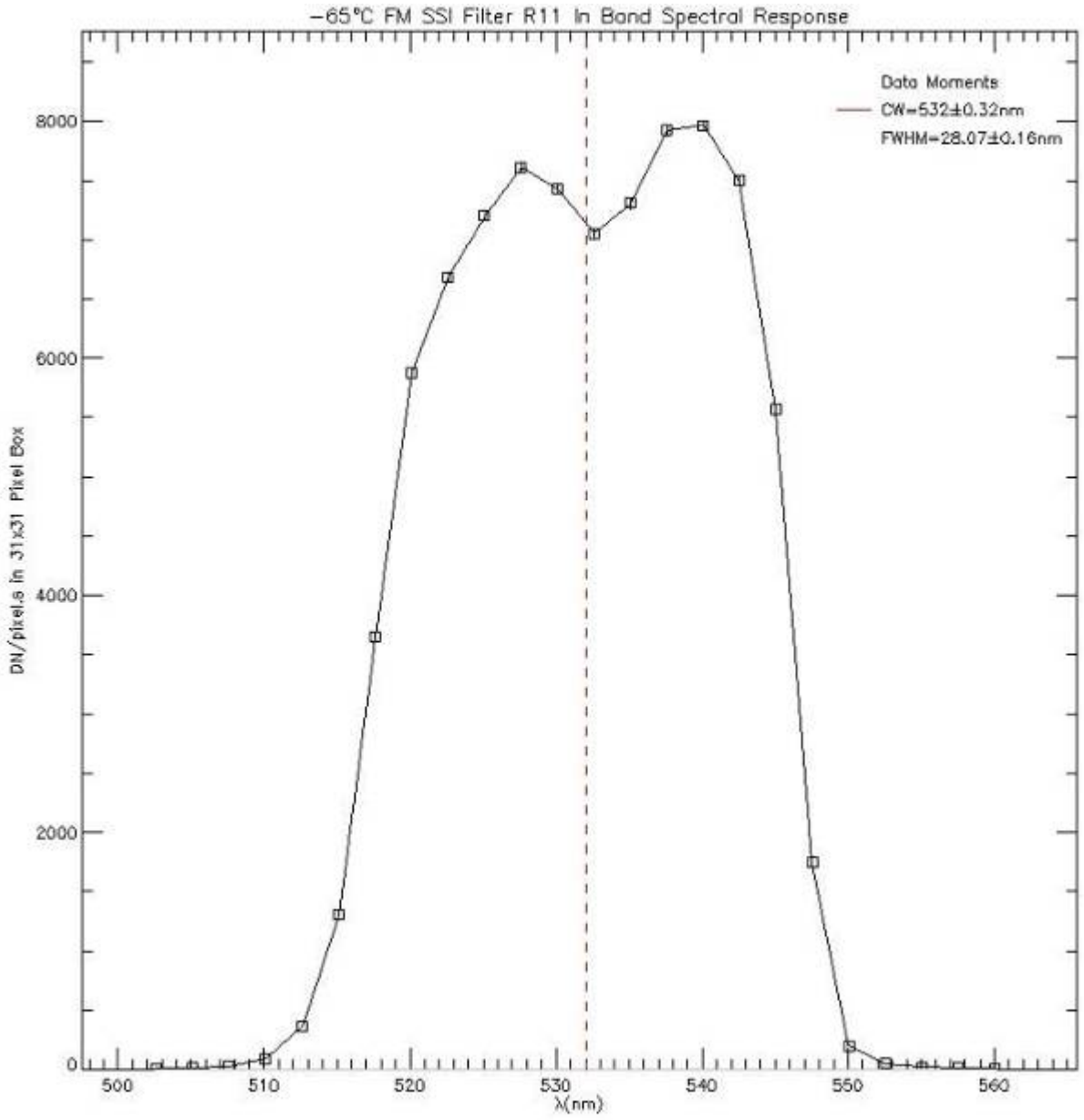

Figure H - 36: R11 -65°C Filter Profile

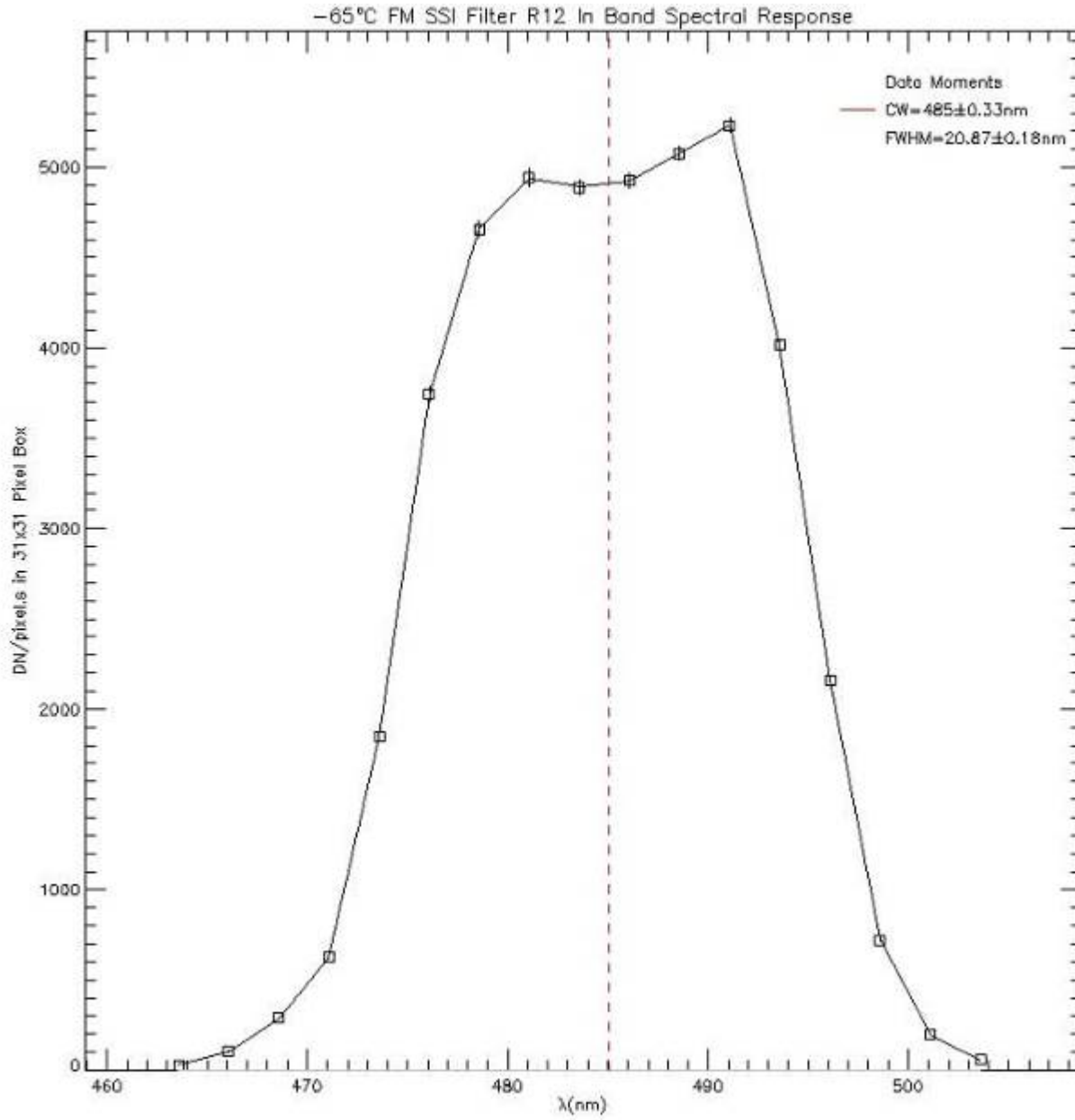

Figure H - 37: R12 -65°C Filter Profile

H.5 Filter Stop Band Test Setup and Data Acquisition.

The test setup was identical to the In-Band setup described above (H.1 Filter In-Band Test Setup and Data Acquisition). Data was taken between 6/24/2006 and 6/25/2006 at a nominal temperature of -65°C (Table H - 26: Complete List of Out of Band Filter Profile Measurement Collected in Thermal Vacuum Temperature, including Bad Data-sets
):

Date	Start Time	End Time	Filter	Out of Band/ Extras	Notes	Nominal Temp
24-Jun	8:02	8:14	L1	OutB	Bad Names	-65
	9:00	10:57	L1	OutB		-65
	11:06	11:43	L2	OutB		-65
	11:50	12:30	L3	OutB		-65
	12:37	13:14	L4	OutB		-65
	13:21	13:58	L5	OutB		-65
	14:05	14:52	L6	OutB		-65
	15:00	15:46	L7	OutB		-65
	15:52	16:29	L8	OutB		-65
	16:35	17:14	L9	OutB		-65
	17:20	18:07	L10	OutB		-65
	18:12	18:50	L11	OutB		-65
	19:07	19:45	L12	OutB		-65
	19:51	20:11	L7	EOutB	Extras	-65
	21:13	21:51	R1	OutB		-65
	21:58	22:38	R2	OutB		-65
	22:44	23:25	R3	OutB		-65
25-Jun	23:32	0:10	R4	OutB		-65
	0:16	0:55	R5	OutB		-65
	1:00	1:39	R6	OutB		-65
	1:45	2:23	R7	OutB		-65
	2:29	3:07	R8	OutB		-65
	3:13	4:04	R9	OutB		-65
	4:11	5:05	R10	OutB		-65
	5:12	5:57	R11	OutB		-65
	8:36	9:50	R12	OutB		-65
	9:55	10:15	R1	InB		-65
	10:31	11:30	R2	InB		-65
	11:16	11:26			EMSSI R2	
	11:40		R2	FPOutB	UV Redo	-65
	11:50		R6	FPOutB	UV Redo	-65
	12:02		R10	FPOutB	UV Redo	-65
	12:14		R11	FPOutB	UV Redo	-65
	12:29		R12	FPOutB	UV Redo	-65

Table H - 26: Complete List of Out of Band Filter Profile Measurement Collected in Thermal Vacuum Temperature, including Bad Data-sets

The monochrometer pre-filter was varied as necessary and the monochrometer slit-width kept at 3mm, except during the UV redo where it was set at 0.68mm. The slit width controlled the bandwidth of the output light, but a narrower slit width also reduced the output light intensity. The pre-filter reduced the possibility of aliasing at unwanted wavelengths.

H.6 Filter Stop Band Analysis Procedure:

The analysis performed was almost identical to that for the in-band measurements (H.2 In Band Analysis Procedure). The primary differences being as follows:

1) The central spots were not fitted; the wide range of input wavelengths appeared to lead to a non-linear spot motion on the Spectralon as wavelength varied. Instead the operator was asked to click in the center of the spot. In the event no spot was visible, the mean location of they located spots was used.
2) In order to directly compare the Out of Band with the In Band response, a correction had to be made for the slit-width variation between the two measurements. A first order approximation of the ratio of the slit-widths was used.
3) The highest and lowest wavelengths tested were outside the range of the spectrometer used to calibrate the monochrometer. For these two points the monochrometer efficiency was extrapolated and constrained to at least 75% of the lowest/highest wavelength efficiency actually measured by the spectrometer.
4) In the event that the spot was saturated (wavelength used was nominally in-band, not out of band) the point was discarded because this would not lead to a useful data point.

The main IDL analysis code is named FMSSI_OutBand_Filters_lem, and utilizes the slightly updated dark/bias model outlined in this report.

H.7 Filter Stop Band Results

The out of band rejection properties of all FM SSI filters were measured between 370nm and 1100nm. The ratio of integrated normalized out of band response to integrated normalized in band response to a nominal Martian spectrum was calculated for each (Table H - 27) producing values of <1:10 for all Solar filters; <1:100 for all water vapor filters; <1:40 for the diopters and <1:10 for 12 of 13 spectral filters, the final one is to be determined via a more detailed analysis.

Filter	Response Ratio	Filter Type
L1	.025	Surface Stereo
L2	.00586	Surface Stereo
L3	.0612	Atmospheric Dust
L4	.0181	Atmospheric Dust/Water Vapor Continuum
L5	.00851	Atmospheric Dust/Water Vapor Continuum
L6	.012	Surface
L7	TBD	Surface
L8	.0101	Surface
L9	.0129	Surface

L10	.0138	Surface
L11	.00991	Surface
L12	.0239	Surface
R1	.0114	Surface Stereo
R2	.00441	Surface Stereo
R3	.00593	Atmospheric Dust
R4	.00279	Water Vapor
R5	.00531	Water Vapor
R6	.00265	Surface Imaging Diopter
R7	.0269	Surface Imaging Diopter
R8	.0287	Surface Polarization
R9	.0286	Surface
R10	.0416	Surface
R11	.00169	Surface
R12	.00379	Surface

Table H - 27: FM SSI Out of Band Rejection Results Summary

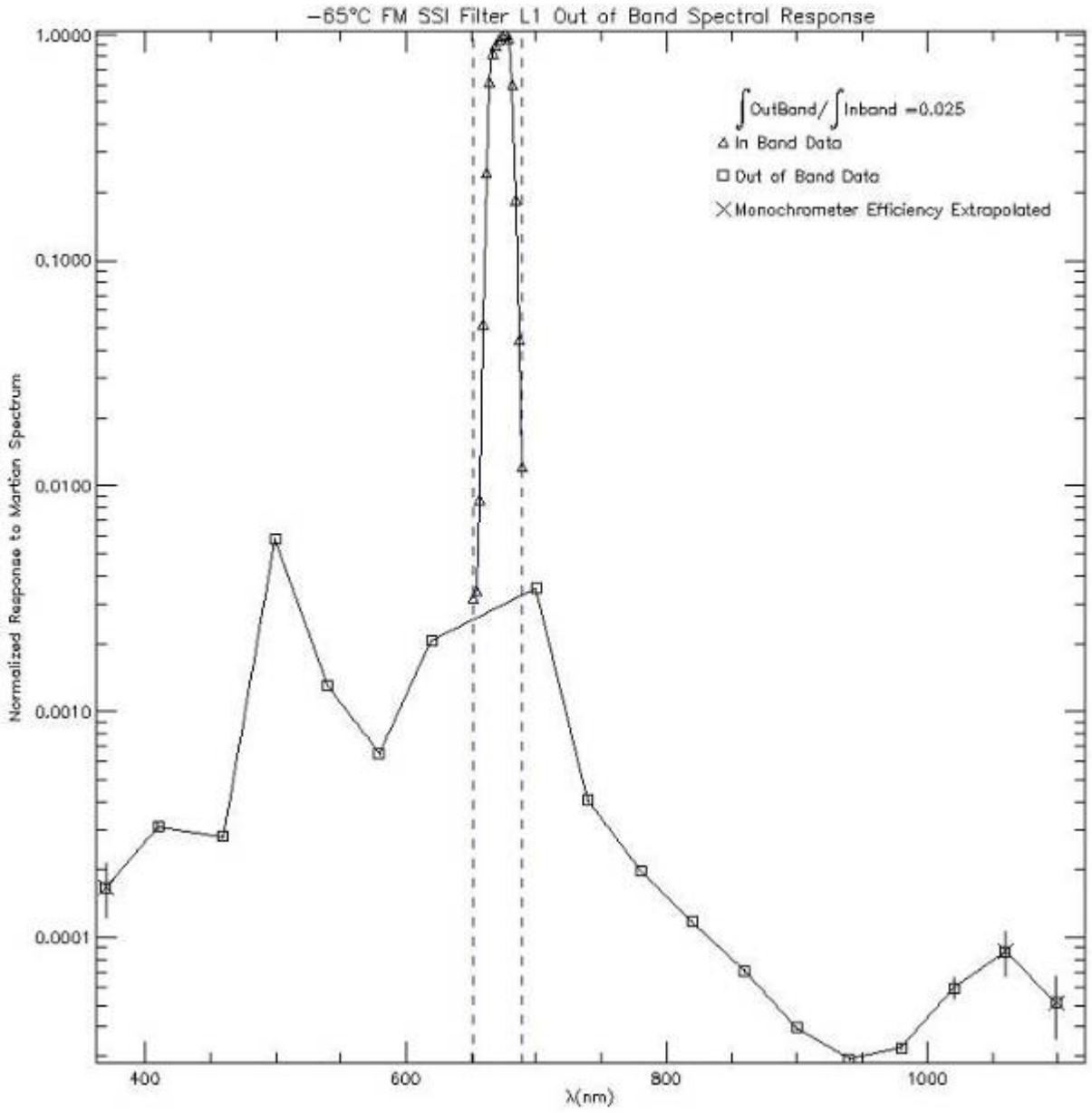

Figure H - 38: FM SSI L1 Stop Band at -65°C

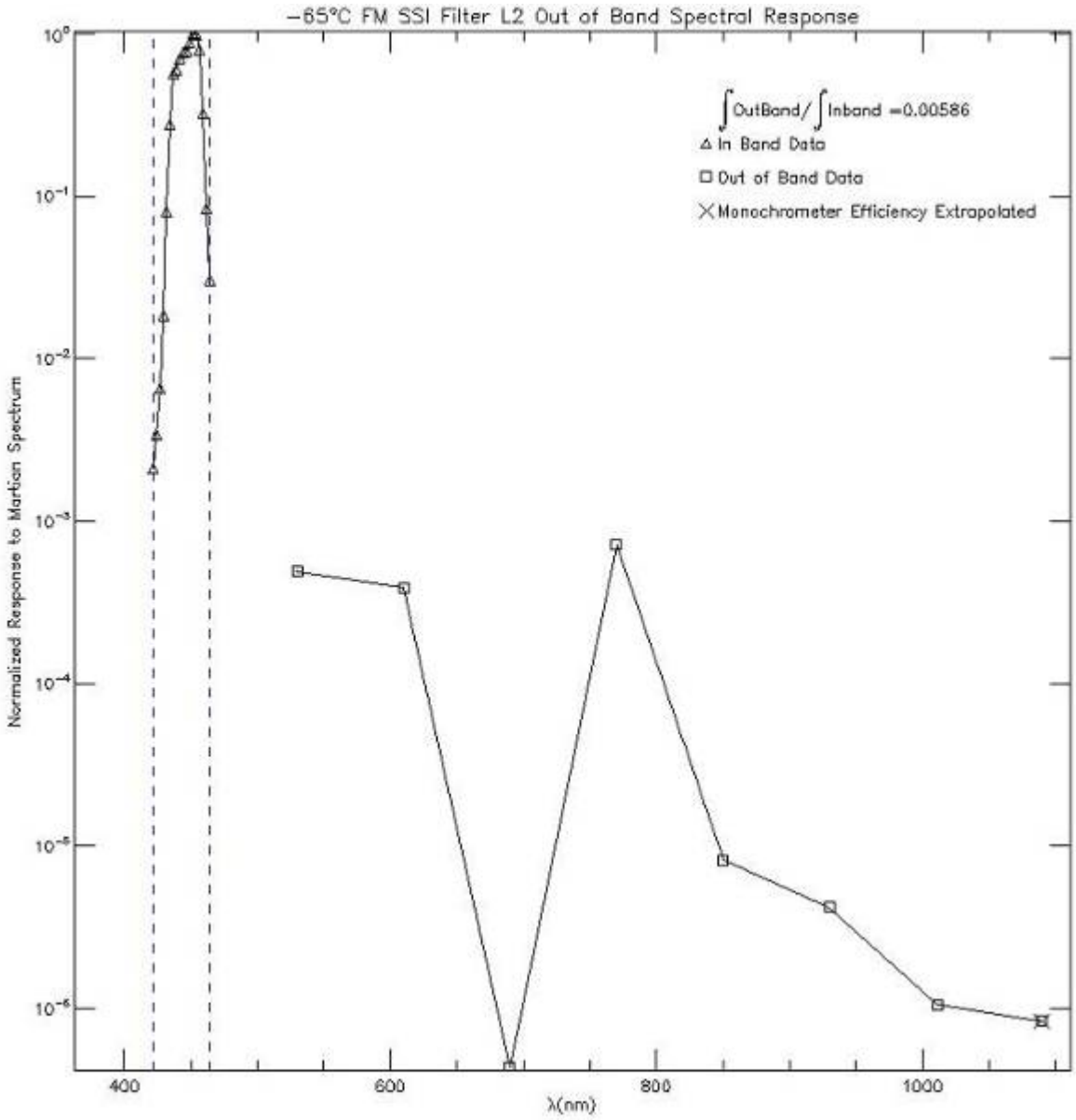

Figure H - 39: FM SSI L2 Stop Band at -65°C
The low wavelength point was not included in the out of band integration due to a lack of a nearest neighbor and is therefore not shown.

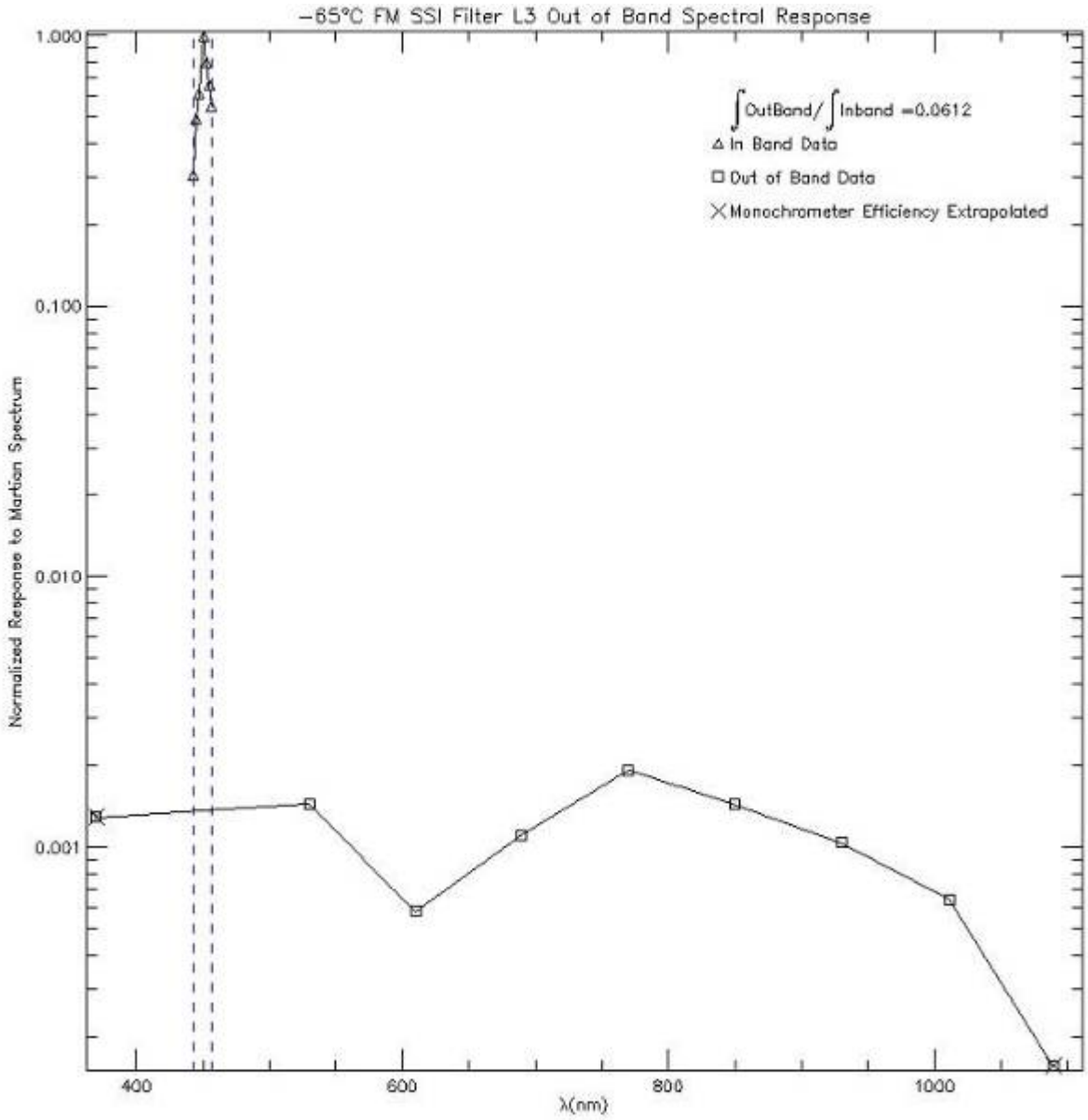

Figure H - 40: FM SSI L3 Stop Band at -65°C

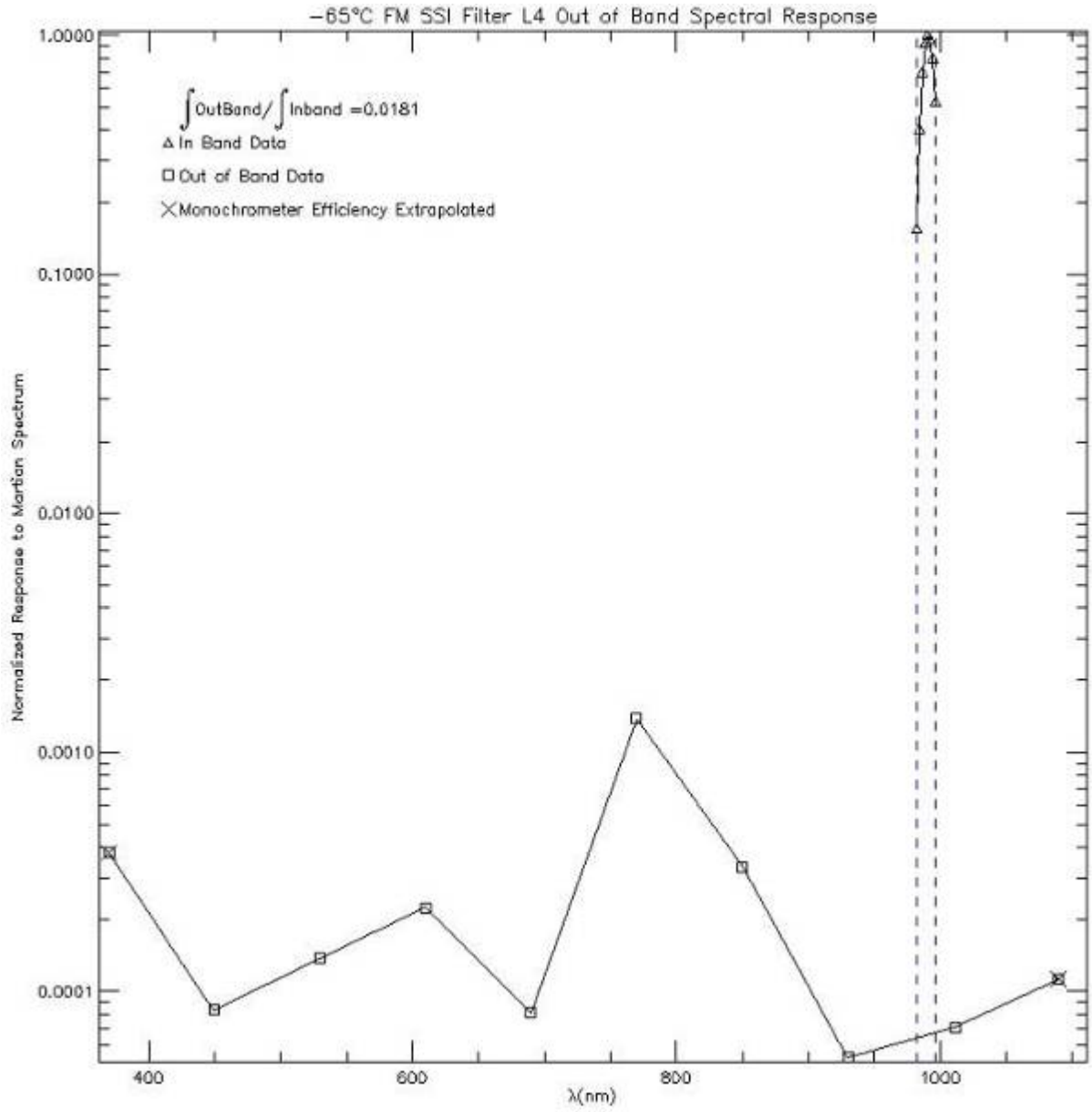

Figure H - 41: FM SSI L4 Stop Band at -65°C

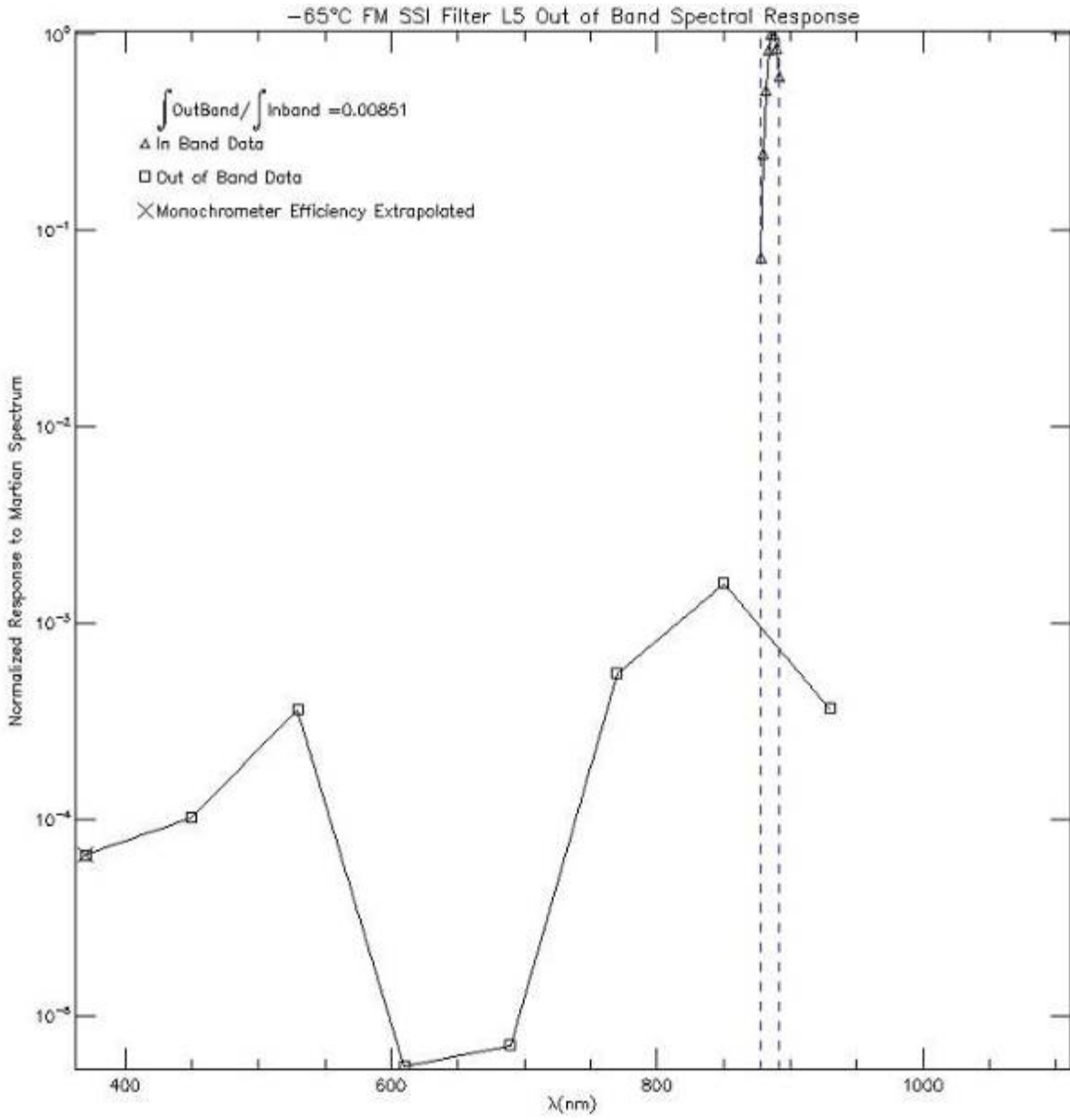

Figure H - 42: FM SSI L5 Stop Band at -65°C

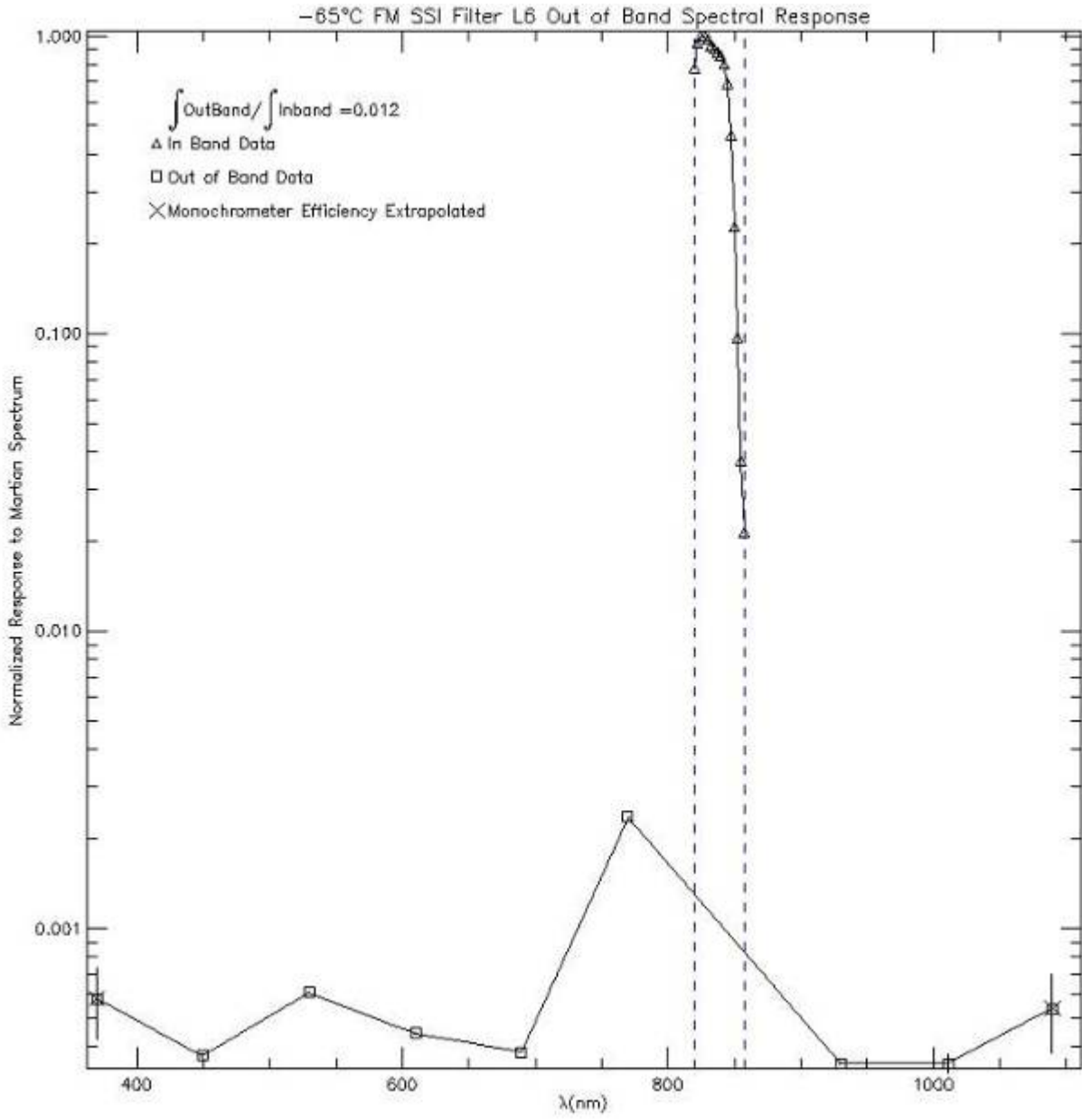

Figure H - 43: FM SSI L6 Stop Band at -65°C

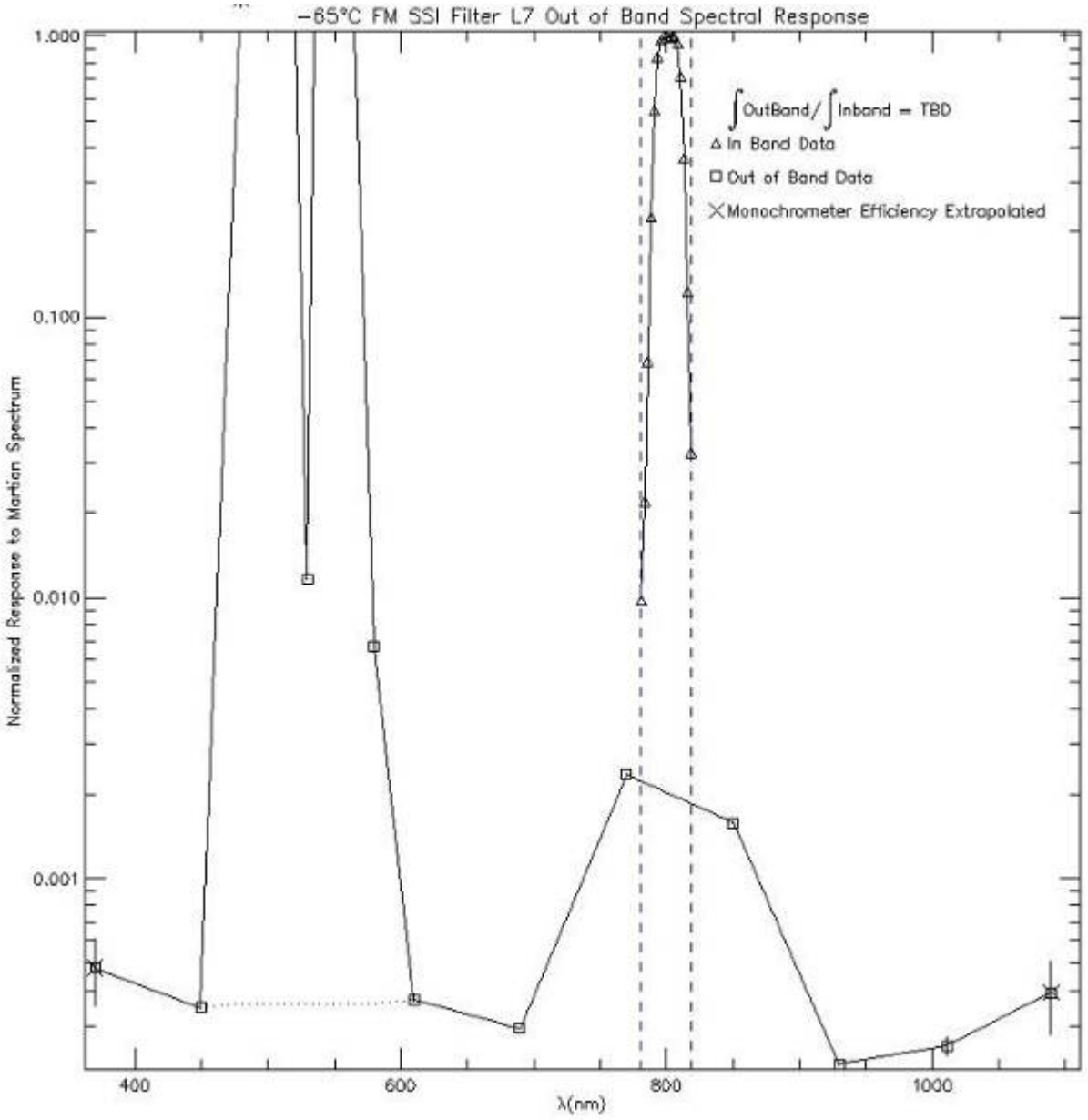

Figure H - 44: FM SSI L7 Stop Band at -65°C

It should be noted that the massive green response seen here at about 500nm is thought to come from a red component produced at certain select wavelengths by the monochrometer. This will be addressed and resolved in full in the next iteration calibration report. The expected level is denoted by the dashed line.

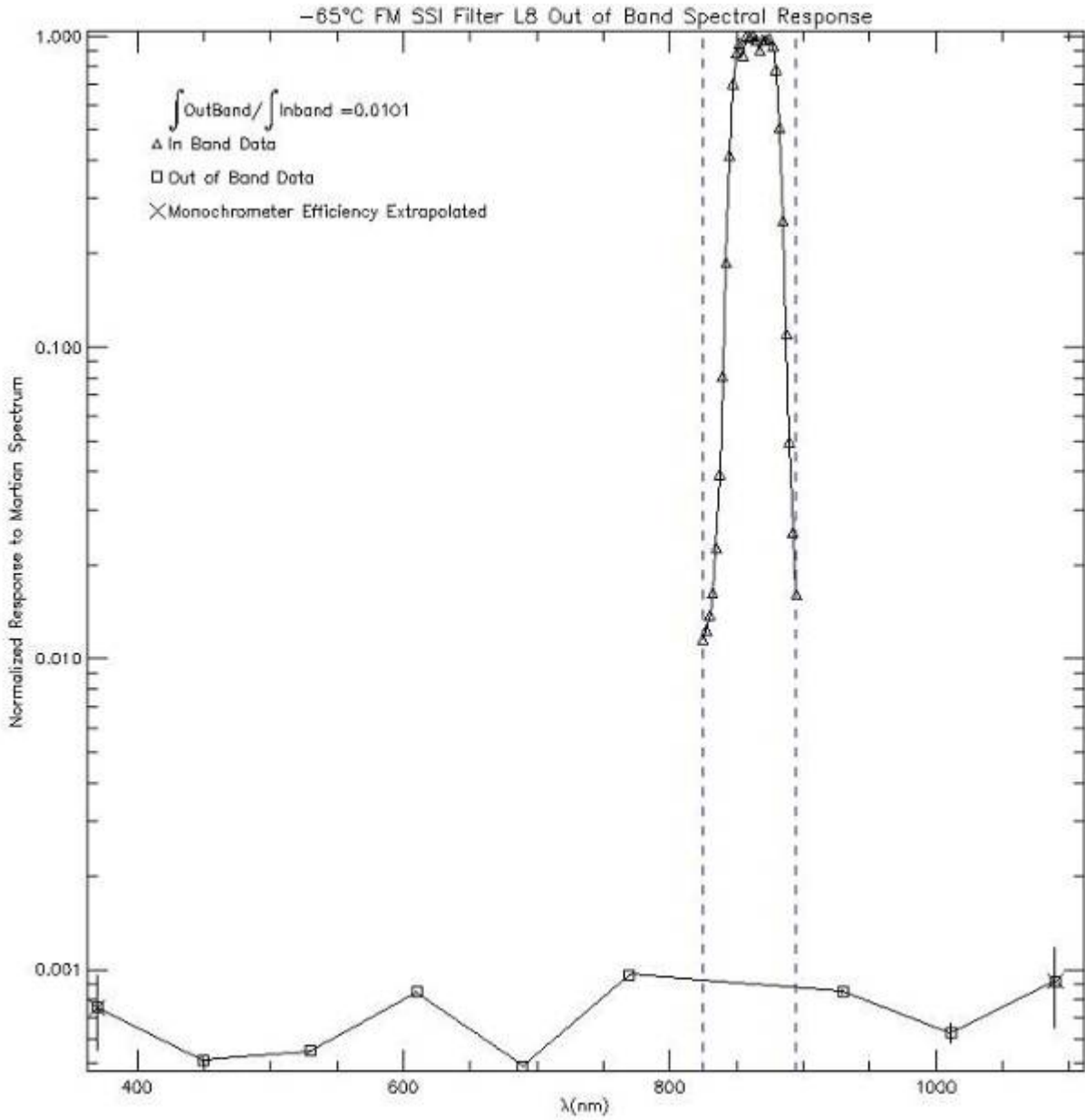

Figure H - 45: FM SSI L8 Stop Band at -65°C

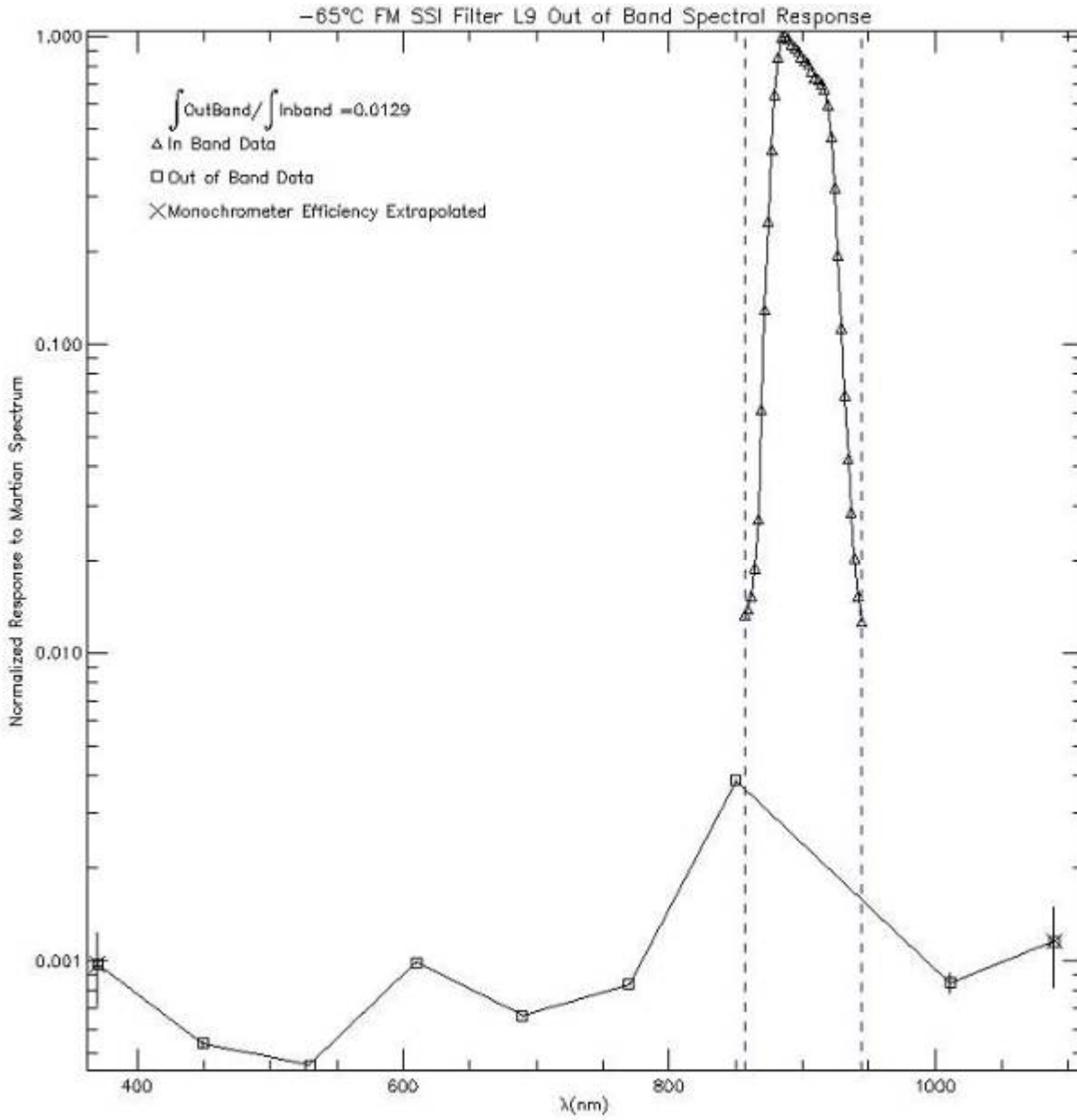

Figure H - 46: FM SSI L9 Stop Band at -65°C

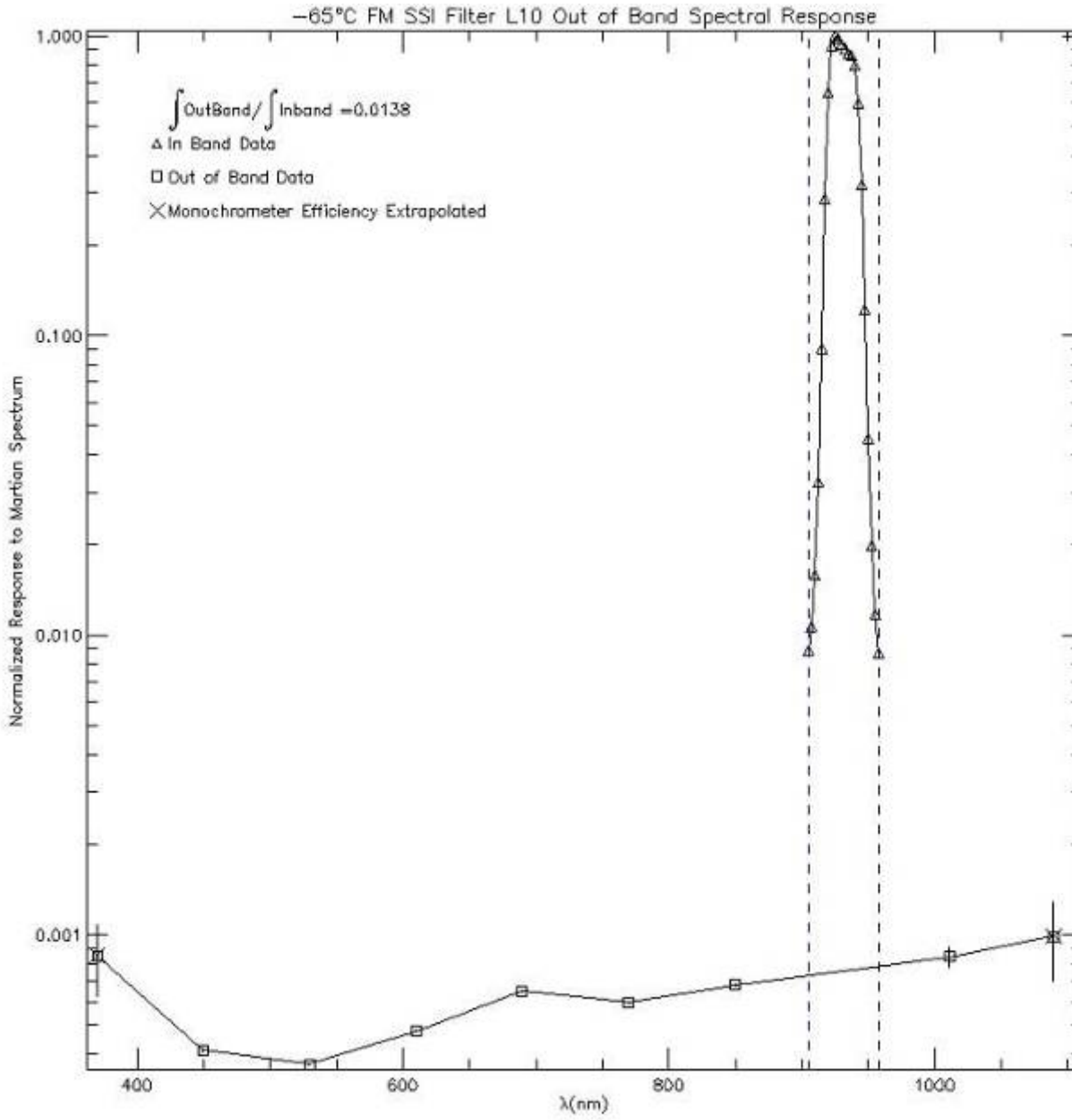

Figure H - 47: FM SSI L10 Stop Band at -65°C

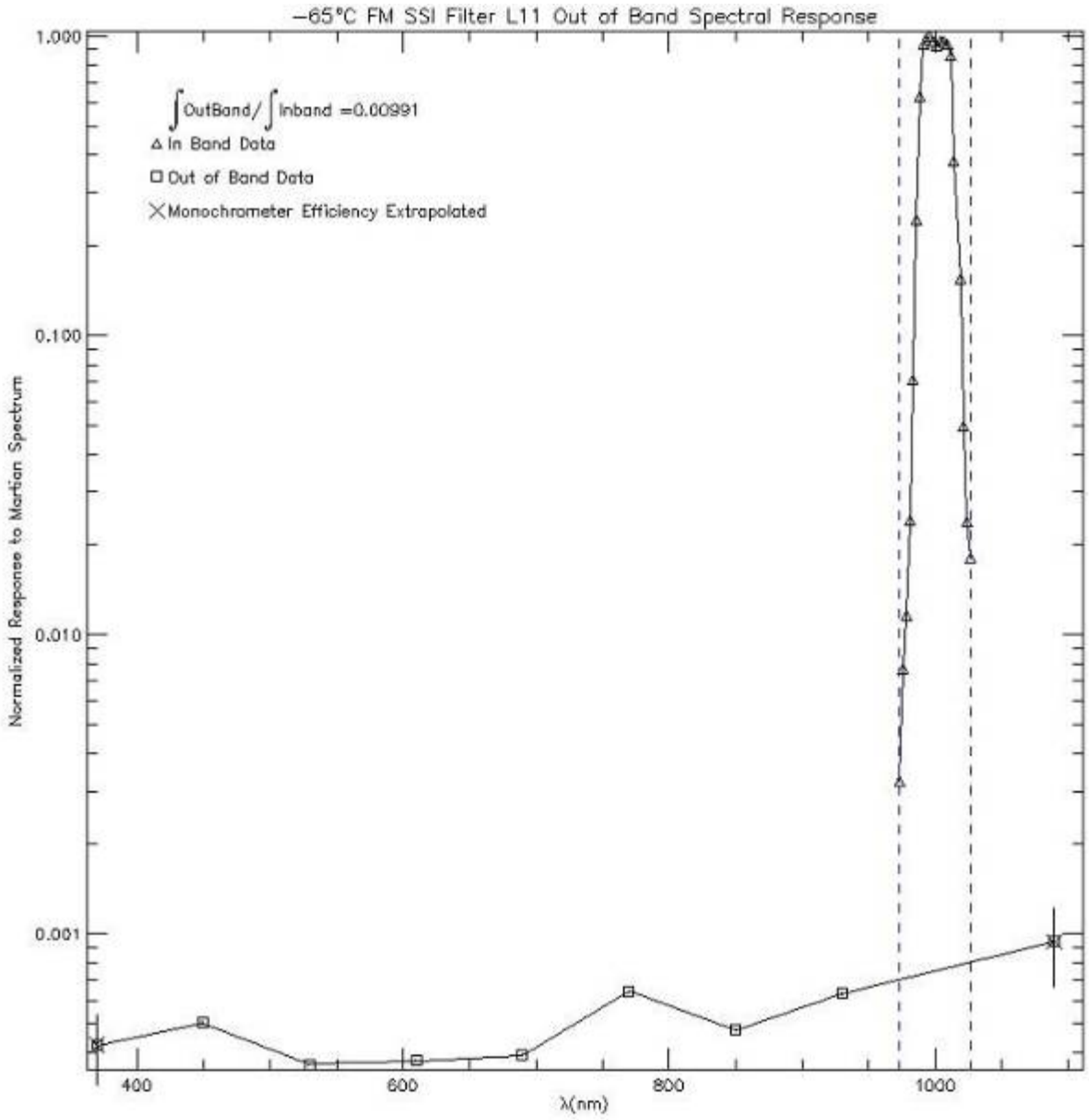

Figure H - 48: FM SSI L11 Stop Band at -65°C

Due to a lack of a complete -65°C data set for the in-band measurements, the comparison here is made to an in-band data set taken at -15°C.

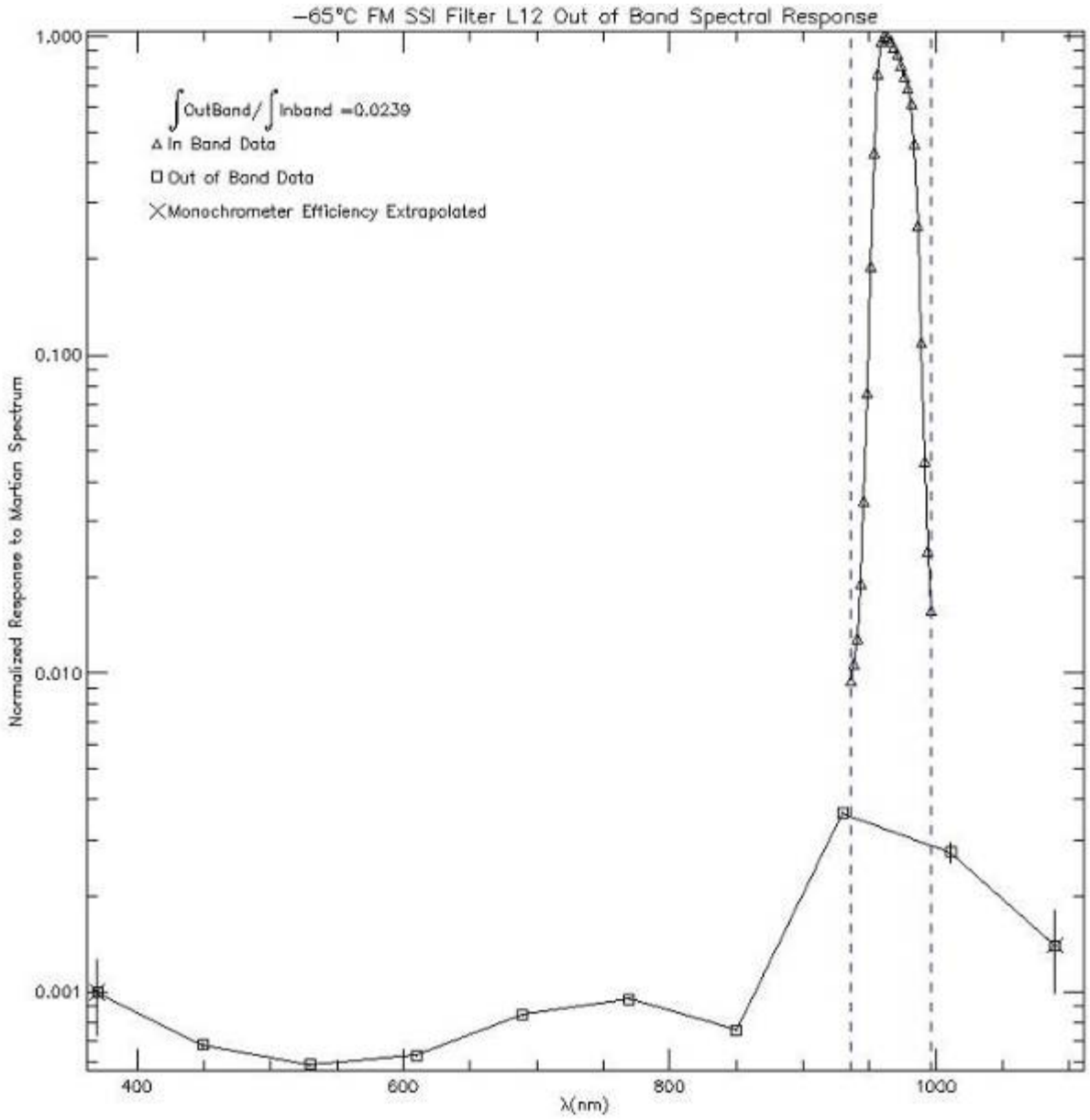

Figure H - 49: FM SSI L12 Stop Band at -65°C

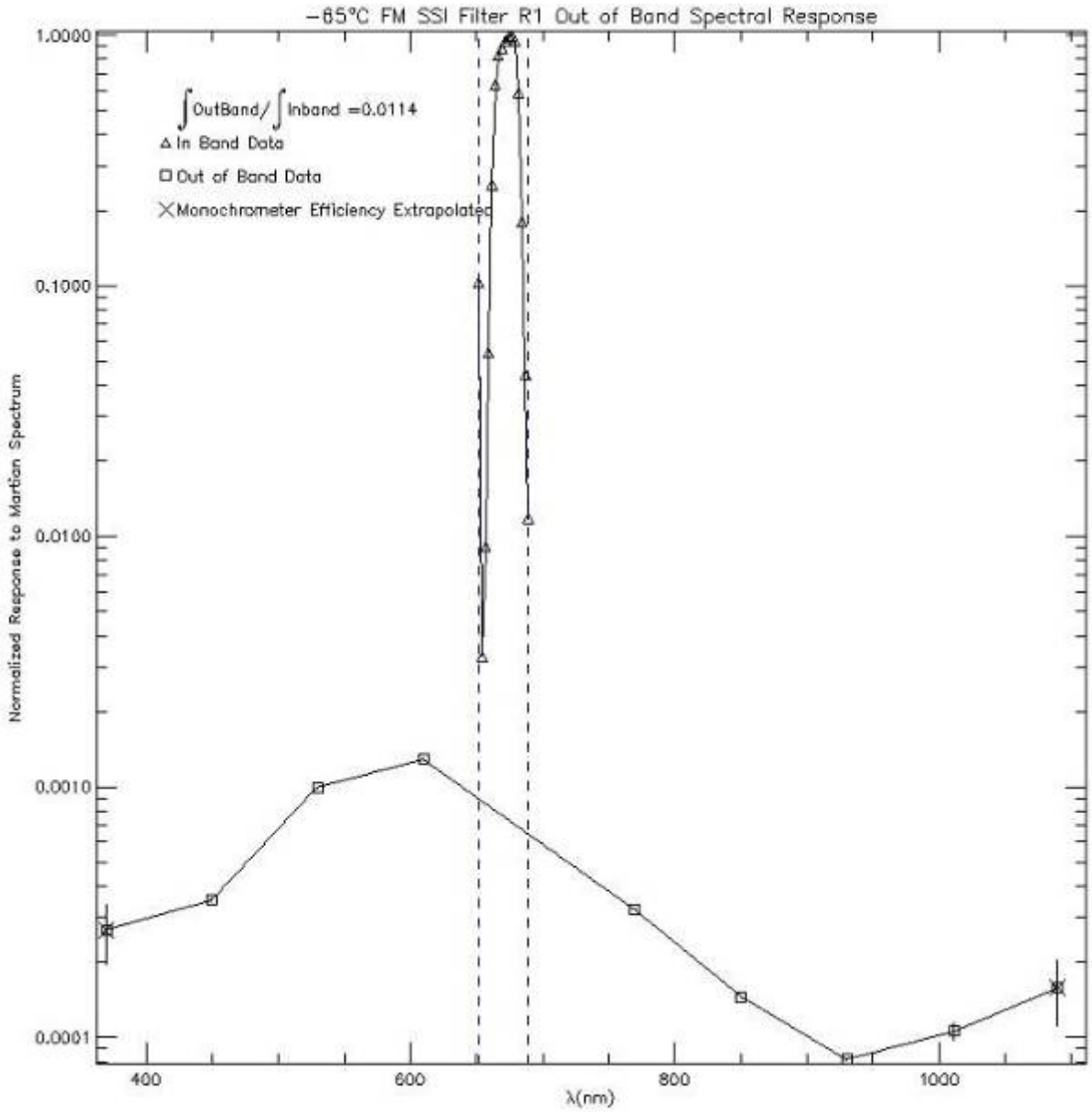

Figure H - 50: FM SSI R1 Stop Band at -65°C

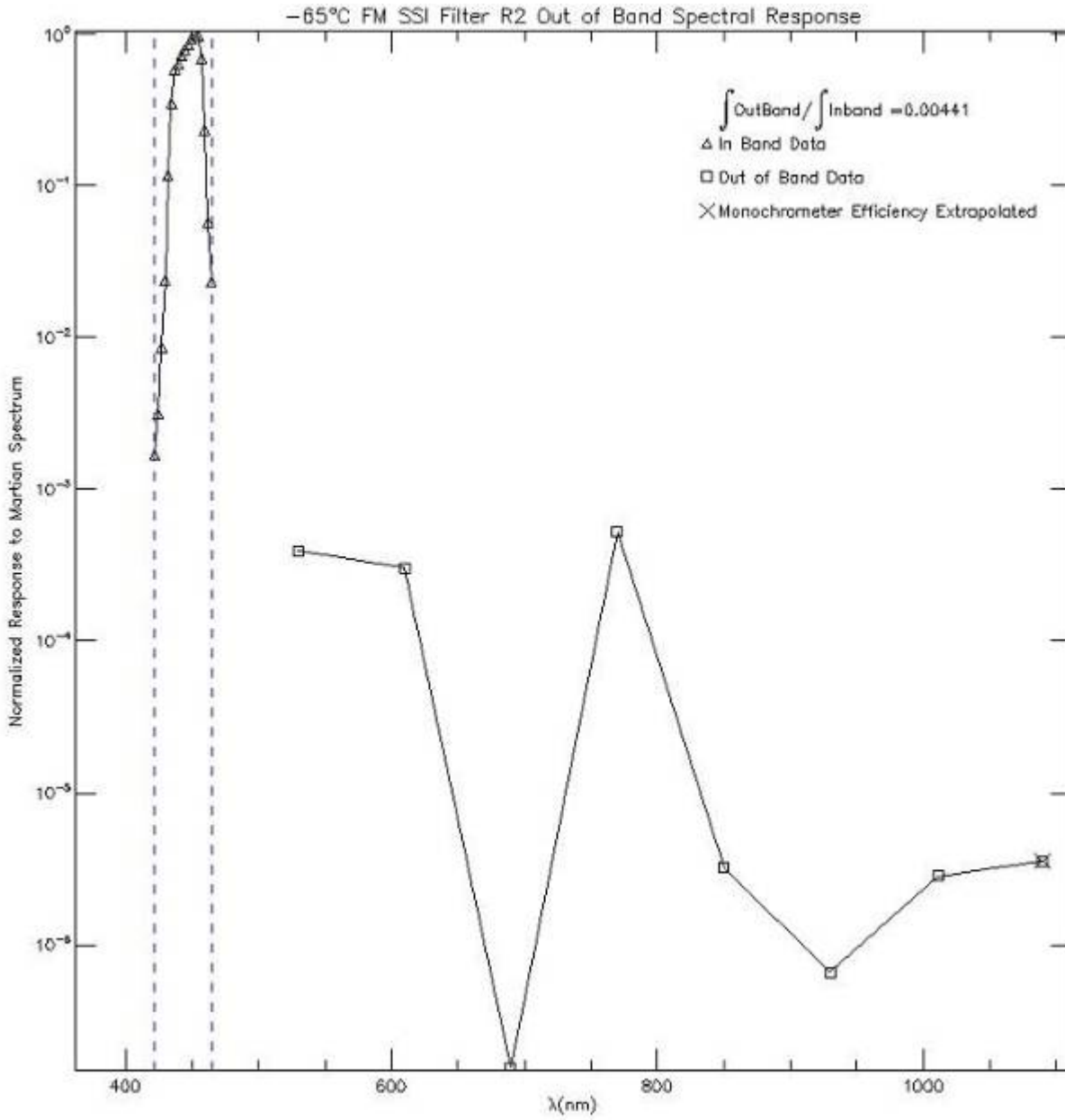

Figure H - 51: FM SSI R2 Stop Band at -65°C

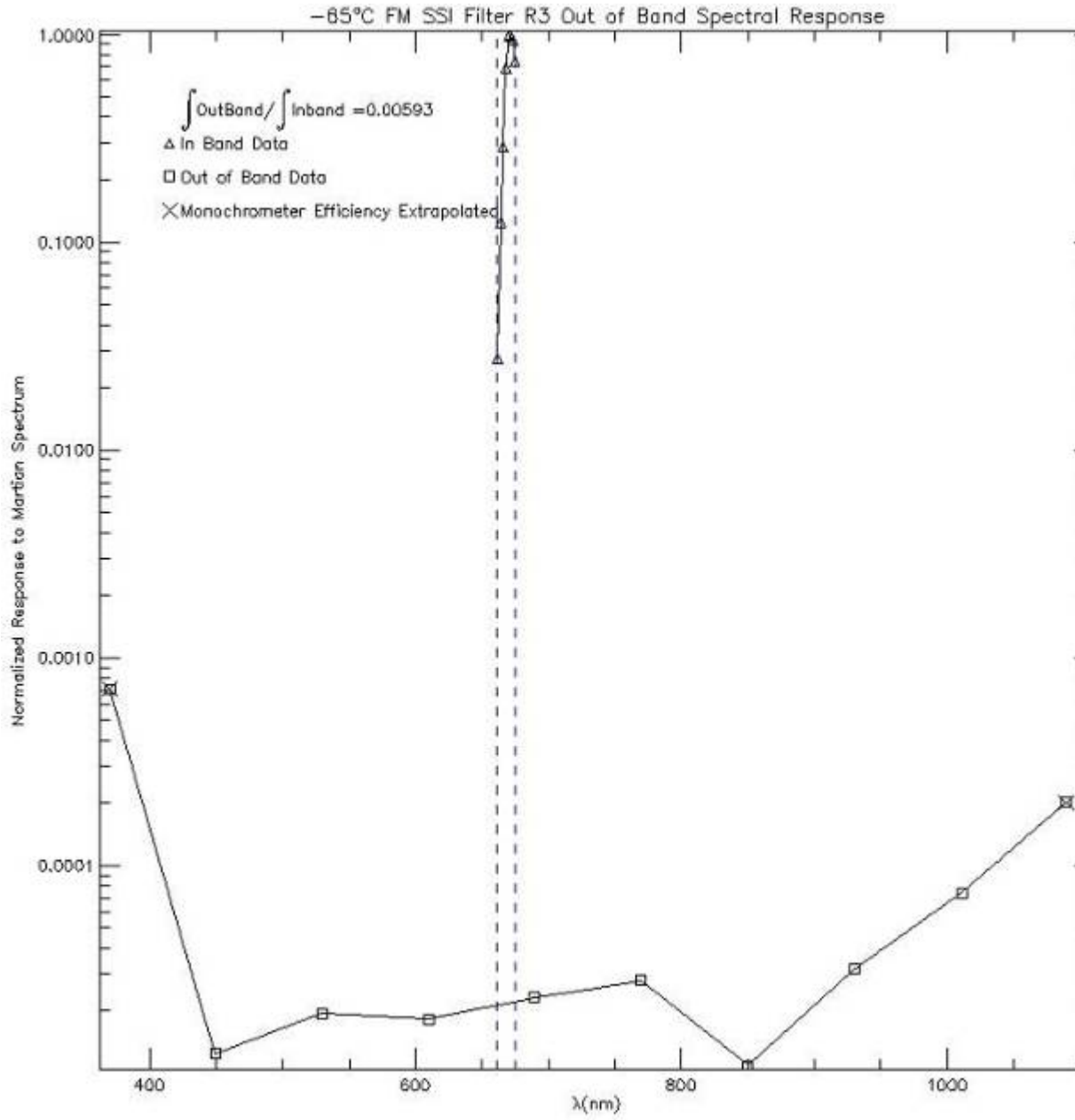

Figure H - 52: FM SSI R3 Stop Band at -65°C

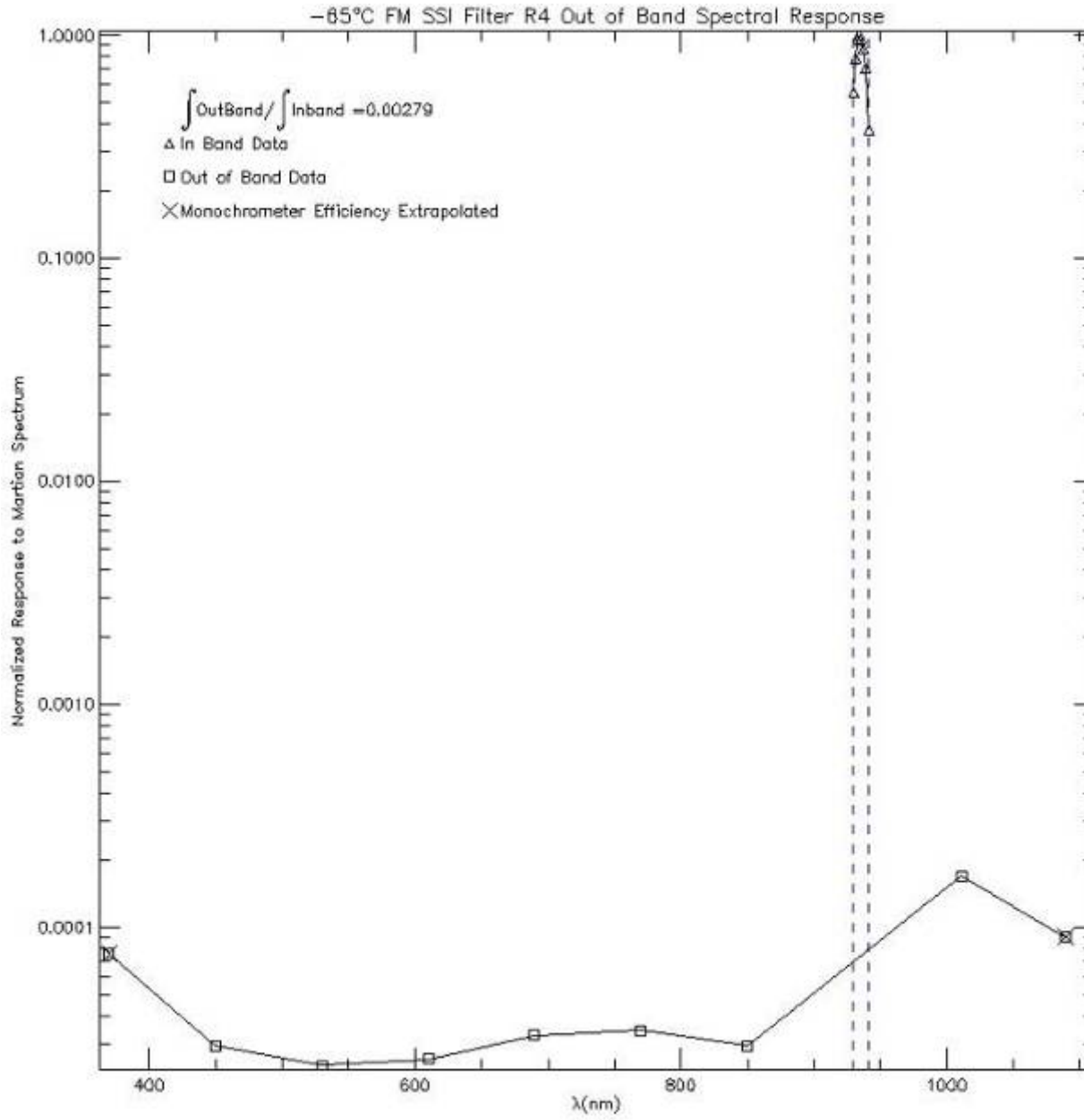

Figure H - 53: FM SSI R4 Stop Band at -65°C

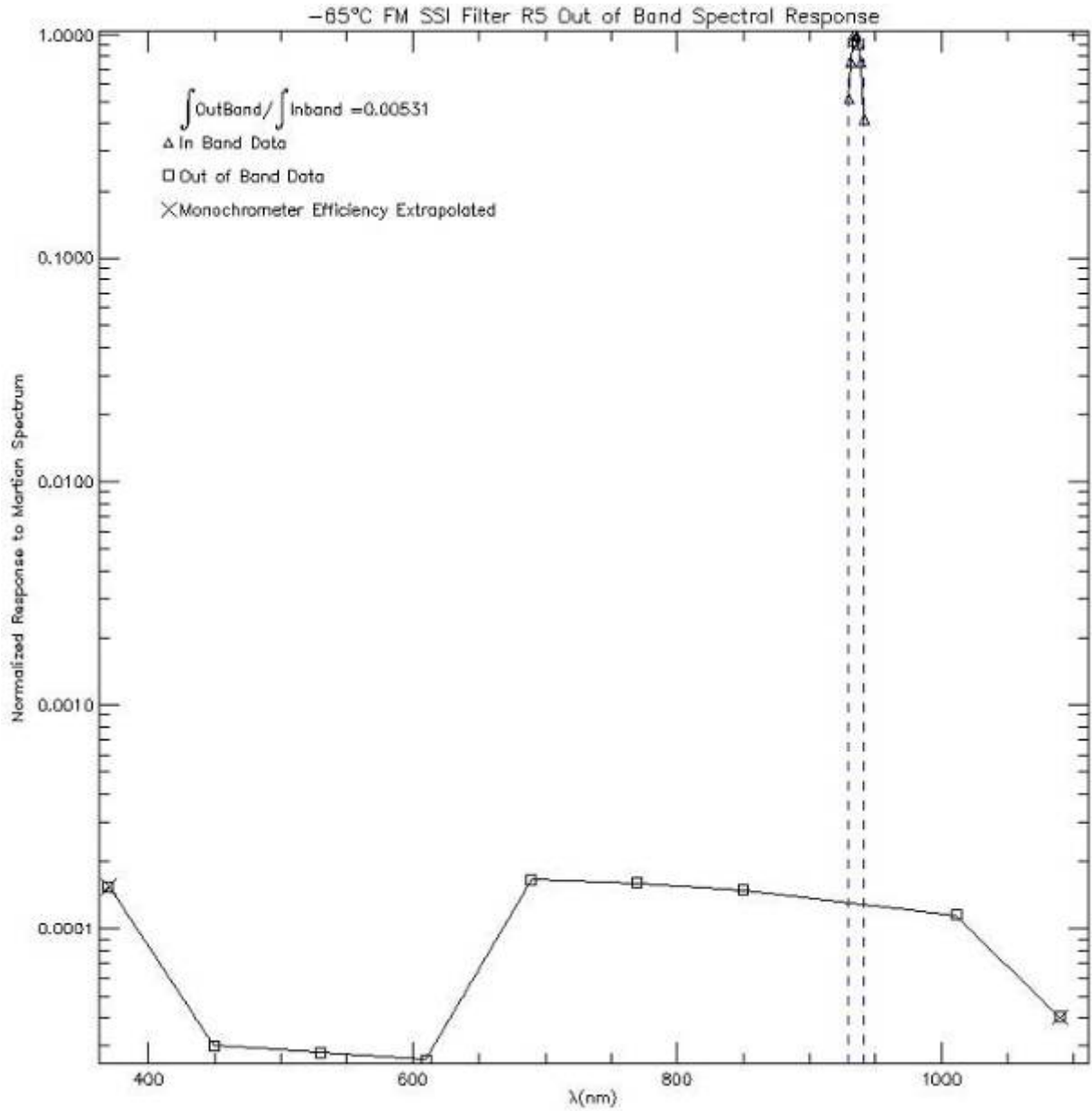

Figure H - 54: FM SSI R5 Stop Band at -65°C

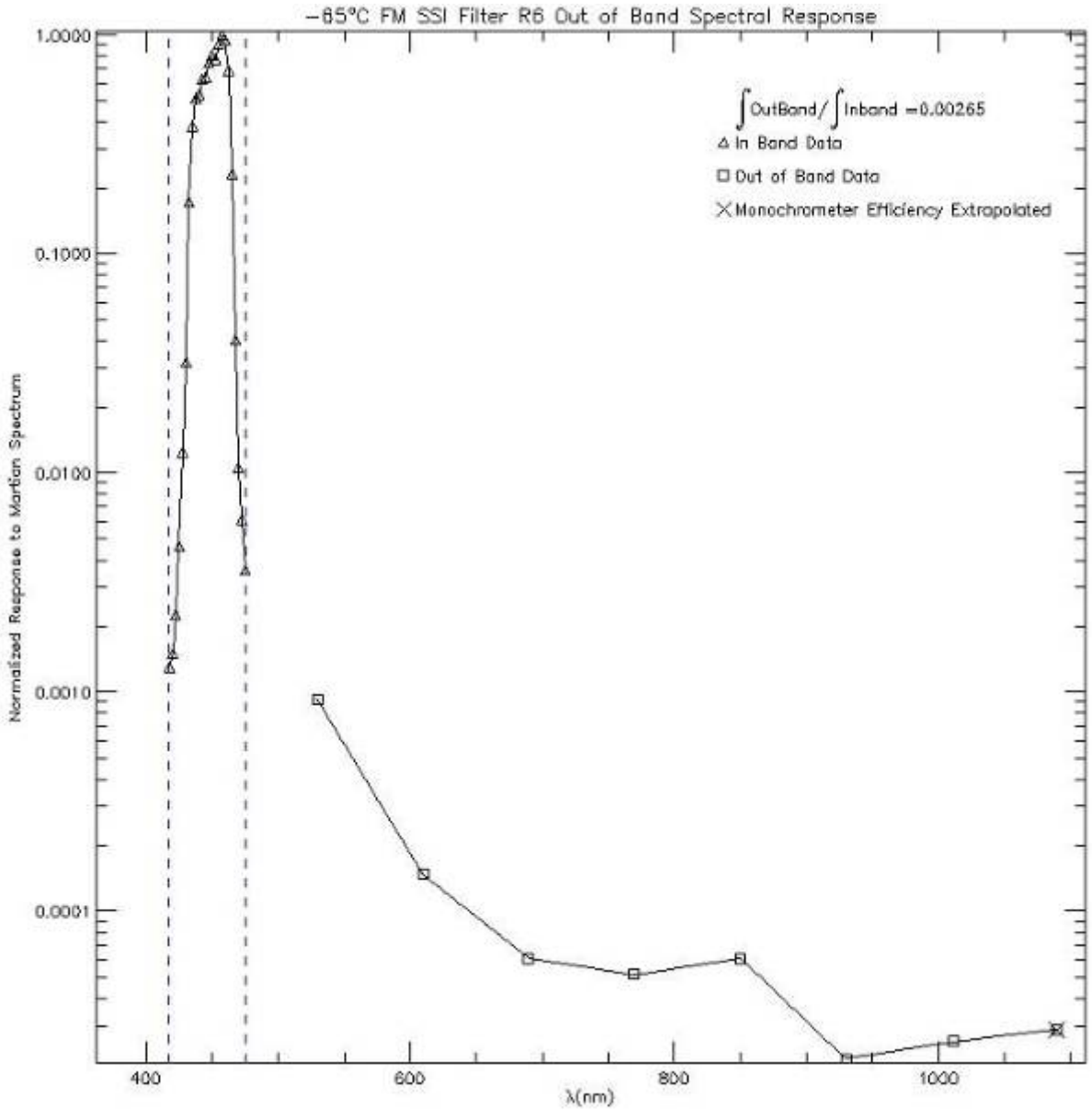

Figure H - 55: FM SSI R6 Stop Band at -65°C

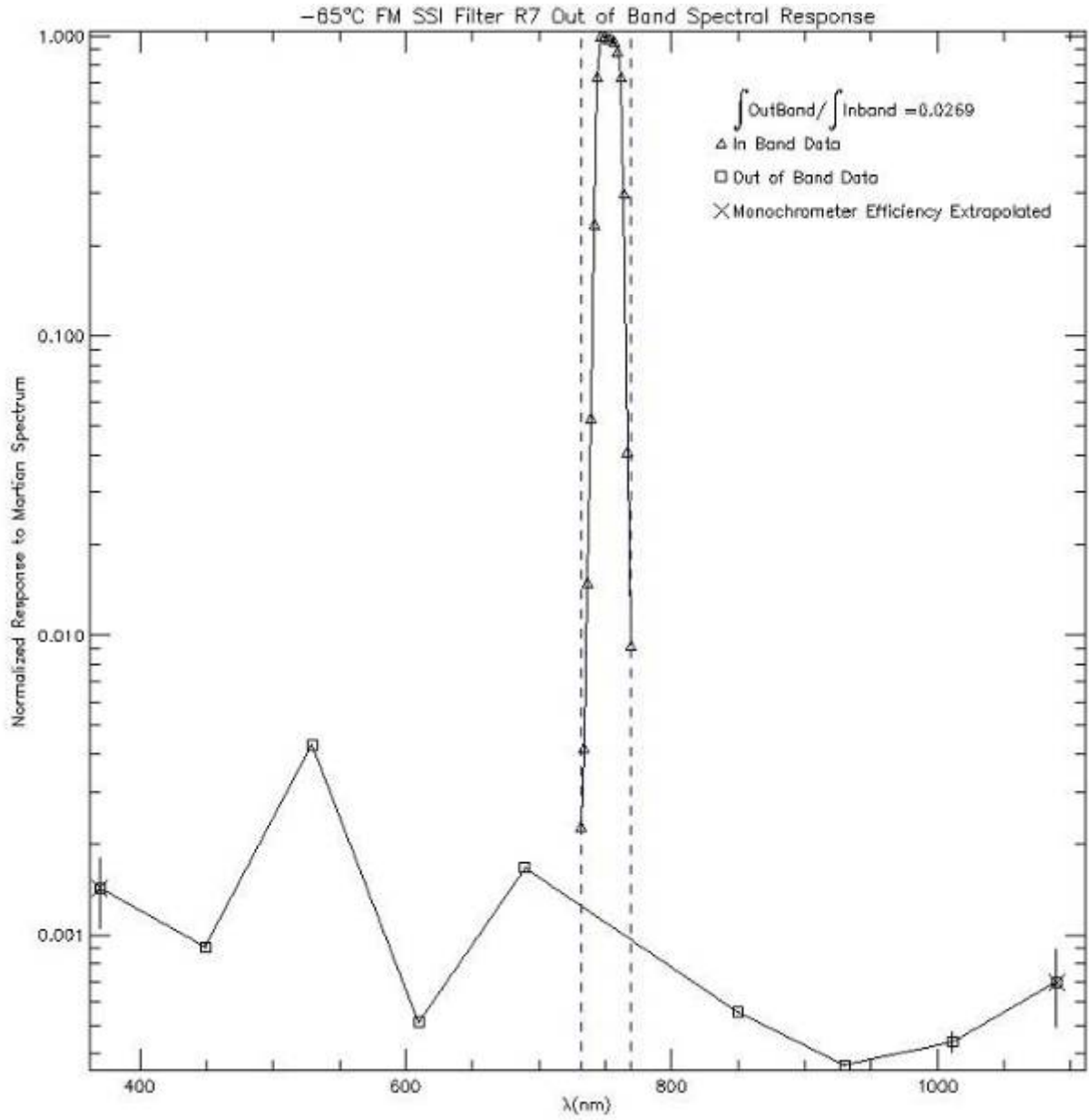

Figure H - 56: FM SSI R7 Stop Band at -65°C

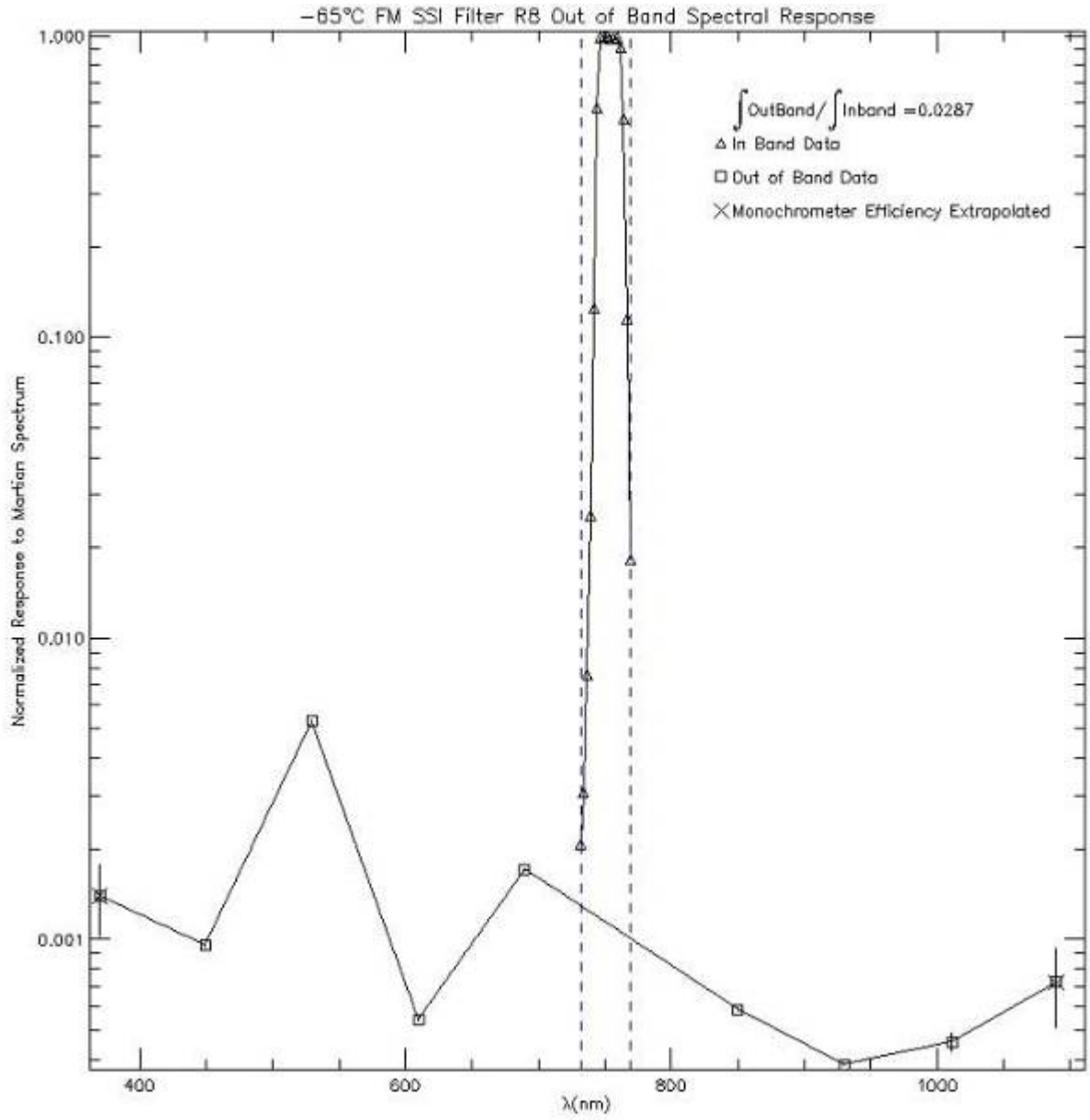

Figure H - 57: FM SSI R8 Stop Band at -65°C

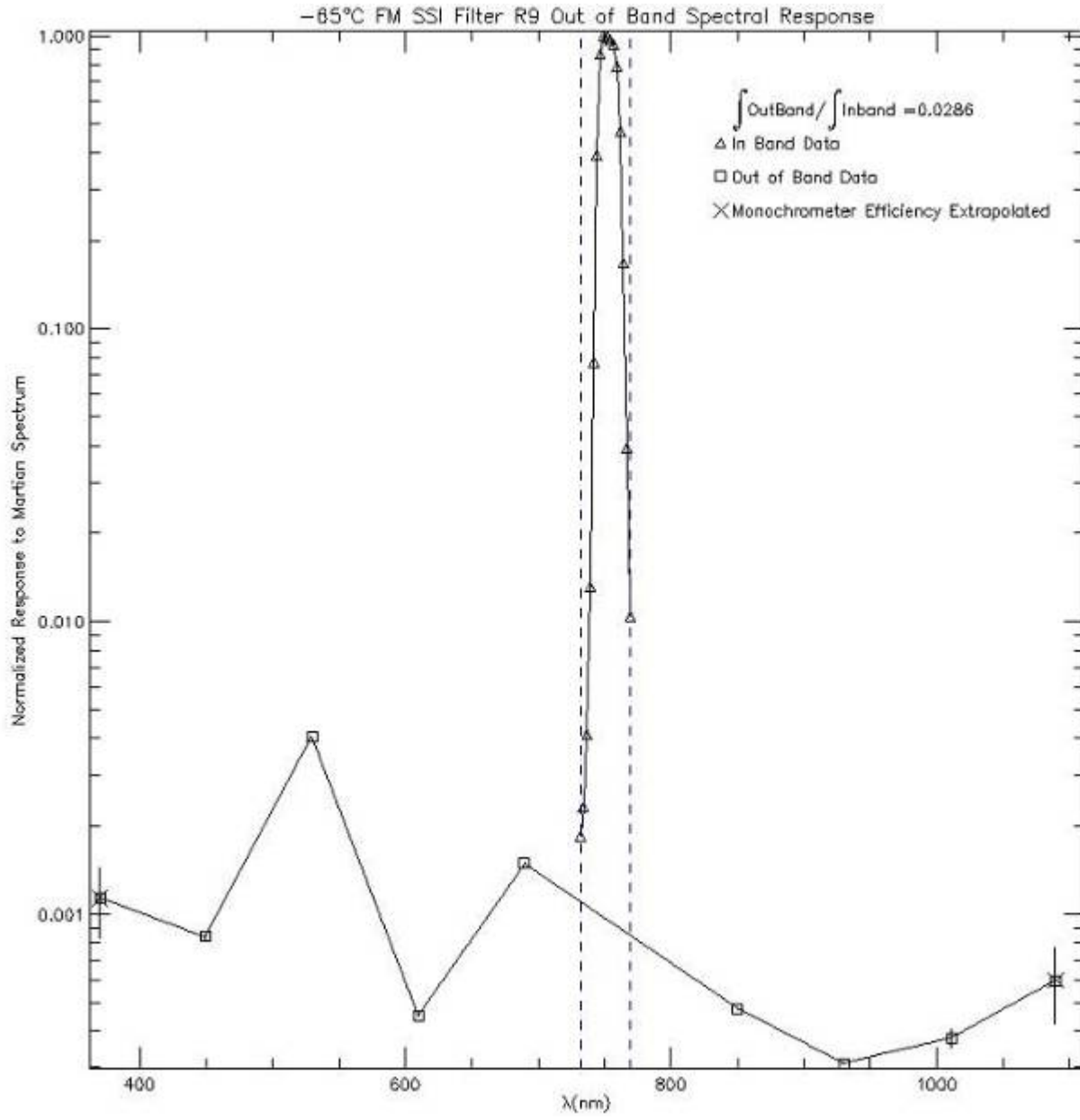

Figure H - 58: FM SSI R9 Stop Band at -65°C

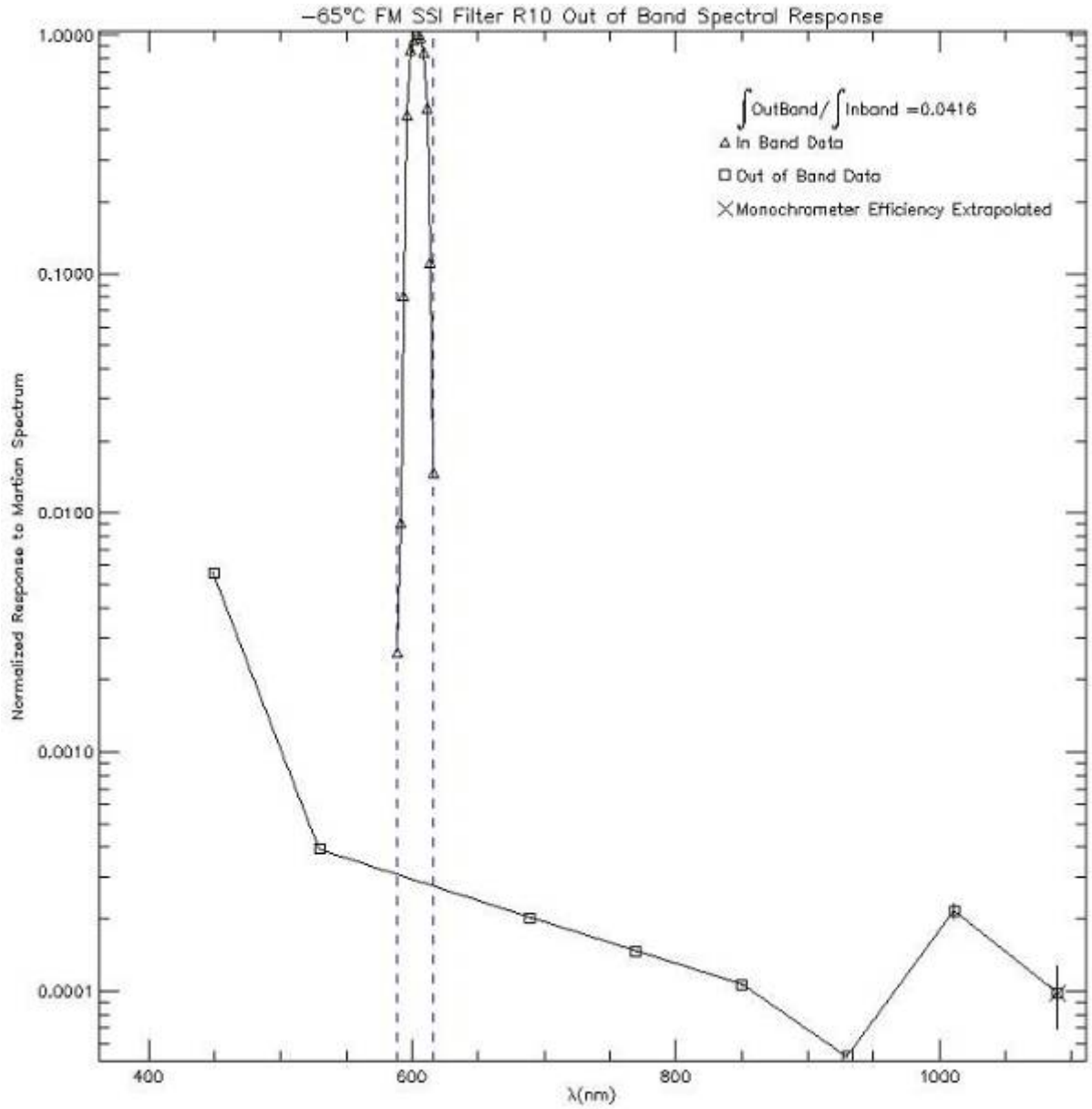

Figure H - 59: FM SSI R10 Stop Band at -65°C

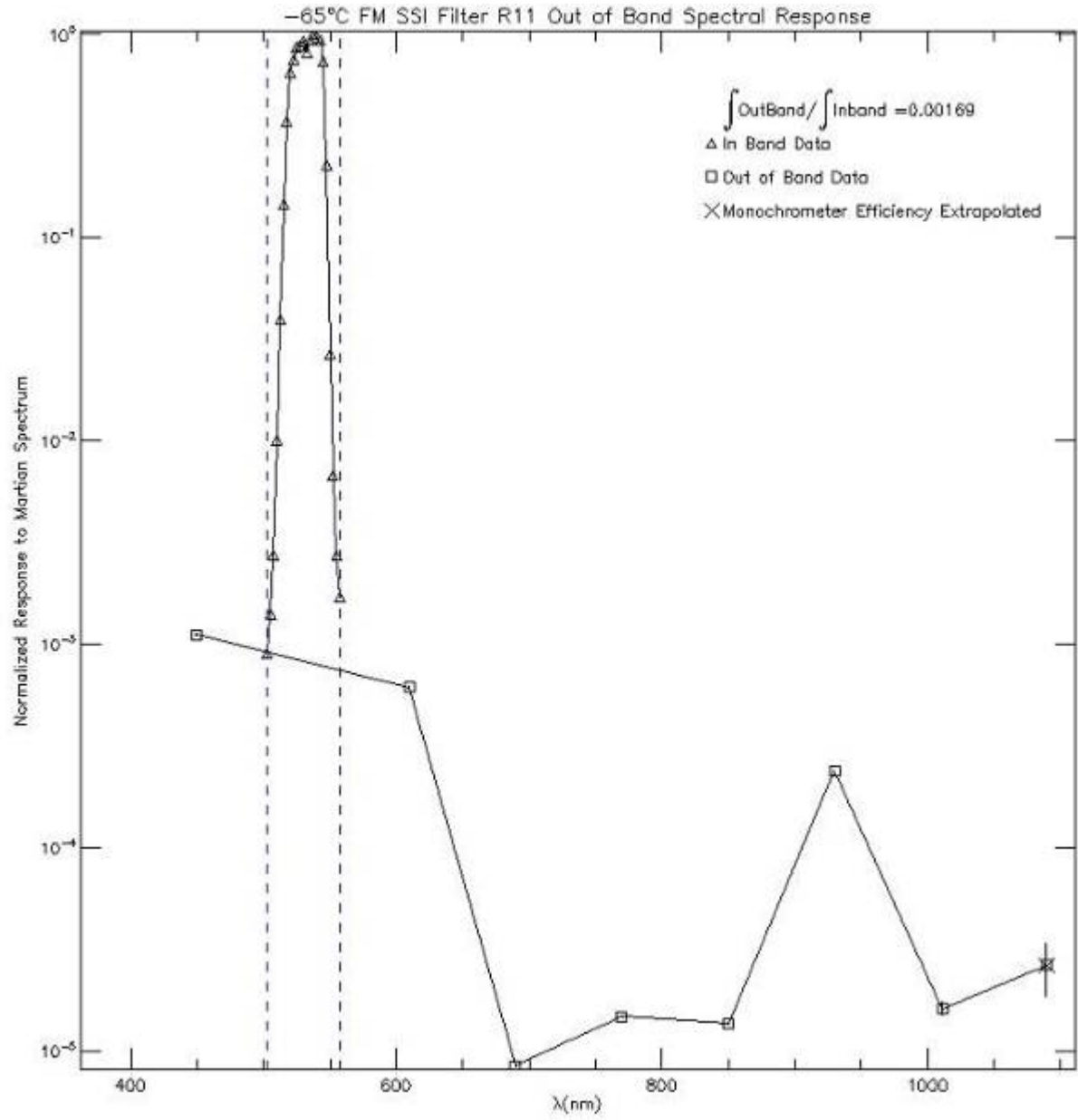

Figure H - 60: FM SSI R11 Stop Band at -65°C

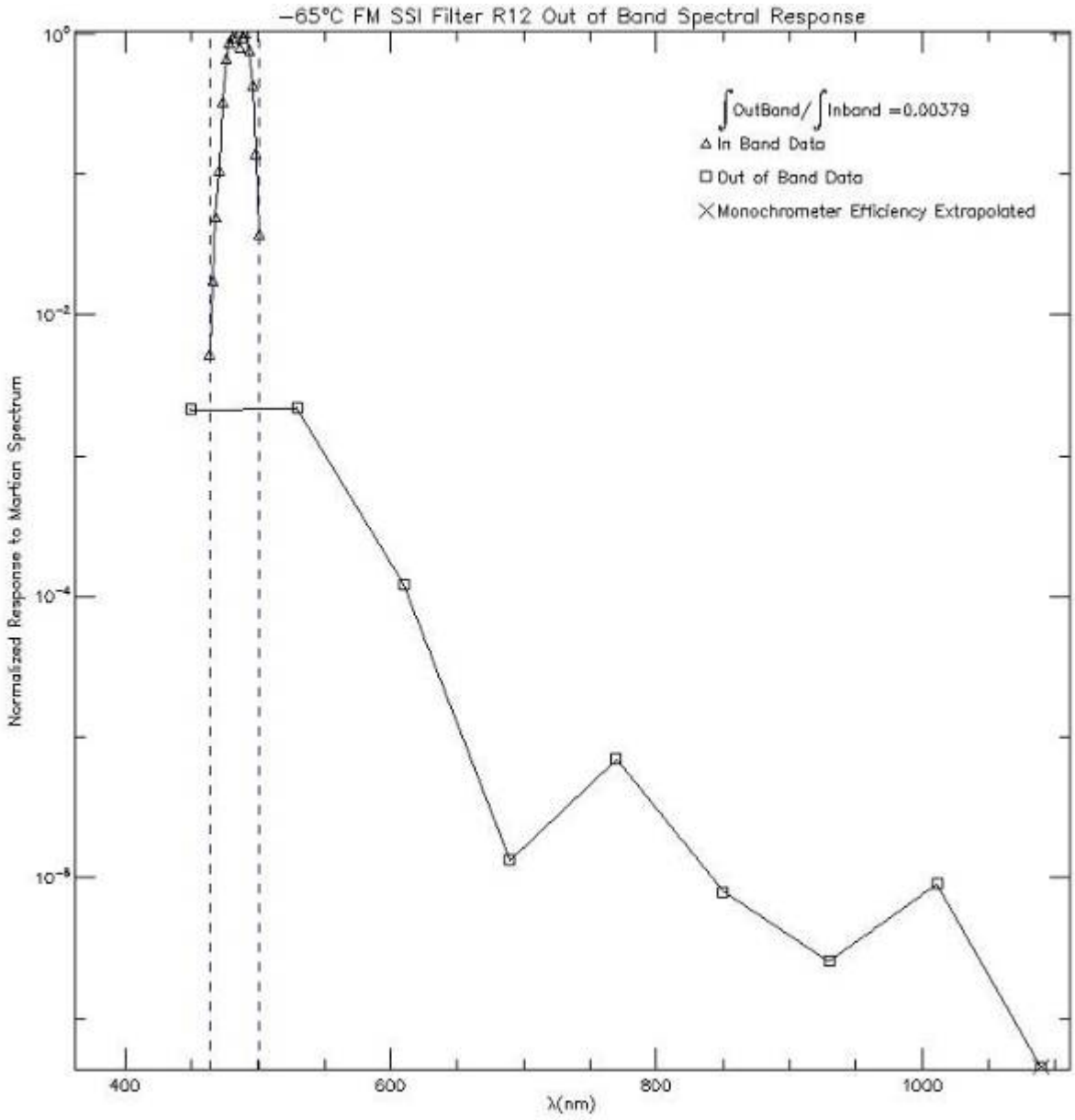

Figure H - 61: FM SSI R12 Stop Band at -65°C

H.8 Stop Band Notes

1) The 'green leak' seen on the out of band filter L7 measurements is thought to be an artifact of the monochrometer. There are other data-sets taken with this filter before it was installed in the camera, and these will be thoroughly examined

during the preparation of the next iteration of the calibration report, as well as a recalibration of the monochrometer to enable removal of the effect in post-processing.

2) The nature of the monochrometer efficiency curve combined with that of the spectrometer, plus the range of measurement of the spectrometer conspire to give very uncertain points at both wavelength extremes of the out of band measurements. Again, there were measurements made that should be able to increase our accuracy and precision in this area that will be fully explored in the calibration report.

3) Missing data points represent a case where the Out of Band response cannot be differentiated from zero by the current method. The data exists and further improvements in processing of the data may help quantify the amount of response, if any.

4) For current purposes the Out of Band response here should be taken as an upper bound on the possible value.

Geometric

I - Design of Camera Mast and Gimbal Assembly - RT

I.1 Mast / Gimbal Mechanical Dimensions

The major properties of the gimbal and mast assembly are shown in Table I-1 below. This data is from the MAGI group ICD drawing 415640-M003 Rev B SSI Mechanical ICD. All these values have not been inspected. The height of the elevation axis when deployed is within 0.5 mm of the table value.

Table I-1. Important Dimensions and Properties of the SSI Camera and Mast assembly.

Dimension – mast stowed.	**Value**	**Units**
Height of elevation axis	175.5	mm
Height of top of camera covers with head parked eyes down.	225.5	mm
Radius of clearance volume for elevation actuator and camera head wires on side of head.	165.2	mm
Diameter of base of mast canister attachment screws.	8.50	inches
Attachment screws	6 x #8	
Dimension – mast deployed.	**Value**	**Units**
Height of elevation axis	793.5	mm
Height of top of camera covers with head aimed at horizon	866.5	mm
Radius of clearance volume for elevation actuator and camera head wires on side of head.	165.2	mm
Height of the optical axis above the elevation axis	12	mm

I.2 Gimbal Operation

The SSI camera has 2 phase stepper motors with reduction gearboxes for driving the azimuth and elevation axes of the gimbal assembly. Each phase of the motor can be driven in both directions giving a four phase sequence to move the motor. The phase normally powered is A, with the current reversed, it is Abar. The other phase is B and when reverse powered, Bbar. The camera has hardware stops that restrict the range of travel for azimuth to approximately 355 degrees and elevation to approximately184 degrees.

Each actuator is coupled to the camera with a titanium flexure which has no backlash. There is backlash in the actuator gearboxes that results in about 0.4 degrees of gimbal travel. The cables that run from the tip plate of the mast up to the camera head are flexed when the camera head moves in azimuth and elevation. These cables provide a preload which can push the camera head against one side of the backlash, providing a consistent position. They also have significant frictional losses which can overcome the preload force and reverse which side of the backlash the camera is on. These cables get stiffer and lossier as they get colder. There are no position sensors; the gimbal is driven by the software but counting steps from the initialization position. To minimize the backlash, an approach procedure is used to make sure the position is approached from the direction that minimizes the variation in the step position.

The software initializes the camera axes by driving each motor for more steps then the full range and stopping on the correct stop phase to be at the hardware stop. The additional steps mean that where ever the camera starts it will find the hardware stop. With the correct stop phase, it will be at the hardware stop on the last step powered, even if it bounced off many times during the initialization. Then it moves to the center of travel for that axis. This starts the camera head at a known position. Steps are counted by the software during all moves to determine the position of the camera head azimuth and elevation. The actuators are sized to be powerful enough that they will position the camera head under all temperature conditions. Once the actuator stops, it is powered off. The unpowered detent torque of the actuator holds the camera in position. The bearings in the gimbal assembly are dry film lubricated and have low running torques under all temperatures. The actuators have wet lubed bearings that will require heating to reach operational temperatures when starting from cold. The heat up time for each actuator is covered in section R of this report.

The total travel in azimuth is 1234 steps at 0.28845 degrees/step for a total range of 355.95 degrees. Subtracting the lost travel winding up the camera against the stop is 0.55 degrees, this leaves a camera head travel of 355.4 degrees. This leaves a

dead zone of 4.6 degrees. The FOV of the camera is 13.7 degrees so there is at least 9 degrees of overlap in azimuth.

The low elevation viewing test determined that the 0 step approached up is at-1.33 degrees elevation. The highest elevation is +316 steps or 309.8 steps above the horizon. This puts the highest elevation pointing at 89.6 degrees above the horizon at the high stop. While this is slightly short of the zenith, the zenith is in the FOV, it is about 0.4 degrees above the center of the image.

Table I-2**.** Stop phases and travel data for the FM SSI

Azimuth axis travel and phases.	Hardware phase	units
Positive Hardstop Phase (max CW position as viewed from top)	Bbar or 3	
Positive Hardstop Position	617	steps
Negative Hardstop Phase (max CCW position as viewed from top).	B or 1	
Negative Hardstop Position	-617	steps
Steps stop to stop	1234	steps
Total no of azimuth positions stop to stop	1235	steps
Initialization direction	CW	
step size in degrees	0.28845	deg
step size in mrad	5.03	mrad
step size in pixels	20.98	pixels
Phase seq for CW	A, B, Abar, Bbar, A	
Phase seq for CCW	A, Bbar, Abar, B, A	
Elevation axis travel and phases.	Hardware phase	
Negative Hardstop Phase (eyes down or max CCW position as viewed from cable side of camera)	A or 0	
Negative Hardstop Position	-317	steps
Positive Hardstop Phase (eyes up or max CW position as viewed from cable side of camera)	B or 1	
Positive Hardstop Position	316	steps
Steps stop to stop	633	steps
Total no of elevation positions stop to stop.	634	steps
Initialization direction	CCW	
step size in degrees	0.28845	deg
step size in mrad	5.03	mrad
step size in pixels	20.98	pixels
step size in encoder counts	52.51	cnts
Phase seq for CW	A, B, Abar, Bbar, A	
Phase seq for CCW	A, Bbar, Abar, B, A	

I.3 Design of Mast

The mast on the SSI camera had to meet the requirements of raising the camera from the compact position which fits inside the aeroshell and the need to raise the camera up to see the workspace and surround terrain as well as possible. The mast is made of epoxy fiberglass longerons and battens. The mast deploys mainly from it own stored energy. The stainless cross wires diagonalize each of the bays. A picture of the camera on the mast assembly is shown in figure I-1.

The mast raises the camera 618 mm from the stowed to deployed position. When deployed the mast is stiff enough to hold the camera steady in the expected winds to prevent image smear. The mechanical properties of the mast are shown in Table I-3. The

drag of the camera head was modeled and the deflection calculated based on the mast stiffness. The expected deflection is less than 0.01 mrad in a 20 m/s wind. This is 0.04 pixels. The modal frequencies predicted are 12 to 22 hertz for the bending and torsion modes. The camera actuators are stepped at 34 and 52 hertz to minimize excitation of these modes. The modes damp out sufficiently quickly that they do not cause image blur after a move by the gimbal assembly.

Table I-3. Beam model of mast and camera assembly

Equivalent beam model properties:	Value	Units
EI	1.789E6	lb-in2
GA	3,908	lbs
GJ	25,321	lb-in2
W/in	8.40E-3	lbs/in
Length to elevation axis	29.5	in
W	7.7	lbs

Table I-4. Preliminary Drag and Vortex-Shedding Loads Assumptions

Ambient Temperature	253 K
Atmospheric Pressure	1067 Pa
Gravitational Acceleration	3.7 m/sec-sq
Wind Speed	0 to 20 m/s
Strouhal Number	0.1 for Re<40 0.21 – 4.41/Re for Re>40
Drag Coefficient for Camera	2.0
Drag Coefficient for Longerons and Battens	1.17
Lift Coefficient for Cylinders due to Vortex Shedding	0.45
Lift Coefficient for Cylinders in VS Resonance	1.6

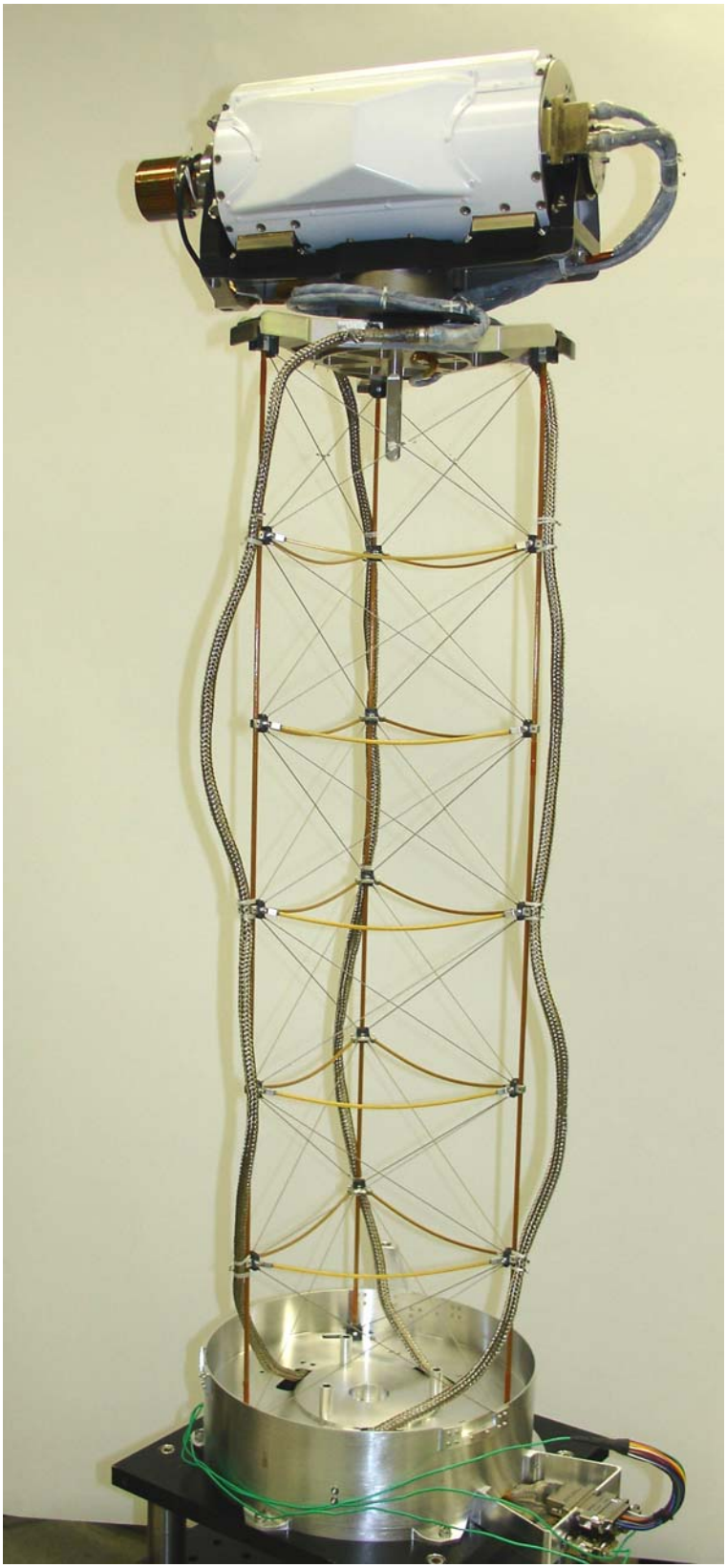

Figure I-1. Image of the FM SSI camera and mast assembly.

J - Optical Design - RT

J.1 Optical Path

The optical layout of the Phoenix SSI is shown in an isometric view in figure J-1. The light enters the front window bounces off the first fold mirrors, passes through filters, the lenses and bounces off the second fold mirror and is imaged on to each of the CCD's. The second fold mirror has a small apex angle and the two paths diverge to image onto two separate CCD's. This allows a complete separation of the optical paths with improvements in stray light from one path affecting the other path. Cutting a section thru the optical head along the cylinder axis shows the main part of the optical path for the Phoenix SSI design is shown in figure J-2. This section shows the optical path passing through the filters before the lenses, putting the filters in the collimated beam. The nominal height of the optical path at the lenses is 12 mm above the elevation axis. The elevation axis is 793.5 mm above the lander deck when the mast is deployed.

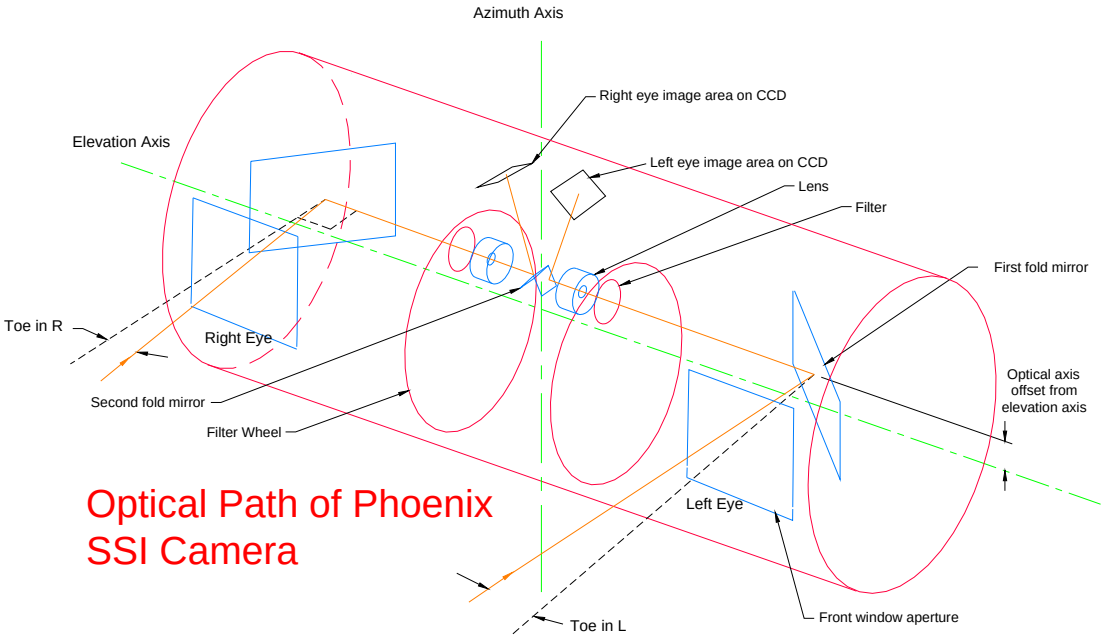

Figure J-1. Isometric view of Phoenix SSI camera showing the path of light entering the camera and reaching the CCD's.

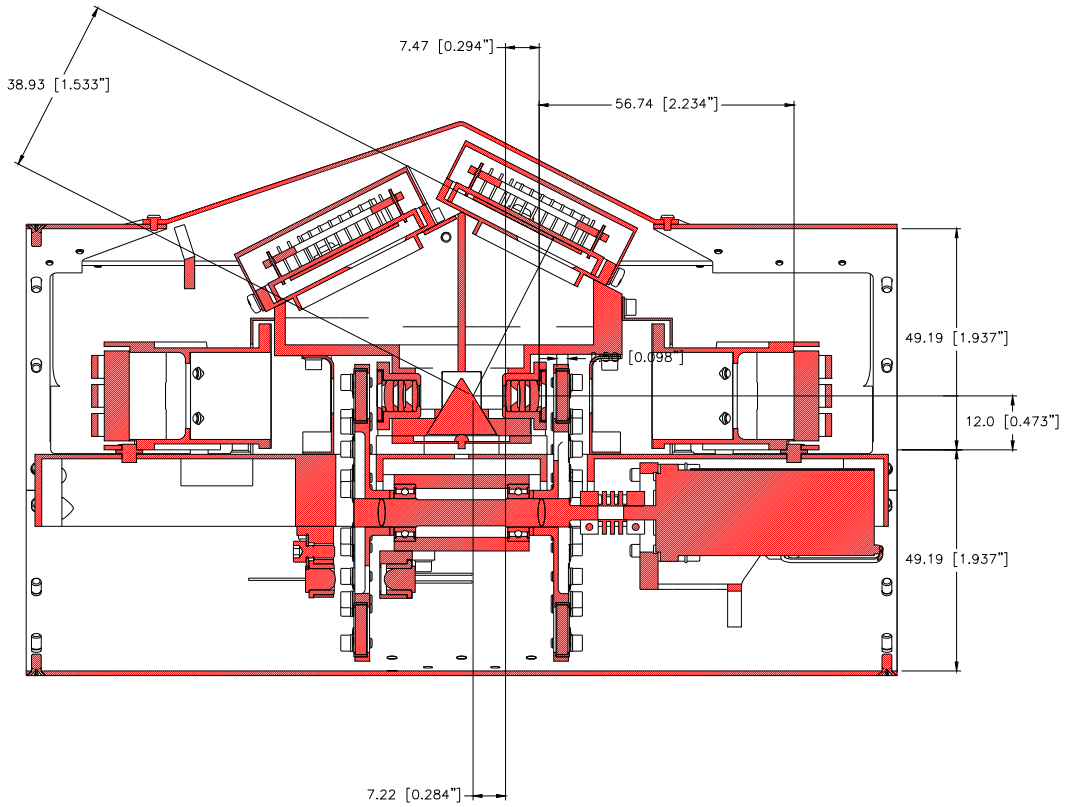

Figure 2. Cross section thru the center of the camera head on the elevation axis. The center of the optical axis is 12 mm above the center of the covers, which is the elevation axis.

J.2 Stereo separation and Camera internal distance

The stereo separation of the two eyes is measured between the two entrance pupils. The entrance pupil is the apparent place where all the optical rays intersect the optical axis. This position was determined by design and analysis. The optical light path for the rays thru the window, filter, and lens elements was determined by ray tracing with the optical design program Zemax. EE Version 8.0. The program was set to do exact ray traces, with no approximations. The program will convert its ray traces into a dxf file for importation into AutoCad. The ray traces were set in the proper location using the nominal dimensions for the pivot point for the fold mirrors. The ray trace was rotated to place the intersection of the optical axis with the mechanical axis of the camera at 3000 mm from the face of the camera; this is the alignment target for the camera. The mechanical axis is the center line of the camera head perpendicular to the elevation axis.

The optical path was unfolded around the fold mirrors. The prism mirror was neglected since it did not affect the position of the entrance pupil. AutoCad was used to determine the position of the entrance pupil graphically. The center ray from the edge of the FOV was intersected with the center FOV ray to find the position of the entrance pupil. The position of the entrance pupil was 2.25 mm behind the first vertex of the first lens element. The top view of the unfolded optical path for the right eye is shown in figure 4. From this layout the position of the entrance pupil can be measured to the mechanical axis as 75.44 mm. The pupil to pupil distance is twice this at 150.88 mm. The angle of the optical axis with the mechanical axis is also determined at 1.389 degrees or 24.25 mrad. This is the nominal toe in angle for each eye. **T**he final alignment angle is at ~23.95 mrad. The length of the optical path inside the camera head is 109.65 mm as measured from the front cover to the entrance pupil. All the target distances for the SSI are measured from the front cover.

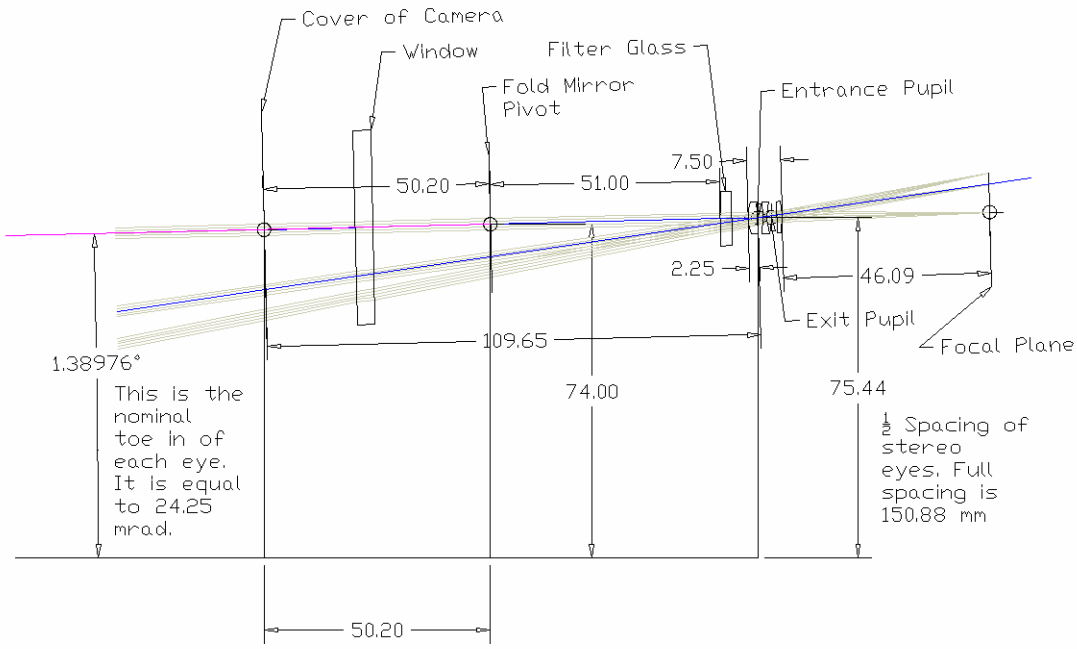

Figure J-3. Top view of the SSI right eye with the optical path unfolded around the fold mirror. The line at the bottom is the center mechanical axis of the camera. The blue line on the left side of the image is the optical axis to the target. It will meet the mechanical axis of the camera at 3 meters from the camera head.

J.3 CCD's

The SSI camera has two MER Rover flight spare CCD's, one for each eye. The figure J-4 image shows the two black CCD carrier holders on top of the optical housing inside the PHX SSI

camera. Each carrier holder holds one CCD. The electronics for each camera is connected to the CCD's by the flat golden ribbon. The CCD's are frame transfer devices. Each of the CCD's has a 1024x1024 pixel image area, an adjacent 1024x1024 storage area and a serial readout register. The readout register has additional null pixels which get readout with the image as shown in figure J-5.

The images read out of the left CCD require a 180 degree rotation to be correctly oriented. The right eye images are correctly oriented as is. There are null strips on each side of the image when read out. The IFSW strips these off and send them separately if commanded. The strip is 17 pixels wide on the left side of the right image, and 15 pixels on the right side. The right most column of the right null strip contains the CCD ID number in the last column. The left eye image after rotation has the 15 pixel wide null strip on the left and the 17 pixel wide strip on the right. The rotations for correct viewing are done by the MAGI Image Viewer based on the eye specified in the image header. The image viewer can also remove the null strips from an image if they are present.

Figure J-4. Image of the camera head without the cover showing the two MER CCD's and two sets of MER electronics. The CCD's are under the two black rectangular pin covers at the end of the gold flex cables which connect the CCD's to their electronics.

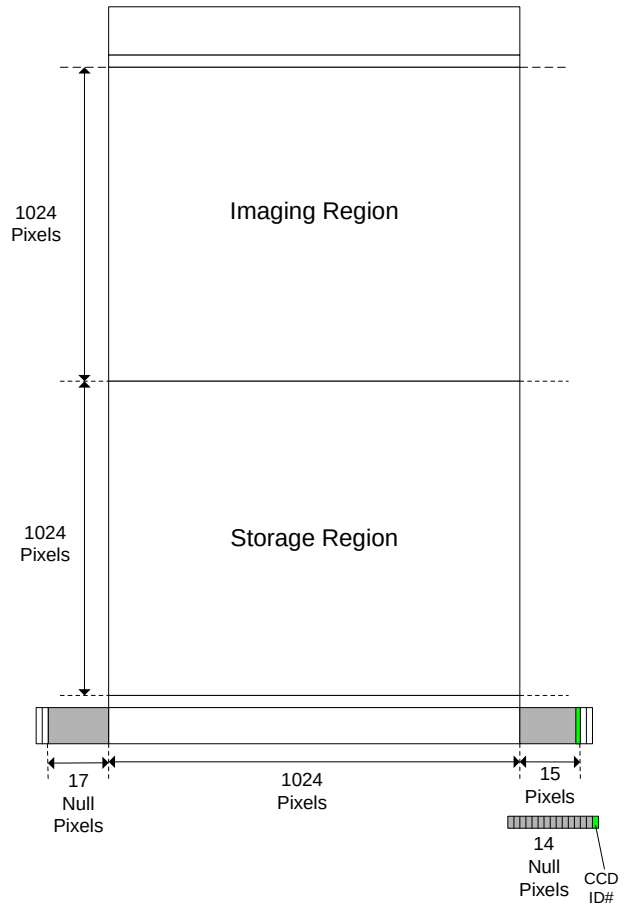

Figure J-5. The image area, storage area and null strip relationships. Drawing by A. Shaw

J.4 Filters

The SSI has two filter wheels, each with 12 positions, 30 degrees apart. Most of the filters are a single piece of 2.5 mm thick BK7 like glass with a hard coated filter applied to one surface and an antireflection coating on the other surface. The polarization filter (R9) has a 1.25 thick filter cemented to a polarization filter glass. The diopter filters have plano-convex diopter lenses cemented to filter elements. The image of the filter wheel assembly in Figure J-6 shows the two filter wheels with filters mounted on the shaft and bearing assembly. The actual center wavelengths, bandwidths, and temperature properties are covered in the filter section of this report.

The filter wheel is connected to a stepper motor that moves the filter wheel in 1 degree steps, or 30 steps per filter position. The system utilizes an optical emitter/detector pair to detect the edge of the slot in the filter wheel. This is used by the software to initialize the filter wheel position. The system will position the filters in the optical path for each eye. Since the filter wheels are on a common shaft, both filters wheels are at the same wheel position. Figure J-7 shows the filter wheel assembly mounted to the bottom of the SSI optical bench.

Figure J-6. The FM SSI Filter Wheel just after assembly. Each wheel is for one eye. The pattern in the filters is the reflection of the screen on the back of the flow bench.

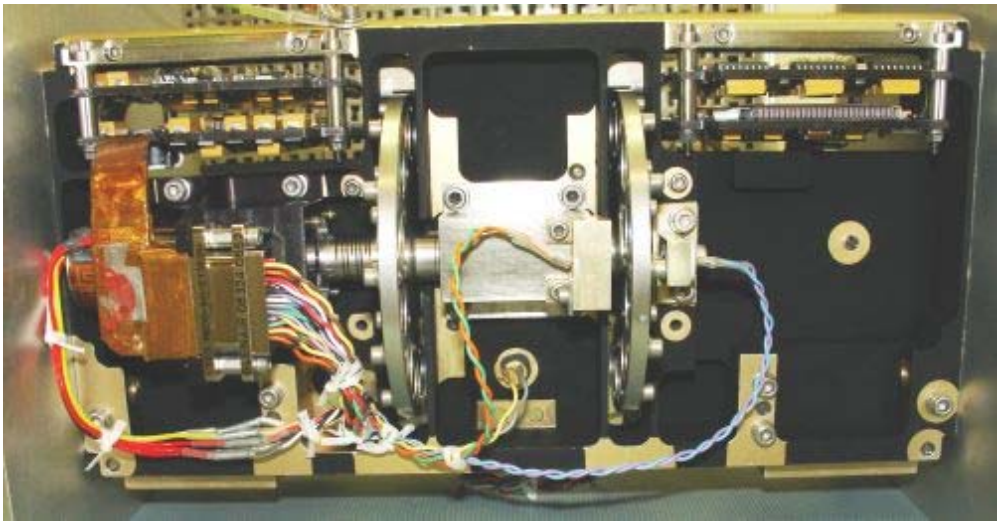

Figure J-7. Image of the underside of the SSI camera head without covers showing the filter wheel installed into the camera head. The flex coupling on the left side of the filter wheel connects the filter wheel motor, which is under the microD 25 connector on the left to the wheel. The optical emitter and detector are positioned on each side of the right filter wheel.

J.5 Windows and Mirrors

The SSI has an entrance window for each optical path which is a 4 mm thick piece of Schott BK7. This window provides a dust tight seal for the optical path to enter the sealed camera head. The window is antireflection coated on both sides. To prevent build up of dust on the window, the standard operational rule is to park the camera head at the low elevation stop which places the window face down and inside a semi sealed chamber formed by the brushes.

The SSI has a set of brushes mounted to each side of the gimbal assembly to seal around 3 sides of the window. The fourth side is sealed by a brush mounted to the top of the window mount. These brushes are shown in Figure J-10. This image shows the camera with the head in the park position showing the sealing of the gap between the gimbal and the window with the brushes.

The first fold mirror is a flat BK7 mirror coated with protected aluminum. This mirror is mounted in a aluminum mirror mount which is blackened with the Martin Black process. The second fold mirror is using one face of a fused silica 63 degree prism coated with the same protected aluminum. This mirror is mounted in a 63 degree V groove in the bottom of the optical housing. The optical housing is painted with Aeroglaze black paint. The mirrors are mounted against precision machined surfaces and held in place with mechanical clamps and silicone. See figures J-8 and J-9.

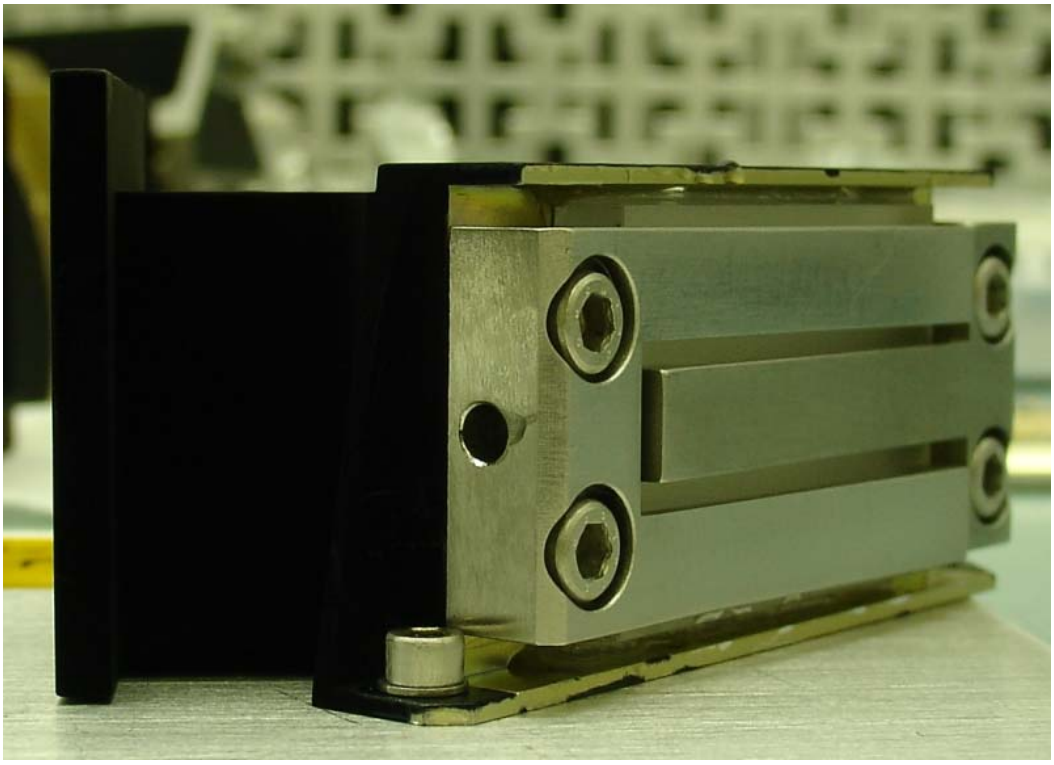

Figure J-8. The back side of the right fold mirror in its mount. The mirror is held in by the titanium flexure clamps seen here and silicone. The silicone is seen here at the top of the mirror between the mirror and the gold mirror mount.

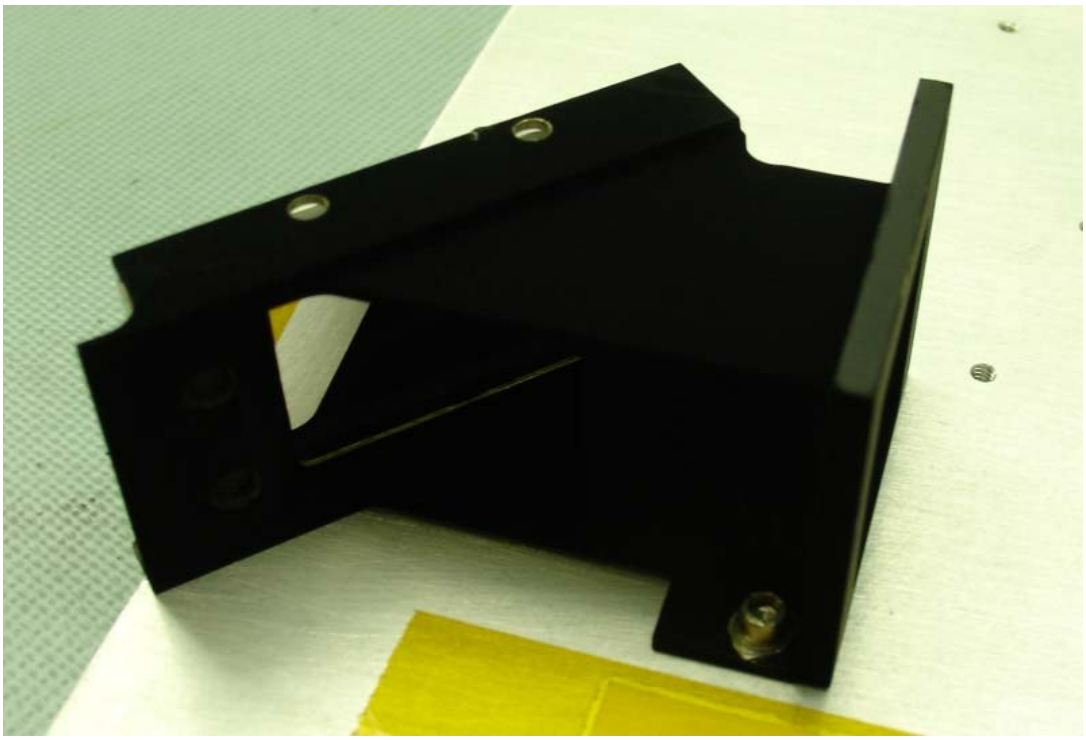

Figure J-9. The right fold mirror and mount assembly. Most of the surfaces of the mount are finished with the Martin Black Process.

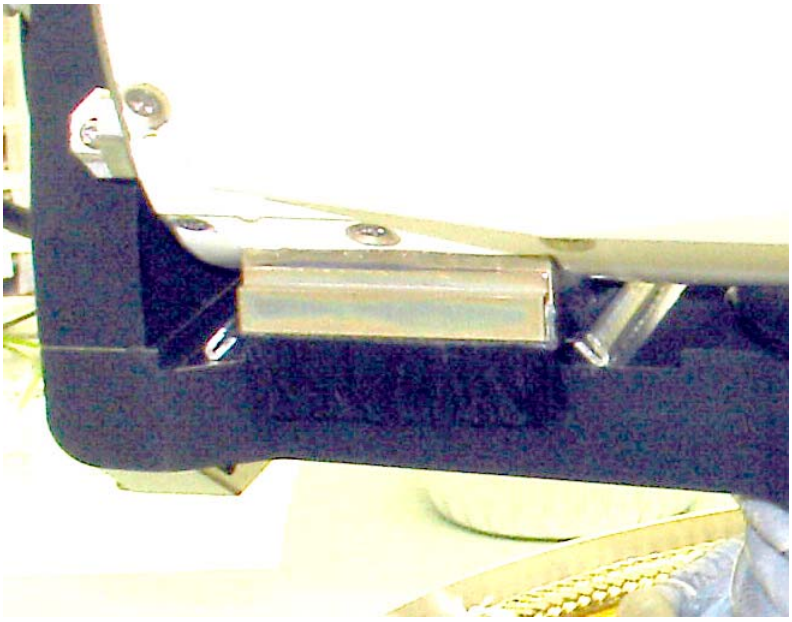

Figure J-10. Image of the front of the camera in the stowed position. The image is contrast stretched to show the black brushes against the black gimbal assembly. The brushes for the side seal are also shown, they are held by the u shaped aluminum channel. They seal against the side of the window mount and the cover.

J.6 Lens Assembly

The SSI uses a triplet lens assembly derived from the IMP/Mars 98 SSI. The comparison of the glasses used for the Phoenix SSI lens and several other spacecraft cameras are shown in Table J-1. The optical prescription is listed in Table J-2. The cross section through the lens cell assembly is shown in figure J-11 and an image of the lens assembly in the optical housing is shown in figure 12.

Table J-1 Schott lens materials for several spacecraft lenses.

Camera	IMP / Mars 98 SSI	Mars 01 Robotic Arm Camera	Mars 01 MECA Optical Microscope	Mars 03 MER PanCam	Beagle II Optical Microscope	Phoenix SSI
Lens 1 material	BK7	SK4	SK7	LAFN21	LAFN21	BK7
Lens 2 material	LF5	F4	SF11	SFL4	SF56A	LF5
Lens 3 Material	BK7	F4	-	LAFN21	LASFN30	BK7
Lens 4 Material	-	SK4	-	-	-	-

Table J-2. Optical Prescription

Surf	Comment	Radius - mm	Thickness - mm	Glass	Clear Aperture – mm	Optics size –dia. or square size - mm
OBJ		Infinity	3500.000	Mars Atm	-	1229.8
1	Camera Cover	Infinity	20.18	Mars Atm	26 sq.	27.0 sq.
2	ENTRANCE WINDOW	Infinity	3.970	BK7	24.3 sq.	27.0 sq.
3		Infinity	26.05	Mars Atm	23.8 sq.	26.3 sq.
4	FOLD MIRROR	Infinity	51.000	Mars Atm	17.3 sq.	19.35 sq.
5	FILTER	Infinity	2.500	BK7	6.0	11.0
6		Infinity	3.700	Mars Atm	5.3	11.0
7	Lens 1 - crown	10.835	2.000	N-BK7	4.0	7.0
8		37.50	1.205	Mars Atm	3.4	7.0
9	Lens 2 - flint	-44.295	1.000	LF5	2.8	7.0

STO		14.410	0.629	Mars Atm	2.5	7.0
11	STOP	Infinity	1.461	Mars Atm	-	2.3
12	Lens 3 - crown	63.87	1.206	N-BK7	2.9	7.0
13		-18.71	46.091	Mars Atm	2.3	7.0
IMA	CCD	Infinity			12.3 square	12.3

Figure J-11. A cross section through the Phoenix SSI lens design showing the contact points for the first and third element. The second element has flat faces both sides.

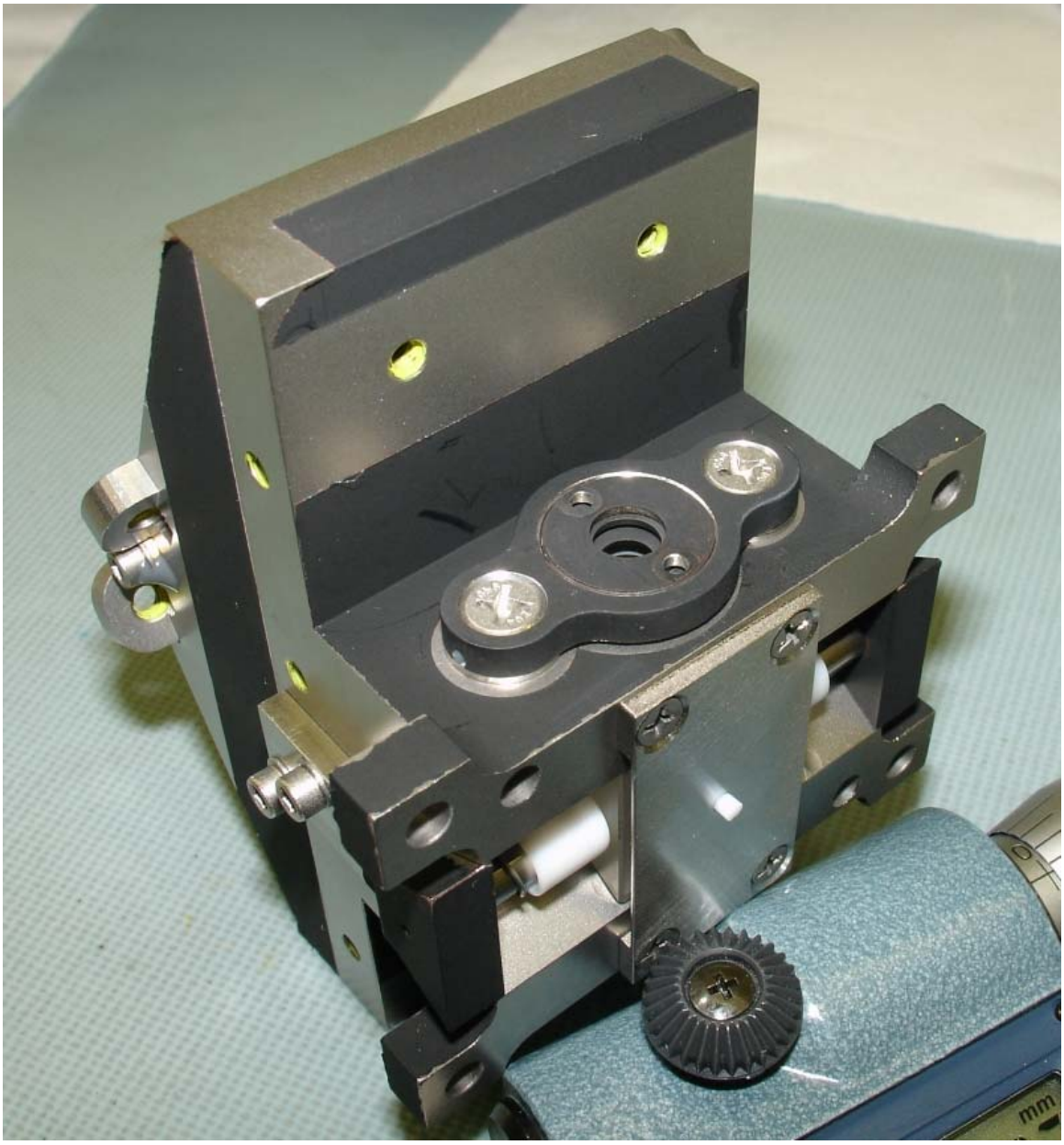

Figure J-12. This image shows the lens cell assembly installed in the optical housing. The prism which acts as the second fold mirror is also shown held in the V groove in the bottom of the optical housing.

K - Optical Alignment - RT

K.1 Optical Alignment Test Setup and Data Acquisition

The FM SSI camera was installed in the Magi Group, Lunar and Planetary Lab, UofA (MAGI) alignment beam fixture in the LPL clean room. The target was the MAGI MTF and alignment target set at 3000 millimeters from the front of the camera end plates. The camera gimbal assembly was assembled to the camera head. The camera head was held by the end plates in a set of V blocks. The covers were off the camera head to expose the optical

bench for adjusting the alignment. The target was set to be at the height of the optical axis which is 12 mm above the elevation axis. The target and camera were set to be perpendicular to the axis from the center of the camera to the center of the target. The data set was taken right after completing the alignment and all the alignment screws torqued. This data set was taken 4/28/2006. The test setup is shown in figure K-1. The alignment values and their uncertainties are shown in table K-1.

The camera was run using an adapter cable to mate the MER BCE to the Camera Head internal cable. The images were downloaded from the MER BCE. The images were taken first in one eye, then the other. The fixture was stiff enough not to cause any shifting in the camera position as the cables were unplugged and plugged to change eyes. For each eye, 3 images were taken along with 3 dark frames in the red stereo filters, filter #1. The images have the null strip attached.

Table K-1. Alignments and uncertainties

Alignment item	value	units	Uncert.	units
Distance from front of optical bench to target	3000	mm	±3	mm
Level of optical bench front/back and side to side	0	mrad	±0.4	mrad
Side to side and front/back alignment of target	0	mrad	±1.0	mrad
Perpendicularity of camera to camera to target axis	0	mrad	±4	mrad
Perpendicularity of target to camera to target axis	0	mrad	±4	mrad
Height difference between optical axis and target center	0	mm	±3	mm
Distance from face of optical bench to entrance pupil	109.65	mm	±0.5	mm
Distance from entrance pupil to center of camera	75.44	mm	±0.5	mm

The distance of the dots on the target were inspected and found accurate to within 0.5 mm of the nominal distance. The nominal distance is shown in table K-2.

Table K-2. Nominal Distance of dots from center dot. This is for both the vertical and horizontal dots. The outer two sets of dots are outside the FOV at 3.0 meters distance.

Distance ID	3.0 m	2.5 m	2 m	1 m	Center	1 m	2 m	2.5 m	3 m
Distance from center on target - mm	354	292	231	115.5	0	115.5	231	292	354

K.2 Optical Alignment Data Processing

Each of the three images was dark corrected with a different dark frame. For some of the computations, the width of the null strip on the left side of the image was removed. It is 17 pixels wide for the right image and 15 pixels for the left image. A raw image file with no header was then saved. This was done with the IDL viewer version 1.03 written by Adam Shaw on 6/6/07 using the image math capability to dark subtract an image.

The dots on the target were centroided by the image viewer with a 20x20 pixel box. The centroid positions were entered into the spreadsheet Initial_alignment_4-28-06.xls. The centroids for each of the vertical dots were averaged for the three images to get an average x,y position for each vertical dot. Then the width of the null strip is subtracted from the average of the x axis positions for the dots. For the y axis the average of the y axis positions was used. This gives a measurement of the center of the target. The actual images used are shown in the spreadsheets where the calculations are done. The images used are in the support directory for this section.

The data for the 3 frames were averaged together and used for the alignment analysis. The width of the null strips was subtracted from the centroid data to calculate the alignment relative to the center of the image area.

The distance to the target was measured from the center of the target to the cover of the SSI camera. The internal optical distance was determined from mechanical design of the camera head and the Zemax model of the lens. The position of the entrance pupil from the first surface was determined from the Zemax model. This model is in the file, 07_Baseline_w_spectrum_radii_FM_Design_12-11-06.zmx. The distance from the cover to the entrance pupil was found to be 109.65 mm. This distance was added to each of the target distances. The data was taken with the target at the 3000 mm distance.

K.3 Optical Alignment Results

The SSI is aligned to within 2 pixels of the ideal center of the target. The left eye is slightly left of center and the right eye is slightly right of center. The actual stereo crossing distance is

calculated by dividing the entrance pupil spacing/2 and dividing by the average toe in and then subtracting the internal distance. This puts the stereo crossing distance at 3042 mm slightly over the target of 3000 mm. The vertical bore site alignment is within 1 pixels or 0.26 mrad of nominal, the difference between the eyes is 0.5 pixels or 0.13 mrad. The alignment results are shown in Table K-3.

Table K-3. Alignment and stereo crossing distance results.

RAW image cooridinates	X - pixels	Y - pixels	Units
Average of Left image vertical dots centers	527.91	510.78	Pixels
Average of Right image vertical dots centers	527.23	511.27	Pixels
Left image null strip width	15		Pixels
Right image null strip width	17		Pixels
Corrected x centers after null strip removal.			
Average of Left image vertical dots centers	512.91	510.78	Pixels
Average of Right image vertical dots centers	510.23	511.27	Pixels
Ideal Center of image. (pixels numbered from 0 to 1023)	511.500	511.500	Pixels
Left Error from ideal center	**1.411**	**-0.716**	Pixels
Right Error from ideal center	**-1.268**	**-0.229**	Pixels
Difference in eyes L-R	**2.679**	**-0.488**	Pixels
Angle of toe in - nominal	24.26		mrad
Angle of Left toe in - actual	**23.92**		mrad
Angle of Right toe in - actual	**23.96**		mrad
Average toe in	23.94		mrad
Vertical Boresite Error - Left	-0.17		mrad
Vertical Boresite Error - Right	-0.05		mrad
Nominal stereo crossing distance	**3000**		mm
Separation of entrance pupils	**150.88**		mm
Actual stereo crossing distance.	**3042**		mm

The rotational alignment of the two eyes to the vertical and to each other is calculated by fitting a line to the center of the vertical dots on the target for each eye. The slope of the line gives the alignment of each eye to the vertical. The difference is the eye to eye rotation alignment. The results show that the SSI CCD's are rotationally aligned to the optical bench to within 1 mrad, and to less than 1 mrad to each other, see table K-4. The uncertainty is about 1.0 mrad is limited by the target vertical uncertainty.

Table K-4. Rotational Alignment results, positive values are rotation in CW direction.

Left Rotation	0.95	mrad

Right Rotation	0.27	mrad

K.4 Filter to Filter Alignment Test Setup

The FM SSI camera was installed in the Magi Group, Lunar and Planetary Lab, UofA (MAGI) Thermal Vacuum Chamber. The camera was not thermally strapped to the thermal plate during this test, only radiative cooling was used. The camera was mounted on the vertical cold plate which is at the back of the horizontal cold plate. The camera elevation is set to the zenith stop with the elevation motors. This positions the camera as close to the windows as possible, eliminating vignetting by the chamber windows, see figure K-3. The camera was aimed at the MAGI MTF and alignment target, see figure K-4. The target has dots which can be centroided with sub pixel precision (±0.1pixels), which allow detection of changes in the alignment when different filters are moved in front of the lenses. The target was aligned to within ±25 mm of the height of the camera in the TV chamber. The target was set at 3 m ±100 mm from the face of the camera, this is the stereo crossing distance for the SSI camera. Because of the large tolerance on the alignment, the absolute position in the images is not accurate, however the relative alignment change between filters, and between temperatures is accurate. The TV chamber was jacked up and down with its adjustable feet to level the optical axis of the camera. Images were taken of the target with IFSW and saved away in the data directory.

The data was taken June 21st and 22nd, 2006 The test conditions were; room temp with the cover off, room temperature with cover on and under vacuum, vacuum at -15C and vacuum at -65C optical nominal temp. The actual optical bench temperature for these conditions was 27C for the room temperature, -18C for the -15C nominal, and -77C for the -65C nominal. The optical bench surrounds the filter wheels and holds them and all the optical components. This temperature should be the most representative temperature for the filters, the optical housing, and optics mounting hardware. These are the items that will control the optical alignment of the camera over temperature. The solar filters were not tested as they could not generate a centroidable image with this target brightness. The temperatures came from the log file

K.5 Filter to Filter Alignment Data Processing

The images were first corrected for the 1 column shift that occurred in the early flight software. This was done using the IDL program, reattach_dark_strips_new.sav which is in the support directory for this section. The program reads in the original image and null strips and assemblies them into the original

1024x1056 image. Then it corrects for the 1 column shift error in the original image. Then it removes the null strips and saves them as separate files. The Instrument Flight software version used at this time had a software bug that caused the image to be shifted by 1023 pixels if viewed as a serial data stream. This meant the image was offset by one column and the first column was off by one pixel vertically.

The images were then dark subtracted and shutter corrected. A image file with no header was then saved, along with a TIF image. This was done with the IDL program alignment_processing.prj dated 5/21/07. The version of dark model used was generate_dark_frame_pro which used a data file, all_dark_coeffs.sav, both dated 9/29/2006. For the -15C and -65 C data there was no measurable change in centroids after the dark and shutter correction, the change for the room temperature data was less than 0.2 pixels and it was random in direction.

The data is stored in the support directory for this section. In that directory there are subdirectories for data at nominal -15C, -65C, and, 23C cover on vacuum. Each directory has three sub directories; RAW for the raw data, 1st col corrected which has the 1 column shift corrected images, and dark_and_shutter_corrected for 1st col corrected images that are also dark and shutter corrected. ~~I used~~T~~-~~he images without the reference strip were used. There were two images and 1 shutter image for each ~~filter,~~filter; ~~I~~ just ~~used~~ the first image and shutter for each filter was used.

Each of the dark and shutter corrected image was centroided with the centroid routine used in program alignment_process2.prj dated 5/22/2007. The centroid routine was elipse_centroid.pro dated, 5/21/2007. The centroid data was written to a file in csv format. This file was read by Excel and incorporated into a spreadsheet, named Alignment_over_temp_Centroiding_2007-7-14.xls. All the IDL programs used and their support programs are in the IDL directory in the support files directory.

Filter L11 was saturated for all dots for the room temperature condition, so there is no data for this condition. In addition, at room temperature, the left side dots were saturated for several left eye filters, therefore these filters have fewer data points than the rest of the filters. The colder temperature data for the left eye was correctly exposed. The right side images were correctly exposed at all temps.

The spreadsheet calculated the difference in the x and y coordinates for each filter relative to filter 1. These were averaged together for each temperature. Then the three temperatures were averaged together.

The optical bench temperature was derived from the log files from the housekeeping system during that time. The file used is SEQ_FLAT_FIELD_FM_TESTING_06-17-06.log which is found in the support directory.

K.6 Filter to Filter Alignment Results

The filter to filter alignment was tested to determine the effect of any wedge in individual filters. The wedge in the filters was controlled to cause less than 1 pixel alignment error. The errors are all less than this except for the diopter and polarization filters verifies that the wedge was controlled for the normal filters. Since the filter surfaces are flat, any positioning errors of the filter wheel will not change the alignment error between a filter and filter 1, the reference.

The filter to filter alignment was compared to filter 1 for each eye. Table K-5 shows the average X axis and Y axis misalignment compared to filter 1 for left eye filter in pixels; Table K-6 shows the same data for the right eye filters. The x axis data is the average of all the x axis differences in dot positions for one temperature. The standard deviation column shows the standard deviation of those differences.

The data for the left eye filters shows that the typical alignment change is 0 to 0.2 pixels. Since the standard deviation of the alignment change is about 0.12 pixels. The centroid uncertainty is about 0.1 pixels. This means the average alignment change at each temperature is not very significant. Therefore averaging of the three temperatures together was done to reduce the uncertainty. The standard error of the mean is significantly less than the average alignment error. The alignment changes are significant if they are more than 3 times the standard error. About half the filters have significant alignment effect, all less than 0.2 pixels.

The right eye filters, are divided into three groups. The first group is normal filters like R2, R8, R10, R11, and R12. These filters all show average alignment changes that much greater than the standard error and so are significant. The alignment change is a maximum of 0.14 pixels and the standard error is typically 0.014 pixels. This error is slightly lower than the left eye filters, due to the right eye exposures being shorter and slightly better SNR images due to the lower dark current.

The second group of right eye filters is the two diopter filters, R6 and R7. These filters have optical power, they are a combination of the normal filter and a plano-convex lens. They show larger alignment differences and much larger standard deviations in these differences. This is due to the sensitivity of the diopter lens to final filter wheel position. The backlash of the filter

wheel motor allows the lens to be slightly off center when the filter wheel stops vibrating from a step. This makes the lens a slight prism and deflects the beam significantly. The largest alignment difference is in the X axis which is the axis of filter motion. The large standard deviations show that this varies each time the wheel is positioned. The differences in alignment are still many times the standard error indicating that these errors are significant. These average alignment differences can be built into a model for pointing by filter, however there still will be large differences from image to image.

The third type of filter is the polarization filter, R9. This filter has a significant alignment difference with R1 due to the two piece design of the filter. This filter is made of a filter element cemented to a polarization element. The polarization element or the cementing operations likely has significant wedge. The result is a consistent alignment difference with R1 of about 2 pixels in X and Y axis which much larger than the standard error of .01 pixels. The standard deviation of the alignment is low at 0.09 and 0.10 pixels indicating very repeatable alignment.

The standard error for the filter to filter alignments is typically 0.025 pixels or 0.006 mrad and the worst case filter is 0.101 pixels which is 0.024 mrad.

Filter to Filter Alignment Summary:

All the filters should have alignment correction to get down to less than 0.1 pixels misalignment. The two diopter filters should still be expected to show large variations in alignment. There does not appear to be any significant temperature related component to the alignment between filters. The recommended alignment corrections are shown in Table K-7. These corrections are applied to a filter N image to align it with the filter 1 image. They are opposite in sign to the errors shown in tables 1 and 2. The conversion from pixels to mrads was done with the conversion factors of 0.2376 mrad/pixel for the left eye and 0.2353 mrad/pixel for the right eye. A positive correction will move the image up and to the right to align with the filter 1 image.

Table K-5. Left eye filter alignment relative to Filter L1 in pixels.

		+27.5 C		-18.3 C		-77.5 C		Average over all temps			
Filter	Axis	Average	Standard Deviation	Average	Standard Deviation	Average	Standard Deviation	Average	Standard Deviation	Standard Error of mean	number of samples
L2	X	-0.06	0.12	0.14	0.05	0.00	0.10	**0.03**	0.13	**0.018**	50
	Y	-0.03	0.11	-0.02	0.06	0.05	0.06	**0.00**	0.09	**0.013**	50
L6	X	-0.22	0.09	-0.05	0.08	-0.14	0.09	**-0.14**	0.11	**0.016**	50
	Y	-0.06	0.11	-0.17	0.09	0.03	0.08	**-0.06**	0.12	**0.017**	50
L7	X	0.03	0.09	0.13	0.07	0.09	0.05	**0.08**	0.08	**0.012**	50
	Y	-0.13	0.09	-0.28	0.07	0.02	0.08	**-0.13**	0.15	**0.021**	50
L8	X	-0.15	0.08	0.05	0.08	0.00	0.07	**-0.03**	0.11	**0.017**	48
	Y	-0.05	0.11	-0.16	0.08	0.01	0.09	**-0.07**	0.12	**0.017**	48
L9	X	-0.19	0.10	0.02	0.09	-0.11	0.10	**-0.10**	0.13	**0.019**	48
	Y	0.00	0.10	-0.12	0.10	0.11	0.08	**-0.01**	0.13	**0.019**	48
L10	X	-0.10	0.08	-0.05	0.08	-0.07	0.10	**-0.07**	0.09	**0.013**	48
	Y	0.03	0.10	-0.06	0.11	0.05	0.10	**0.00**	0.12	**0.017**	48
L11	X			-0.02	0.10	-0.13	0.14	**-0.07**	0.13	**0.022**	34
	Y			-0.16	0.09	0.04	0.12	**-0.06**	0.15	**0.025**	34
L12	X	0.22	0.26	0.20	0.08	0.17	0.12	**0.20**	0.15	**0.023**	45
	Y	0.23	0.18	0.01	0.13	0.18	0.11	**0.14**	0.17	**0.025**	45

Table K-6. Right eye filter alignment relative to filter R1 in pixels.

		+27.5 C		-18.3 C		-77.5 C		Average over all temps			
Filter	Axis	Average	Standard Deviation	Average	Standard Deviation	Average	Standard Deviation	Average	Standard Deviation	Standard Error of mean	number of samples
R2	X	0.09	0.08	0.04	0.09	0.08	0.09	**0.07**	0.09	**0.012**	51
	Y	-0.12	0.09	-0.16	0.09	-0.11	0.12	**-0.13**	0.10	**0.014**	51
R6	X	0.87	0.69	0.89	0.68	0.89	0.73	**0.88**	0.69	**0.096**	51
	Y	0.33	0.70	0.29	0.73	0.47	0.78	**0.36**	0.72	**0.101**	51
R7	X	-1.13	0.55	-1.08	0.57	-1.14	0.63	**-1.12**	0.57	**0.080**	51
	Y	0.30	0.50	0.21	0.57	0.33	0.57	**0.28**	0.54	**0.075**	51
R8	X	0.11	0.08	0.05	0.06	0.11	0.08	**0.09**	0.08	**0.011**	51
	Y	0.04	0.08	0.07	0.08	0.14	0.07	**0.08**	0.09	**0.012**	51
R9	X	-1.98	0.07	-2.04	0.10	-1.94	0.06	**-1.98**	0.09	**0.013**	51
	Y	1.96	0.08	1.90	0.10	2.04	0.07	**1.96**	0.10	**0.014**	51
R10	X	0.11	0.05	0.09	0.08	0.11	0.08	**0.10**	0.07	**0.010**	51
	Y	0.03	0.07	0.03	0.06	0.06	0.06	**0.04**	0.06	**0.009**	51
R11	X	0.16	0.07	0.11	0.09	0.16	0.09	**0.14**	0.08	**0.012**	51
	Y	-0.05	0.07	-0.07	0.09	0.02	0.09	**-0.03**	0.09	**0.013**	51
R12	X	0.16	0.05	0.08	0.09	0.15	0.08	**0.13**	0.08	**0.011**	51
	Y	-0.04	0.07	-0.08	0.09	0.06	0.10	**-0.02**	0.10	**0.014**	51

Table K-7. Recommended alignment corrections for each filter to align images to Filter No1.

Alignment correction to be applied to images in these filters to make them align with filter 1 images.							
Filter	Axis	Pixels	mrad	Filter	Axis	Pixels	mrad
L2	X	-0.03	-0.006	R2	X	-0.07	-0.016
	Y	0.00	0.000		Y	0.13	0.030
L6	X	0.14	0.033	R6	X	-0.88	-0.208
	Y	0.06	0.015		Y	-0.36	-0.085
L7	X	-0.08	-0.020	R7	X	1.12	0.263
	Y	0.13	0.031		Y	-0.28	-0.066
L8	X	0.03	0.008	R8	X	-0.09	-0.021
	Y	0.07	0.016		Y	-0.08	-0.019
L9	X	0.10	0.023	R9	X	1.98	0.467
	Y	0.01	0.002		Y	-1.96	-0.462
L10	X	0.07	0.018	R10	X	-0.10	-0.024
	Y	0.00	-0.001		Y	-0.04	-0.009
L11	X	0.07	0.017	R11	X	-0.14	-0.033
	Y	0.06	0.015		Y	0.03	0.008
L12	X	-0.20	-0.047	R12	X	-0.13	-0.030
	Y	-0.14	-0.034		Y	0.02	0.005

K.7 Alignment change with temperature

The same set of data was analyzed in a different way to determine the change in alignment with temperature. The SSI has 3 point mounts for all optical components and the optical housing, optical bench, and CCD carriers are of Titanium, Aluminum, and Aluminum respectively. When the temperature change is large the different thermal coefficient of expansion will cause stress and distortion of these two components. The 3 point mount for the optical housing and CCD carriers are not symmetric, which will cause the CCD's to be shifted and rotated relative to the room temperature alignment.

The alignment over temperature shows a significant change in alignment. The data shown in Table K-8 shows that each eye points down with decreasing temperature and the camera becomes more cross eyed. The change is plotted with temperature in figure K-3. We expected 0.3 to 0.6 pixels of vertical change from our structure/thermal modeling; the actual change was 5.1 and 7.7 pixels vertical. The lateral error was 6.5 pixels from the model as compared to the 6.7 pixels measured. So while the model compared well with the lateral motion, the vertical motion was an order of magnitude off.

Some of the vertical change in pointing could be due to shrinkage and bending of the copper thermal plate when cold. We

did not have a means in place to measure this source of test error. The camera would have moved down 0.4 pixels due to the vertical shrinkage of the camera. The majority o Also there is a potential for tilt due to curvature of the rails the cold plate was mounted to. The rails are thermally isolated from the cold plate by stainless flexures. As the cold plate shrinks, the rails do not change in temperature as much and so shrink very little. The flexures put a bending moment on the rails that will cause them to curve up. Since the rails were only anchored at the front, any curvature would have raised the back of the camera up. This will tilt the camera down. The weight of the cold plate and camera assembly is significant in opposing this bending. If the runner tried to curve up, the weight would have forced it back against the base plate. The situation has been modeled and the amount of tilt would be small, less than 0.1 pixels. While this means the up down pointing with temperature should be primarily due to camera optical tilt, the complexity of the fixture leaves some possibility that some or all of this tilt is due to fixture bending. Other error sources are still possible, the cold plate them selves could develop some curvature with temperature change. They are made from OFHC copper which should have a consistent thermal expansion coefficient across the plate.

The data was generated by averaging the difference in the X values between each temperature for each filter. Then the filter data was averaged together to generate a shift due to temperature. This shift is significant, almost 8 pixels in the left and 5 pixels in the right. This is significantly more than the standard error. The correction is linear for the Y components and quadratic for the X components as shown in Figure 1. The correction was expected to be linear with temperature; the reason for the quadratic component measured for the x axis is not understood at this time. The accuracy for these corrections is given by the standard error of the mean, which is 0.045 pixels max.

The alignment change was only measured down to -75 C since testing of the camera has shown that the optical bench starts at -90C, it will be at a temperature of -~~65~~ 75 C by the time the PCB's and filter wheel motor have been heated to operational temperature of -45C.

Alignment over Temperature Summary.

The changes in optical axis pointing caused by temperature changes are significant and should be corrected with the data in Table K-9. This gives a formula for correcting any image to room temperature.

Table K-8. Average displacement of image center due to temperature change across all filters.

	O. B. Temp - Deg C	Mean displacement of all filters - Pixels		Std Dev of all filters - pixels		Standard Error of Mean - pixels		No of samples	
		X	Y	X	Y	X	Y	X	Y
Left Eye	27.5	0	0	0	0				
	-18.3	-2.47	3.36	0.12	0.06	0.044	0.021	8	8
	-77.5	-3.77	7.70	0.13	0.06	0.045	0.022	8	8
Right Eye	27.5	0	0	0	0				
	-18.3	0.82	2.26	0.04	0.04	0.015	0.013	9	9
	-77.5	2.89	5.11	0.02	0.05	0.006	0.018	9	9

Table K-9. Recommended corrections to images to correct for pointing changes with temperature of the optical bench in the camera head. The formula for the correction is Corr (in pixels) = C0 + C1*T+C2*T^2

	OB Temp - deg C	X		Y		Fit to data - pixels		
		Pixels	mrad	Pixels	mrad	Coefficient	X	Y
Left Eye	27.5	0.00	0.000	0.00	0.000	C0	1.634	-2.0179
	-18.3	2.47	0.586	-3.36	-0.799	C1	-5.11E-02	0.0734
	-77.5	3.77	0.894	-7.70	-1.830	C2	-3.05E-04	0
Right Eye	27.5	0.00	0.000	0.00	0.000	C0	-4.10E-01	-1.3466
	-18.3	-0.82	-0.193	-2.26	-0.531	C1	1.94E-02	0.0486
	-77.5	-2.89	-0.681	-5.11	-1.201	C2	1.63E-04	0

Figure K-1. The SSI camera head alignment test setup showing the SSI camera head about to be clamped in the alignment fixture. The target is shown at 4.3 meters distance. Here the upper cover is on the camera for protection.

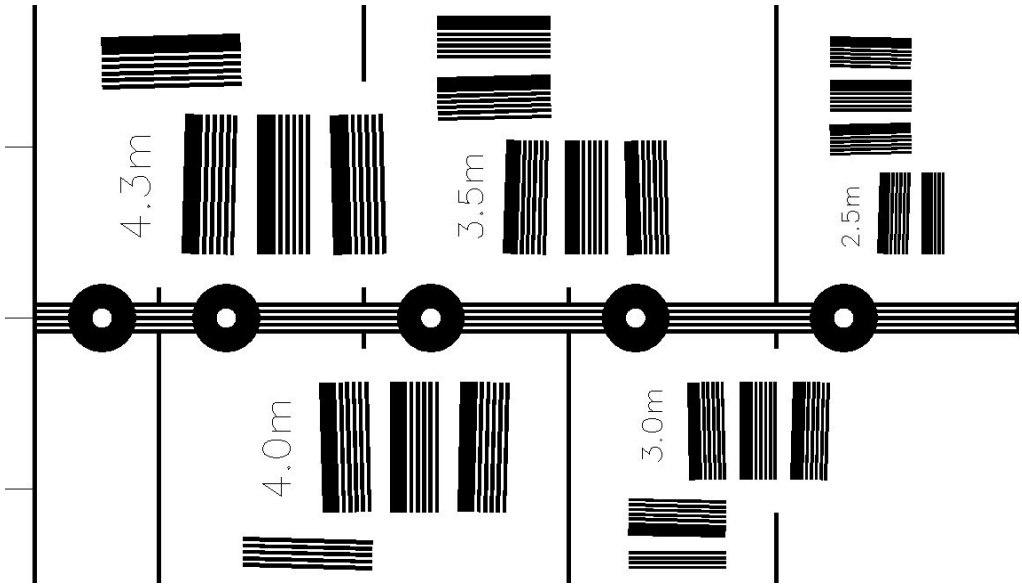

Figure K-2. Section of the MAGI group MTF and Alignment Target. The white dots in the black circles are the centroid targets. The bars are for MTF testing.

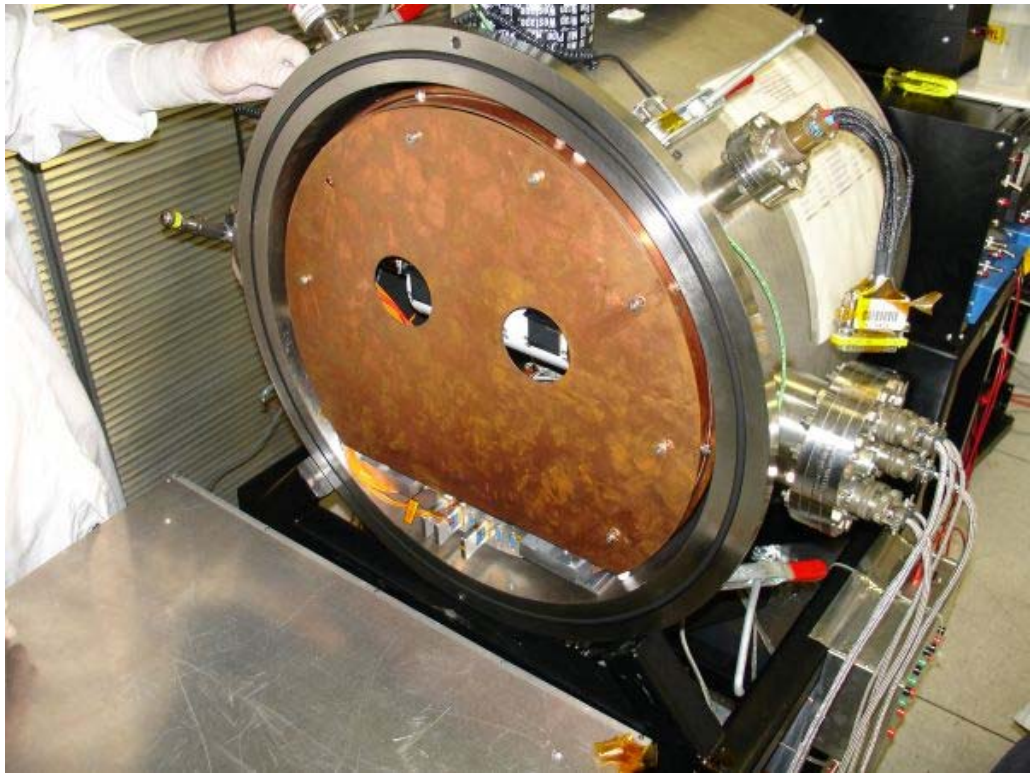

Figure K-3. The camera installed in the MAGI Thermal Vacuum Chamber. The chamber cover is not installed yet. The camera views the outside though the holes in the shield and two windows in the cover in line with the holes.

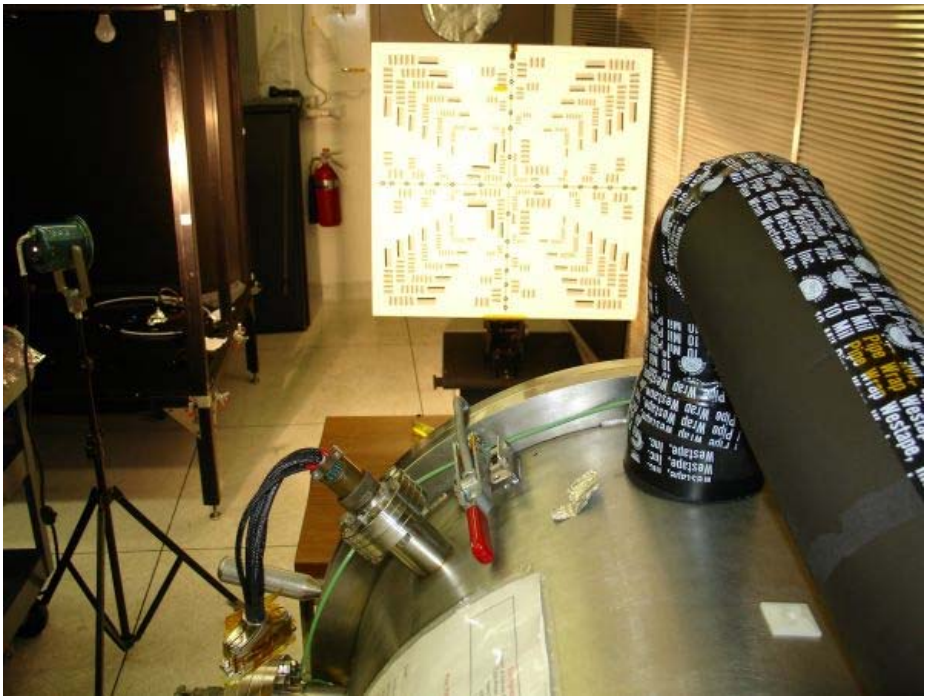

Figure K-4. The camera's view of the target.

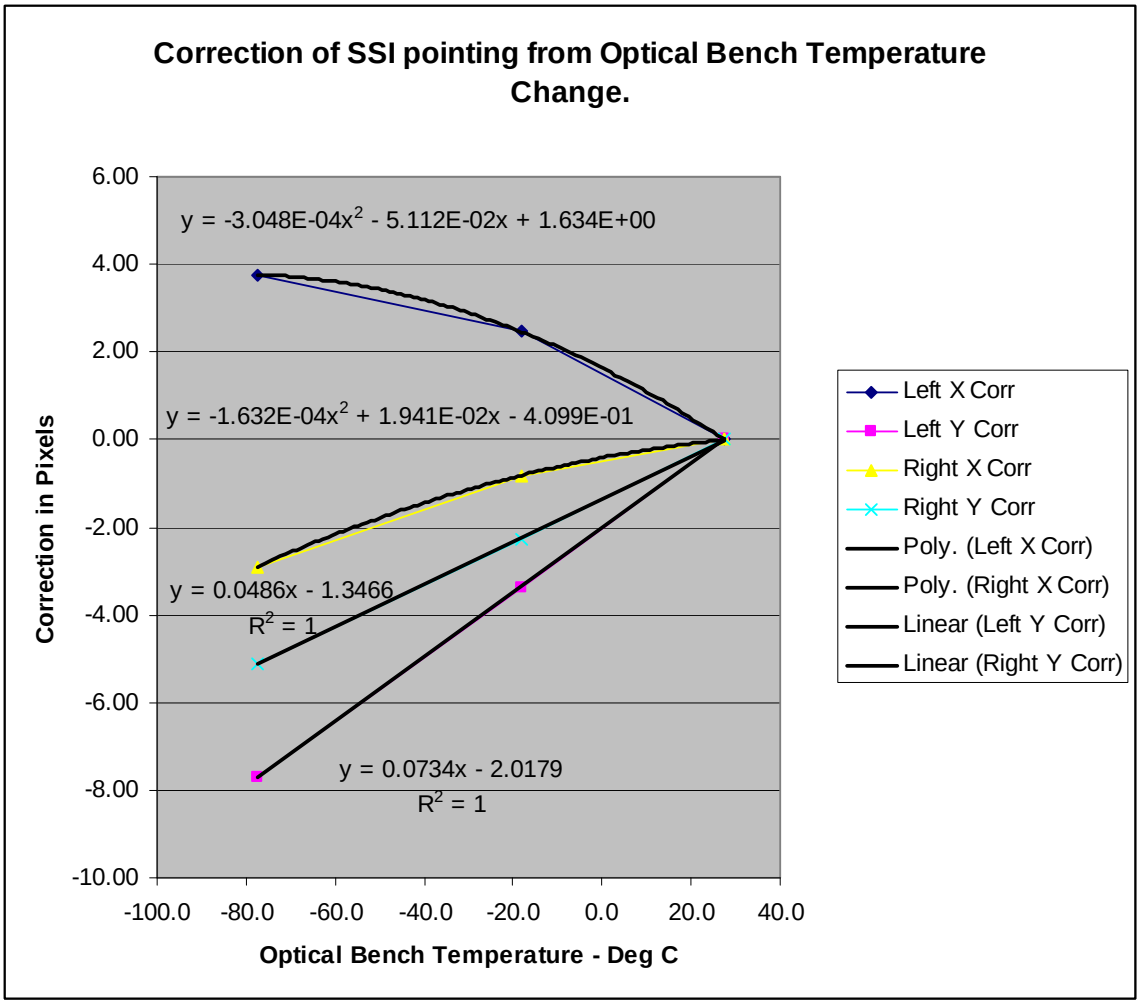

Figure K-5. Shape of correction vs. temperature for each eye and direction.

L - Image Scale and Distortion - RT

L.1 Image Scale and Distortion Test Setup and Data Acquisition

The images for image scale calculation came from the following three data sets. The data sets correspond to the following events:

4-28-06 Finish of alignment of CCD's and fold mirrors during assembly.
5-3-06 Finish of vibration acceptance testing.
7-14-06 Just before camera was shipped, after thermal cycling and all other

There was no significant change in image scale during this period, at least less than the test to test repeatability. For the 4-28-06 data set, the images were dark subtracted and three images for each eye were averaged in the analysis. The 5-3-06 and 7-14-06

data set were based on a single image in each eye, which was not dark subtracted. All the data was taken in the red stereo filter, (L1, R1) and with the target at 3.0 m.

The test setup for the 4-28-06 data is described in section K.1 of this report. For the later data sets the setup was slightly different. The camera was installed in the Magi Group, Lunar and Planetary Lab, UofA (MAGI) alignment beam fixture. The camera was fully assembled and was tested with the mast stowed on a support fixture with the camera head optical axis at the height of the MAGI MTF and alignment target. The camera was rotated with its gimbal motors to align with the target. The camera was run with the MAGI GSE and the IFSW, version 4.2. The images are available in the support directory for this section, in the Image Data subdirectory. The uncertainties in the test setup are the same as listed in table K-1.

L.2 Image Scale and Distortion Data Processing

The positions of dots in the images were centroided with the Phoenix image viewer, versions 1.00 and 1.03. The positions were entered into a spreadsheet and the image scale over the field of view was calculated and fit with a second order curve to account for the distortion. The 4-28-06 data is in the spreadsheet – Initial_alignment_4-28-06_data.xls. The rest of the data is in the spreadsheet – Scale_dist_after vib_and_last_images_5-3-06_and_7-14-06_data.xls.

The image scale for this camera is nominally 0.236 mrad/pixel. The actual image scale for each eye was determined by measuring the position of the dots in pixels. The distance in pixels was calculated for each dot from the center dot. For the vertical target dots, the angle the target dot was from the center was calculated as:

AngleOp = arc tan (dist from center dot / (distance to target+camera head internal dist))

Image scale = AngleOp / pixels from center

For the horizontal target dots, the angle had to account for the toe in angle of the camera and the offset of each eye from the center of the camera-target axis. The horizontal dots were only used in the scale calculations for the 4-28-06 data set. The calculation was as follows:

The angle of the dot from the mechanical axis of the camera head is calculated:

AngleM = Arctan ((Distance of dot from center on target ± Pupil offset) / Distance to target)

Where the pupil offset is 75.4 mm for each eye and the distance to target was 3109.65 mm.

The angle the dot is from the optical axis is then the toe in plus-minus this angle.

AngleOp = Toein ± AngleM

Image scale = AngleOp / pixels from center

The distance of each dot from the center was found from the drawing for the target. The target was inspected and found to be within ±0.5 mm of the drawing distance. The distances for each set of dots are shown in table L-1. They are labeled for the distance that they would just fit into the SSI FOV.

The distance in pixels was divided by the actual angle of the dot to get the average image scale from the center to that dot in mrad/pixel. The distortion caused the average image scale to each dot to drop slightly as the dots distance increased from the center of the field. This is barrel distortion; the squares on the image target are slightly bowed out at the middle of the side. For each data set, the image scale was fit to a curve for image scale that has a second order term to account for the distortion. Then the fit equation coefficients from each data set were averaged together to get a single set of coefficients for the image scale equation. This equation was used to get the image scale at the center which is reported as the image scale. The equation was also used to get the image scale from the center to the edge to get the Field of View (FOV). This value was multiplied by 2 and converted to degrees to get the total width of the FOV.

Table L-1. Distance for each dot from the center on the MAGI MTF and distortion target.

Dot identification	Dist from center - mm
1.0 m	115.5
2.0 m	231
2.5 m	292
3.0 m	354
3.5 m	415
4.0 m	476
4.3 m	513

L.3 Image Scale and Distortion Results

The image scale and fit curves for three tests are shown in Figures L-1, L-2 and L-3. Each of the data sets is fit very well with its fit curve, typically with a R^2 value of >0.98. The fit data for the three data sets is shown in Table L-2. While the first data set looks like it is slightly smaller scale than the other two, the difference is very small and can be accounted for by a 0.7 mm change in the camera to target distance. The accuracy this distance was set to was ±3 mm.

The center scale (C0) and the distortion factor (C2) were the average of the fit data from the three data sets. Each of the three data sets is compared to the averaged fit curve in Figure L-4. The uncertainty of the center scale is less than 0.05%. The uncertainty in the C2 factor is larger at 6.4 and 2.2%; however this results in an image scale uncertainty in the corner of less then 0.07%. So the scale uncertainty over the FOV is less than 0.07%.

The image scale for a selection of pixel distances from the center is shown in Table L-3. The corner of the image is at 724 pixels from the center. This table also uses the value for image scale at the edge 512 pixels to calculate the FOV. The results are 13.88 degrees for the left eye and 13.74 degrees for the right eye. The overlap requirement for panoramas is minimum 20 pixels (.27 degrees) plus the pointing uncertainty (0.5 degrees). This is about 0.77 degrees. This means that a 12 degree step for a pan will still have 1.74 degrees of overlap, compared to the 0.77 degree requirement.

Table L-2. Summary of scale and scale factor for distortion.

Center scale	**Center scale - L - C0**	**Center Scale - R - C0**	**Eye mismatch**	**L scale factor C2**	**R scale factor - C2**
4-28 3.0 m data	0.23751	0.23517	0.99%	**-4.2502E-03**	**-3.84E-03**
5-23 3.0 m data	0.23758	0.23533	0.95%	-3.9333E-03	-3.8665E-03
7-14 3.0 m data	0.23755	0.23537	0.92%	-3.7471E-03	-4.0019E-03
Average All	**0.23755**	**0.23529**	**0.96%**	**-3.9769E-03**	**-3.9013E-03**
Std dev of all	0.00004	0.00010		2.54E-04	8.85E-05
St dev in %	0.01520%	0.04460%		6.39719%	2.26941%

Table L-3. Image scale from fit curve, distortion, and FOV calculations.

C0	0.23755	C0	0.23529	
C2	-3.9769E-03	C2	-3.9013E-03	
Pixels off axis	Image scale - mrad/pixel - LEFT	Distortion - %	Image scale - mrad/pixel – RIGHT	Distortion - %

0	0.23755	0.00%	0.23529	0.00%
100	0.23751	-0.02%	0.23525	-0.02%
200	0.23739	-0.07%	0.23513	-0.07%
300	0.23719	-0.15%	0.23494	-0.15%
400	0.23691	-0.27%	0.23467	-0.27%
500	0.23655	-0.42%	0.23431	-0.41%
512	0.23651	-0.44%	0.23427	-0.43%
600	0.23612	-0.60%	0.23389	-0.60%
724	0.23546	-0.88%	0.23324	-0.87%
Image scale = C0 + C2 * (pixels from center / 1000)^2				
	LEFT		RIGHT	
FOV - Degrees	13.88		13.74	

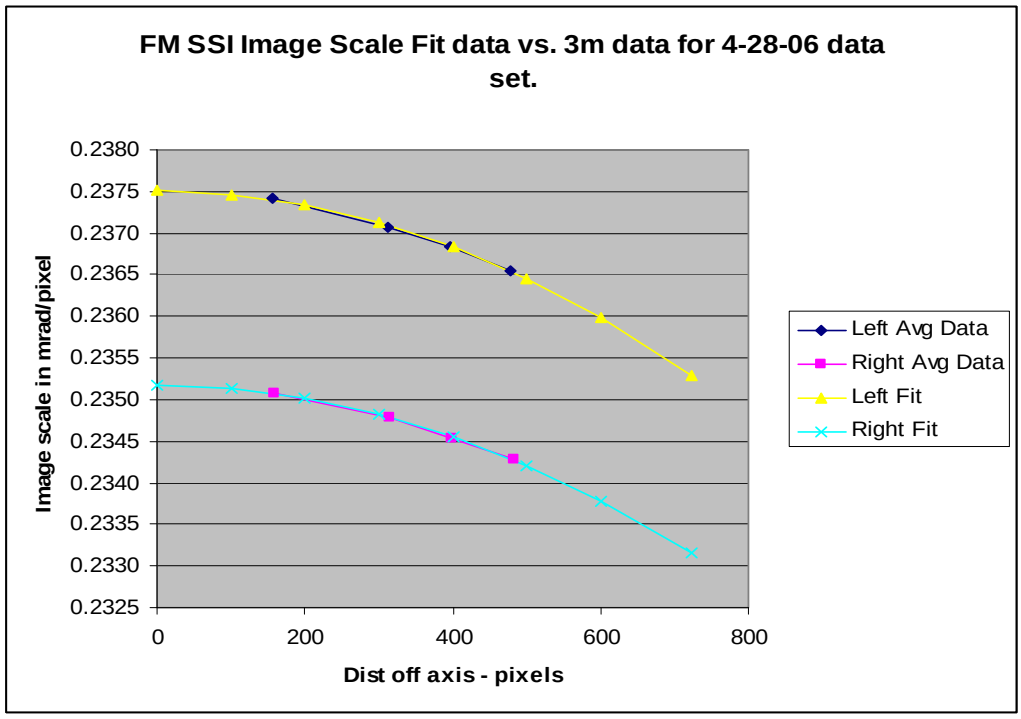

Figure L-1. Image scale and fit for 4-28-06 data set.

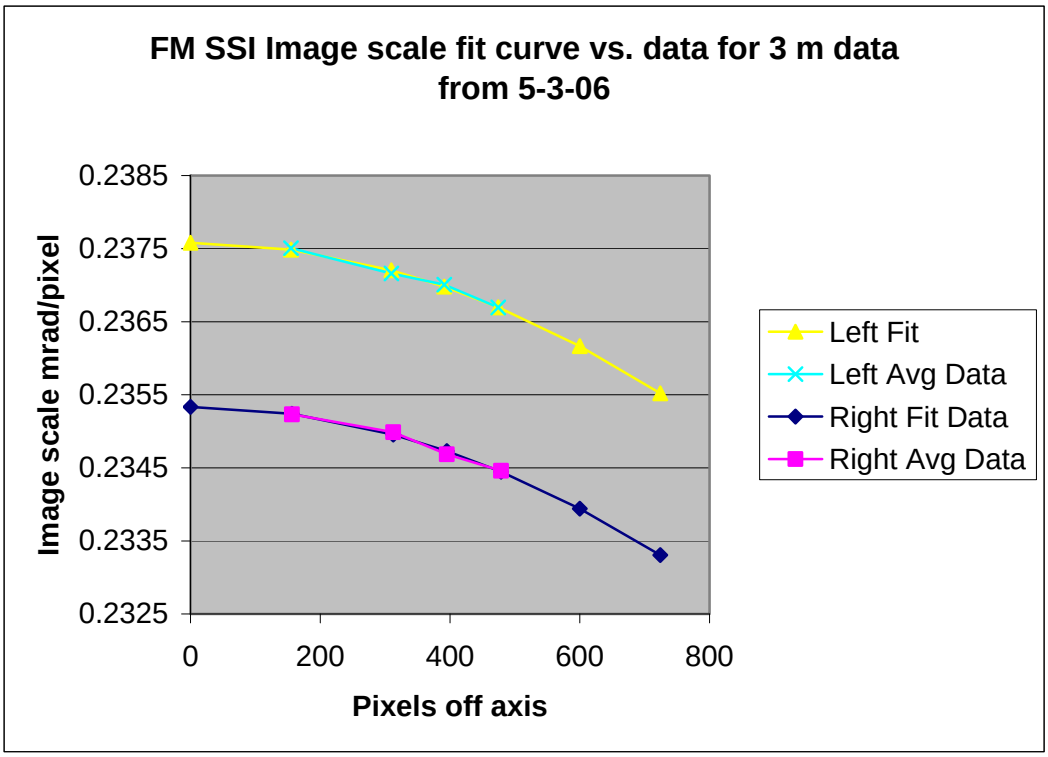

Figure L-2. Image scale and fit for 5-3-06 data set.

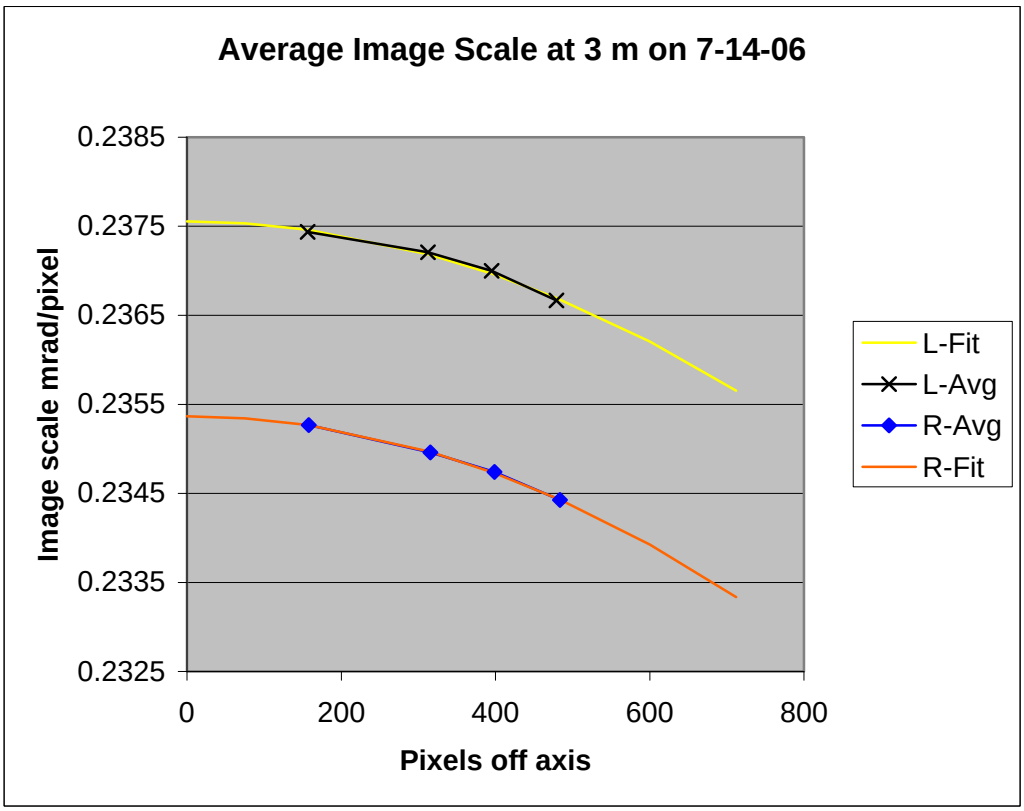

Figure L-3. Image scale and fit for 7-14-06 data set.

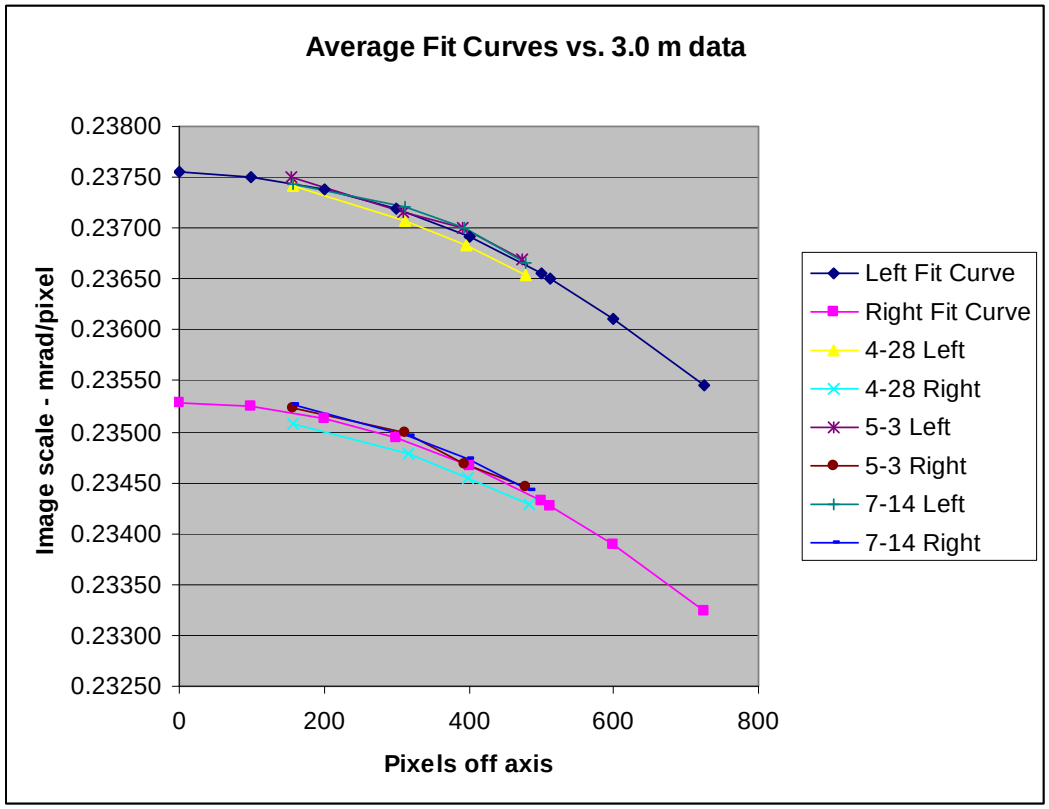

Figure L-4. Comparison of the three data sets with the average fit curve for each eye.

L.4 Image Scale Change with Temperature Test Setup and Data Acquisition.

The test setup and data acquisition was the same as the filter to filter alignment testing described in K.4.

L.5 Image Scale Change with Temperature Data Analysis

The data processing and analysis was done the same as the filter to filter alignment processing described in K.5.

L.6 Image Scale Change with Temperature Results

The image scale was expected to increase with decreasing temperature due to the contraction of the optical housing reducing the lens to CCD distance with temperature. This change in spacing for the Titanium optical housing is should increase the image scale +0.09% when going from room temp to -77C. The positive change is due to the lens to CCD distance decreasing, which increases the angle subtended by each pixel. The data actually shows a negative

change in image scale with decreasing temperature, which means each pixel is subtending a smaller angle. In addition, the change in image scale is different for the X and Y axis, see Figures L-5 to L-8. The average over all the filters is shown in Figure L-9. This shows a slightly non linear change with temperature. The amount of change in the X axis is about twice of that in the Y axis. The scale change is not significantly different in each filter.

At this time the reason for the difference is speculative. The first fold mirror could cause this affect due bending of the mirror in its cell. This bending would have to form the mirror into a 75 m concave radius for the X axis or long dimension and a larger radius in the y axis or short dimension. This is a very slight bend; the sag is just 4.5 microns. The reason for the scale change asymmetry could be due to the difference in bending in each axis, the mirror may bend about twice as much in the x axis (mirror long axis) as the vertical axis (mirror short axis). This bending would not have much effect on the image quality since the footprint of any one pixel on the first fold mirror is only 2.5 mm in diameter. The mirror mount for the first fold mirror is very stiff in the x axis and so may stress the mirror more when it shrinks more than the mirror at low temperature. The Y axis of the mount is much more compliant and the mirror is stiffer resulting in a smaller amount of deflection.

The data in Figure L-9 was fit with quadratic curves and the coefficients are given in Table L-4. The correction curves calculation is also listed in the table. The correction would be 0.35 percent for the left eye X axis. This is about 1.75 pixels at the edge of the image which corresponds to about 2.6 cm of distance error. It must be corrected to do any accurate stereo range mapping at the edges of the image. The change with different filters is less than 10% of the amount of the correction, so the correction can be applied independent of filter.

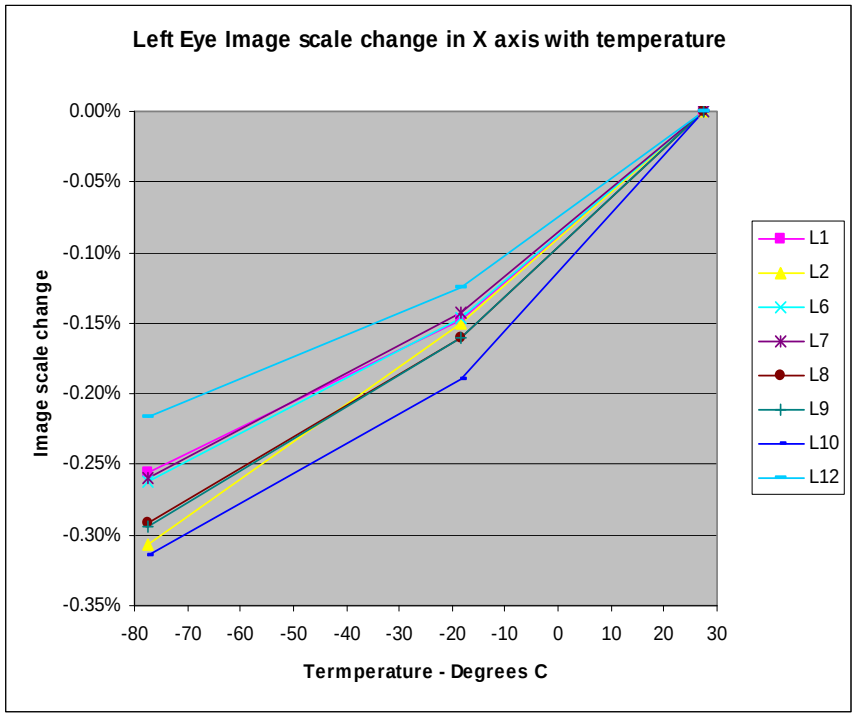

Figure L-5. Change in left eye image scale for the X axis for each filter.

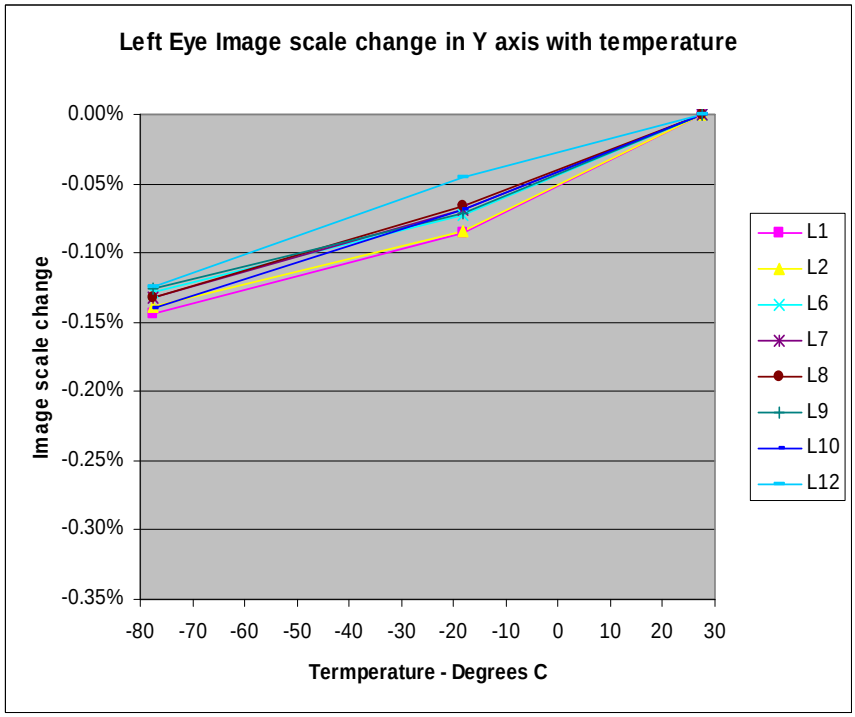

Figure L-6. Change in left eye image scale for the Y axis for each filter.

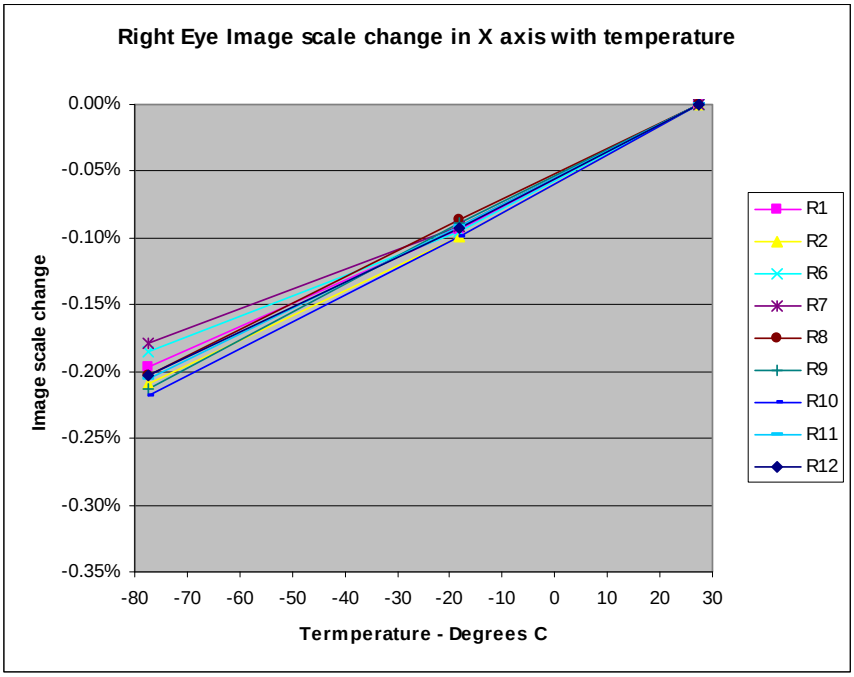

Figure L-7. Change in right eye image scale for the X axis for each filter.

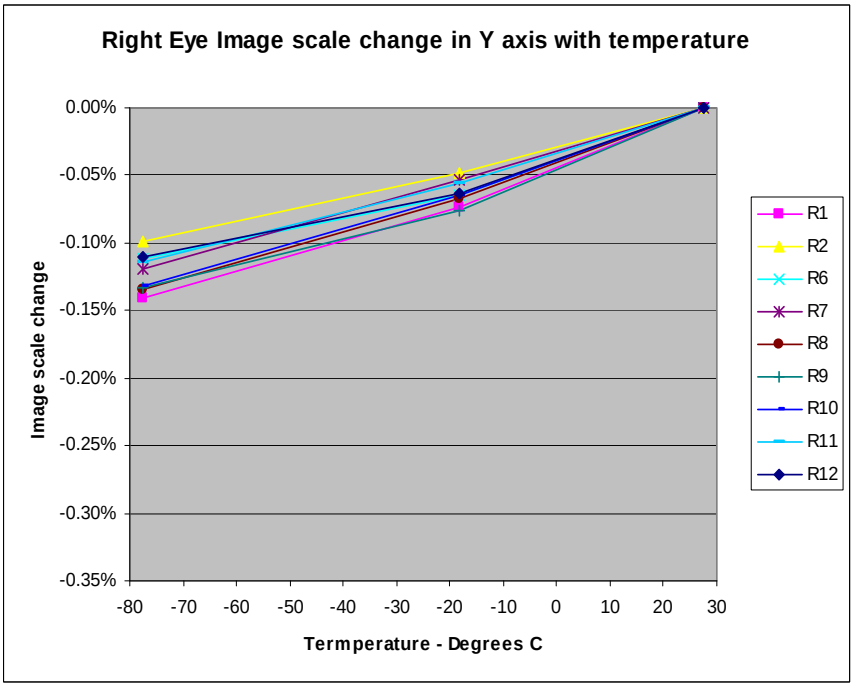

Figure L-8. Change in right eye image scale for the Y axis for each filter.

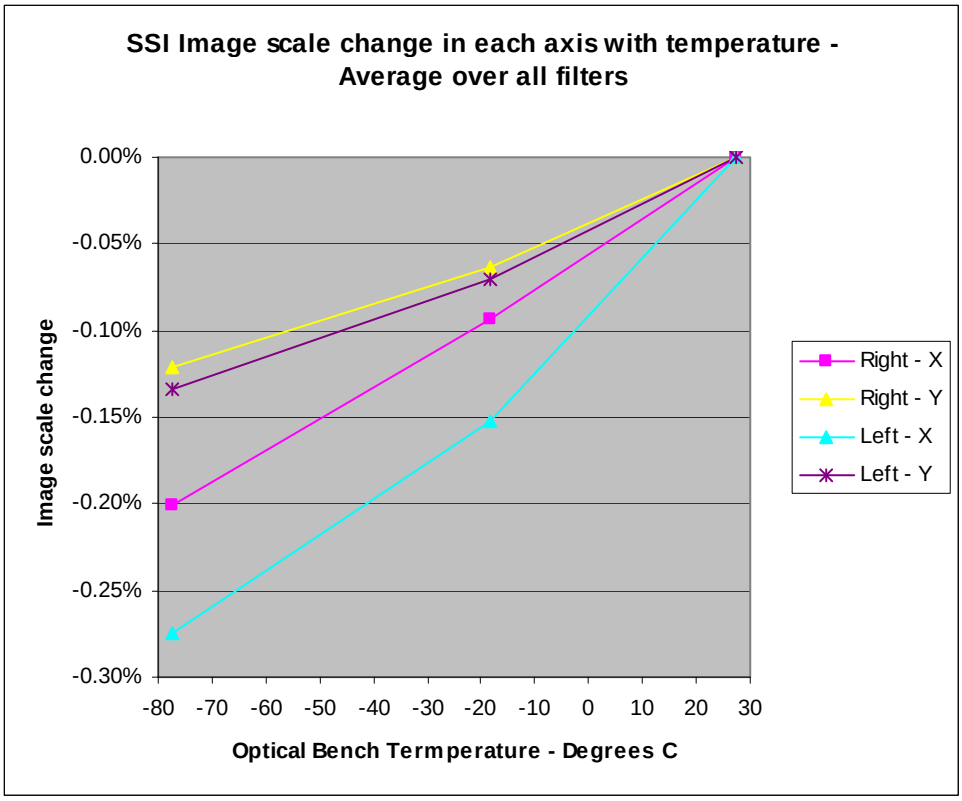

Figure L-9. Change in image scale averaged over all filters for each eye and axis.

Table L-4, Scale change formula from quadratic fit curves.

Scale change with optical bench temperature			
	Fit to data coefficients		
	Coefficient	X	Y
Left Eye	C0	-9.7660E-04	-4.4395E-04
	C1	3.2249E-05	1.4937E-05
	C2	1.2051E-07	4.4697E-08
Right Eye	C0	-5.6756E-04	-3.9616E-04
	C1	2.0142E-05	1.3417E-05
	C2	1.9072E-08	3.6692E-08
scale change = C2*T^2+C1*T+C0			
New scale = 1+scale change, Correction factor would be 1/(new scale)			

M - Pointing Performance - RT

M.1 Test Setup for Stop Phases and Travel Ranges.

The SSI camera and mast assembly were tested mounted to a plate on the optical table in the MAGI clean room. The camera was run with a PST and the test program TMV2 was used to command the camera. The camera was commanded to move toward each stop a step at a time to determine the stop phase when at the stop. After each move the test program would output the step position and last phase powered. The camera head was pulled lightly by hand to determine if the camera was against the stop properly. When the camera is properly against the stop, the backlash in the actuator gearbox cannot be felt. The actuator can travel slightly past the stop, by deflecting the flexure connecting the actuator to the camera and parts of the gimbal structure. If the deflection torque on the flexure is greater than the detent torque of the actuator, when the actuator is powered off, the actuator will rotate backward and "bounce" off the stop. The actuator stop phase is the phase where the stop position is firmly against the stop, but does not bounce off. This required repeated attempts to arrive at the same position without bouncing back. The testing was done both with the mast stowed and deployed and there was no significant difference in the results.

After testing the camera with TMV, the stop phases and travel ranges are entered into the parameter file for the flight software. The flight software is then loaded onto the PST. A script was then run that repeatably runs the camera into its stops to demonstrate that the camera will be at a known position when at each stop and will not bounce off. The script file used was named init_stops.scr which is in the support directory for this section. The resulting data is in UofA document SSI_FM_EM_constants_7-5-06_415640-1120_A.xls. A subset of that data is shown in table I-1.

M.2 Warm Pointing Test Setup and Data Acquisition

The test procedure used to gather the test data is described in 415640-1114_SSI_FM_Warm_pointing_Test_Procedure_6-10-06.doc. The camera was mounted into a fixture which held a precision rotary encoder. The encoder is accurate to 0.096 mrad or 0.034 degrees. The encoder was coupled to the camera with a dual flexure shaft to minimize affect on the camera pointing and to eliminate stress on the encoder. The camera was tested with the mast in the deployed position. The camera was run with flight software running a script. The script point_el.scr was used for elevation pointing and point_az.scr for azimuth pointing. The script was repeated several times to determine the variability in the pointing. This was an absolute pointing measurement. Although it only measures the camera head motion, the optical path components are very rigidly mounted and the optical pointing

should be the same. The script stepped the actuator 20 steps with smaller steps at the end to stop exactly at the hardware stop.

M.3 Warm Pointing Data Processing

The encoder counts for each camera position were recorded in a file and entered into a spreadsheet, FM_SSI_AZ_Warm_Pointing__VandV_version_10-20-06.xls which is in the support directory for this section. The encoder counts were converted into absolute angles. The absolute angle is then compared to the ideal angle for a constant step size. The error from this ideal step size is then plotted out. By examining the error curve the step size was adjusted to minimize the skew in the flat part of the curve. The curves will show the backlash as the difference in the two direction curves where the approach direction matters to the cable torque. Similarly, the elevation pointing was measured and entered into the spreadsheet FM_SSI_EL_Warm_Pointing__VandV_version_7-11-06.xls. The elevation test was repeated 5 times.

M.4 Warm Pointing Results

The azimuth run results are plotted in figure M-1. This plot shows the step error from an ideal step. The step size was 0.28845 degrees/step. The data shows a typical hysteresis curve. The spikes at each end are where the gimbal contacts the hardware stops and the actuator can make a few steps with no motion, by deflecting the flexure connecting the actuator to the camera gimbal and parts of the gimbal itself.

The average of the data sets is shown in figure M-2. The error bars are ±1 standard deviation. These curves shows that the uncertainty is low for certain azimuth ranges in each direction. The area from -100 to +250 steps is where the pull from the cable reverses causing the actuator to move to the other side of the backlash. This allows a pointing procedure to utilize an approach direction to reduce the pointing uncertainty. This procedure is outlined in the SSI Pointing Rules 1-25-07.doc. This leaves the uncertainty in applying the correction for steps in between those tested and the uncertainty in each step. For the usable ranges of each direction, the typical standard deviation is less than 0.02 degrees.

The maximum backlash occurs at step +77 steps in azimuth and it 0.37 degrees. The step size is 0.28845 degrees. The average error for each step is interpolated between the steps tested and is listed in the file, az_pointing_lut_7-4-07.csv. This file is used in the MIPL pointing model to correct for the errors in the

pointing of the camera. What is left is the uncertainty in which side of the backlash curve you are on. By applying the pointing rules this uncertainty is reduced from 0.34 degrees to 0.03 degrees. The rule specifies approaching all azimuths from -617 to +100 steps from a CCW direction. The rest of the range, from +100 to +617 is approached from the CW direction.

The elevation pointing errors are plotted in figure M-~~4~~3. The elevation actuator flexure which connects the actuator to the camera has to be much more flexible to accommodate axial thermal contraction of ~~the thethe~~ camera when cold. This allows the actuator to deflect the flexure more as it approached the hardware stop. This shows up in the longer spikes at each end of the travel. Figure M-4 shows the average curve along with the ±1 standard deviation points. The same step size, 0.28845 degrees was used for this analysis. The maximum backlash of 0.37 degrees occurs at several points on the curve. The larger area of hystersis shows that the deflection of the cables at the elevation axis produces less torque, and the cable loss is greater relative to the spring force. The step size is the same as azimuth at 0.28845 degrees/step The average error for each step is interpolated between the steps tested and is listed in the file el_pointing_lut_7-4-07.csv. This file is used in the MIPL pointing model to correct for the errors in the pointing of the camera. What is left is the uncertainty in which side of the backlash curve you are on. By applying the pointing rules this uncertainty is reduced from 0.37 degrees to 0.03 degrees. The rule specifies approaching all elevation from -317 to +160 by moving down, +160 to +316 is approached by moving up.

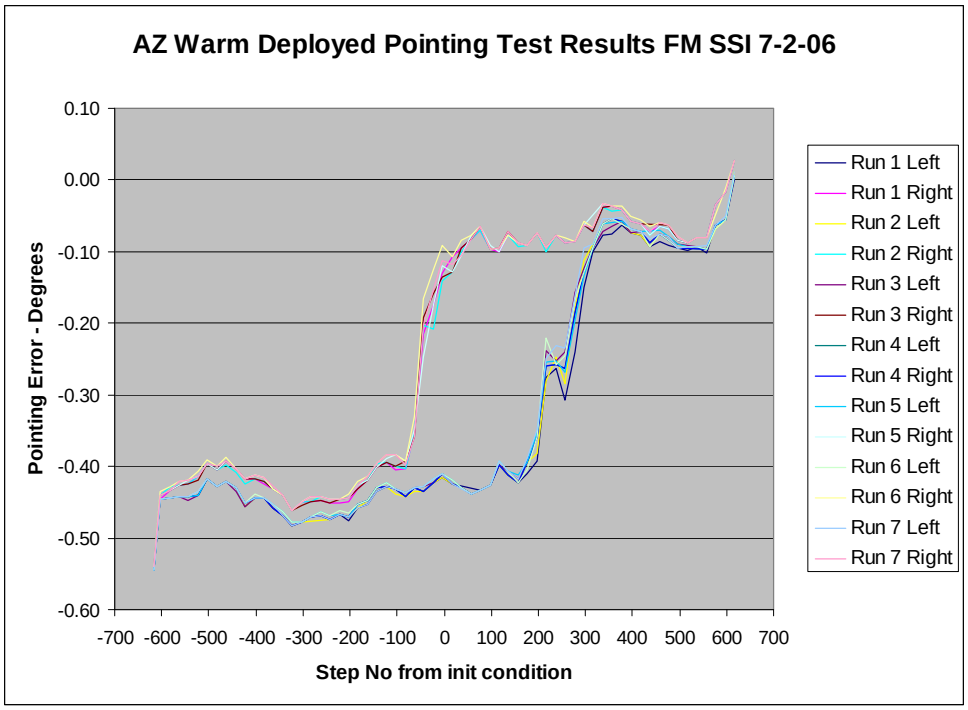

Figure M-~~2~~1. Pointing errors from ideal step motion for azimuth. 7 runs in each direction are overplotted.

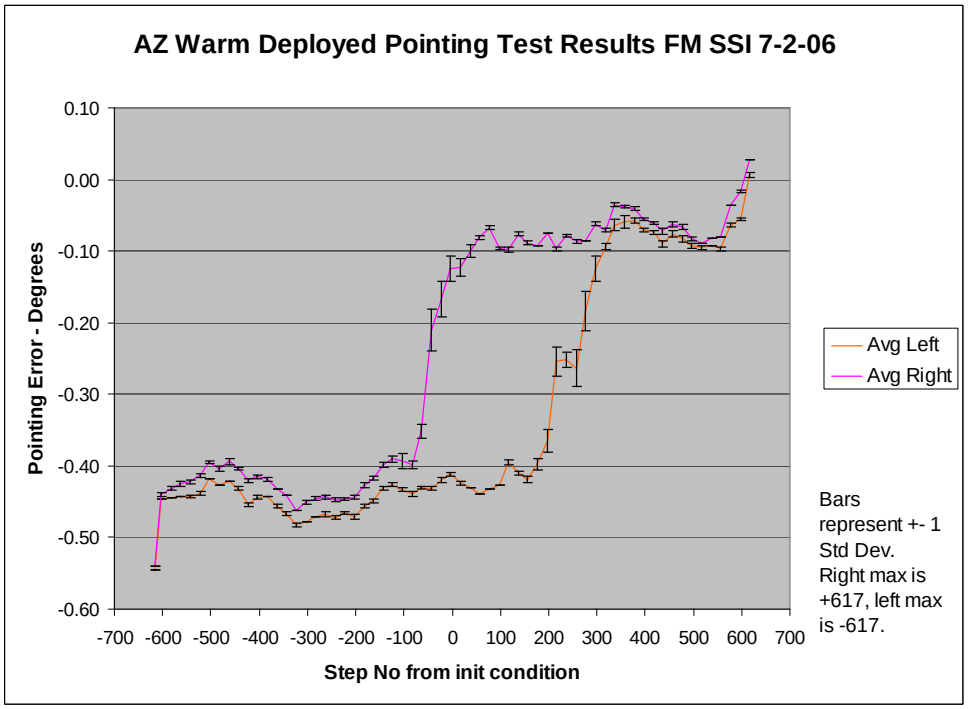

Figure M-~~3~~2. Average of the seven curves along with ±1 standard deviation error bars.

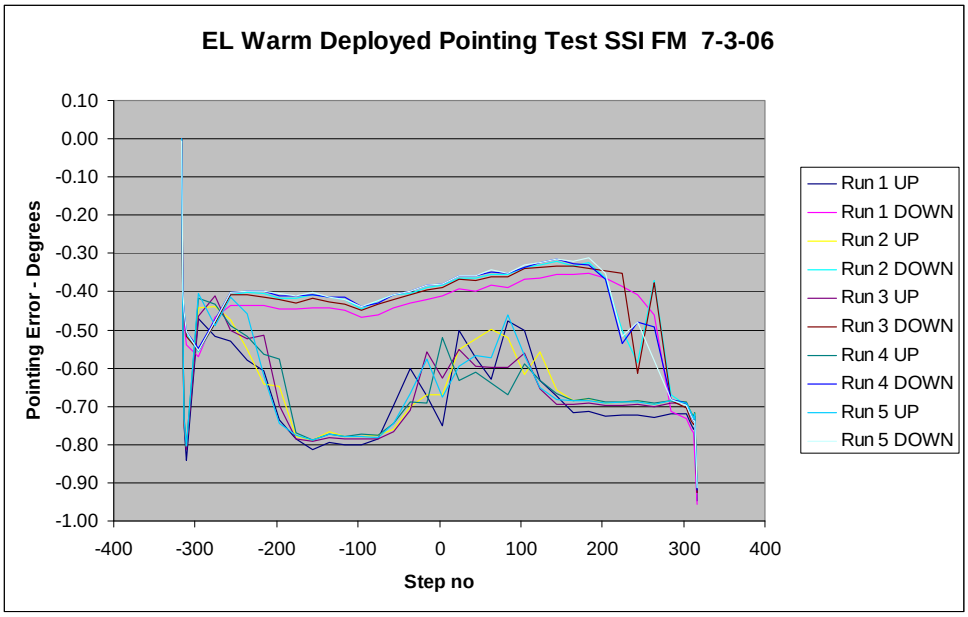

Figure M-43. Errors in elevation pointing for each of the 5 elevation runs.

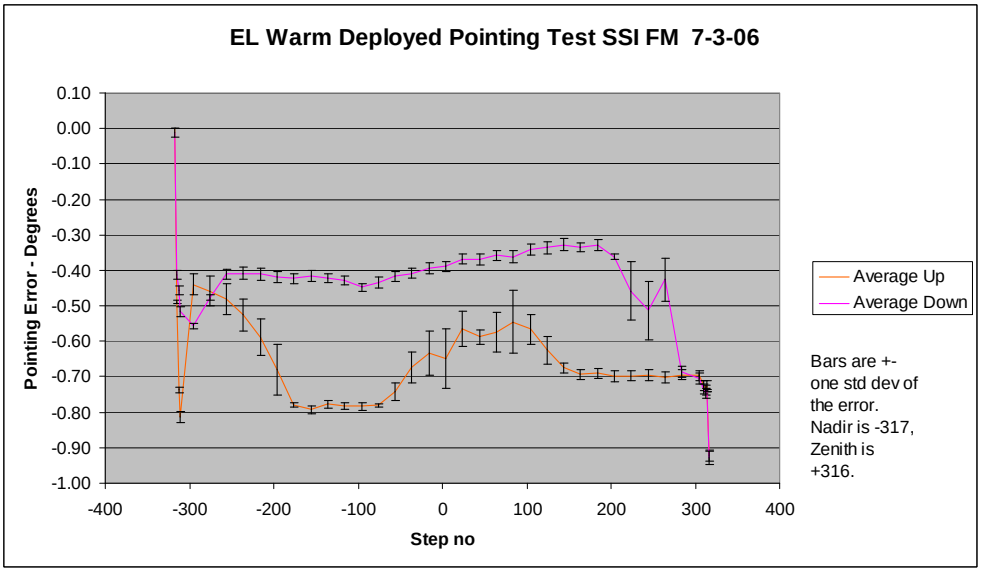

Figure M-~~5~~4. Average pointing error in elevation for each direction along with the ±1 standard deviation of the errors.

M.5 Cold Pointing Test Setup and Data Acquisition

The test procedure for the FM camera cold pointing test is described in the 415640-TC933 Phoenix SSI Thermal Pointing Test Report, by P. Woida. The camera is mounted in the MAGI thermal vacuum chamber along with a ring with centroidable targets. The camera is in the stowed configuration. This has minimal effect on pointing; the camera cables only lightly contact the mast canister at a couple of points during azimuth motion, and

they are covered in Teflon to reduce the friction of the contact. The ring is shown in figure M-5 being installed into the chamber. The camera sits inside it and as it rotates it can image the dots on the inside of the ring. The test was run imaging with the blue diopter filter, R6 to reduce the blur due to the target being so close and out of focus. There is a set of blue LED's mounted to the camera head to provide illumination for imaging as shown in figure M-6. The images have a centroidable target that gives the position of the camera in a relative to the previous position. The test is run at room temperature (+20C) to develop a baseline for backlash and uncertainty in pointing. The targets were imaged every 30 degrees in azimuth and elevation, and approached from each direction. The target is not accurate from a absolute sense, in that the position of the dots was not known accurately to measure the absolute position. The test will show that the room temperature and cold pointing for a specific dot will not change significantly.

Initially, the camera was run at room temperature and the images taken every 30 degrees in both axes approaching from each direction.

The test was repeated at -40 degrees C where the camera actuators will not need preheating to operate, but the cables are significantly stiffer. The scrip was run 8 times, although the last run was problematic due to the wire powering the LED's coming loose. This run was removed from the data set. The test was stopped and the wires retaped to the camera head.

Then the camera was cooled to -102C (protoflight limit) and held there for one hour. Then a cold start was done, warming the actuators and CCD electronics up to the minimum operational temp. The actuators were then put into background heating mode to maintain their temperature. The parameters for the heating mode and the script were not well adjusted at that time. During the first 7 runs the parameters were adjusted and the run repeated until a clean run could be obtained. The problem was the heating event was delaying an exposure until the exposure request timed out and then the exposure was skipped. The pointing test was repeated 14 times. The test ran correctly after run no7. So the data is the average of runs 8-14.

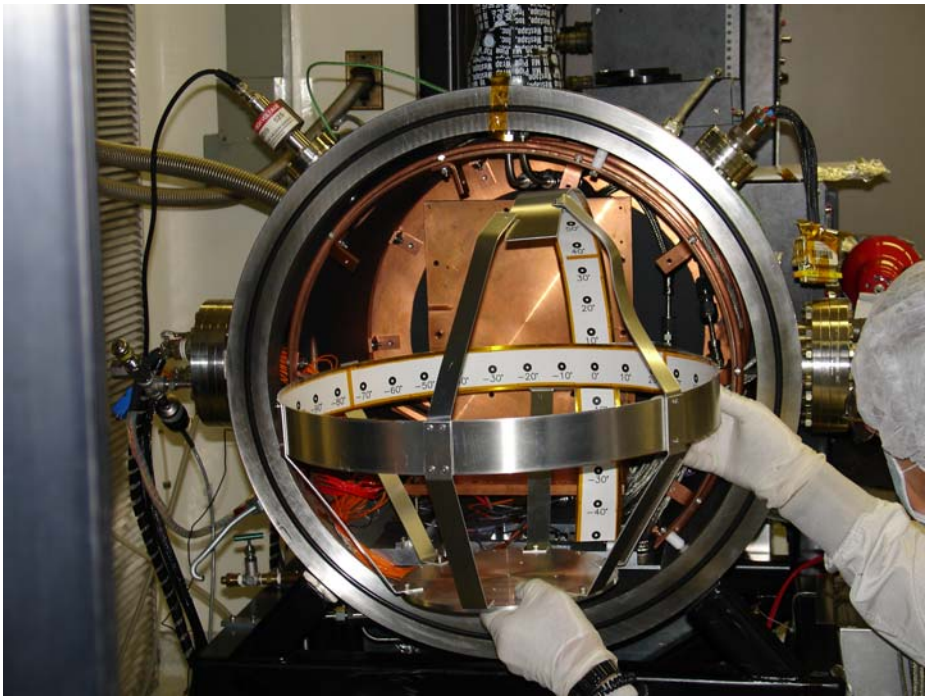

Figure M-~~6~~5. Cold Pointing Fixture Test Rings being installed in the TVC.

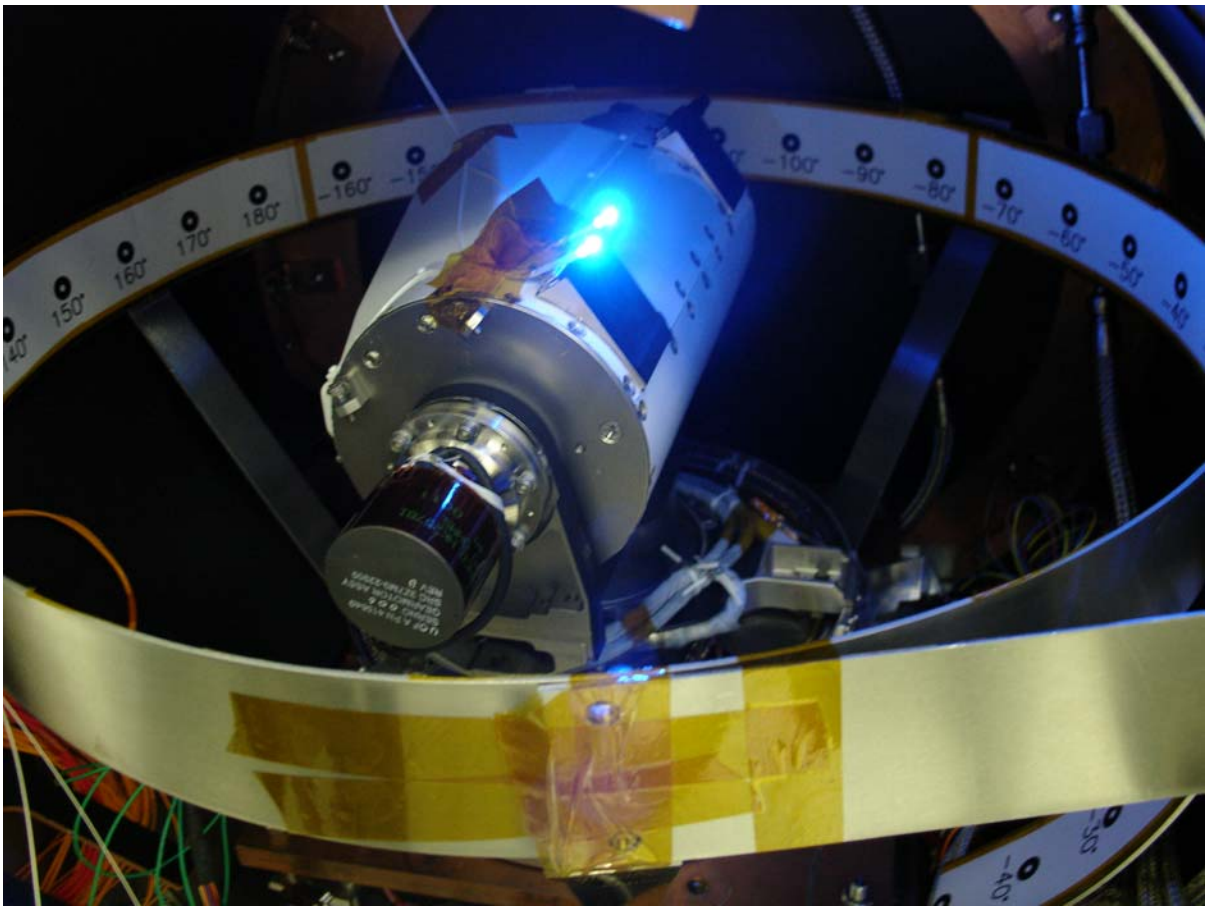

Figure M-6. Camera in test fixture with LED's on to provide illumination for imaging.

M.6 Cold Pointing Data Processing

For each image taken the spot was centroided with the software in the Phoenix Image Viewer, figure M-7 shows a sample image. The box for the centroid was adjusted to include as much of the black ring as possible without including any of the surrounding white space. The resulting X,Y cooridinates were entered into the spreadsheet Cold_pointing_spreadsheet_VandV_8-29-07.xls. Since the fixture, the camera, and the mounting plate will all change size with temperature at different rates, the absolute pointing was not considered meaningful. The change in relative pointing was calculated by comparing the X and Y position of the centroid from the CW and CCW approach and comparing that over temperature.

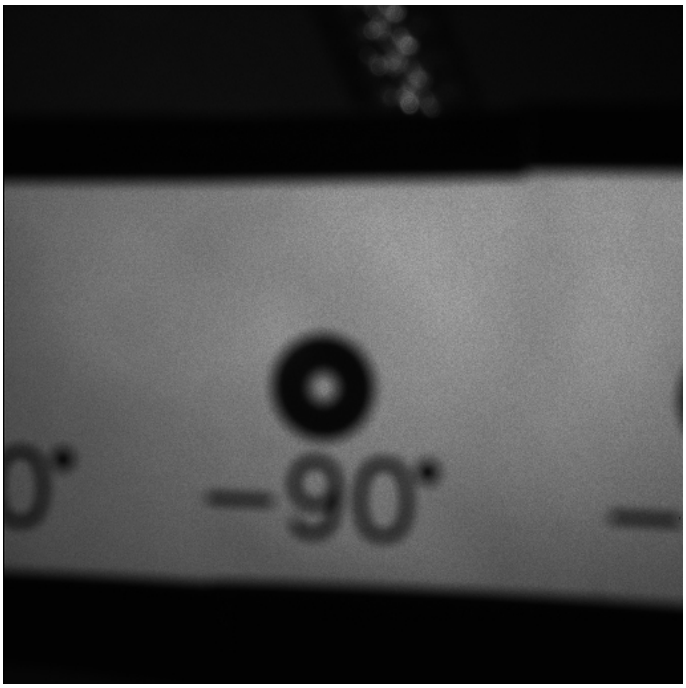

Figure M-7. Example of Image taken at 90°C to be reduced with centrioding software.

M.7 Warm Pointing Results

The change in absolute pointing in azimuth is shown in figure M-8 for the x position of the centroid. This is a plot of the difference between the average CW and CCW pointing at +20 and the lower two temperatures. The change from +20 to -40C is shown by the black curve and it ranges from +0.05 to -0.35 degrees. The -102C data ranges from 0 to -0.45 degrees. The difference is greatest for the extremes where the difference approached the amount of backlash. The steppers used in the azimuth and elevation actuators will reach the same physical

position each time, unless they slip. If they slip, they will typically be off, 4 steps or about 1.15 degrees. Since the centroids were off less 0.45 degrees, the change in pointing over temperature is due to fixture shrinkage and warping and changes in cable torque and hysteresis with temperature. The comparable plot for elevation is shown in figure M-9.

While the R6 filter used for this test has large alignment uncertainty compared to the other filters, the X axis uncertainty for the diopter filter is about 0.7 pixels or 0.01 degrees so it is not the major source of uncertainty. Also, the filter was moved into the optical path at the start of the script and not moved after that. So backlash measurements would not be affected for each script run, just the run to run variability. The change in optical pointing with temperature is shown in the optical alignment part of this report to be about a 3 pixel change or 0.04 degrees shift in x axis optical alignment with temperature for the right eye; this is not the major cause of the changes.

The backlash was calculated by comparing the average pixel value for a target when approached from one direction with the average value for the same target approached from the other direction. The backlash is plotted for the azimuth steps tested, along with the uncertainty at each step of the X centroid position in Figure M-10. The backlash shows a peak in the same region as the room temperature test ran before with low uncertainties. The colder curves show the backlash increasing across most of the temperature range along with uncertainty. The worst case backlash is 0.37 degrees.

The elevation backlash curve is shown in figure M-11. The backlash stays relatively the same over temperature and the uncertainty remains low. The worst case backlash is 0.37 degrees.

The uncertainty at each azimuth and elevation position is summarized for each script run is shown in figures M-12 and M-13 for -40C and in Figures M-14 and M-15 for -102C. The curves show that at -40 C, using the best approach direction will reduce the positioning uncertainty for a typical value of 0.06 degrees to 0.005 degrees for both azimuth and elevation. However at -102C, the uncertainty remains high at 0.08 degrees for most of the azimuth range and is 0.02 degrees for the elevation range.

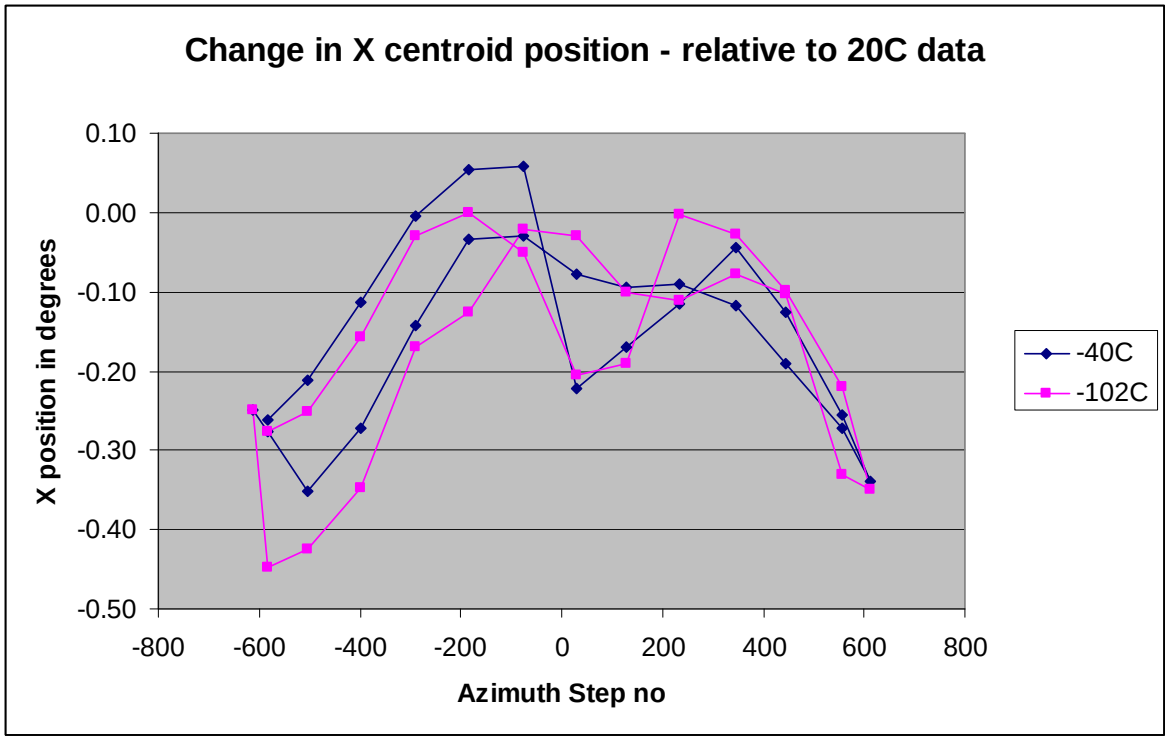

Figure M-8. Change in X position of dot centroid for two lower temperatures.

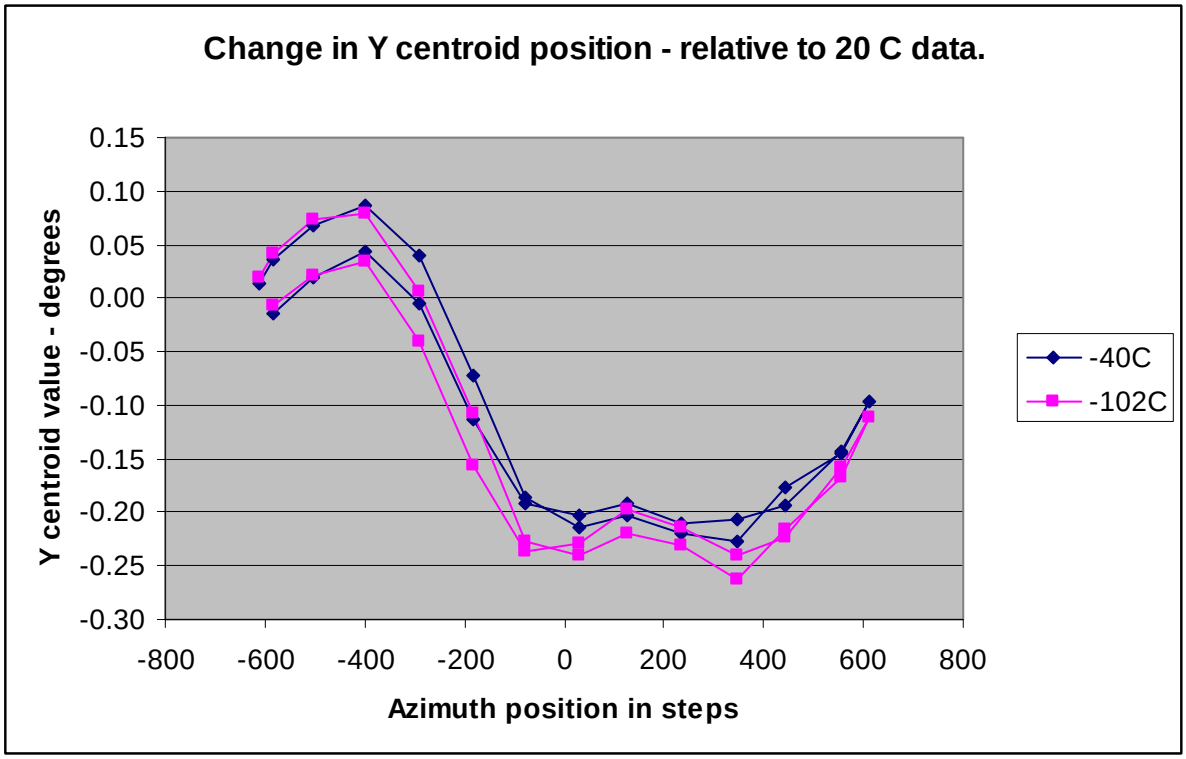

Figure M-9. Change in Y position of dot centroid for two lower test temperatures.

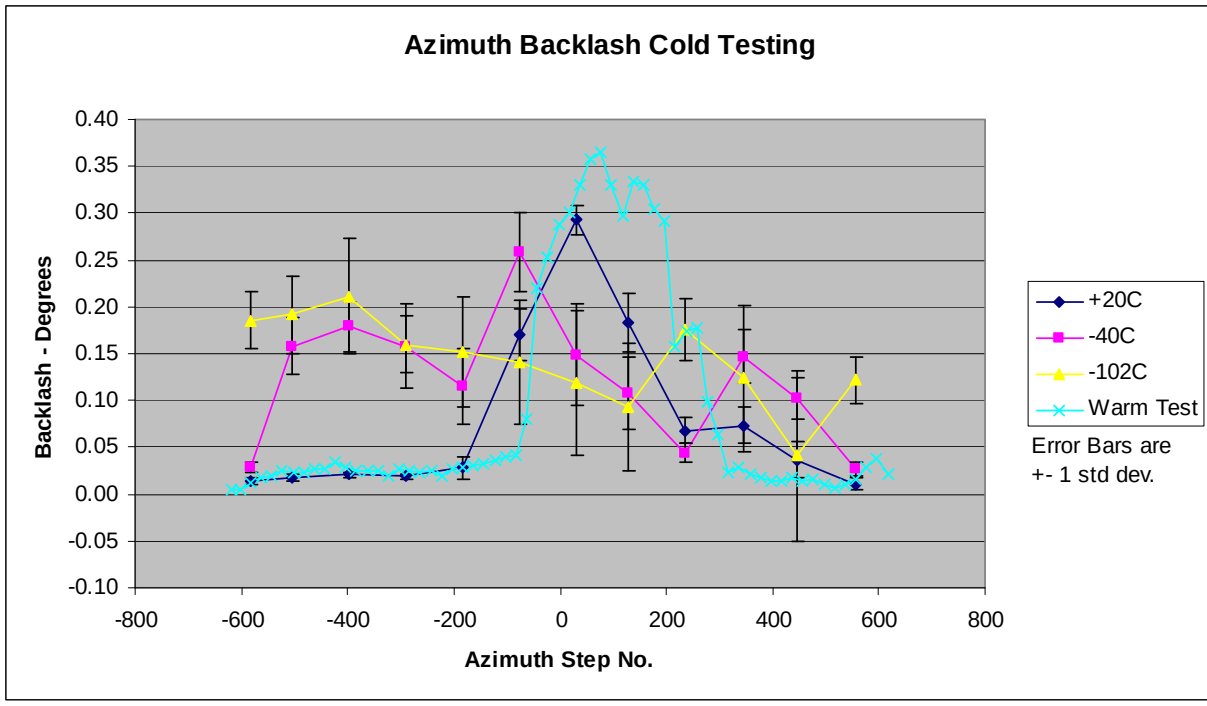

Figure M-10. Azimuth Backlash and uncertainty in backlash.

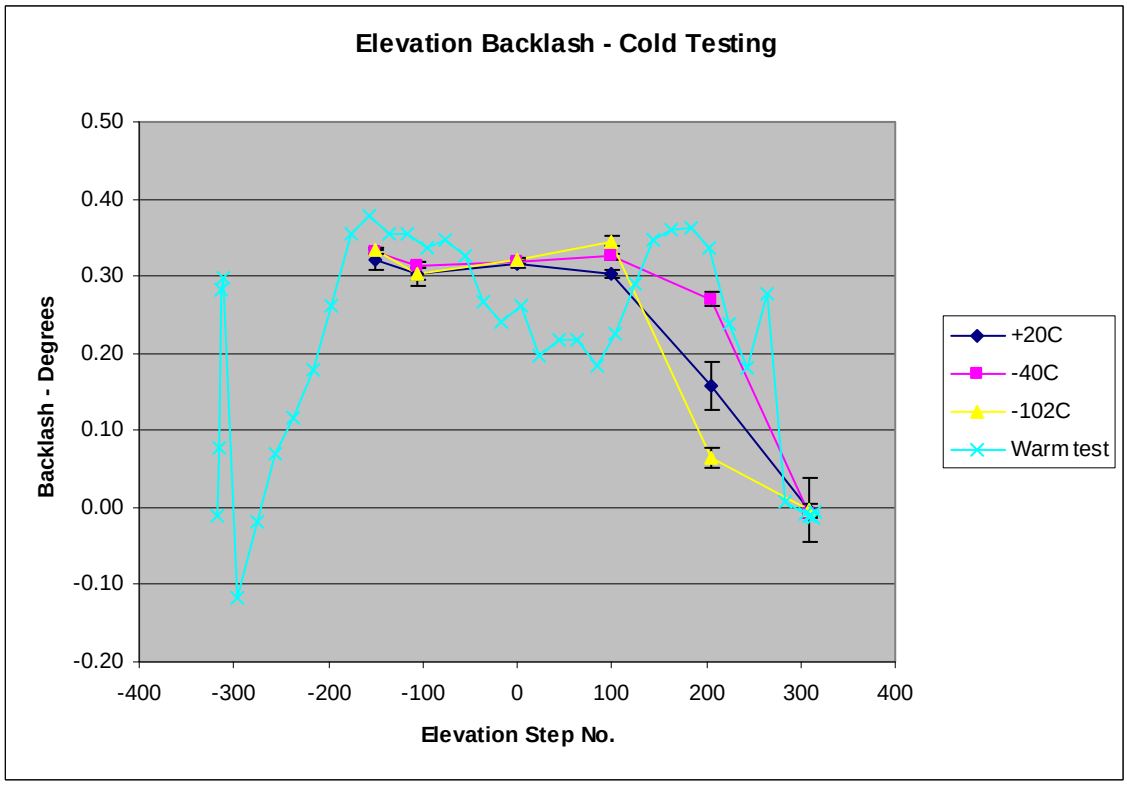

Figure M-11. Elevation Backlash and uncertainty in backlash, error bars are ±1 standard deviation.

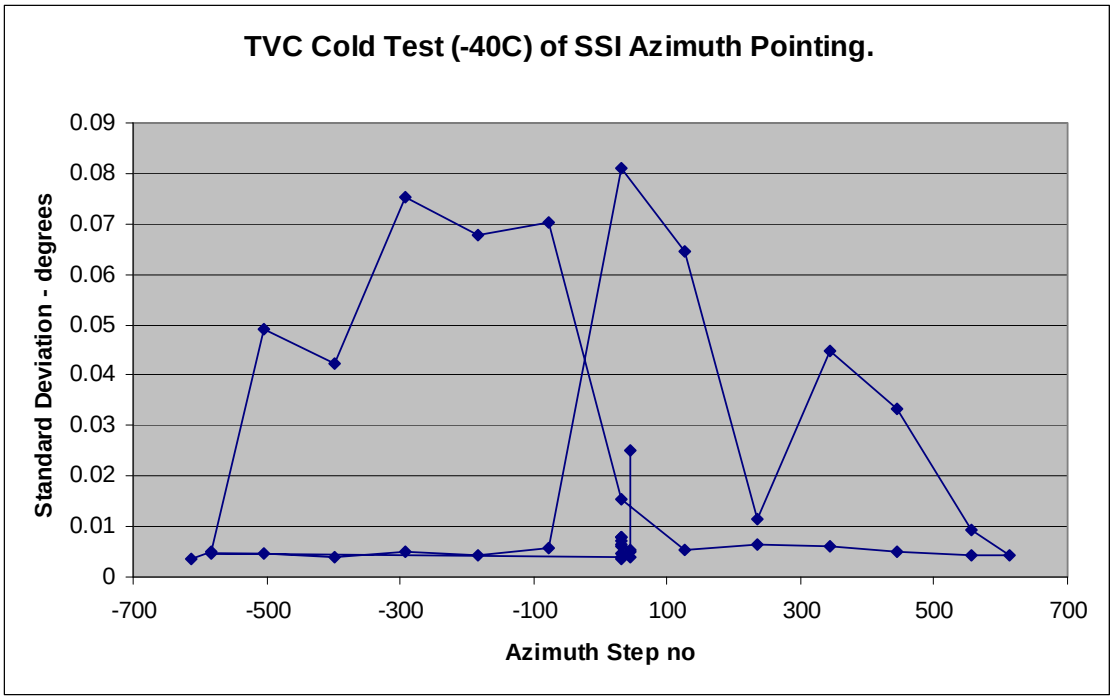

Figure M-12. Aveage uncertainty in azimuth position during test at each azimuth position for both approach directions.

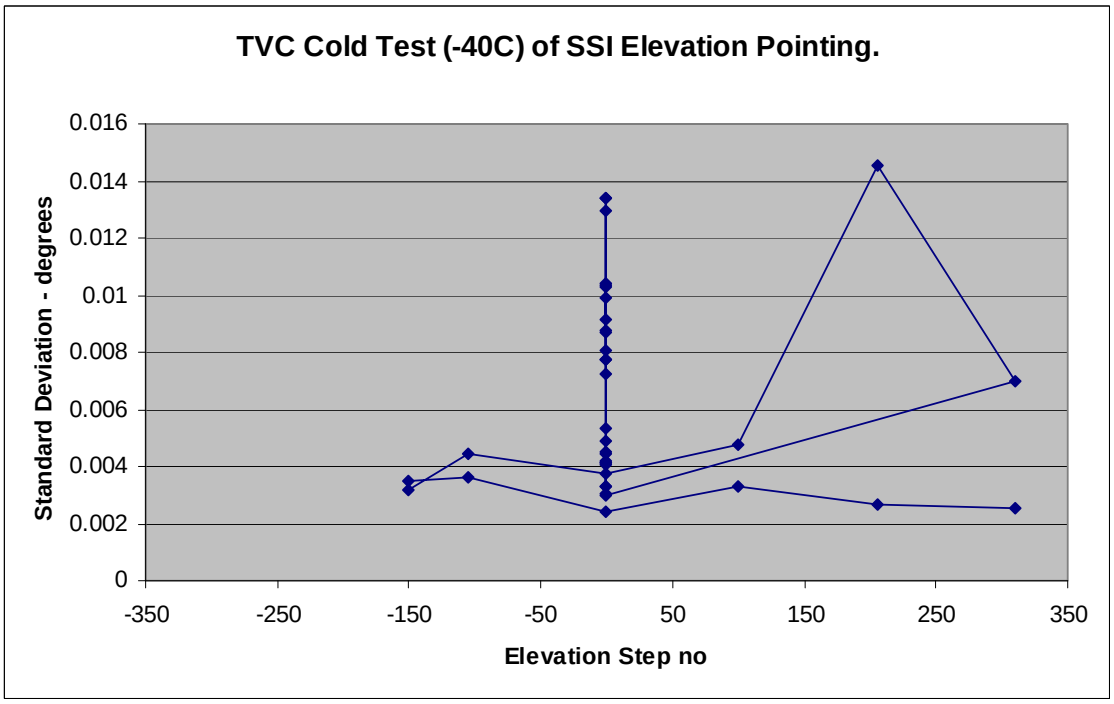

Figure M-13. Average uncertainty in elevation position during test at each elevation position for both approach directions.

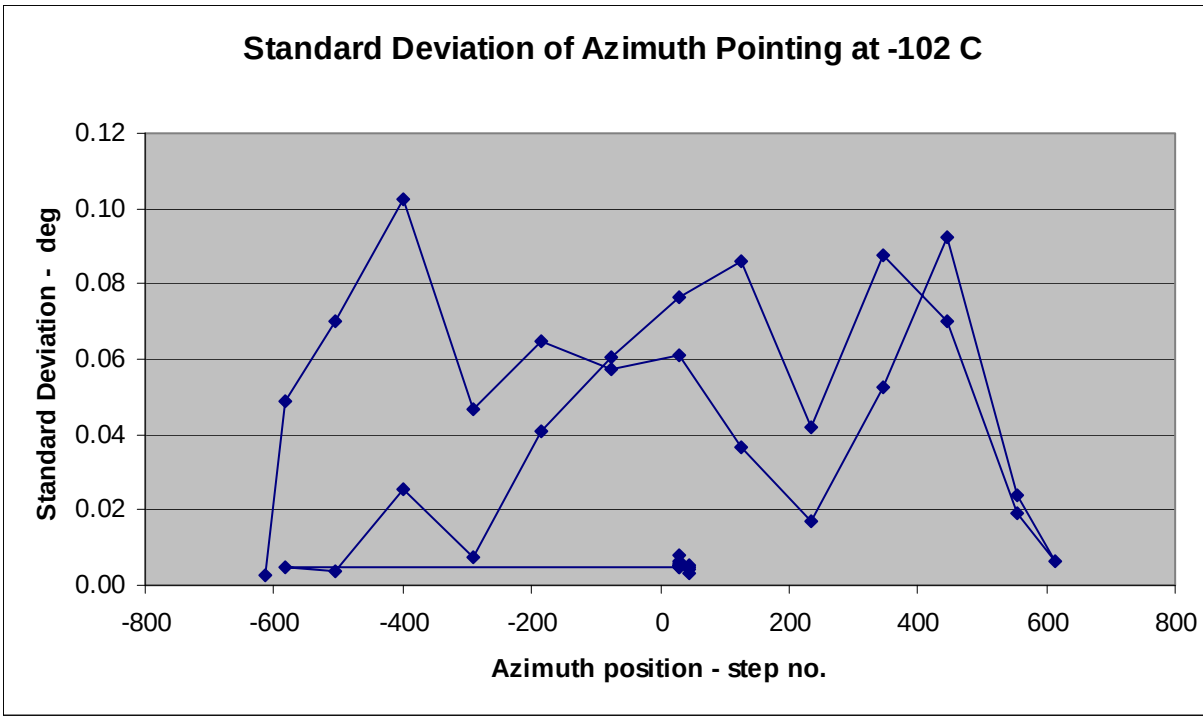

Figure M-14. Average uncertainty in azimuth position during test at each azimuth position for both approach directions.

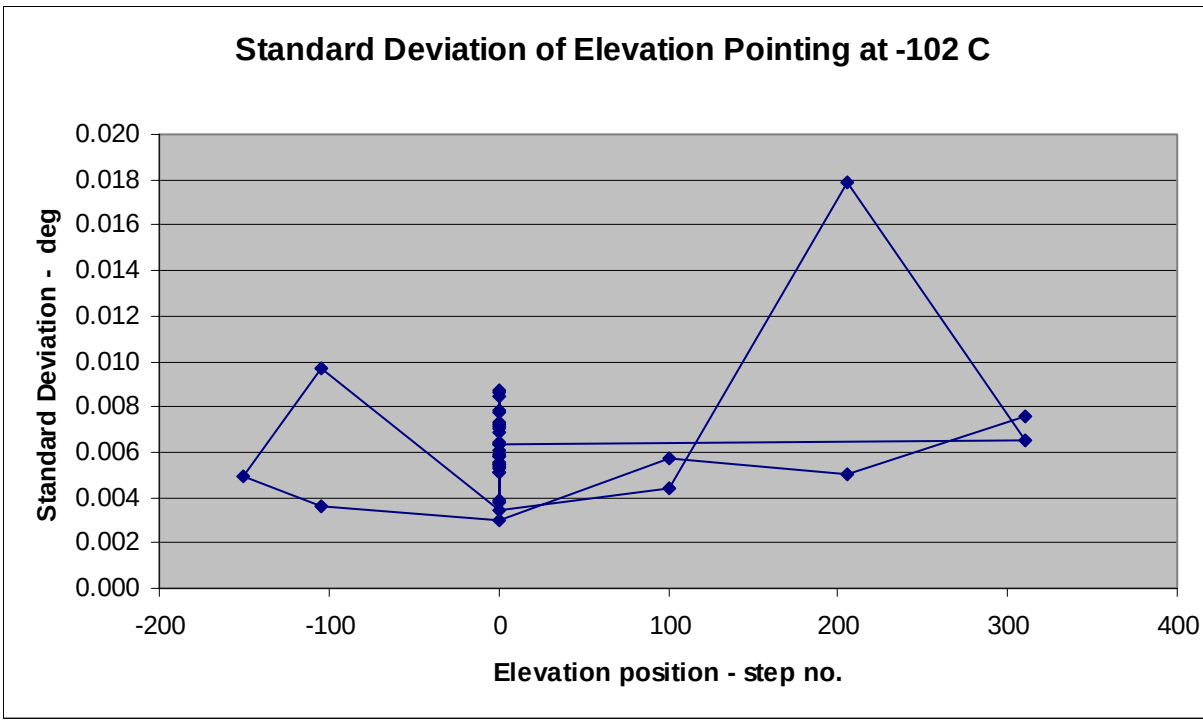

Figure M-15. Average uncertainty in elevation position during test at each elevation position for both approach directions.

N - Low Elevation Viewing - RT

The FM SSI camera, with the mast deployed, was tested to determine the obscuration for low elevations by the tip plate, gimbal, and cables. The obscuration varies with azimuth; therefore the testing was done at various azimuths and elevations. The result of the test is the height of the obscuring item in the image at various azimuths at several elevation step positions. In order to accurately determine the elevation of the camera at a given step, the elevation of step 0 was measured in a separate test and calculated. This data was combined with the warm pointing error results to determine the nominal elevation for a given step.

N.1 Test Setup and Data Acquisition for Step 0 elevation.

The elevation of the 0 step position relative to the lander deck is determined by analysis of images taken during the second ATLO camera model calibration run on April 5th, 2007. The procedure number was 336710-P510. The target was the MER calibration target mounted to two light stands. The target was setup at 3.0 meters from the camera head along the +Y payload axis and at the height of the optical axis. A laser tracking surveying system was used to measure the position of all the elements of the test. The coordinate system was set by surveying the lander deck and using the coordinates of the deck points to setup the payload coordinate system. The actual position of the camera and the target was surveyed at the same time. The system was used to determine the axis of the camera's motions. The camera head axis was within a fraction of a mm of the nominal position. The test setup at ATLO is shown in figure N-1.

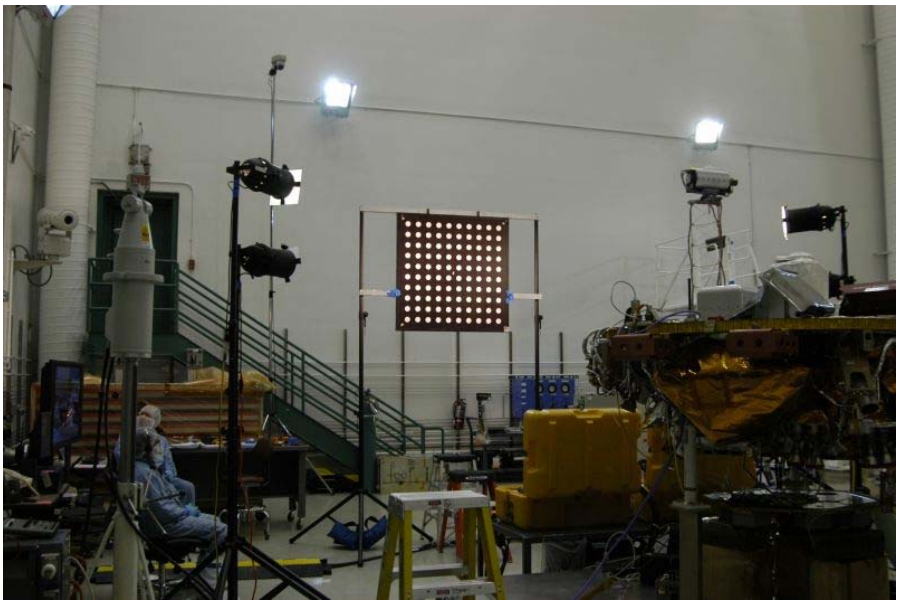

Figure N-1. Test setup at ATLO showing the target illuminated by lamps on stands, and the SSI at the right side of the image. The

laser tracker that measured the positions is the green cylindrical object, tapered at the top, on the stand at left of the image.

N.2 Calculation of Step 0 elevation.

The center 4 spots on the target that were closest to the center of the SSI FOV were used to determine the center of the target; these were rows 4 and 5 in columns 4 and 5. The target has a 10x10 array of dots. The average of the vertical coordinates in the left eye for these 4 spots is the vertical center of the target. The coordinates of each spot was determined by coordinate transform from the corner spot coordinates generated by the survey and the spot spacing. The pixel coordinates were generated by centroiding the spots in the images. The center of the target was 2.9 mm above the height of the optical axis at the camera. This results in a slope up toward the target center by 0.055 degrees. The optical axis was pointed above the target center by 0.027 degrees since the center coordinates are 2 pixels below the center of the CCD. The total angle from horizontal is then 0.082 degrees. The positive number means it is pointed above the horizontal.

The camera was at step 4, approached going down. The direction determines which side of the pointing error curve you are on; see the pointing performance section for more details. The pointing error curve gave the difference between step 4 down and step 0 up as -1.41 degrees. So the actual position of step 0 up approach is 0.08 -1.41 = -1.33 degrees. The errors from sources are: uncertainty in position of the camera head and target at ±1 mm, uncertainty in centroid of dot, ±0.1 pixel, and uncertainty in the distance between the camera, also ±2 mm and uncertainty in the position of the camera head during the test. The resulting errors are dominated by the camera head positioning uncertainty at ±0.02 degrees. In actual operation, at cold temperatures, the position uncertainty will be significantly larger, up to the backlash of 0.45 degrees see the pointing section for more details. These calculations are details in the spreadsheet FM_EL_Home_Offset_Calcs_8-9-07.xls. The image used for this calculation is ST096EDR860304931L107C95DM1.VIC which is found in the low elevation support file directory associated with the calibration report. The calculations are shown in the table N-1. A positive height or angle means the target is above the camera axis or CCD center.

Table N-1. Calculations of step 4 angle approached in the down direction.

Procedure 510 @ 3m		Payload Coords (m) target dot array. - m			Centroid position of dots - pixels	
Row	Col	x	y	z	X	Y
4	4	-0.412971	3.08741	-0.859241	519.4	579.8

5	4	-0.412926	3.08859	-0.757662	519.5	439.3
4	5	-0.514405	3.08718	-0.859102	659.7	579.7
5	5	-0.51436	3.08836	-0.757523	659.8	439.3
Average		-0.4636655	3.087885	-0.808382	589.6	509.5
Payload coords elevation axis		x	y	z		
Coordinate of elevation axis center.		-0.4434001	0.114298	-0.793492		
Translate to height of optical axis.		-0.4434001	0.114298	-0.805492		
Translate to entrance pupil for left eye		-0.5188401	0.054848	-0.805492		
Distance to target		3.034	m			
Elevation difference (Z axis difference)		0.0029	m			
Angle of optical axis to target center		**0.055**	degrees			
Distance of target center from center of CCD		2.0	pixels			
Pixel scale for left eye		0.01361061	deg/pixel			
Angle of target center from optical axis		**0.027**	deg			
Total angle for step 4 approached down		**0.082**	deg			
Angular size of 4 steps down		1.1538	deg			
Step 0 down approach elevation angle		**-1.072**	deg			
Step 0 up approach elevation angle		**-1.332**	deg			

N.3 Results for Step 0 elevation.

The elevation at step 0 approached up is at -1.33 degrees ±0.07 degrees. This is the normal camera head SSI elevation position after an elevation initialization. Since in this range of the elevation travel the approach direction is down for accurate pointing, the more important position is step 0 down approach. The position for step 0 down is -1.07 degrees. The pointing errors are up to ±0.20 degrees, and the uncertainty of 0.02 degrees in the step 0 position from the test will not significantly increase the pointing errors. The warm and cold pointing section will detail the pointing error for each step position.

N.4 Test Setup and Imaging for Low Elevation Deployed Viewing test.

A target was plotted on large paper, 1.5 m x 1.5 m in four sections. The sections were taped to the floor in the MAGI clean room. The camera mast canister outline was also plotted on the sections. The camera was set on the outline and aligned to ±1 mm of the outline. There was a ½ in plate bolted to the bottom of the mast, which raised the camera ½" above the surrounding target. This would make the resulting radius slightly conservative. Then the mast canister was weighted down to keep the camera from walking around during the stepping of the gimbal. The target accuracy was checked, it was accurate to ±1 mm in 1.5 meters. The test was run on July 13, 2006. The camera was commanded to do a full initialization and then commanded to do a pan at various

elevations. Since all of the elevations were approached from a down direction the pointing should be accurate to less than 0.02 degrees. The target was marked for every 20 degrees in angle and 10 mm in radius for the inner circles, changing to 50 mm radius farther out than 325 mm radius. An image of the target with the camera is shown in figure N-2.

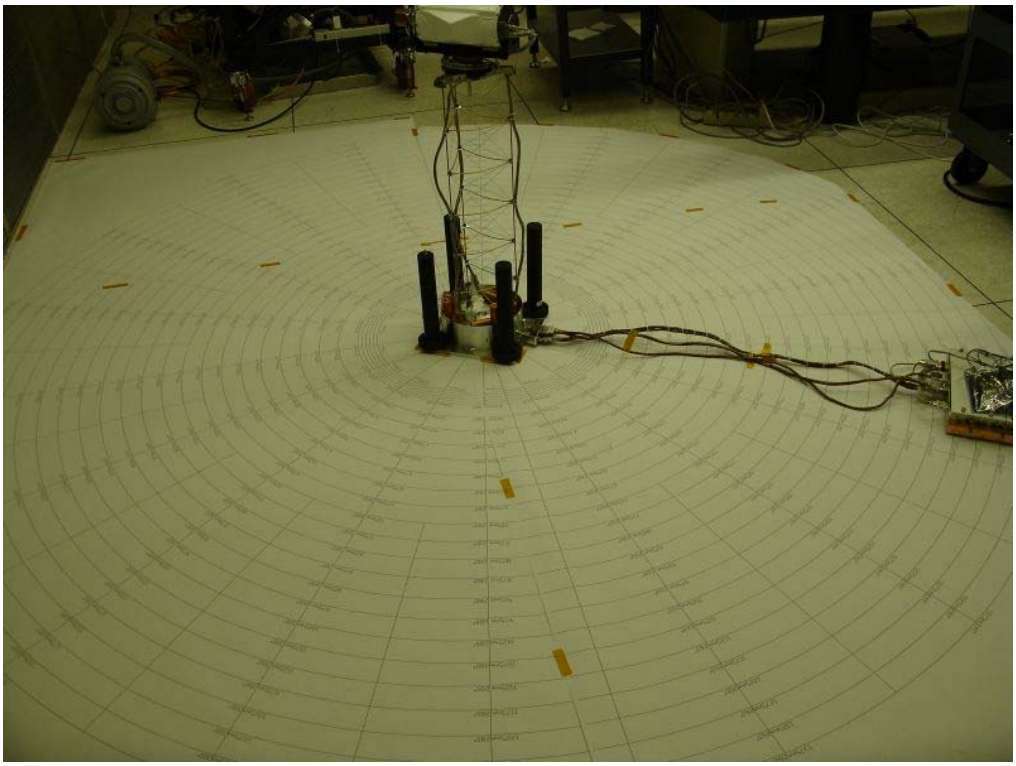

Figure N-2. Image of the target and FM camera. The black columns are heavy steel stands that are holding the camera mast down to prevent vibration from moving the camera.

N.5 Image Processing.

The images have been corrected for the first column issue with the version of the flight software used at that time. This was done using the IDL program, reattach_dark_strips_new.sav which is in the directory /home/mars/Phoenix/IDL/FMSSI_Cal_Image_Correction/. The program reads in the original image and null strips and assemblies them into the original 1024x1056 image. Then it corrects for the 1 column shift error in the original image. Then it removes the null strips and saves them as separate files.

No further processing was required to generate these results; the height of the obscuration in the FOV is directly measured with the MAGI Image Viewer, version 1.02 or later. The images are in the support files for low elevation viewing directory associated with the calibration report. The images are in a

subdirectory for each tier. There is a file named file_index.csv in each directory which lists the image no and the azimuth and elevation for each image.

N.6 Low Elevation Deployed Viewing Results

The camera can see down to the 295 mm radius line at the lowest point in the frame and can see to the 325 mm radius across the whole frame width. There is some dimming from partial gimbal obscuration at the bottom of the frame at that elevation, see figure N-3. Figure N-4 shows the typical obscuration by the tip plate. The tip plate is out of focus and blocks the view behind it. Figure N-5 shows the worst case obscuration from the camera cables wrapped around the gimbal. The most common obscuration item is the tip plate. The highest elevation taken in the low elevation viewing test was not high enough to clear the tip plate, as all three tiers show the obscurations. The actual elevations for each tier of the low elevation viewing test are shown in table N-2. The results of the viewing test are summarized in the Tables N-3. The pixel height in the image for the top of the tip plate obscuration is shown in each column followed by the item in the FOV. The amount of obscuration decreases with each tier. There are azimuths even at the lowest pointing angles where there is no obscuration.

The elevations for the lander deck pan at ATLO are also shown in the table N-2. The lander deck tier 3 pan does not shown any obscurations from the tip plate. This is at an elevation of -38.9 degrees.

Table N-2. Actual elevations for Low Elevations Viewing Test and ATLO Lander Deck Pan.

Low Elevation Viewing Test.				
Tier	Elevation - steps all approached down	Elevation Angle - degrees.	Elevation at bottom of frame - degrees	0 step down elevation - degrees
Inner Tier	-217	-63.7	-70.6	-1.07
Middle Tier	-195	-57.3	-64.2	Step size - degrees
Outer Tier	-170	-50.1	-57.0	0.28845
Atlo Deck Pan				
Tier 1	-216	-63.4	-70.3	
Tier 2	-173	-51.0	-57.9	
Tier 3	-131	-38.9	-45.8	
Tier 4	-88	-26.5	-33.4	

Table N-3. Obscuration height in Pixels for each Azimuth and Elevation tested and obscuring object.
TP = Tip Plate, C = Cable.

AZ	**Left -217 steps**		**Left -195 steps**		**Left -170 steps**		**Right -217 steps**		**Right -195 steps**		**Right -170 steps**	
Steps	Y val	Comp	Y val	Comp	Y val	4omp	Y val	Comp	Y val	Comp	Y val	Comp
-617	376	TP	38	TP	0		528	TP	206	TP	0	
-582	0		0		0		824	TP	464	TP	92	TP
-547	0		0		0		986	TP	656	TP	284	TP
-512	0		0		0		1023	TP	730	TP	358	TP
-477	0		0		0		58	TP	0		0	
-442	0		0		0		0		0		0	
-407	0		0		0		0		0		0	
-372	0		0		0		0		0		0	
-337	1023	TP	714	TP	350	TP	0		0		0	
-302	1023	TP	712	TP	346	TP	0		0		0	
-267	876	TP	550	TP	186	TP	112	TP	0		0	
-232	644	TP	316	TP	0		256	TP-C	0		0	
-197	346	TP	236	TP	0		566	TP-C	238	TP	0	
-162	0		0		0		812	TP	490	TP	120	TP
-127	0		0		0		1010	TP	676	TP	304	TP
-92	0		0		0		1023	TP	730	TP	358	TP
-57	0		0		0		140	TP	0		0	
-22	0		0		0		0		0		0	
13	0		0		0		128	C	0		0	
48	72	TP	0		0		260	C	0		0	
83	1023	TP	720	TP	350	TP	332	C	0		0	
118	1023	TP	708	TP	342	TP	350	C	82	C	0	
153	862	TP	538	TP	170	TP	370	C	96	C	0	
188	620	TP	300	TP	0		376	TP-C	98	TP	0	
223	316	TP	0		0		584	TP-C	258	TP	0	
258	146	TP	0		0		834	TP	504	TP	136	TP
293	128	TP	0		0		1023	TP	686	TP	314	TP
328	0		0		0		1023	TP	732	TP	356	TP
363	0		0		0		98	C	0		0	
398	0		0		0		90	C	0		0	
433	0		0		0		0		0		0	
468	0		0		0		0		0		0	
503	1023	TP	722	TP	350	TP	0		0		0	
538	1023	TP	688	TP	326	TP	250	TP	0		0	
573	846	TP	514	TP	152	TP	0		0		0	
608	592	TP	276	TP	0		300	TP	0		0	
617	518	TP	206	TP	0		390	TP	66	TP	0	

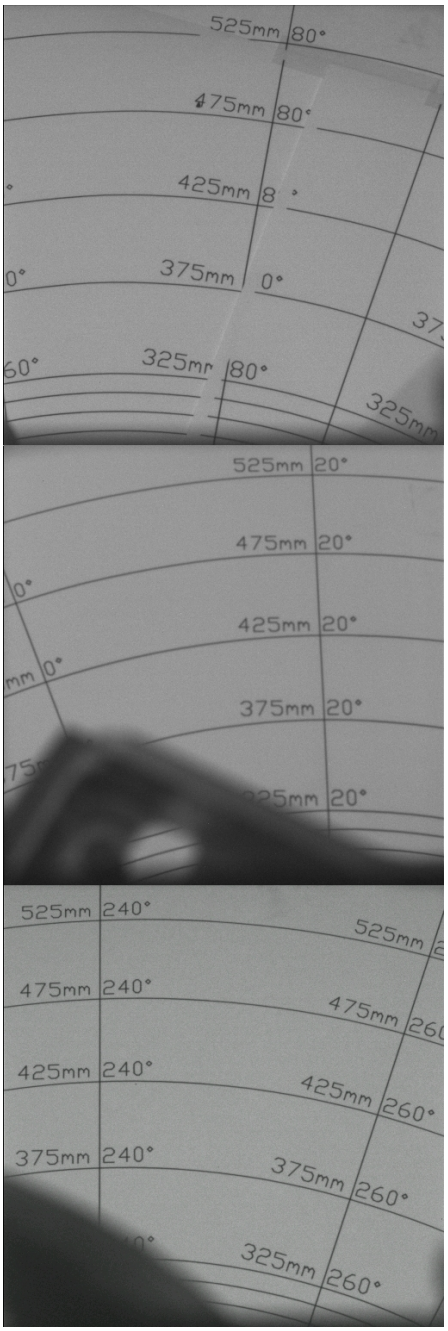

Figures N-3, 4, 5. The left image (N-3) shows the vignetting at the bottom of the frame from the gimbal at -217 steps. The middle frame (N-4) shows the typical vignetting from the tip plate. The right image (N-5) shows the worst case cable obscuration from the cables wrapped around the camera gimbal.

N.7 Calculation of the elevation with no obstructions

The highest elevation in the viewing test was the Outer Tier with an elevation of -170 steps or -50.1 degrees pointing. There were still some obscurations from the tip plate at this

elevation as shown in table N-3. The highest y axis pixel value was 358 for the right eye. Multiplying this value by the angular size of each pixel (0.01348 deg/pixel) gives the angle to raise the elevation to eliminate the obscuration. This is 4.83 degrees. So the elevation angle of no obscuration is -50.1 + 4.83 = -45.3 degrees or -153 steps elevation.

The lander deck pan from ATLO is shown in figure N-6. All the tiers are mosaiced together to form a continuous image by A. Shaw of University or Arizona, Lunar and Planetary Lab. As can be seen in this image, by choosing the azimuths to use and eliminating the obscured part of the deck from each eye, a complete mosaic can be made with very little obscured parts of the deck. For the elevations corresponding to the sample dump sites on the TEGA and MECA instruments, the obscurations in one eye do not exist for the other eye.

For the workspace azimuths, the low elevation view is not limited by camera gimbal, not the lander deck. The bottom of the FOV at the lowest useful pointing is -70.6 degrees. This allows viewing part of the one lander footpad in the workspace, see figure N-7. This is a blue stereo pair taken during the landed thermal vacuum test of the lander at LM. These were taken at ATLO on Feb. 28, 2007 with the FM camera running sequence ssi_deckpan_1. The azimuth is 416 steps, elevation is -216 steps. It shows the part of the footpad and leg spring.

The area of the workspace that is projected to be visible from the SSI was modeled in the Lockheed Martin CAD system by Tim Thames. The resulting area is limited by the dig area of the arm at the inner and out radius, and at the right and left edges by solar panel and lander deck obscuration. The resulting area is shown in figure N-8. The part of this area which is projected to have viewing in only one eye is shown in the figure as cross hatched.

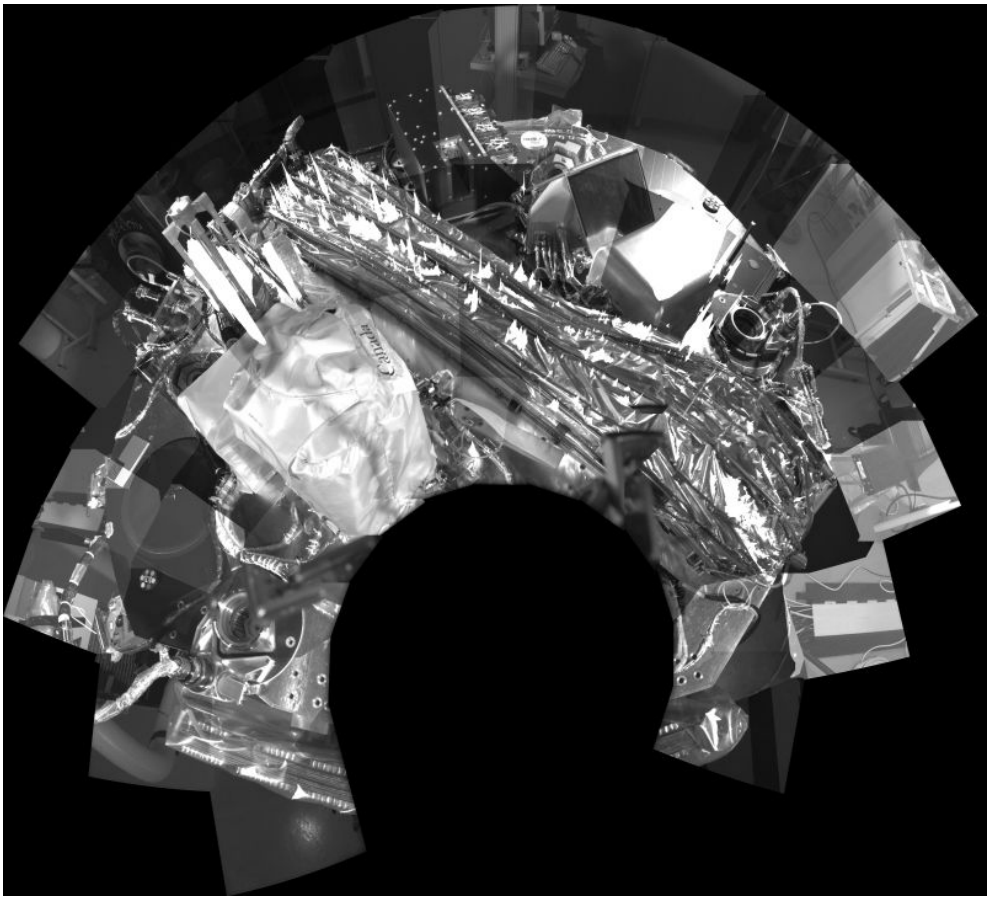

Figure N-6. “Noon” Deck Pan Mosaic of Flight Lander in ATLO made up of >100 individual SSI Images. Mosaic by Adam Shaw of University of Arizona.

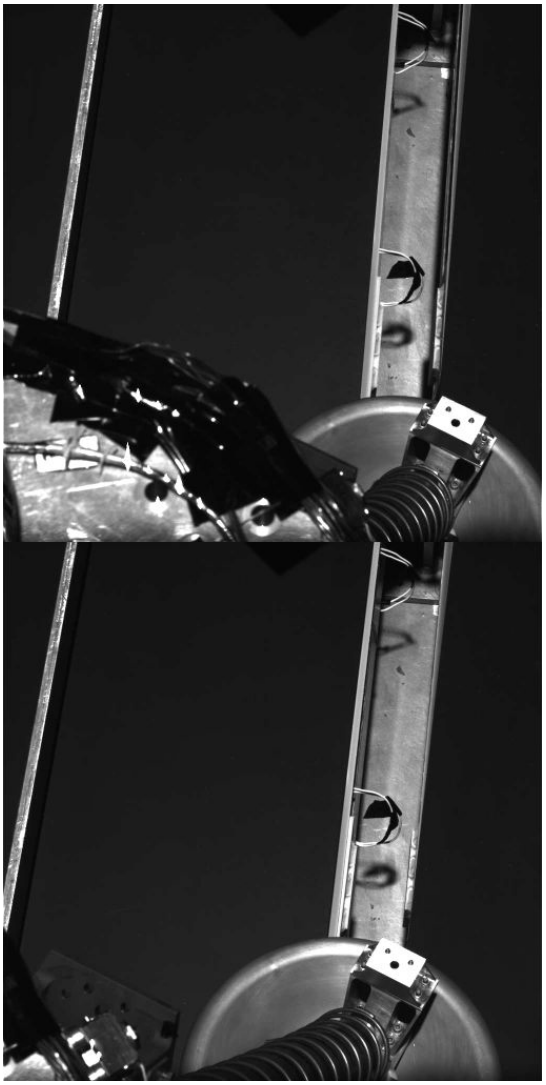

Figure N-7. Stereo pair of images of the workspace showing the foot pad at the bottom of the image. The images are ST___EFF85719288800003_2LM1.jpg and ST___EFF EFF85719288800003_2RM1.jpg.

Figure N-8. Computer modeling of SSI FOV and obscuration from tip plate. The orange colored area is the stereo workspace area viewable from the SSI. The hatched part of that area shows viewing area only seen with one eye. Image and analysis by Tim Thames at Lockheed Martin.

N.8 Low Elevation Viewing Stowed

When the SSI camera is in the stowed position, the gimbal assembly is prevented from rotating in azimuth by a pin in the mast canister that engages a slot in the gimbal assembly. This still allows the elevation axis to move. Since the camera is balanced in elevation, the detent torque of the elevation stepper motor is sufficient to prevent the camera head from moving during launch. After landing on Mars the camera head can move in elevation to image a slice of the landing site before deployment of the mast. The camera is pointed toward the workspace area and will see the edge of one of the solar panels. Figure 10 shows the azimuth of the camera head with the SSI in the stowed position. The camera can take a vertical slice or pan of the ground to the zenith in this direction.

Figure 11 shows an image taken with the SSI in the stowed position of the cold pointing target. This target is only 150 mm from the camera head and so is out of focus. The elevation for this image is -150 steps, this converts to -45.1 degrees elevation. This shows that the mast canister does not vignette the FOV. There are about 20 pixels of vignetting at the bottom of the FOV from the bracket mounting the target. The mast canister would be in front of this and is not seen.

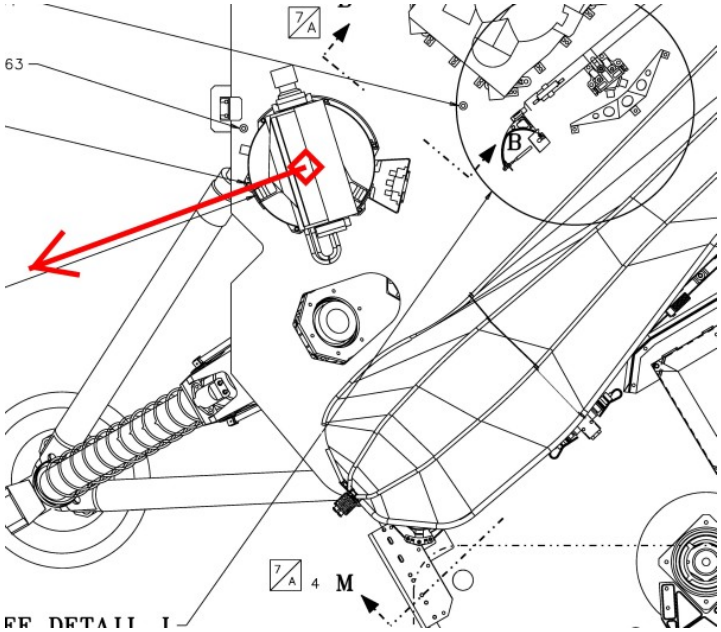

Figure 10. The top view of the lander deck layout with the SSI shown in the stowed position. The red arrow shows the viewing direction of the camera.

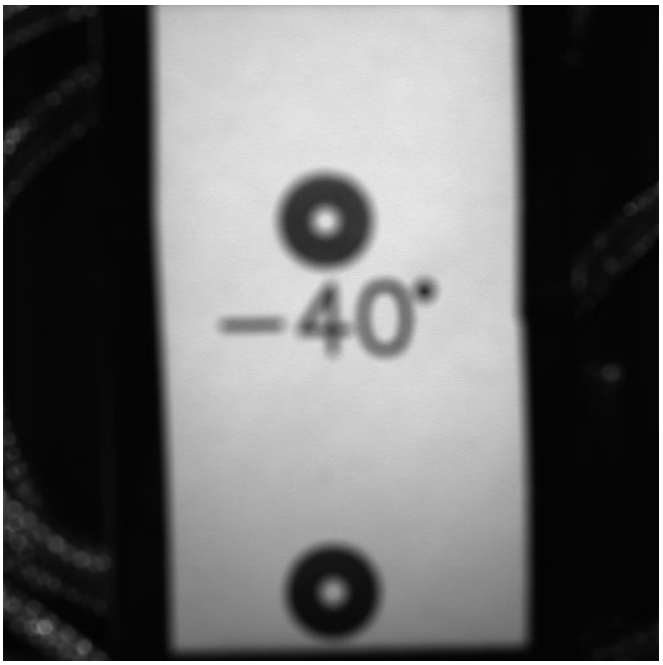

Figure 11. Image of the cold pointing target in MAGI Thermal Vac Chamber at -40C. This image is of a target that is only 150 mm from the camera head and so is considerably out of focus.

O - Focus and MTF Performance – RR

The objective of this test is to analyze the focus characteristics of the SSI over distance to verify that acceptable focus is achieved over the range from 2 meters to infinity through the regular (non-diopter) surface filters, and that best focus is achieved in the range 1.0 to 1.4 meters with the diopter filters. The analysis should also demonstrate that a resolution of 3 mm can be achieved at a distance of 3 meters.

O.1 Test Setup and Data Acquisition for surface filters

Images of a special MTF test target (shown in Figure O-1) were taken at distances of 2, 3, 3.5, and 4.3 meters using red (670nm) and blue (440nm) filters in left and right eyes. The target was placed so the appropriate pattern was placed alternately TBC at the center, corners, and edges of the field of view of each eye. The target is designed to exhibit the correct width bars for both 1 pixel/bar and 2 pixel/bar sampling at the appropriate test distances. These measurements were taken as part of Procedure 415640-1098 Rev.A Procedure and Record for Focus Shim Selection, and were repeated as the focus shim thicknesses were optimized to achieve the best focus.

O.2 Data Processing for surface filters

The Phoenix MTF images were processed using the IDL program general_mtf.pro dated 9/2/05. The program computes the contrast transfer function (CTF) and modulation transfer function (MTF) of regions selected by the user. The MTF was computed and plotted for both 1 pixel/bar sampling, as represented by the second row of patterns in the target, and 2 pixel/bar sampling, as represented by the bottom row of patterns. The computed MTF's were compared to the theoretical values as computed by the Zemax optical design program dated 9/18/03 for the SSI lens, as shown in Figures O-2 through O-5. Because the Zemax plots are for the lens only and do not take into account the sampling of the CCD, the measured values are expected to be equal to 0.7 * Zemax values.

O-3 MTF vs. distance results for surface filters

The computed MTF values for left eye red images are shown in tabular form in Table O-1 and are plotted in Figure O-6.

These plots show acceptable agreement between the theoretical and measured distances at which best focus is achieved, as well as an MTF of at least 0.150 from 2 meters to 4.3 meters. The lens was designed to have the same MTF value for objects at infinity as at 2 meters, and so is expected to provide MTF values of at least 0.150 at infinity. The data taken using the USAF MTF target at ATLO was inconclusive for extending the focus curve to 8 meters due to alignment problems with the standard target.

O.4 Diopter MTF vs. distance

Table O-1. Computed MTF values for filter L1, 670 nm, Red Stereo

R/L	Distance	Horizontal - 1 pixel/bar sampling								
		Upper Left	Upper Center	Upper right	Left	Center	Right	Lower left	Lower center	Lower Right
L	2	0.15	0.146	0.147	0.154	0.171	0.139	0.174	0.165	0.168
L	3	0.179	0.163	0.179	0.168	0.199	0.189	0.173	0.174	0.171
L	3.5	0.178	0.172	0.173	0.189	0.181	0.197	0.183	0.171	0.19
L	4.3	0.154	0.155	0.157	0.158	0.15	0.161	0.156	0.154	0.154
		Vertical - 1 pixel/bar sampling								
		Upper Left	Upper Center	Upper right	Left	Center	Right	Lower left	Lower center	Lower Right
L	2	0.148	0.163	0.141	0.164	0.127	0.139	0.173	0.15	0.179
L	3	0.181	0.163	0.171	0.151	0.202	0.166	0.173	0.187	0.186
L	3.5	0.166	0.173	0.164	0.185	0.208	0.159	0.174	0.173	0.184
L	4.3	0.159	0.169	0.151	0.152	0.169	0.155	0.162	0.171	0.16
		Horizontal - 2 pixel/bar sampling								
		Upper Left	Upper Center	Upper right	Left	Center	Right	Lower left	Lower center	Lower Right
L	2	0.471		0.443		0.482		0.475		0.477
L	3	0.499		0.492		0.515		0.514		0.498
L	3.5	0.498		0.496		0.439		0.492		0.52
L	4.3	0.469		0.447		0.477		0.458		0.486
		Vertical - 2 pixel/bar sampling								
		Upper Left	Upper Center	Upper right	Left	Center	Right	Lower left	Lower center	Lower Right
L	2	0.429		0.427		0.435		0.469		0.452
L	3	0.492		0.489		0.501		0.476		0.446
L	3.5	0.494		0.502		0.502		0.481		0.475
L	4.3	0.442		0.464		0.453		0.454		0.436

		Corner avg	Edge avg	Center	Corner Avg - 2x bars	Center avg - 2x bars
L	2	0.160	0.153	0.149	0.455	0.4585
L	3	0.177	0.170	0.201	0.488	0.508
L	3.5	0.177	0.177	0.195	0.495	0.4705

L	4.3	0.157	0.159	0.160	0.457	0.465

Table O-2. Computed MTF values for filter R1, 670 nm, Red Stereo

R/L	Distance	Horizontal - 1 pixel/bar sampling								
		Upper Left	Upper Center	Upper right	Left	Center	Right	Lower left	Lower center	Lower Right
R	2	0.159	0.144	0.148	0.137	0.174	0.139	0.178	0.145	0.17
R	3	0.184	0.188	0.181	0.176	0.197	0.17	0.186	0.191	0.186
R	3.5	0.182	0.171	0.179	0.199	0.191	0.181	0.147	0.182	0.174
R	4.3	0.155	0.146	0.14	0.172	0.176	0.177	0.141	0.16	0.144
		Vertical - 1 pixel/bar sampling								
		Upper Left	Upper Center	Upper right	Left	Center	Right	Lower left	Lower center	Lower Right
R	2	0.123	0.145	0.151	0.156	0.168	0.179	0.155	0.169	0.158
R	3	0.162	0.184	0.168	0.163	0.189	0.166	0.161	0.179	0.159
R	3.5	0.148	0.197	0.152	0.166	0.186	0.182	0.143	0.171	0.166
R	4.3	0.155	0.145	0.142	0.121	0.156	0.172	0.142	0.145	0.132
		Horizontal - 2 pixel/bar sampling								
		Upper Left	Upper Center	Upper right	Left	Center	Right	Lower left	Lower center	Lower Right
R	2	0.472		0.477		0.482		0.472		0.496
R	3	0.506		0.489		0.534		0.497		0.495
R	3.5	0.473		0.489		0.422		0.489		0.486
R	4.3	0.432		0.429		0.455		0.441		0.421
		Vertical - 2 pixel/bar sampling								
		Upper Left	Upper Center	Upper right	Left	Center	Right	Lower left	Lower center	Lower Right
R	2	0.441		0.471		0.447		0.464		0.468
R	3	0.495		0.502		0.477		0.455		0.45
R	3.5	0.487		0.465		0.446		0.456		0.445
R	4.3	0.446		0.438		0.42		0.401		0.39

	Corner avg	Edge avg	Center	Corner Avg - 2x bars	Center avg - 2x bars
2	0.155	0.152	0.171	0.470	0.4645
3	0.173	0.177	0.193	0.486	0.5055
3.5	0.161	0.181	0.189	0.474	0.434
4.3	0.144	0.155	0.166	0.425	0.4375

Table O-3. Computed MTF values for filter L2, 670 nm, Blue Stereo

R/L	Distance	Horizontal - 1 pixel/bar sampling

		Upper Left	Upper Center	Upper right	Left	Center	Right	Lower left	Lower center	Lower Right
L	2	0.303	0.299	0.241	0.233	0.247	0.26	0.303	0.304	0.351
L	3	0.344	0.4	0.42	0.373	0.4	0.413	0.411	0.409	0.388
L	3.5	0.347	0.352	0.335	0.372	0.408	0.368	0.402	0.417	0.408
L	4.3	0.27	0.315	0.31	0.322	0.359	0.309	0.346	0.339	0.344
		Vertical - 1 pixel/bar sampling								
		Upper Left	Upper Center	Upper right	Left	Center	Right	Lower left	Lower center	Lower Right
L	2	0.244	0.234	0.235	0.346	0.245	0.3	0.29	0.284	0.299
L	3	0.362	0.352	0.381	0.4	0.405	0.359	0.393	0.35	0.352
L	3.5	0.354	0.396	0.39	0.44	0.389	0.354	0.369	0.327	0.346
L	4.3	0.339	0.321	0.31	0.323	0.38	0.337	0.38	0.367	0.337
		Horizontal - 2 pixel/bar sampling								
		Upper Left	Upper Center	Upper right	Left	Center	Right	Lower left	Lower center	Lower Right
L	2	0.532		0.5		0.527		0.56		0.56
L	3	0.639		0.651		0.659		0.678		0.671
L	3.5	0.686		0.712		0.619		0.662		0.719
L	4.3	0.589		0.652		0.611		0.586		0.605
		Vertical - 2 pixel/bar sampling								
		Upper Left	Upper Center	Upper right	Left	Center	Right	Lower left	Lower center	Lower Right
L	2	0.534		0.514		0.515		0.63		0.559
L	3	0.627		0.637		0.674		0.666		0.667
L	3.5	0.615		0.637		0.644		0.686		0.654
L	4.3	0.586		0.598		0.618		0.611		0.61

		Corner avg	Edge avg	Center	Corner Avg - 2x bars	Center avg - 2x bars
L	2	0.283	0.283	0.246	0.549	0.521
L	3	0.381	0.382	0.403	0.655	0.6665
L	3.5	0.369	0.378	0.399	0.671	0.6315
L	4.3	0.330	0.329	0.370	0.605	0.6145

Table O-4. Computed MTF values for filter R2, 670 nm, Blue Stereo

R/L	Distance	Horizontal - 1 pixel/bar sampling								
		Upper Left	Upper Center	Upper right	Left	Center	Right	Lower left	Lower center	Lower Right
R	2	0.265	0.312	0.275	0.309	0.312	0.322	0.311	0.37	0.345
R	3	0.379	0.424	0.378	0.422	0.378	0.396	0.387	0.421	0.405
R	3.5	0.38	0.428	0.394	0.428	0.429	0.384	0.36	0.371	0.398
R	4.3	0.366	0.316	0.371	0.393	0.337	0.325	0.338	0.295	0.284
		Vertical - 1 pixel/bar sampling								
		Upper Left	Upper Center	Upper right	Left	Center	Right	Lower left	Lower center	Lower Right
R	2	0.298	0.279	0.277	0.289	0.253	0.347	0.358	0.292	0.389

R	3	0.334	0.368	0.323	0.308	0.398	0.408	0.38	0.419	0.375
R	3.5	0.365	0.399	0.388	0.362	0.372	0.333	0.373	0.347	0.363
R	4.3	0.362	0.352	0.322	0.316	0.37	0.266	0.238	0.334	0.231
		Horizontal - 2 pixel/bar sampling								
		Upper Left	Upper Center	Upper right	Left	Center	Right	Lower left	Lower center	Lower Right
R	2	0.669		0.663		0.612		0.649		0.61
R	3	0.695		0.733		0.708		0.727		0.696
R	3.5	0.609		0.667		0.621		0.627		
R	4.3	0.561		0.649		0.651		0.574		0.608
		Vertical - 2 pixel/bar sampling								
		Upper Left	Upper Center	Upper right	Left	Center	Right	Lower left	Lower center	Lower Right
R	2	0.566		0.557		0.637		0.633		0.656
R	3	0.639		0.687		0.656		0.685		0.65
R	3.5	0.614		0.62		0.68		0.692		0.615
R	4.3	0.614		0.601		0.671		0.518		0.581

		Corner avg	Edge avg	Center	Corner Avg - 2x bars	Center avg - 2x bars
R	2	0.315	0.315	0.283	0.625	0.6245
R	3	0.370	0.396	0.388	0.689	0.682
R	3.5	0.378	0.382	0.401	0.635	0.6505
R	4.3	0.314	0.325	0.354	0.588	0.661

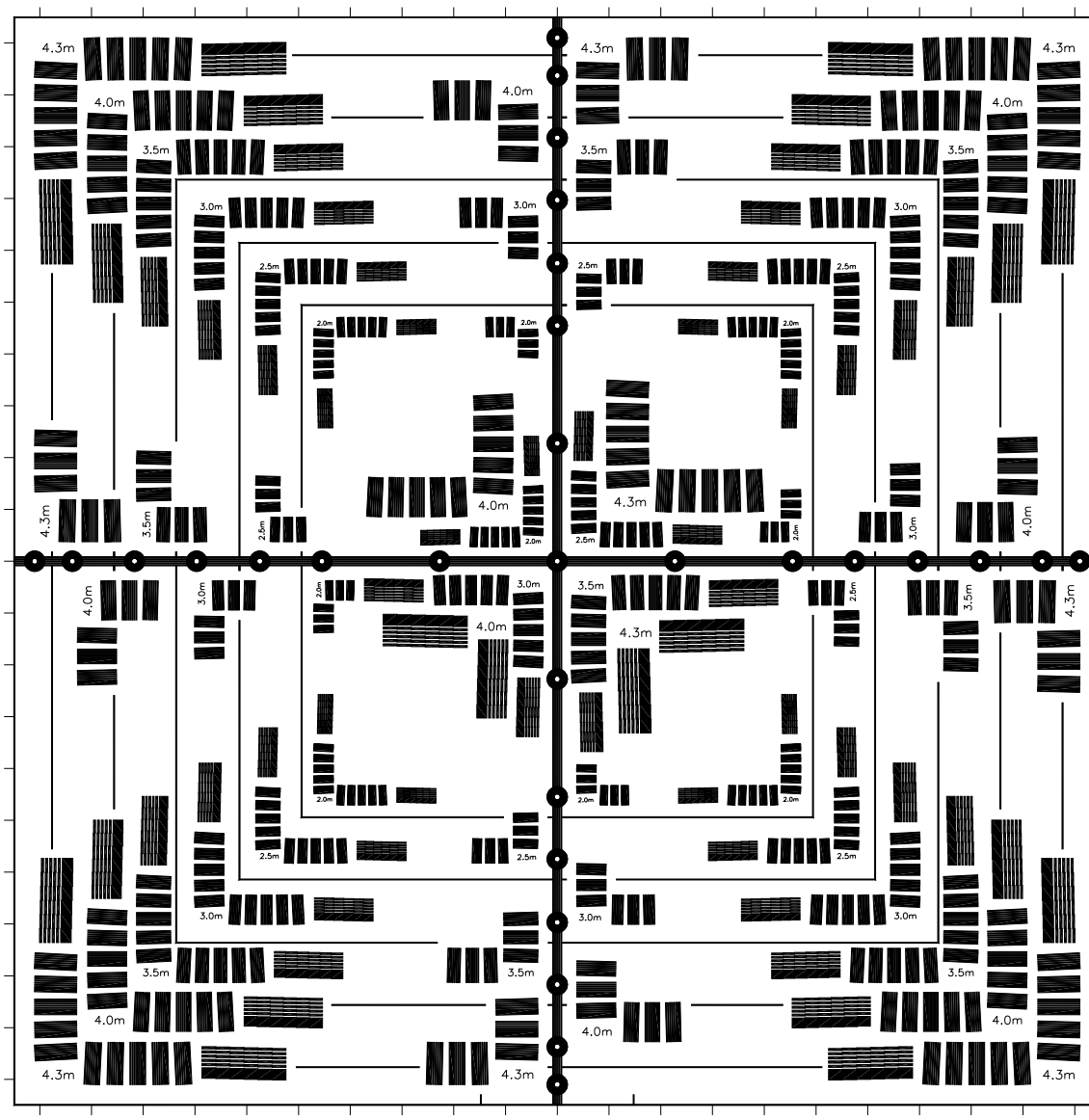

Figure O-1.The MTF test target. Each column is for the distance listed at the bottom. The top row is an MTF beyond what the CCD can sample. The second row (with the line under) is the max resolution, where each line and space is the width of a pixel at that distance. While this is the maximum resolution the camera should be capable of, this row is susceptible to aliasing depending on the phase of the image on the CCD. This phase changes with sub pixel alignment changes of the target to the camera. The bottom row is where the resolution is 60% of the maximum resolution. This row is much less susceptible to aliasing, and was used for the focus test.

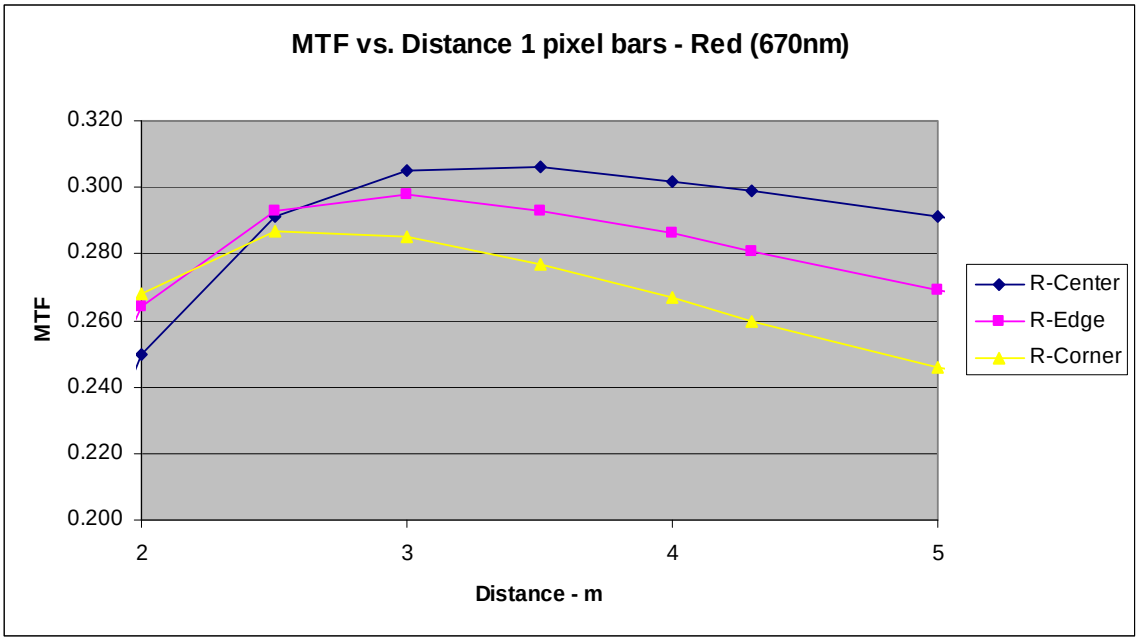

Figure O-2. Theoretical MTF vs. Target Distance (λ =670 nm) for several points on the CCD.

Figure O-3. Theoretical MTF vs. Target Distance (λ =670 nm) for several points on the
CCD for target bars having a width of 2 pixels.

Figure O-4. Theoretical MTF vs. Target Distance (λ =440 nm) for several points on the CCD.

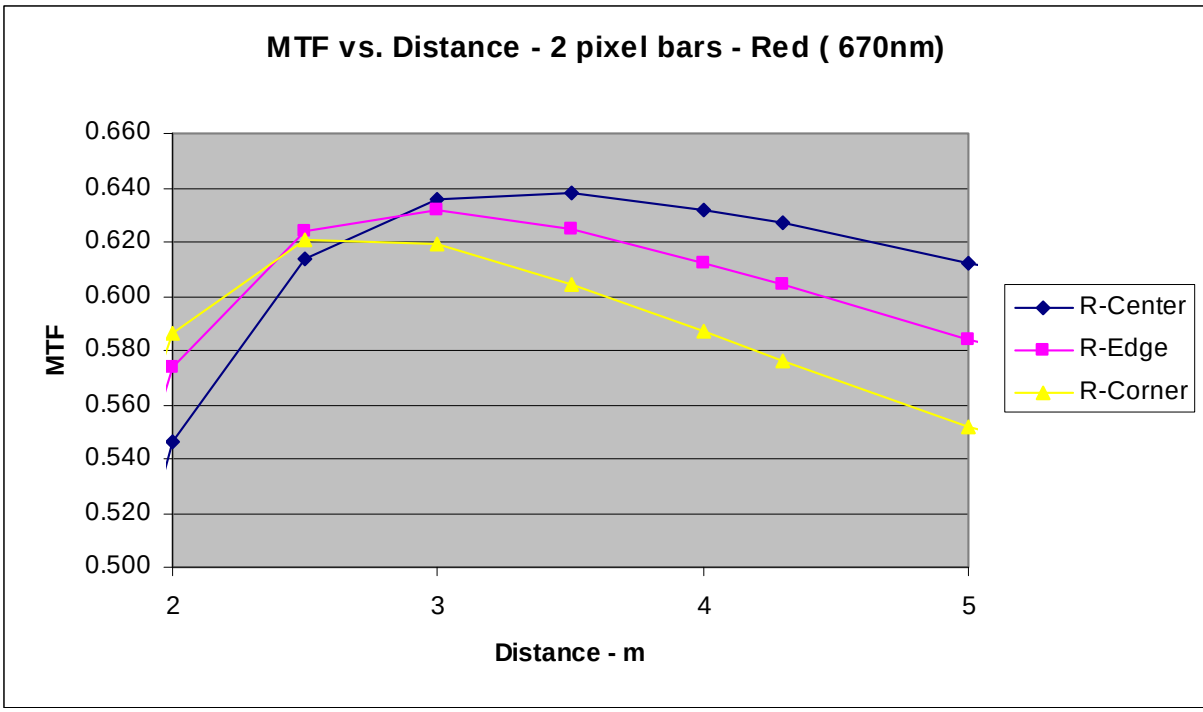

Figure O-5. Theoretical MTF vs. Target Distance (λ =440 nm) for several points on the
CCD for target bars having a width of 2 pixels.

Figure O-6. Measured MTF vs. Target Distance (λ =670 nm) for several points on the left CCD.

Figure O-7. Measured MTF vs. Target Distance (λ =670 nm) for several points on the
right CCD.

Figure O-8. Measured MTF vs. Target Distance (λ =440 nm) for several points on the
left CCD.

Figure O-9. Measured MTF vs. Target Distance (λ =440 nm) for several points on the
right CCD

P - MIPL Camera Model – RR/BD

The SSI camera employs the standard CAHV system for describing the optical and geometric parameters of the left and right eyes, to determine an accurate mapping between the three-dimensional coordinates of points viewed by a camera and the two-dimensional coordinates of the corresponding points on the detectors in the left and right eyes. The CAHV (Center, Axis, Horizontal, Vertical) models are based on the system originally developed by Yakimovsky and Cunningham for extracting three-dimensional measurements from a stereo pair of cameras, later extended by Gennery to include radial distortion and termed CAHVOR (CAHV plus optical, radial).

P.1. Test Setup and Data Acquisition

Each CAHVOR model is based on both on both intrinsic and extrinsic parameters of the camera, as well as on 3D-2D correspondence data described below. The intrinsic parameters, listed in Table P-1, consist of the focal length of the lens, the number of rows and columns in the detector, and the horizontal and vertical pixel spacing in the image plane.

The extrinsic parameters consist of the camera location (usually represented by the lens entrance pupil) in the relevant coordinate system, the camera pointing vector, and the camera up vector (orientation of images). The location is derived from a surveyed position of the camera head, combined with design and fabrication data on the lens and internal mounting. The camera pointing vector is based on the location of the target at which the camera is pointing, and the up vector is based on the image orientation.
The 'ground truth' for generation of the models is based on 3D-2D correspondence data, which consists of accurate locations of 3D points in the camera field of view and 2D locations of those points on the image sensor. To gather this data, a dot array target consisting of a dot grid of known size and spacing is set up in the camera field of view and the 3-D space coordinates of all the dots determined by survey using standard survey equipment. The camera is then pointed in the target direction and fixed, and images acquired of the target at a range of target distances ideally bounding the distances at which the camera will be used. For the SSI cameras, target distances of 2, 3, 4.5, and 8 m were used.
Since the optical characteristics of the left and right eyes differ slightly and since the parameters also vary with wavelength, a separate camera model is required for each surface filter in each eye. Images were thus acquired of the target at all distances in both eyes using all surface filters.

P.2. Data Processing

Intrinsic and extrinsic camera parameters are input to software developed by JPL's MIPL group, along with information about the target and the surveyed locations of the dots. Software locates the target features (dots) using a centroiding algorithm and associates the 2D locations with the 3D locations input separately. The program then performs a least-squares adjustment in which the camera model parameters are adjusted to minimize the sum of the squares of the residuals (differences between measured and adjusted positions of points) in the image plane. This process is repeated for each of the models bawsed on eye and filter number.

Camera model Accuracy

Table P-1. Camera model intrinsic parameters

Parameter	Value	Units
Focal length of lens	5E-2	meters
Number of detector rows and columns	1024	
Horizontal pixel spacing in image plane	1.2E-5	meters
Vertical pixel spacing in image plane	1.2E-5	meters

Table P-2. Derived camera model parameters

SSI Camera Model parameters

Eye	Filter	C1	C2	C3	A1	A2	A3	H1	H2
Left	L1	-0.365740	0.055607	-0.804866	-0.019707	0.999792	0.005334	-4205.562939	453.7537
Left	L2	-0.365788	0.055649	-0.804933	-0.019155	0.999802	0.005431	-4204.759974	453.9055
Left	L7								
Right	R1								
Right	R2								
Right	R6								
Right	R7								
Right	R8								
Right	R9								
Right	R10								
Right	R11								
Right	R12								

		V1	V2	V3	O1	O2	O3	R1	R2
Left	L1	-5.802463	518.494990	4198.399878	-0.025911	0.999413	0.022422	0.000323	-0.0205
Left	L2	-5.611334	518.419365	4197.45423	-0.029999	0.999338	0.020569	0.00034	-0.0157
Left	L7								
Right	R1								
Right	R2								
Right	R6								
Right	R7								
Right	R8								
Right	R9								
Right	R10								
Right	R11								
Right	R12								

Figure P-1. Dot array target used in gathering 3D-2D correspondence data

Figure P-2. Test setup for imaging dot array target at ATLO

General

Q - Power and Mass - RT

R - Cold Start Heating - AS

S - Temperature Calibration - RT

T - Differences between FM and EM cameras - RT

U - SSI FM and EM reference AZ, EL, FW Axis Parameters – RT

V - Image Acquisition and Processing Time -

W - Appendices